UNIVERSITY OF CALIFORNIA,
IRVINE

Electronic Conductivity in Supramolecular Biomaterials

DISSERTATION

submitted in partial satisfaction of the requirements
for the degree of

DOCTOR OF PHILOSOPHY

in Materials Science and Engineering

by

Nicole Leilani Ing

Dissertation Committee:
Professor Allon I. Hochbaum, Chair
Assistant Professor Shane Ardo
Assistant Professor Han Li

2018

DEDICATION

To

My parents, Steven and Lani Ing

TABLE OF CONTENTS

Page

LIST OF FIGURES

Page

Page

ACKNOWLEDGMENTS

First and foremost, I'd like to thank my parents, Steven and Lani Ing, for their amazing love and support. Their continual faith in me pushes me to be the best version of myself, and my accomplishments have been made possible through their love. Without their sacrifices, none of this would be possible.

I would also like to thank my advisor, role model, and mentor, Professor Allon I. Hochbaum, for all of his guidance and support over these past few years. I am truly grateful to him for providing me with the opportunity to work on this incredibly exciting project, and for both the space and guidance he's provided to allow me to grow as a scientist. I thank him for teaching me how to critically analyze scientific problems, an invaluable skill that I will carry with me for the rest of my life. It was truly an honor to learn from him.

I'd like to thank Professor Regina Ragan and Professor Albert Yee for helping me write the National Science Foundation Graduate Research Fellowship proposal that funded most of my PhD, and Professor Martha Mecartney for appointing me a Graduate Assistance in Areas of National Need fellow, making this final year of my PhD possible.

I would like to thank Dr. Tyler D. Nusca for being an incredible mentor and being instrumental to developing my laboratory skills. I would also like to thank Dr. Ryan K. Spencer for synthesizing a host of peptides and for his valuable expertise. This dissertation would not be possible without them both.

I would also like to thank Dr. Mohit Kumar and Dr. Rein Ulijn from the Advanced Science Research Center at City University of New York, and Dr. Tom Guterman and Dr. Ehud Gazit at Tel Aviv University for the opportunity to participate in two fruitful collaborations discussed in this work.

I'd also like to thank the friends who've endured the rigorous journey of grad school with me. I'd like to thank Jackie Unagnst for being the best roommate and friend that I could ever ask for. Our discussions about science, life, and politics kept me grounded and always reminded me of reasons to be thankful. I'd also like to thank Arunima Bhattacharjee, Jasmine Wong, Torin Dupper, Long Phan, Phi Pham, Vinnet Nair, Sophia Lin, Chen Wang, Adrian Garcia, Alex Hwu, and Jacob Fenster for their friendship both inside and outside of the lab. I will value these relationships and the many memories we've made for the rest of my life.

And last, but certainly not least, I'd like to thank my absurdly significant/significantly absurd other, Amir Mazaheripour, for creating meaning for me within the void. I would not be who I am today without him.

CURRICULUM VITAE

Nicole Leilani Ing
2115 Baypointe Drive · Neworport Beach, CA 92660
(808) 282- 4218 · ingn@uci.edu

EDUCATION

University of California, Irvine
PhD in Materials Science and Engineering, GPA 3.995 June 2018
- National Science Foundation Graduate Research Fellow
- Graduate Assistant in Areas of National Need Fellow
- NASA NSPIRES Space Technology Research Fellowship Recipient

MS in Materials Science and Engineering, GPA 4.0 June 2014

Occidental College
BA in Physics, GPA 3.89 June 2012

TECHNICAL SKILLS

- **Surface Property and Imaging Techniques:** atomic force microscopy (tapping, contact, conductive, scanning kelvin probe, and electrostatic force modes), transmission electron microscopy (TEM) microscopy (fluorescence, bright field, reflectance) scanning electron microscopy (SEM), X-ray diffraction (XRD)
- **Spectroscopic and Electrochemical Characterization Techniques:** UV-visible absorbance spectroscopy, fluorescence spectroscopy, attenuated total reflection Fourier-transform infrared spectroscopy (ATR-FTIR), electrochemistry (cyclic voltammetry, chronoamperometry, bipotentiostat operations, *etc*.)
- **Other Characterization Techniques:** rheology, matrix-assisted laser desorption/ ionization (MALDI-TOF mass spectrometry)
- **Biological Techniques:** protein purification, SDS-PAGE, protein assays, bacteria culturing (aerobic and anaerobic strains), biofilm growth (aerobic and anaerobic strains), microbial fuel cells
- **Device Fabrication and Testing:** circuit building and design, photolithography, thermal evaporation, sputtering, clean room processing (mask alignment, plasma etching, spin coating, *etc*.), mask design, field effect transistor measurements
- **Software**: Origin, Excel, COMSOL, Matlab, Mathematica, Solid Works, Design Cad, Lab View, Adobe Illustrator

RESEARCH EXPERIENCE

UCI, Nanomaterials Research:
Conductive Amino Acid Based Materials September 2012 - June 2018
Principal Investigator: Professor Allon Hochbaum

- Founded and Lead project on demonstrating amino acids as building blocks for a novel class of functional materials, with applications in nanoelectronics and bioelectronics interfacing

- Used techniques from environmental microbiology and analytical chemistry to isolate, purify, and characterize bacterial protein
- Used scanning probe microscopy, microfabricated devices, and electrochemistry to characterize structural and conductive features of protein and peptide nanofibers
- Designed peptide nanofiber-enzyme devices for enzyme electrocatalysis and sensing applications
- Participated in several national and international research collaborations

Occidental College, Independent Undergraduate Research:
Solar-Powered Golf Cart 2011-2012

- Wrote and received funding for an independent research project
- Worked with physics lab director to build a solar-powered golf cart
- Programmed and designed an LCD display to track battery life, power consumption, and speed

LIGO, Summer Undergraduate Physics Research:
Gravitational Wave Observatory Summer 2011

Advisor: Dr. Koji Arai

- Designed and built detector to assess vibration isolation of damping system in a LIGO mirror prototype
- Identified cross-coupling noise in mirror design
- Published technical note in LIGO database

Occidental College/Caltech, Summer Undergraduate Materials Science Research:
Sol Gel Synthesis Summer 2010

Advisors: Professor Adrian Hightower, Professor Sossina Haile

- Recipient of NSF Summer Undergraduate Research in Materials Science fellowship
- Explored single crystal growth of solid acid $Ba_{3-x}K_xH_x(PO_4)_2$ for fuel cell applications
- Used sol-gel synthesis to grow macroscopic single crystals for directional conductivity studies

Occidental College, Summer Undergraduate Physics Research:
Fluid Dynamics Simulations Summer 2009

Advisor: Professor Janet Scheel

- Wrote scripts in Python and C++ to track parameters in simulated turbulent systems
- Found geometry-dependent trends for large-scale circulation and heat transfer

PUBLICATIONS AND PATENTS

- **Ing N.L.,** Spencer R.K., Luong S.H., Nguyen H.D., and Hochbaum A.I., "Electronic conductivity in biomimetic□α-heical peptide nanofibers and gels." *ACS Nano*. **2018**, *12*(3), 2652-2661.
- **Ing N.L.**, Nusca T.D., and Hochbaum A.I., "*Geobacter sulfurreducens* pili support ohmic electronic conduction in aqueous solution." *Phys. Chem. Chem. Phys*. **2017**, *19*, 21791-21799.

- Kumar M, **Ing N**, Narang V, Wijerathne N, Hochbaum A, Ulijn R, "Active chemical encoding and pathway selection of transient supramolecular nanostructures." *Nat. Chem*. **2018**, *10*, 696-703.
- Gutterman T., **Ing N.L.**, *et al*., "Electrical conductivity selective adhesion and biocompatibility in bacteria-inspired peptide-metal self-supporting nanocomposites." *In preparation.*
- **Ing N.L.**, El-Naggar M.Y., Hochbaum, A.I., "Going the Distance: Long-Range Conductivity in Protein and Peptide Bioelectronic Materials." *Submitted*
- **Ing N.L.** Hochbaum, A.I. "Bioelectronic Interfacing of Conductive Peptide Nanofibers." *In preparation.*
- Yee AF, Liang E, **Ing N**, Gibbs M, Dickson MN. "Bactericidal surface patterns." U.S. Patent US20150273755 A1, application October 1, 2015.

HONORS AND AWARDS

- **Graduate Assistance in Areas of National Need Fellow** 2017—2018
- **National Science Foundation Graduate Research Fellow** 2013—2016
- **Recipient of the NASA NSPIRES Space Technology Research Fellowship** 2013
- **Phi Beta Kappa** Accepted 2012
- **National Physics Honor Society** Accepted 2012

VOLUNTEERING/LEADERSHIP EXPERIENCE

- **President, Secretary, First-Year Representative** 2012—2016
  ChEMS Graduate Students Association, UCI
  - *Organized career workshop and career panels for graduate students, oversaw outreach programs with Discovery Cube OC, interviewed potential faculty hires, organized student-faculty events, organized prospective PhD student recruitment, coordinated weekly departmental coffee hour*
- **UCI School of Physical Sciences Mentor** 2015—2017
  - UCI School of Physical Sciences Mentorship Program
- **Undergraduate Research Mentor in Hochbaum Lab** 2013—2018
  - *Mentored undergraduate and high school students pursuing independent research in microbial fuel cells*
- **Rocket Science Tutors Volunteer** 2015—2016
  - Henry Samueli Academy
  - *Led afterschool laboratories for middle school students, helped teach engineering classes*
- **Solar Cup Workshop Coordinator** 2012—2015
  - Metropolitan Water District of Southern California

- *Designed and led workshops geared toward teaching high school students math, physics, and electronics for solar-powered boat construction; safety evaluator for solar-powered boats*

TEACHING EXPERIENCE

- **UCI, Teaching Assistant** Fall 2016
  "Crystalline Solids" (Graduate Course)
  - Held weekly office hours to help students understand crystal structure and structure-property relationships
  - Lectured class in place of professor when needed
- **UCI, Teaching Assistant** Winter 2017
  "Nanomaterials" (Graduate and Undergraduate Course)
  - Held weekly office hours to help students understand structure-property relationships of materials at nanoscale.
  - Lectured entire class in place of professor when needed
- **UCI, Teaching Assistant** Spring 2017
  "Optical and Electronic Properties of Materials" (Undergraduate Course)
  - Served as teaching assistant for course of more than 150 students
  - Led multiple weekly discussion sessions to help students understand solid-state physics fundamentals while emphasizing engineering applications
  - Lectured entire class in place of professor when needed
- **Occidental College, Academic Mastery Program**
  Physics Workshop Coordinator 2011—2012
  - Designed weekly workshops to emphasize applications of concepts in class and develop analytical thinking (General Mechanics and Wave Mechanics)
- **Occidental College, Center for Academic Excellence,**
  Physics and Mathematics Tutor 2008—2012
  - Daily tutor for college students, developing their analytical thinking and systematically increase average scores on assignments and exams
- **Occidental College Private Physics and Mathematics Tutor** 2010—2012
  - Tutored high school and middle school students in physics and math, tailoring teaching styles to specific learning needs of individual students, systematically increasing average scores on assignments and exams

ABSTRACT OF THE DISSERTATION

Electronic Conductivity in Supramolecular Biomaterials

By

Nicole Ing

Doctor of Philosophy in Materials Science and Engineering

University of California, Irvine, 2018

Professor Allon I. Hochbaum, Chair

Proteins and peptides may be a promising route to develop conductive materials capable of interfacing biological components with electronics for bioelectronic applications. Amino acid sequences can drive the self-assembly of supramolecular nanostructures, whose high surfaces area, soft material surfaces may be suitable for interfacing with biology. These sequences can be coupled with conjugated small molecules or metals to drive the aqueous self-assembly of water soluble, electronically-conductive nanomaterials, or these sequences, by themselves, can form electronically-conductive supramolecular structures. In this work, we demonstrate long-range, non-redox, and non-thermally activated electron transport in biological protein nanofibers purified from *Geobacter sulfurreducens*, and we replicate these unique conduction properties in non-π-stacked, self-assembled nanofibers constructed from a *de novo* peptide sequence. We demonstrate that natural amino acids can be used to form supramolecular nanofibers with high conductivities, comparable to conjugated materials, in the absence of delocalization. This micrometer-scale transport does not fit within the framework of long-range conduction mechanisms in organic materials, and thus suggests a rethinking of current electron transport models. We also characterize electronic and electrostatic properties in two other amino acid

based supramolecular systems, demonstrating how amino acids can be used to tune the self-assembly and electronic properties of conductive materials. These findings suggest that amino acid based materials may be a viable platform for designing functional bioelectronic materials.

CHAPTER 1 Long-Range Conductivity in Protein and Peptide Bioelectronic Materials

1.1: Introduction

Bioelectronic materials interface biology with synthetic devices by interconverting electronic and biological signals and processes. The biological components interfaced to these materials range from biomolecules[1,2] to cells[3,4] and living organisms[5,6]. By seamlessly bridging the synthetic-living interface, without significant perturbation to biological function, bioelectronic materials may improve our understanding of biological systems or even control their functionality. Bioelectronics promise to enhance and prolong human life through biomedical technologies such as implantable power sources[7,8], wearable sensors[9,10], therapeutic[11,12], and prosthetic implants[13,14]. They can also harness functional biological components, such as enzymes, to enhance the sensitivity of non-biomedical sensors[15–17] as well as improve the efficiency of electrocatalytic syntheses for energy production[18,19] and pharmaceutical applications[20,21].

Bridging the biotic-abiotic interface is nontrivial, and all the aforementioned bioelectronic technologies will benefit from the development of materials that more seamlessly integrate the two. These materials should be biocompatible and stable under physiological conditions while maintaining effective transduction of electronic and biological signals. For interfacing with organs and tissue, the mismatch in mechanical stiffness between electronic and biological components poses compatibility issues for both wearable and implantable bioelectronic devices[22–24]. For catalysis and sensor technologies, immobilization substrates and techniques can interfere with enzyme functionality[25–27].

Peptides and proteins are promising building blocks for materials that address these concerns. They are soft materials capable of self-assembling into nanostructures with highly tunable properties[28–31], including access to a range of dynamic assembly pathways[32] and transient

structures[32,33]. Certain peptides and proteins exhibit excellent biocompatibility in terms of eliciting a minimal immune response[34–36], the ability to be safely degraded/absorbed by the body after use[37,38], and controllable degradation kinetics[39–41]. Additionally, the chemical diversity of peptides allows for highly optimized enzyme immobilization[42,43] and cellular interfacing[44–46]. Many natural and designed proteins and peptides are also capable of self-assembling into supramolecular nanostructures, such as sheets, wires, and tubes[47,48]. The high aspect ratio of these features may offer additional benefits for interfacing with biological components[49,50], and these dimensions can be achieved without the difficulties and costs associated with many more traditional nanofabrication processes[51]. Lastly, some peptide and protein nanostructures conduct electronic charge and are therefore excellent candidates for bridging the bio-electronic interface.

Electronic conduction across individual peptides and proteins may be categorized either as electron transfer or electron transport[52,53] (Fig. 1.1A) and, for the purposes of this review, will be considered "short-range." Short-range *electron transfer (*ET*)* refers to the exchange of an electron that occurs as a redox event between an ionically-conductive electrolyte and a protein in contact with the electrolyte. Ions in solution screen the change in electric potential during electron transfer events. Conversely, short-range *electron transport* (ETp*)* refers to the case in which electrons flow through a protein in the absence of electrolyte or electrolyte participation[52]. Short-range ETp therefore requires electron flow across a protein or peptide between two electronically-conducting electrodes in the absence of charge-screening electrolyte. Short-range ET and ETp are distinct for several reasons. In short-range ET, electron flow is driven by the difference in the chemical potential (i.e. redox potential) between redox-active species. For short-range ETp between two electrodes of the same material, an externally-applied electrical potential difference drives electron flow, and this transport typically occurs under dry or vacuum, as opposed to aqueous, conditions.

Short-range ET and ETp are also distinct because ET requires a change in charge state, whereas, for the most part, ETp preserves electroneutrality. Cahen *et al.* have demonstrated that the primary models used to understand short-range ET are also applicable to short-range ETp through single peptides and proteins[53].

Although these models were developed for single molecules, it is unclear how these short-range mechanisms extend to transport across longer distances, such as through supramolecular structures. Developing an understanding of the transport mechanisms across supramolecular structures, as opposed to single molecules, is critical to designing better bioelectronic interfaces. Long range electronic conduction can be formulated in terms of sequential ET processes[54], but this model invokes strong coupling between electronic states typical of inorganic, not biological, materials. In practice, however, there are many examples of long range electronic transport through extended supramolecular structures of peptide and protein building blocks[55–60]. The physical mechanisms supporting electronic conduction in these materials are often poorly understood.

In this review, we will discuss examples and mechanisms of electronic conduction occurring over micrometer or longer length scales in supramolecular protein and peptide structures. We will categorize electronic processes at these length scales as "long-range" to distinguish them from the ET and ETp observed through single molecules, which we will refer to as "short-range." We note that single molecule ETp has been previously identified as "long-range," given the impressive tunneling distances observed through single molecules[61,62], but such mechanisms over micrometer distances would yield vanishingly small currents inconsistent with experimental observations. As a result, we maintain this distinction since the operative mechanisms within the two transport distance regimes are likely distinct. Our discussion of short-range ET and ETp through single proteins and peptides will be brief and discussed in the context

of building an understanding of longer-range mechanisms. We direct interested readers to several excellent reviews on short-range ET[63–66] and ETp[52,53] through peptides and proteins.

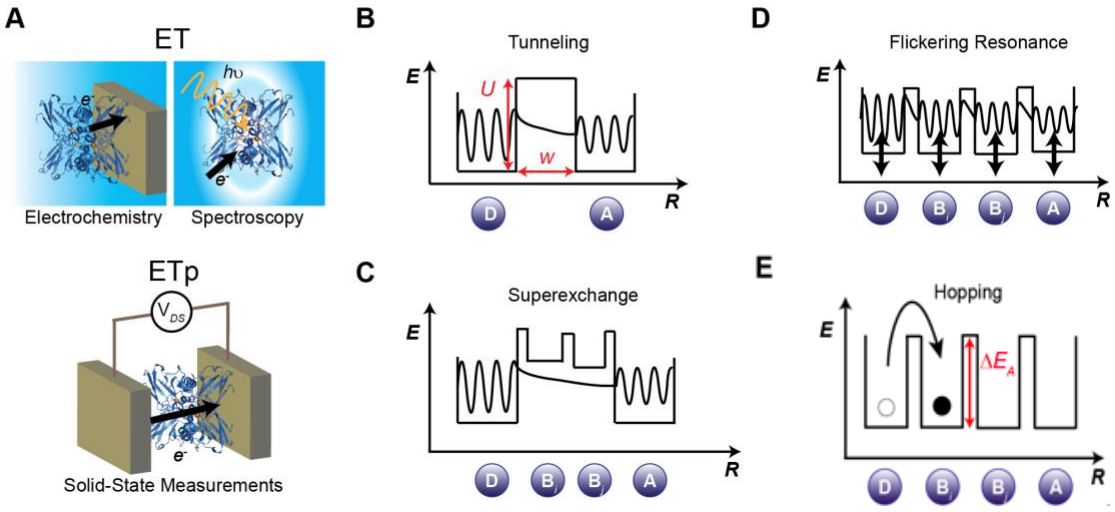

Figure 1.1: Mechanisms of short range electronic conduction. (A) Schematic showing ET measurement techniques in electrolyte (*top*) and solid-state ETp measurements between two electrodes under low pressure or ambient conditions (*bottom*), with *Pseudomonas aeruginosa* azurin (**PDB 4AZU**). Energy diagrams representing the electron wave function in relation to the donor *D*, acceptor *A*, and bridge *B* states during single-step tunneling (B), superexchange (C), and flickering resonance (D). Energy diagram representing the localization of the wave function or particle-like behavior of the electron during hopping, with an activation energy barrier ΔE_A. (E).

1.2: Mechanisms of Short-Range Electron Conduction

Short-range (angstrom to nanometer) ET and ETp through peptides and proteins have been extensively studied from both a biological and molecular electronics perspective. Proteins almost exclusively conduct through ET in their native environments, but many of them also support short-range ETp when removed from their natural environments and integrated into solid-state junctions, demonstrating conductivity comparable to conjugated molecules across distances spanning several nanometers[52,53,67]. The solid-state ETp mechanism through a protein need not be the same its biological ET mechanism, although experimentally, ET and ETp characteristics are correlated[68,69] and there is likely a fundamental connection between the two processes[53].

Short-range ET and ETp in protein and peptide materials can be described using an electron donor (D) and acceptor (A) model, in which D and A can be coordinated metal atoms, amino acids, electrodes, or small organic molecules[70]. We will start by briefly introducing the single-step D to A electron transfer process described by Marcus Theory[71,72], which is the underpinning for the three major ET/ETp short-range mechanisms: superexchange, flickering resonance, and hopping.

1.2.1: Tunneling

Nonadiabatic tunneling is a single step electron transfer process between a D and A (Fig. 1.1B). The ET reaction rate k_{ET} depends on $-\Delta G^0$, the driving force for electron transfer between D and A, λ, the total nuclear reorganization energy associated with the electron transfer, and H_{AD}, the temperature-independent tunneling transmission coefficient:

$$k_{ET} = \frac{2\pi}{\hbar(4\pi\lambda kT)^{1/2}} {H_{AD}}^2 e^{-\frac{(\Delta G^0+\lambda)^2}{4\lambda kT})} \qquad \text{(Equation 1.1)}$$

In the square barrier tunneling model, which has been strongly supported by experimental evidence[73], H_{AD} is defined by an exponential decay with regards to distance, R-R_0, and has a β decay constant proportional to the barrier height U:

$$H_{AD} = Ae^{-\beta(R-R_0)/2} \qquad \text{(Equation 1.2)}$$

$$\beta = 2(Um_{eff})^{1/2} \qquad \text{(Equation 1.3)}$$

$$A = 2U(Um_{eff})^{1/2} \qquad \text{(Equation 1.4)}$$

where m_{eff} is the effective mass of the electron. Thus,

$$k_{ET} \propto e^{-\beta(R-R_0)} e^{-\frac{(\Delta G^0+\lambda)^2}{4\lambda kT})} \qquad \text{(Equation 1.5)}$$

The ET rate decays exponentially with the distance between D and A and has a temperature dependence $(k_{ET} \propto T^{-\frac{1}{2}} e^{-\frac{energy}{kT})})$, the effect of which is predominantly dependent on the

relationship between ΔG^0 and λ. The maximum ET rate is achieved when $\Delta G^0 + \lambda = 0$, at which there is no temperature-dependent activation barrier to transport. Indeed, when ΔG^0 and λ are comparable, k_{ET} is essentially temperature-independent[54,74]. The ET rate is therefore dominated by an exponentially decaying distance dependence, and conductance can be expressed solely as a function of distance[75]

$$G = G_c e^{-\beta R} \qquad \text{(Equation 1.6)}$$

where G_c is the contact conductance. Gray and Winkler have estimated 20 Å to be the upper limit for efficient biological ET[76], while Dutton places the limit at 14 Å[77]. Remarkably, ETp tunneling distances up to several nanometers have been experimentally observed. This difference may be attributed to the difference between electron flow in a charge neutral environment and one in which a localized state undergoes a change in the formal charge state, associated with ETp and ET, respectively[53].

Multistate ET models have been developed to explain biological charge transport occurring over longer distances, such as in respiratory chain complexes. Charge transport in these systems is achieved through chains of redox-active cofactors, conjugated molecules, or metal ions that can act as sites for the formal exchange of localized charge. Adjacent cofactors are situated within tunneling distances to facilitate consecutive tunneling steps or a single tunneling event across several states. These multistate ET models have also been used to describe mechanisms of solid-state ETp through single peptides and proteins[53], namely superexchange, flickering resonance, and hopping.

1.2.2: Superexchange

The superexchange model (*SE*) is a single step tunneling mechanism in which there may be multiple bridge states in between D and A (Fig. 1.1C). In this mechanism, thermal fluctuations

bring the D and A levels into resonance (i.e. the D and A levels become energetically degenerate), causing the electron to tunnel along the bridge states from D to A. The bridge states remain off-resonant during ET, meaning that the electron does not populate the bridge. Rather, the bridge states collectively increase the electronic coupling between D and A, effectively lowering the tunneling barrier. The coupling constant is therefore similar to that of tunneling

$$|H_{AD}|^2 \propto e^{-\beta(R-\Delta R)} \qquad \text{(Equation 1.7)}$$

where ΔR is the spacing between each state for *N* states ($\Delta R = R/(N+1)$). ET rates via SE share a similar weak or negligible temperature dependence with standard tunneling. They also exhibit an exponentially decaying dependence on distance, albeit slightly weaker than that of tunneling since the β term for SE is distinct from the square barrier tunneling term (Equation 1.3)

$$\beta = \frac{2}{\Delta R} ln \left| \frac{\Delta E_{D/A} - \Delta E_B}{V} \right| \qquad \text{(Equation 1.8)}$$

The SE decay term scales inversely with between-site spacing and is proportional to the ratio of the energy spacing between the D/A and bridge levels $\Delta E_{D/A} - \Delta E_B$ and the electronic coupling between sites V [63].

1.2.3: Flickering Resonance

Beratan and coworkers recently reformulated the discussion of ET, introducing an alternative short-range, single-step transport mechanism known as flickering resonance (*FR*)[78] (Fig. 1.1D). In FR, the D, A, and bridge sites are simultaneously brought into a temporary resonance. This is distinct from SE, where the bridge states remain off-resonant (unoccupied) during ET, and it is distinct from hopping since the coherence of the wave function is maintained.

FR may be possible when the D, A, and bridge energy levels are similar, such that thermal fluctuations of these states occurs on the same scale as the energy gaps between the states (~tenths

of an eV)[79]. The vibronic broadening of these energy levels may facilitate a transient and simultaneous alignment between all of the D, A, and bridge states, which would then allow for what Beretan *et al*. refer to as ballistic charge transfer[78,79]. The ET rate for FR is given by

$$k_{ET} = \frac{2\pi}{\hbar(4\pi\lambda kT)^{1/2}} V^2 P_{match}(2) \qquad \text{(Equation 1.9)}$$

where $P_{match}(2)$ is the probability of matching between two electronic states, such that the difference between the D and A energy levels is less than the electronic coupling *V*. Extending FR resonance across multiple states, the probability of matching *N* site energies decreases multiplicatively by one multiplier per site[78]. In the nonadiabatic limit (specifically, the case in which coupling energy fluctuations V_{rms} are smaller than site energy fluctuations σ_E) the matching probability $P_{match}(N)$can be expressed as

$$P_{match}(N) \approx e^{-\Phi(R)} \qquad \text{(Equation 1.10)}$$

$$\Phi = \frac{1}{\Delta R} ln\left[\sqrt{\frac{\pi}{2}}\frac{\sigma_E}{V_{rms}}\right] \qquad \text{(Equation 1.11)}$$

Here, the distance between adjacent sites ΔR scales inversely with the total distance of the system, facilitating a weaker distance dependence than tunneling and one similar to that of SE. FR is expected to occur over nanometer-scale distances[78], although it may have implications for longer-range biological charge transport[79]. Distinct from tunneling, the distance decay exponent Φ has a temperature dependence. Since σ_E increases with temperature and V_{rms} has a weak temperature dependence, the FR decay exponent Φ should increase with temperature, such that the electron transfer rate decays faster with distance as temperature increases.

1.2.4: Hopping

Hopping is a multi-step ET process, in which charge is transferred through a series consecutive tunneling events (Fig. 1.1E) (i.e. tunneling between individual and sequential bridge

states). In contrast to SE and FR, charge hopping is incoherent, with a localized charge temporarily residing at each site before hopping to the next via oxidation (or reduction). The hopping model is essentially a multistep tunneling model, the efficiency of which is dependent on the driving forces motivating electron flow and the particular arrangement of the redox centers[62]. These redox centers are localized molecular units that can undergo formal electron transfer and the nuclear reorganization associated with a change in charge state. This localization will occur when the Boltzmann probability of occupying a bridge state between D and A exceeds the probability of a single tunneling event between D and A. Since room temperature kT ~ 26 meV and a typical protein β ~ 1.2 Å^{-1} [74], hopping is expected to occur for distances greater than 30 nm and for energy activation barriers (ΔE_A) ~ 1 eV, such that $e^{-\frac{\Delta E_A}{kT}} > e^{-\beta R}$ (Fig. 1.1E)[79].

In this collection of tunneling events, k_{ET} no longer exhibits an exponential dependence on distance, instead varying inversely with the number of hopping steps N and the hopping rate k_N [75,80],

$$k_{ET} \propto k_N N^{-\eta} \qquad \text{(Equation 1.12)}$$

where η may take on values between 1 and 2.

Hopping has a much stronger thermal dependence than a single tunneling event. Since the wave function is momentarily localized at each state, thermal activation is required to bring the next state into energetic alignment and facilitate the next redox event. Hopping therefore has an exponential temperature dependence that can be expressed in terms of the activation barrier ΔE_A. This is known as an Arrhenius temperature dependence, in which increased temperature facilitates an increase in conduction[75].

$$G \propto e^{-\frac{\Delta E_A}{kT}} \qquad \text{(Equation 1.13)}$$

1.3: Mechanisms of Long-Range Electron Conduction

The above short-range mechanisms for single peptides and proteins may have some relevance to electronic conduction on the micrometer-scale through supramolecular assemblies, although the transition from single peptide or protein to multiple peptides or proteins warrants a similar expansion of ET and ETp definitions (Fig. 1.2). As discussed above, for single peptides and proteins, ET and ETp can be distinguished by the presence or absence of electrolyte participation. Extended to supramolecular or multi peptide/protein systems, long-range ET can be modeled as a series of sequential short-range ET events, such as a series of redox hopping, FR, or SE events, where each event constitutes electron transfer to a non-degenerate energy state (Fig. 1.2A). For a series of adjacent redox hops between discrete, localized states, known as "nearest neighbor hopping" or thermally-activated hopping[54,81,82] (Fig. 1.3A), long-range conductivity σ follows the Arrhenius temperature dependence seen in multistate hopping through a single peptide or protein:

$$\sigma \propto e^{-\frac{\Delta E_A}{kT}} \qquad \text{(Equation 1.14)}$$

For a series of FR (Fig. 1.3B) or SE (Fig. 1.3C) events, in which hopping occurs between partly delocalized states and is thus considered to be "variable range"[83–85], conductivity is expected to scale as

$$\sigma \propto e^{-(\frac{T_0}{T})^{1/4}} \qquad \text{(Equation 1.15)}$$

It may be difficult to distinguish between adjacent redox hops between localized states and hops across delocalized states (via a series of FR or SE events), since supramolecular biomaterials are much more sensitive to thermally-induced structural changes than the solid materials for which the

theory of variable range hopping was developed. Particularly in the case of FR, the theoretical temperature dependence of Equation 1.15 may compete with opposite temperature trends associated with Equation 1.11, convoluting the overall expected temperature dependent trend. Barring high resolution structural data over the full range of temperatures tested, it may be difficult to control for structural-induced conductivity changes which may occur over the range of temperatures required to experimentally resolve between thermally-activated and variable range hopping. Nevertheless, the possibility of sequential SE or FR may be inferred if the distances and differences in energy levels between adjacent electronic states are sufficiently small, and if kinetic calculations for nearest neighbor hopping are inconsistent with experimental observations[79,85].

Conversely, long-range ETp can be analogously defined as continuous electron flow through degenerate electronic states, in which the states may be indistinguishable and take the form of electronic bands (**1.3.2**) (Fig. 1.2B, 1.3E). However, this technical distinction has not been established in nomenclature, where terms such as the mitochondrial or photosynthetic "electron transport chain" refer to a series of redox events technically constituting sequential ET processes, as opposed to ETp. Thus, we will focus this review on identifying possible long-range conduction mechanisms, in lieu of a long-range ET vs. ETp classification. In this section, we will discuss amino acid-based materials and their potential mechanisms of conduction over long distances (> 1 μm).

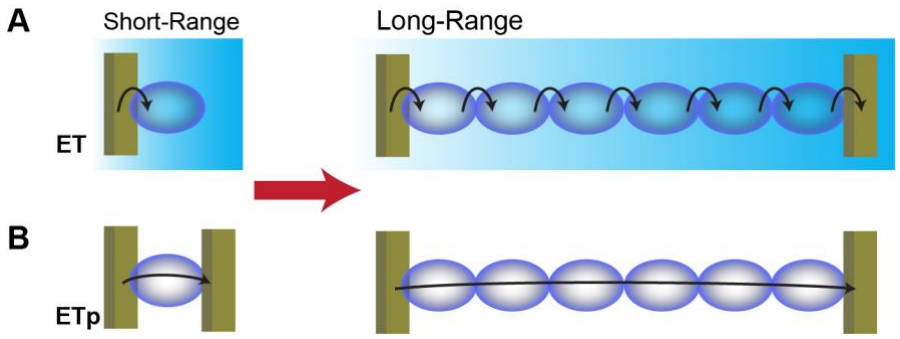

Figure 1.2: (A) Extending short-range ET through a single peptide or protein to long-range transport through multiple peptides or proteins constitutes a series of short-range ET events. (B) Short-range ETp can be analogously extended to constitute long-range band-like transport through multiple peptides or proteins.

1.3.1: Long-Range Conduction via Redox Centers

Extending biological redox-mediated conduction across longer distances (i.e. from nanometers to microns) typically invokes a thermally-activated hopping mechanism (Fig. 1.3A), analogous to that observed in short-range ET (Equation 1.14). However, as discussed above, it may also be possible to achieve this conduction through sequential FR or SE steps, if, for each step, the distance between redox centers is sufficiently short for effective tunneling ($\leq$ 20 Å) and if the energy levels of the redox centers are similar[79].

In peptides and proteins, these redox centers may be bound cofactors, the metal centers of metalloproteins, or redox-active aromatic side chains[77,80]. These redox centers can facilitate both short-range and long-range ET by acting as stepping stones for nearest-neighbor hopping, where each step constitutes a redox reaction. While oxidation of the amide bond backbone is highly energetically unfavorable, hemes, iron-sulfur, and copper clusters in metalloproteins have low redox potentials (less than 400 mV vs. NHE) suitable for redox reactions in physiological conditions[86]. The oxidation potentials of aromatic amino acid side chains may likewise be suitable for facilitating electron hopping, particularly those of tyrosine and tryptophan[87–89] , with redox potentials ~ 1 V vs. NHE[90]. Histidine may also potentially function as a redox-active amino acid,

with a redox potential ~1.17 V[91], although it has been implicated only in poorly efficient ET processes[89,92]. Phenylalanine has recently been proposed as a potential relay amino acid, although the redox potential of alkylated phenyl groups is notably higher ~2 V[93]. It is important to note, however, that the measured redox potentials and reorganization energies associated with these amino acids are highly sensitive to their molecular and solvent environment[87]. In biological charge transfer between aromatics, this electron transfer typically requires a coupled proton transfer event to help reduce the energetic costs associated with a change in the charge state[94–96].

For a material with fixed redox centers, a concentration gradient or electric field can act as a driving force for hopping (Fig. 1.3A), analogous to that observed in redox polymers with discrete redox centers[97–99]. In this model, which has been implicated in biological charge transfer through some bacterial communities[100–102], a redox gradient (i.e. concentration gradient between oxidized and reduced species) provides the driving force for long-range charge transport. Current across the material can be measured and maximized by situating the material between two electrodes and applying a potential near the formal potential of the redox cofactors. Ions in solution will screen the potential applied across the entire material, but redox centers near the electrodes are capable of direct oxidation or reduction. Consequently, the material will develop a concentration gradient of reduced and oxidized species under steady-state conditions, and this gradient provides a driving force for hopping. In the absence of electrolyte and/or ion screening, an applied electric field can provide the driving force for electron flow across a redox-active material.

If the redox centers have some mobility, either through flexibility of their linker chains or solution solubility, diffusion may also contribute to the redox gradient and subsequent electron flow[103,104] (Fig. 1.3D). Diffusion-assisted hopping is particularly relevant in cases where the redox centers are spaced too far apart to facilitate consecutive tunneling between adjacent redox sites

(thermally-activated hopping). The conduction path can be divided into bounded diffusion and hopping components, whereby hopping dominates at high concentrations of redox-active moieties and bounded diffusion dominates at low concentrations. Conductivity scales linearly with the concentration of redox-sites and may exhibit a similar temperature dependence as thermally-activated hopping[98].

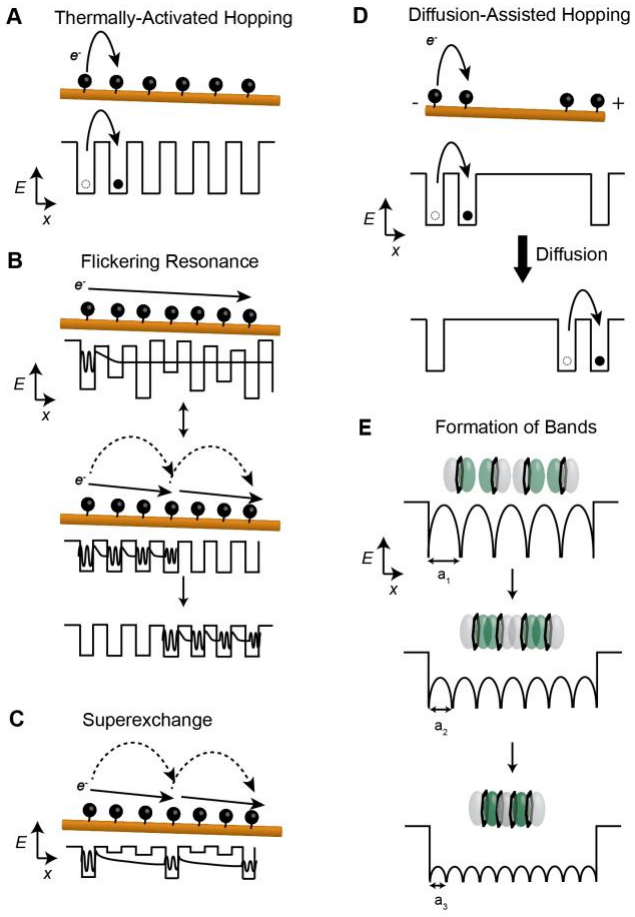

Figure 1.3: Potential mechanisms for long-range electron transport through peptide and protein supramolecular structures. Redox centers or aromatic moieties may facilitate hopping mechanisms, which can be (A) between adjacent and discrete electronic states, known as thermally-activated hopping or between partly delocalized states and occur through a series of (B) flickering resonance or (C) superexchange steps. In each flickering resonance step, thermal fluctuations temporarily bring discrete states into short-lived coherence, and hopping occurs between a series of transient coherent states. Multistep superexchange constitutes a series of tunneling through delocalized states. If the redox centers have some mobility, electron transport may occur through a diffusion-assisted hopping mechanism (E), in which a redox gradient provides a diffusive driving force to assist in hopping over longer distances. (F) Aromatic

side chains may also facilitate band formation, given sufficient electronic overlap between adjacent states. Increasing the amount of overlap between aromatic residues lowers the height and width of the barrier between them ($a_1 < a_2 < a_3$), until the barriers effectively disappear at a finite temperature and a continuous, delocalized band emerges.

1.3.2: Long-Range Conduction via Delocalized States

Long-range conduction can also occur through the formation of bands, electronic states which are delocalized across the entire material. In these delocalized states, the dynamics of charge carriers (electrons or holes) are no longer governed by the discrete state equations described by Marcus Theory (Equations 1.1 to 1.13). Band like conductivity, σ, is expressed as

$$\sigma = ne\mu \qquad \text{(Equation 1.14)}$$

where n is the charge carrier density, e is the elementary charge, and μ is the carrier mobility. This formulation describes ohmic carrier transport, in which free (conducting) electrons or holes can be modeled as classical particles moving in continuous bands of delocalized electronic states.

Band formation occurs in crystalline or otherwise highly periodic organic materials. These bands can be considered metallic, semiconducting, or insulating, depending on the band gap energy, E_g, *i.e.* the energy required to generate free charge carriers. The electronic properties of conventional solids are determined by E_g near the Fermi level, E_F, the energy between the highest occupied and lowest unoccupied states at $T = 0$ K. Metallic conductors have no band gap near E_F and electrical conductivity scales inversely with temperature (Fig. 1.4A). For semiconductors, $E_g \leq 4$ eV near E_F and electrical conductivity scales with temperature in an Arrhenius dependence as more free charge carriers are thermally excited from donor/acceptor ionizable impurities and across the band gap[105] (Fig. 1.4B). Although electron hopping conduction also exhibits an Arrhenius dependence, these two mechanisms are distinct in that hopping occurs between localized electronic states, whereas semiconducting transport occurs over a continuum of states delocalized over part or all of the material. If E_g is small (less than 0.2 eV), transport may exhibit little or no

temperature dependence near room temperature and a strong temperature dependence, similar to that observed for thermally-activated hopping, at low temperatures[106]. If E_g exceeds ~ 4 eV near E_F, the material is considered to be electronically insulating (Fig. 1.4C).

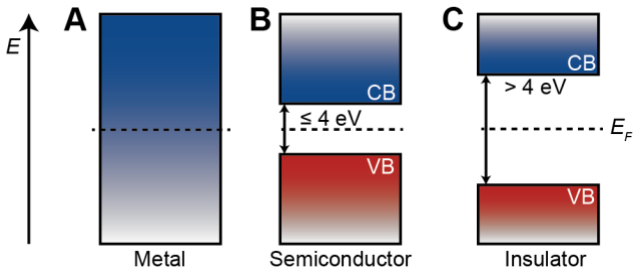

Figure 1.4: Band diagrams for a (A) metal, (B) semiconductor, and (C) insulator.

In peptides and proteins, the periodicity of the peptide backbone produces band gaps which are calculated to range from semiconducting (≤ 4 eV) to insulating (> 4 eV)[107–109]. E_g may be lowered by incorporating aromatic residues to promote delocalization through π-π orbital interactions, called π-stacking. The resulting electronic orbital overlap contributes to the formation of delocalized states, given that the twist angle and distances between aromatic residues (≤ 3.4 Å) are optimized[106]. π-stacking supports semiconducting or metallic-like delocalized electron transport in organic conducting polymers and may facilitate similar transport in peptides and proteins if *(1)* the distance and torsional angles between neighboring aromatics is sufficient for delocalization between adjacent residues and *(2)* if the π-π interactions possess the long-range periodicity required to facilitate delocalization along the length of the supramolecular structure. If the π-stacking periodicity is broken or localized such that it is insufficient to support band-like transport between electrode distances, long-range conduction may still occur through thermally-activated hopping between discrete adjacent states (Fig. 1.3A)[110], analogous to the sequential redox

hopping observed in cofactor chains. FR (Fig. 1.3B) has been proposed as another possible mechanism to form extended band-like states, as a consequence of short-lived (~fs) coherences, yet it has not been experimentally verified beyond nanometer distances and may instead may be coupled to a hopping process to achieve micrometer-scale distances[78,79]. Notably, the distance between natural (proteinogenic) aromatic amino acid side chains in folded proteins and peptides typically exceed the 3.4 Å upper limit for efficient π-orbital delocalization[111–113], making hopping a more likely mechanism for transport through supramolecular peptide and protein structures composed of natural amino acids, provided that the oxidation potentials are suitable to allow efficient multi-step hopping, as discussed above. More efficient overlap may be obtained through the incorporation of conjugated small molecules **(section 1.4.2.1)** or non-natural (non-proteinogenic) amino acid side chains **(section 1.4.2.2)**.

1.3.3: Chemical Structure of Peptides and Proteins Affecting Short-Range Electronic Conduction

Chemical features of peptides and proteins reduce the activation barrier to short-range charge transport by variation of the HOMO and LUMO energies and/or enhancement of intramolecular electronic state coupling[114–116]. Although these contributions have only been demonstrated for single step tunneling and multi-step hopping mechanisms over nanometer length scales in short chain peptides, they may have relevance to lowering barriers to long-range transport through a supramolecular system over micrometer length scales.

Side chain chemistry strongly affects short-range ET and ETp. Aromatic amino acids, including tryptophan and tyrosine, can enhance ET (or ETp) rates through single molecules by lowering the energy barrier for tunneling and improving electronic coupling to electrode

contacts[115]. Tyrosine and tryptophan can also act as redox relay stations to facilitate biological ET reactions[94,117,118]. Biological ET involving aromatic amino acid oxidation in electrolyte may require the energetic stabilization of coupled proton transfer[96,119,120]. Charged side chains also affect short-range ET and ETp. Protonation of amine side chains has been demonstrated to lower the tunneling barrier for ETp through single peptides[114,121]. For short-range ET mechanisms, in which coordinating ions may affect charge migration, protonation of the amine groups can either increase or decrease the rate of transfer through a single peptide, depending on the coulombic interactions between charges. Protonation near a positively charged electron acceptor increases the ET rate, whereas protonation near an electron donor, such as tyrosine, which releases a proton during oxidation, lowers the ET rate[122].

Helical secondary structures, such as α- and 3_{10}-helices, significantly enhance short-range ET and ETp in individual peptides and monolayers. In homopeptides, ETp through a helical configuration is up to 400 times greater than through the equivalent random coil[114] Density functional theory (DFT) calculations suggest that this difference is due to a decrease in the HOMO-LUMO gap, and that torsional angles between amide groups in helical structures enhance electronic coupling through amide bonds along the peptide backbone relative to non-helical structures[116].

Secondary structure may also affect short-range ETp and ET by determining the strength of the molecular dipole present along a peptide or protein structure, with the direction of the dipole oriented from the C- to N-terminus. The effect of the dipole is most prominent in helical structures, with the molecular dipole increasing by 5.0 and 4.5 D per residue in α- and 3_{10}-helices, respectively. Conversely, for β-strand structures, the molecular dipole only increases by 0.25 D per residue[123]. Consequently, the dipole moment may significantly improve ET through single α-

helical peptides, with an observed 5 to 27 fold increase in ET rate along the dipole (C to N) relative to ET against it (N to C)[124]. These directional differences are not observed in random coil peptides, where the net dipole is approximately zero. Spectroscopic studies and *ab initio* calculations indicate that this dipole moment may also lower the oxidation potentials of amide groups at the C-termini of α- and 3_{10}-helices, potentially facilitating a hopping mechanism through amide groups and hydrogen bonds[126,127].

1.4: Peptide and Protein Materials Exhibiting Long-Range Electronic Conductivity

In the following sections we discuss examples of supramolecular peptide and protein structures demonstrating long-range electronic conduction. As this field lies at the intersection of electronics and biology, its achievements are motivated from both a molecular electronics perspective and a desire to replicate and understand natural charge transport phenomena. We will present both biological and synthetic systems composed of natural and unnatural components. It is important to note that the femto to sub-femtosecond details exclusive to distinct electron transport processes are either difficult or currently impossible to experimentally resolve[63]. Thus, we can only indirectly infer the role of a mechanistic model based on structure and observable parameters, such as the temperature or distance dependence of transport. Moreover, the application of complimentary and independent methods of structure and transport characterization are necessary to adequately support a proposed mechanism of conduction. Lastly, it is possible that multiple mechanisms interplay within a particular system, especially under different experimental conditions, and our discussions are limited to identifying the dominant, rather than exclusive, mechanism from available experimental data.

1.4.1: Cofactor-Based Conductors

In nature, biological long-range electronic conduction primarily occurs through redox chains, such as photosynthetic[128,129] and respiratory systems[130,131]. Conduction via this paradigm is predominantly attributed to electron hopping from cofactor to cofactor along the length of a supramolecular scaffold. The cofactors are typically porphyrins, metal clusters, redox-active small molecules, or redox-active side chains that act as stepping stones for micron-scale transport. As discussed in **section 1.3.1**, the mechanism of transport – multistep tunneling (hopping) or diffusion-assisted hopping – depends on the distances between cofactors. FR may also be a possible long-range transport mechanism, but its role in mediating transport beyond several nm remains speculative, and, as discussed above, FR may be coupled to hopping when applied to farther distances.

Long-range transport has been observed in microorganisms, some of which have evolved extracellular respiratory pathways utilizing immobilized redox cofactors capable of delivering current across micrometer distances. One of the most commonly studied species is the anaerobic microbe *Geobacter sulfurreducens* (Fig. 1.5A), which forms electrically conductive biofilms (Fig. 1.5B) that have been used in microbial fuel cells to produce electricity from organic material[132]. These biofilms can generate the highest current densities of any monoculture species[133,134] and utilize cytochromes, heme-containing proteins (Fig. 1.5C-E), to facilitate current production[135,136]. In *G. sulfurreducens* biofilms, these cytochromes form a stratified redox gradient to drive hopping charge transport[100,137]. This type of gradient-driven electron transport (Fig. 1.3D) may be a useful motif for bioelectronics applications, as it has demonstrated energy storage utility in redox-active polymers[138,139].

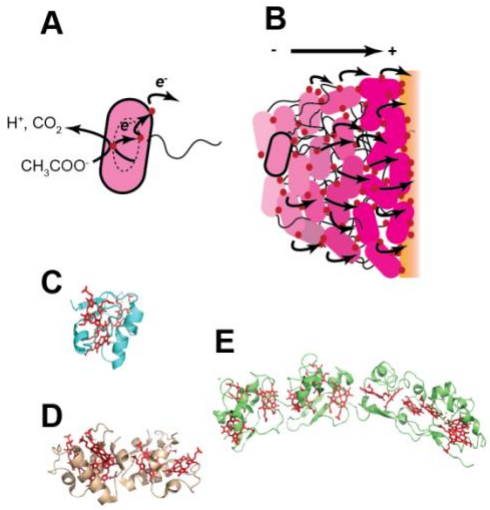

Figure 1.5: (A) Schematic illustrating *G. sulfurreducens* bacterium metabolism and (B) predominantly redox-gradient-driven electron transport through *G. sulfurreducens* biofilm. Crystal structures of a few of many *G. sulfurreducens* cytochromes: (C) PpcA (**PDB 2LDO**), (D) PpcD **(PDB 3H4N)**, and dodecahmeme GSU 1996 cytochrome **(PDB 3OV0)**. Heme residues are shown in red.

These scaffolds have also been replicated in synthetic peptide and protein systems, in which redox-active molecules have been appended to self-assembling peptide and protein sequences to form conductive nanostructures. Inspired by redox-mediated current production in *G. sulfurreducens* biofilms, Altamura *et al.* created nanofiber films from a chimeric protein composed of an amyloid sequence, known to self-assemble into fibers, and a redox-active protein, rubredoxin (Rd), which contains a $Fe^{2+/3+}$ active site, chelated by four cysteines[140]. The 1 nm distance between iron centers is sufficient for a hopping mechanism (Fig. 1.3A), although the flexibility of the amyloid domain N-terminus, connected to the Rd, permits some mobility of the redox site and therefore suggests some dynamics associated with charge transfer, for which a diffusion-assisted hopping mechanism may be relevant. This flexibility may slightly alter the ET rate relative to more rigidly-bound redox centers, but the exact k_{ET} was not measured. Films cast from these fibers exhibited wet conductivities of 3.1 μS/cm and dry conductivities of 2.4 μS/cm, which are comparable to conductivities of peeled *G. sulfurreducens* biofilms[57]. These chimera

nanofibers were also able to reduce oxygen via electron transfer from the electrode, along Rd sites and to crosslinked laccase enzyme.

Redox-active protein nanowires have also been demonstrated using diphenylalanine (FF) supramolecular scaffolds (see **section 1.4.3.2)**, a sequence motif found in amyloid-forming proteins and capable of self-assembly into nanofibers and nanotubes[141]. By attaching ferrocene onto FF, Wang *et al.* formed nanowires capable of delivering charge from an electrode to immobilized glucose oxidase. Although the conductivity of FF nanostructures alone ranges from semiconducting[142] to electrically-insulating[143,144], the ferrocene moeities conjugated to the peptide fibers were spaced closely enough to form a redox conduit capable of transporting charge across the fiber scaffolds up to a micrometer in length. While ferrocene is not formally a cofactor for enzyme function, as a coordinated Fe^{2+}/Fe^{3+} center, it is capable of reversible redox reactions and facilitating redox hopping charge transport.

Shewanella oneidensis MR-1 is another well-studied model organism capable of extracellular electron transport to and from[145] solid-state electrodes, including in microbial fuel cells[146]. This functionality relies on structurally and electrochemically characterized multiheme MtrF cytochrome complexes that span the cell envelope[147]. Long-range redox transport has also been observed in biological nanowires produced by *S. oneidensis*. Once thought to be primarily protein 'pilus-like' fibers[148], these nanowires were later revealed to be cytochrome-decorated membrane extensions[149]. Nevertheless, these redox scaffold membrane nanowires provide bioinspiration for long-range electron conduction[150]. Electron cryo-tomography reveals that these nanowires are decorated with patches of tightly-packed cytochromes (~7-9 nm center-to-center), extending tens of nanometers in length along the nanowires, with inter-patch distances exceeding tunneling distances[103]. This structural information suggests that electron transport along the

nanofibers is facilitated through a combination of direct hopping events and diffusion-assisted hopping (Fig. 1.3D) between neighboring redox proteins[104].

1.4.2: Hybrid Bio-Organic Proteinogenic and Nonproteinogenic Conductors

Apart from redox-mediated systems, long-range conduction may also be possible through the formation of delocalized states. Since the 3.4 Å packing distance required for efficient delocalization is difficult to achieve with proteinogenic amino acid side chains, multiple studies have swapped natural aromatic side chains for non-proteinogenic ones or have used peptides as a supramolecular scaffold to guide conjugated small molecule packing.

The mechanism of long-range transport through delocalized states is highly dependent on the degree and length of conjugation. If the conjugation axis is persistent along the length of the supramolecular structure, potentially forming delocalized states, transport can be metallic-like or semiconducting. The type of band-like conduction in these systems is determined by observing the relationship between temperature and conductivity. For metallic-like conductors, temperature scales inversely with conductivity, as increasing temperature reduces carrier mobilities; for semiconductors, conductivity scales with temperature, due to thermal excitation of charge carriers. If conjugation is restricted to localized regions along the supramolecular structure, hopping may be required for micrometer-scale transport. This hopping mechanism would be akin to the sequential reduction and oxidation events observed in redox-mediated hopping and would therefore also exhibit a temperature-dependent conductivity. Since semiconducting and hopping behaviors both have an Arrhenius temperature dependence and their conductance scales inversely with length (Pouillet's law), a crystal structure and/or spectroscopic evidence may be required to demonstrate the electronic delocalization that would distinguish the two. For a delocalized system, temperature-dependent conductivity measurements can be used to distinguish between metallic-

like versus semiconducting transport. Hall measurements may also be a valuable tool in distinguishing between band and hopping carriers, since hopping charges in organic semiconductor films will drift in an opposite direction to band carriers subject to an orthogonal magnetic field[152]. This measurement may be particularly useful, since thermal disorder can compete with π-stacking interactions and simultaneously induce both band and hopping transport in organic semiconductors[152].

1.4.2.1 Hybrid Bio-Organic Proteinogenic Conductors

The molecular and organic electronics community has pursued peptide-small molecule conjugates for the formation of self-assembling organic conductors. Amino acids are an ideal candidate to merge with conjugated molecules since they offer both water solubility and a self-assembly pathway for the formation of electronically delocalized nanostructures. These systems typically incorporate short peptide sequences predisposed to form supramolecular structures, such as coiled-coils, β-sheets, α-helices, collagen, or elastin mimics[153]. Some notable conjugates include oligothiophenes[154,56,155–157], naphthalene diimides (NDI)[158–160], perylene diimides[160–165] and fluorenyl-9-methoxycarbonyl (Fmoc)[55,166,167].

These conjugates may facilitate long-range ETp through the formation of delocalized states. The nature of interstate coupling, in these cases π-π interactions, determines whether band-like transport has a metallic-like or semiconducting temperature dependence (**section 1.3.2**). However, if the aromatic residues are spaced too far apart to form delocalized states, or if the delocalization lengths are broken by molecular distortions, long-range ETp may occur through thermally-activated electron hopping, analogous to that observed with redox cofactors (**section 1.4.1**).

Design considerations in this paradigm are especially critical, given that a peptide's intermolecular hydrogen bonding network can directly influence the geometry, and therefore the degree and direction of intermolecular π-π interactions[168]. Govindaraju *et al.* created two dipeptide-conjugated naphthalene diimides: one with a non-proteinogenic amino acid, Aib-Aib, and the other with a natural amino acid, Ala-Ala, with Aib only differing from Ala by an extra methyl group[169]. However, the two dipeptides are known to adopt either helical or β-sheet structures, which, in turn, resulted in two distinct nanostructures with different conductivities. The Aib-Aib NDI-conjugate formed 1-D nanotapes with a co-facial orientation of the NDI groups and a conductivity of 3.5×10^{-6} S/m, while the Ala-Ala NDI conjugate formed 2-D nanosheets with an edge-to-edge (coplanar) NDI orientation and less than half the conductivity, 1.6×10^{-6} S/m. Indeed, Tovar *et al.* have shown that modest changes to a peptide sequence can result in vastly different electronic coupling regimes: disordered excimeric structures (a dimeric species associated in a short-lived excited electronic state[170]) or ordered electronically-coupled states[169]. The operative conduction mechanism in each regime may be distinct, as ordered electronically-coupled states facilitate a metallic or semiconducting band-like transport, whereas disordered excimeric structures conduct through hopping between localized states.

Although hydrogen bonding plays a significant role on the resultant hybrid structure, it cannot be the only factor driving structural formation if delocalization is to be preserved. These periodic π-π-interactions require that the conjugated component contribute to the assembly and structural stability of the hybrid nanostructure, since assemblies exclusively stabilized by β-sheet hydrogen bonds have intermolecular distances (typically~ 4.7 Å) that preclude efficient orbital overlap (3.4 Å)[171,172]. The β-sheet secondary motif is commonly used in polymer-peptide conjugates due to its tendency towards strong intermolecular aggregation[173]. Work by Bäuerle *et*

al. [157] demonstrates the importance of tempering the dominance of peptide hydrogen bonding. They designed two conjugated systems combining a quaterthiophene derivative, tetra(3-hexylthiophene) (T) with peptide sequences (P) known to form β-sheet domains, in both a T-P diblock oligomer and a P-T-P configuration. Although these structures formed nanofibers in organic solvent, assembly was dominated by β-sheet hydrogen bonding, as opposed to π-π interactions, and electronic delocalization was not observed in either arrangement. Conductance measurements were not performed, albeit low conductivities would be expected in the absence of π–stacking.

Several approaches have been used to preserve π-stacking interactions in peptide-conjugate hybrid systems. Stupp *et al.* achieved delocalized hybrid nanostructures by creating a bolaamphiphile[156]. Bolaamphiphiles differ from single-headed amphiphiles in that they have hydrophilic groups flanking a sufficiently long hydrophobic chain; their design can be dissected into three parts: polar amino acids at the ends for solubility, structure-forming amino acids for assembly, and an aromatic core for conductivity. A quinquethiophene molecule was chosen as the center segment, and alkyl spacers were added to confer flexibility, which allowed for simultaneous π-stacking and hydrogen bonding in the resultant hydrogel. Conductance measurements were not performed, but circular dichroism and absorption/emission measurements suggest the presence of π-stacking between bolaamphiphile building blocks.

Hodgkiss *et al.* developed nanofibers using two different modes of attachment to a perylene dimide core[162]. In the "forward-attached" case, a self-assembling β-sheet peptide sequence was attached using a glycine linker at the N-terminus; while in the "reverse-attached" case, the peptide sequence was attached using an ethylamino linker at the C-terminus. In the forward-attached design, the peptide backbone extends N to C away from the core, while in the reverse-attached

design, the peptide backbone extends C to N away from the core. These two designs gave nanofibers with distinct aqueous spectral profiles: the forward-attached peptide conjugate exhibited strong coupling between delocalized π-orbitals (consistent with H-aggregation), while the reverse-attached peptide conjugate exhibited a spectral signature suggestive of a rotational offset between the perylene units. Upon solid-state gating, films of forward-attached nanofibers exhibited weak semiconducting p-type behavior (majority of charge carriers are mobile holes), which was unexpected given the n-type behavior (majority of charge carriers are mobile electrons) associated with perylene materials and the high electron affinity of the perylene core. This unexpected change in electronic structure is likely due to the integration of the peptide, but electronic structure calculations, such as DFT, were not performed to validate a mechanism for the charge carrier polarity inversion. Although electronic measurements were not performed on the reverse-attached peptide, the lack of delocalization implies that any conductivity in the system would be mediated through hopping and would have significantly lower values than the delocalized forward-attached peptide system, due to weaker electronic coupling.

Tovar *et al.* have developed several π-conjugated peptide nanostructures by directly embedding the conjugated unit into the peptide backbone. In this design, they have flanked oligothiophenes[68,69,82,83], diacetylene (later photopolymerized into polydiacetylene)[176], naphthalene, perylene[160], and other aromatic compounds[177] between two β-sheet forming peptides to create water soluble peptide-conjugate building blocks. This design encourages the aqueous self-assembly of ribbon and gel structures, which, on a molecular level, promote co-facial aggregation of the conjugated organic compounds[154,160]. Upon gating, films of these nanostructures exhibited hole mobilities as high as 1.7×10^{-2} cm^2 V^{-1} s^{-1} for quaterthiophene-containing peptides[175] and 3.8×10^{-5} cm^2 V^{-1} s^{-1} for sexithiophene-containing peptides[177]. Notably, the best

performing quaterthiophene-peptide variant demonstrated mobilities comparable to those observed in films of quaterthiophene derivatives not bound to peptides[178], suggesting that the presence of peptide in this system did not adversely affect conductivity. Spectroscopic evidence for delocalization suggests that these materials are band-like conductors and their ability to gate conductivity electrostatically is a characteristic feature of semiconductor band transport. Tovar and coworkers have also developed a straight forward solid phase resin synthesis to incorporate commercially-available semiconducting and fluorescent chromophore units into oligopeptide backbones, bypassing many synthetic and solubility hurdles with creating semiconducting small molecule-peptide conjugate materials[160,177].

Another approach has been to incorporate aromatic moieties to the N-terminus of hydrophilic peptides (or single amino acids), creating amphiphilic peptide systems[153,159,166,179,180]. Based on structural studies on Fmoc-diphenylalanine (FF), Ulijn *et al.* have proposed that these amphiphile peptide systems form π-π interlocked β-sheets[79]. The same group measured the conductivity of conjugates with Fmoc appended to a leucine tripeptide (Fmoc-L_3)[55] (Fig. 1.6), which, of the several amphiphile variants tested, demonstrated the most electron delocalization, according to fluorescence measurements[180]. The resulting π-stacked β-nanotubes had minimum sheet resistances of 0.1 MΩ/sq in ambient conditions. Although this conductivity value is low compared to conjugated polymer films, these peptide amphiphile systems have the unique feature of enzyme-triggered assembly (Fig. 1.6A & B), which may allow for better reproducibility and control over the self-assembly process[181]. Access to tunable kinetic control potentially expands the functional applications of these conductive materials, as enzyme-mediated assembly of the conjugated materials have demonstrated refuelable assembly and disassembly kinetics that may be particularly useful for reconfigurable bio-interfacing applications[33,182]. Red-shifts in the

fluorescence spectra of assembled gels suggest they form delocalized structures and, as with other π–stacked systems in this classification, these amino acid conjugates are expected to be semiconducting.

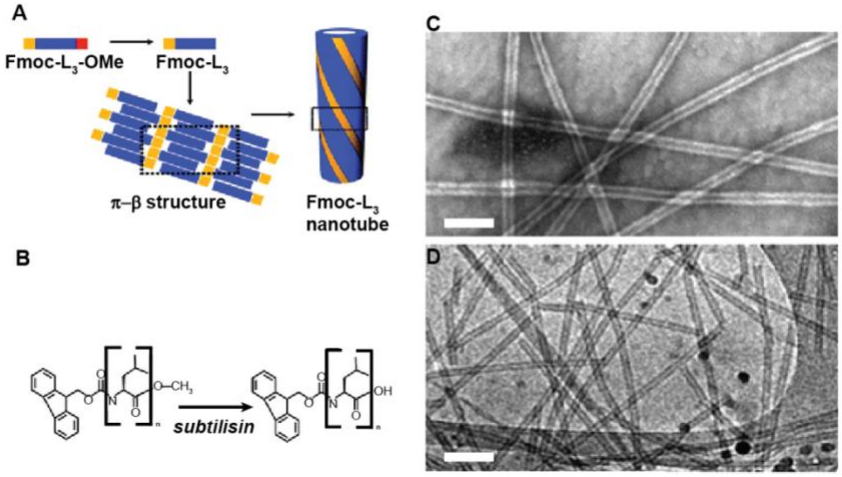

Figure 1.6: (A) Scheme for self-assembly of nanotubes assembly of Fmoc-L_3, which is converted from Fmoc-L_3-OMe via enzymatic hydrolysis (B). (C) Transmission electron micrographs of nanotube structures stained with 2% uranyl acetate and (D) AFM images of nanotubes on mica. Adapted from ref [55]

1.4.2.2: Conductive Peptides Incorporating Non-Proteinogenic Amino Acids

Since aromatic delocalization is difficult to achieve using natural amino acids, Ashkenasy *et al.* have attempted to restore π-stacking in pure amino-acid systems by developing a new category of amino acid conductors, in which natural amino acid side chains have been replaced by small aromatic compounds. They have demonstrated nanotubes with delocalized states by adding NDI side chains to otherwise electronically insulating[183–185] cyclic D, L- α-peptide nanotubes[186,187] (Fig. 1.7). Cyclic D, L-α peptides, although less promiscuous than their linear counterparts, have a lower entropy that tends to a greater degree of control and predictability[188] over their nanotubular self-assembly[186,187] (Fig. 1.7A). In nanotubes, the aromatic structures adopt a tilt with an inter-

aromatic distance of 3.6 Å, thereby facilitating intermolecular electronic delocalization[186] (Fig. 1.7B). Subsequent studies with cyclic D, L-α-peptides, with both natural amino acid side chains and napthyl substituents, suggest proton, rather than electron, hopping to be the dominant transport mechanism in dehydrated and hydrated environments[189]. In dehydrated films, aromatic stacks provide proton channels, promoting proton conductivity through hydrogen bonding. In hydrated films, a water adlayer on the surface of the peptide facilitates proton conduction, wherein proton-donating carboxylic acid side chains become important for conductivity. Although the electronic conductivity in these systems is very low (with the greatest contribution being ≤ 20% of total current, achieved under vacuum conditions), proton conducting materials have potentially useful applications and represent a common biological charge transport mechanism[190–193].

Proton involvement in these systems may suggest a hopping mechanism, in which protons stabilize electron transfer, such as at low relative humidity. As discussed in **section 1.3.3**, protons may be essential in assisting short-chain redox reactions involving aromatic amino acids[96,120]. Nevertheless, the minor role of electronic transport through this system is difficult to characterize, since a predominant hopping mechanism suggests the presence of discrete states, whereas the observation of delocalization suggests a continuum of states. However, such a conflict is not entirely surprising, since the dominant charge carriers are protons, as opposed to electrons, and are governed by a different set of transport mechanisms. Proton conduction mechanisms are beyond the scope of this review, but we direct interested readers to several excellent reviews on the subject[194–196].

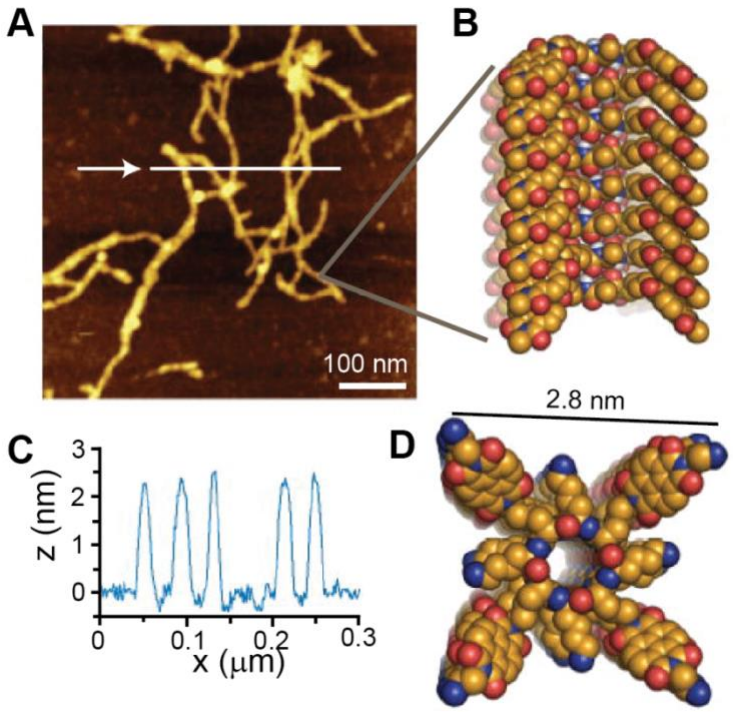

Figure 1.7: (A) AFM image of peptide fibers formed from cyclic nanotubes on mica (B) Suggested space-filling model for self-assembled cyclic peptide. The lateral cross section determined by topographical height profiles (C) is consistent with the diameter of the peptide nanotube (D). Reproduced from ref [186].

The Ashkenasy group has also incorporated non-proteinogenic aromatic side chains into fiber-forming amyloid β sequences. They formed spectroscopically-delocalized states in amphiphilic Glu-Phe dyads fibers by replacing, in each peptide sequence, two phenylalanine residues with two diaminopropionic acids bearing NDI side chains[197]. In another amyloid-β-derived sequence, they showed enhanced nanotube film conductivity when replacing the FF domain with two non-natural 2-thienylalanine (2-Thi) amino acids, achieving pS conductances under low pressure conditions[93]. Although these conductances are low, further investigation suggested a strong proton contribution to conductivity, based on observations of increasing conductance with increasing relative humidity[199]. From these humidity studies, Ashkenasy *et al.* concluded that below 60% relative humidity, conduction was mediated through both electrons and

protons (1:2 ratio, respectively), while at high humidity, conduction (increased to the order of nS) was mediated by protons. Nevertheless, these humidity studies were not conducted with Pd hydride electrodes, which are typically used to demonstrate proton conductivity, making it difficult to distinguish changes in conductivity due to proton conduction from those induced by humidity-dependent structural or morphological changes.

1.4.3: Conductive Peptides and Proteins Composed of Proteinogenic Amino Acids

1.4.3.1: π-stacked Peptides and Proteins

Long-range electron transport through natural amino acids is nontrivial, as it is difficult to achieve efficient packing distances using natural side chains. Protein nanofibers produced by the *Geobacter* species may be an exception, although the presence of delocalized states remains a point of great interest and contention[57,200,201,101,202,203]. As with non-proteinogenic side chain and peptide-conjugate hybrid structures, long-range conduction in proteinogenic, π-stacked systems could occur through metallic-like or semiconducting bands, given sufficient overlap and carrier injection via redox reactions or electrostatic gating. If π-stacking is not sufficient for complete delocalization along the length of the fiber, long-range transport may occur through hopping between localized low-energy states.

Although live *G. sulfurreducens* biofilms primarily demonstrate long-range, redox-mediated electron transport **(section 1.4.1),** conductive nanofibers isolated from *G. sulfurreducens* cultures demonstrate micrometer-scale conductivity[201,204] that is facilitated entirely by natural amino acids. These nanofibers are presumably composed of the structural protein PilA, which is over 85% α-helical in nature[205] (Fig. 1.8A) and is arranged into supramolecular helical coils *via* a complex, membrane-associated secretion system [206]. The nanofiber conductivity is exceptionally

high compared to many π-stacked amino acid based nanofibers, with single fiber values ranging from 50 mS cm^{-1} to 5 S cm^{-1} [201,204] (Figure 1.8B) and comparable to organic metals[200].

Although cytochromes play a key role in electronic transport through respiring *Geobacter* biofilms (**section 1.4.1**) and bacterial appendages produced by *S. oneidensis*[148,149] (**section 1.4.1**), conduction through these nanofibers does not exhibit signatures of redox-mediated conduction[207]. Reguera *et al*. have demonstrated that the diffusion-assisted redox conduction observed in live *G. sulfurreducens* biofilms is not contradictory with the presence of intrinsically conductive pili produced by bacteria within the biofilm[208]. Their work suggests that conduction through a network of these nanofibers becomes a significant contributor for biofilm exceeding 10 μm in thickness.

Conductivity in these *G. sulfurreducens* nanofibers increases with decreasing temperature, [57,136] (Fig. 1.8C), suggestive of a non-hopping mechanism. Reguera *et al*. have observed an opposite temperature dependence when comparing single fiber measurements at room temperature versus 77 K[201]. Although this measurement is suggestive of hopping, it is likely that, as with other soft materials, different conduction mechanisms are relevant for different temperature ranges. Thus, a thermally-activated mechanism under cryogenic conditions need not be inconsistent with non-thermally activated conduction at much higher temperatures. Malvankar *et al.* measured a crossover temperature ~ 260 K for conductivity of these nanofiber films[57]. Above 260 K, conductivity increased exponentially upon cooling, whereas below 260 K, conductivity decreased exponentially upon heating. This exponential dependence and crossover have also been observed in organic metals[209] and was attributed to reduced phonon scattering in metallic-like band transport above the transition temperature and trap localization below it[57]. In an aqueous environment and over a physiologically-relevant range of temperatures (275 K to 338 K), Hochbaum *et al*. measured a much weaker exponential temperature dependence composed of two regimes[136] (Fig. 1.8D). This

weak temperature dependence may be a result of temperature-dependent conformational changes in the protein nanofibers. The authors suggested a possible FR mechanism, since thermal disorder can diminish the probability of coupling between electronic states[78,79]. However, since FR has not been demonstrated over the micrometer distances associated with single nanofibers, any FR mechanism would likely be coupled to hopping, which has an opposite temperature dependence. Because it is unclear whether temperature dependent conductivity would be dominated by a reduction in thermal disorder or hopping, the role of FR in *Geobacter* nanofiber conduction remains speculative. Measurements performed by these three groups were all done under different environmental conditions and may thus be linked to different mechanisms. Regardless of the conduction mechanism in these nanofibers, a chemical or structural basis for the observed conductivity remains elusive.

Lovley, Malvankar and coworkers have attributed the conductivity in these bacterial nanofibers to metallic band formation due to the π-stacking of aromatic side chains[57,200,210,211]; though this claim has been heavily contested by other groups[201,205,212]. Powder X-ray microdiffraction of purified *G. sulfurreducens* nanofibers showed a 3.2 Å peaks, which was attributed aromatic stacking of phenyl rings, as these peaks were not present in nanofibers purified from a mutant expressing PilA lacking key aromatic residues[200]. Several homology models based on sequence similarities to such cellular appendages in other microbial species have been invoked to justify the inter-aromatic distances in *G. sulfurreducens* nanofibers. The sum of the homology models and one docking model, assembled by docking PilA monomers, present conflicting conclusions as to the possibility of π-stacked delocalization along the nanofibers[200,210,213,212,205,214]. Verification of π-stacking is contingent upon obtaining a direct atomic structure model of the *G.*

sulfurreducens nanofibers, and spectroscopic evidence of electronic delocalization has yet to be demonstrated.

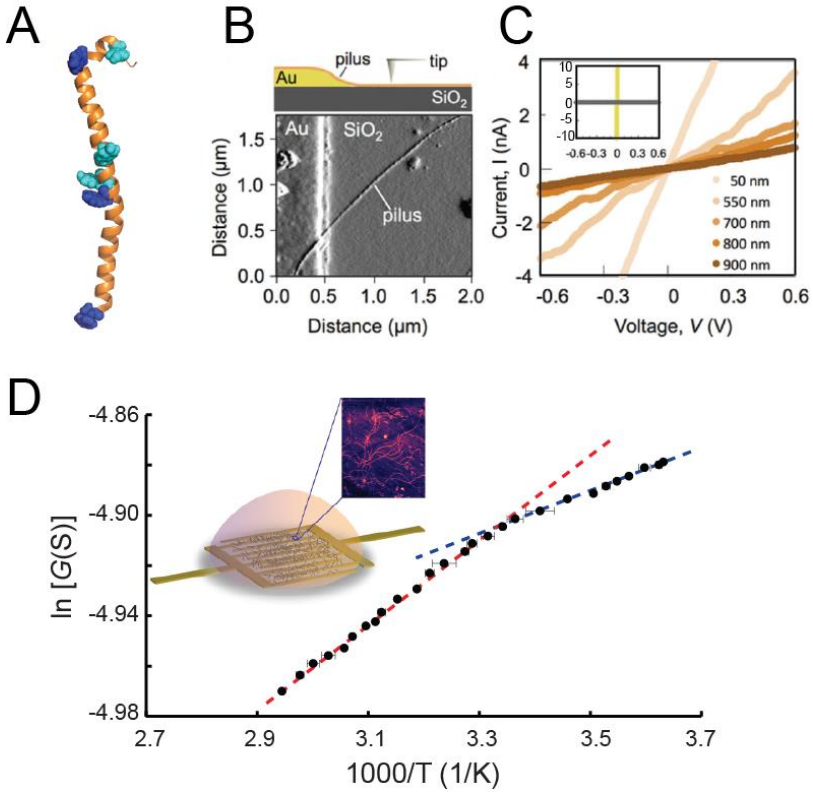

Figure 1.8: (A) Homology model for *G. sulfurreducens* PilA, with aromatic residues highlighted in blue (PDB 2M7G[205]). (B) Schematic (top) and AFM amplitude image (bottom) illustrating two-point conductive probe measurements on *G. sulfurreducens* nanofiber (pilus) contacting gold electrode. (C) Representative *I-V* measurements of single nanofiber at various distances from the electrode; inset: *I-V* plots of gold electrode (yellow) and silicon background (gray). (D) Temperature-dependent conductivity characteristics of a film of conductive *G. sulfurreducens* nanofibers (schematic, *inset*) conducted in aqueous environment. Dotted lines show two different regions of liner temperature dependence. Adapted from ref [201] and [136].

Nevertheless, modifications to the PilA sequence suggest that the conductivity is sensitive to changes in the aromatic amino acid content. Lovley and coworkers showed that the conductivity of conductive *G. sulfurreducens* nanofibers decreased appreciably when five aromatic amino acids in the PilA sequence were mutated to aliphatic side chains (Ala)[211], with single fiber conductivity

measurements suggesting a three order of magnitude decrease relative to wild type (WT) protein (38 ± 1 μS cm^{-1} compared to 51 ± 11 mS cm^{-1})[191]. These findings were corroborated by Reguera *et al.*, who found that a single replacement of one of the tyrosine residues with an alanine residue in the PilA sequence resulted in a 6-fold decrease in conductivity, from 4.7 S cm^{-1} to 0.77 S cm^{-1}[201]. Similarly, a modified PilA sequence, in which the phenylalanine and tyrosine near the C-terminus of PilA were replaced by tryptophan, resulted in enhanced conductivity, with single nanofiber conductivities at least 500 fold greater than in the wild type (WT) nanofibers[215]. This correlation between aromatic content and conductivity is also supported by comparisons of homologous nanofibers produced by other species in the *Geobacter* genus[216]. Nevertheless, the importance of aromatics does not constitute the presence of delocalized states. Reguera *et al.* have proposed that the aromatic amino acids instead function as discrete stepping stones for hopping[208,213]. Thus, the mechanism behind *G. sulfurreducens* pili remains a point of contention[217].

π-stacking has also been reported in a *de novo* peptide sequence composed entirely of natural amino acids, GFPRFAGFP[218]. This peptide, presented as a synthetic analogue to study *Geobacter* nanofiber conductivity, formed nanofibers which exhibited fluorescence spectra characteristic of π-stacking between phenylalanine side chains. In spite of the presence of π-stacking, the conductance of fiber films was low, ~10^{-11} S, albeit higher than conductances observed in amyloid β fibers.

1.4.3.2: Non-π-Stacked Peptides and Proteins

Although π-stacking is believed to play a critical role in the aforementioned examples of proteinogenic supramolecular conductors, it may not be necessary to long-range conduction through all peptide and protein materials. Despite affirmative evidence as to the significance of

aromatic residues, most of the proposed *G. sulfurreducens* homology models do not support long-range electron delocalization via aromatic side chain overlap[217]. The presence of aromatics may be critical to conduction, but delocalization via overlap may not be necessary and/or the only factor relevant to long-range conductivity.

This point is perhaps most clearly evident through a self-assembling *de novo* peptide sequence designed to form α-helical coiled coil hexamers with a supramolecular helical structure reminiscent of *Geobacter* nanofibers[59]. The core of these peptide nanofibers is rich in phenylalanine residues, yet the crystal structure of the hexamer indicates that the system is not π-stacked[219]. Phenyl rings in the hydrophobic core are in a canted orientation and too distant for π orbital overlap, and no spectroscopic evidence was observed to support electronic delocalization. Nonetheless, single nanofiber fiber conductivities exceeded those measured for *Geobacter* nanofibers[201,204]. Bipotentiostatic measurements, which distinguish between redox-mediated and non-redox mediated conduction[136], reveal similar non-redox mediated current responses for both the bacterial and the synthetic nanofibers. Additionally, both nanofiber systems exhibit a positive Arrhenius slope (S/K^{-1}) in buffer at physiologically-relevant temperatures. This temperature dependence rules out a thermally-activated mechanism at these temperatures but cannot be used to conclusively identify a precise conduction mechanism within the framework of known long-range conduction mechanisms. True metallic conduction is unlikely, particularly due to the large band gap expected for peptides and in the absence of π-stacking delocalization. Although these studies do not identify a conduction mechanism, they demonstrate that an α-helical secondary structure and supramolecular ordering are determining factors for peptide conductivity in this system. They further show that conductivities comparable to conjugated polymers can be achieved in a non-π-stacked amino acid system.

The presence of aromatic residues alone may not be able to account for the high conductivity values observed in *Geobacter* and non-π-stacked peptide nanofibers. This point is clearly illustrated by the purely aromatic amino acid sequence, diphenylalanine (FF). Inspired by the β-amyloid polypeptide, FF is a minimal dipeptide known to form disparate nanostructures based on the choice of solvent [220,221]. Some self-assembly conditions result in porous nanotubular crystals, in which six interlocks, each composed of two linear diphenyls, surround an amide backbone "tube." The hydrogen bonds between the β-sheets forming these tubes participate in proton transfer and can exist either at the C or N terminus of strands between β-sheets. This configuration creates a double-well ground-state potential, which, in combination with the aromatic interlocks, reduces the band gaps to the semiconducting region. Regardless, conductance values remain low or insulating[143,144], and the typical 4.7Å distance between peptides may be too far to facilitate delocalization[113,144].

Changing the bonding environment of the FF nanotubes directly impacts semiconducting properties. *I-V* measurements through nanotube networks demonstrated a 5 fold increase in conductivity, from 0.3 nS to 1.6 nS upon replacing one of the phenylalanines in the dipeptide with a tryptophan[143] (Fig. 1.9A & B), owing to a reduction of the molecular interstitial regions and proximity of aromatic overlap. This electronic change is supported by first-principles calculations, which show a reduction in nanotube bandgap from 4.48 eV to 3.04 eV upon switching from FF to FW[222] (Fig. 1.9C). Changing the arrangement of the dipeptide within the nanotubes from the conventional hexagonal arrangement of linear diphenyls (linear FF) to a cyclic arrangement (cyclo-FF), in which the terminal carboxylic acid and amine groups fuse to form a cyclic amide backbone, also increases the *I-V* behavior from insulating to semiconducting due to better π-overlap in the cyclo-formation[144]. In this arrangement, the distance between phenylalanine residues

is comparable to that of the non-π-stacked nanofiber[59]; nevertheless, unlike *Geobacter* nanofibers and the coiled-coil nanofibers, the cyclo-FF exhibits low conductances (~hundreds of pS) and a negative Arrhenius slope (S/K^{-1}). Conductivity in cyclo-FF may thus be thermally-activated hopping between aromatic moieties or semiconducting transport with a narrowed band gap due to aromatic side chain interactions.

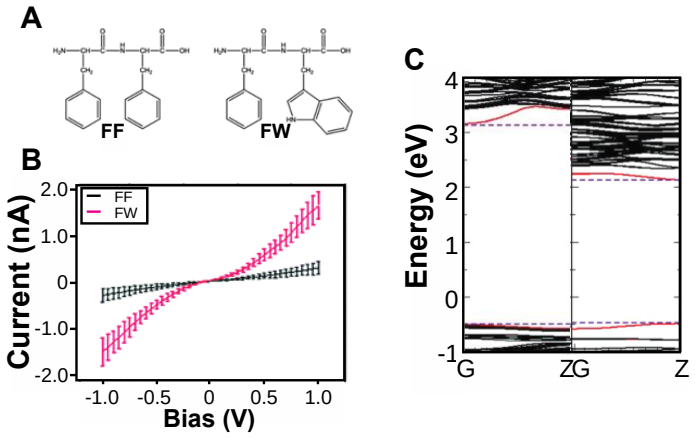

Figure 1.9: (A) Diphenylalnine (FF) and tryptophan-substituted (FW) peptides (B) I-V characteristics of dipeptide fibrils. (C) Band structures along the tube axis for FF (left pannel) and FW (right pannel). The valence band maxima and conduction band minima are shown in red, Dashed lines indicate the borders of the bandgaps. Adapted from ref [143] and ref[222].

A separate class of proteinaceous bacterial appendages, known as curli, have been engineered to facilitate long-range conduction via aromatic amino acid redox hopping sites. Curli form aggregated amyloid fibers that are expressed on the surface of many Enterobacteriaceae, such as *Escherichia coli* and *Salmonella*[223]. These proteins derived from model organisms provide an experimental platform for developing conductive biological nanofibers[58]. The curlin fiber is composed of two structural proteins: a major subunit, CsgA, and a minor subunit, CsgB[223,224,225,224]. CsgA monomers have demonstrated robust fibrilization in a variety of *in vitro* conditions[226,227], suggesting a tunable platform for synthetic modification. Seker and coworkers appended aromatic tripeptides, composed of tyrosine, tryptophan, histidine, or phenylalanine, onto the amyloidogenic

region of the CsgA protein, R5T peptide[58]. They observed fiber assembly in all of the variants, with the tyrosine and tryptophan-modified R5T exhibiting the highest conductivity. These results informed subsequent experiments, in which they engineered tyrosine and tryptophan modifications to a CsgA fusion protein incorporating an 11 amino acid sequence borrowed from the *G. sulfurreducens* PilA protein (**Section 1.4.3.1)**[204,215] (Fig. 1.10). *E. coli* biofilms expressing these modified CsgA proteins exhibited a 1.7- to 4-fold increase in conductivity relative to biofilms expressing WT CsgA. Seker *et al.* concluded from molecular structure models that while CsgA fibers are not expected to form long-range π-stacked interactions, conduction is most likely facilitated through redox hopping along the side chains of tyrosine residues. While temperature dependent conductivity data would be helpful in further supporting this claim, it is unclear whether the observed differences in conductance can be entirely attributed to the lowered redox potentials of tyrosine and tryptophan, since mutations to the CsgA sequence can produce differences in both film conductance and fiber morphology. Just as with the *Geobacter* nanofibers, additional structural information and complimentary conductivity studies, such as temperature dependent and single-fiber conductivity measurements, as well as spectroscopic investigations, are critical to supporting a specific conduction mechanism.

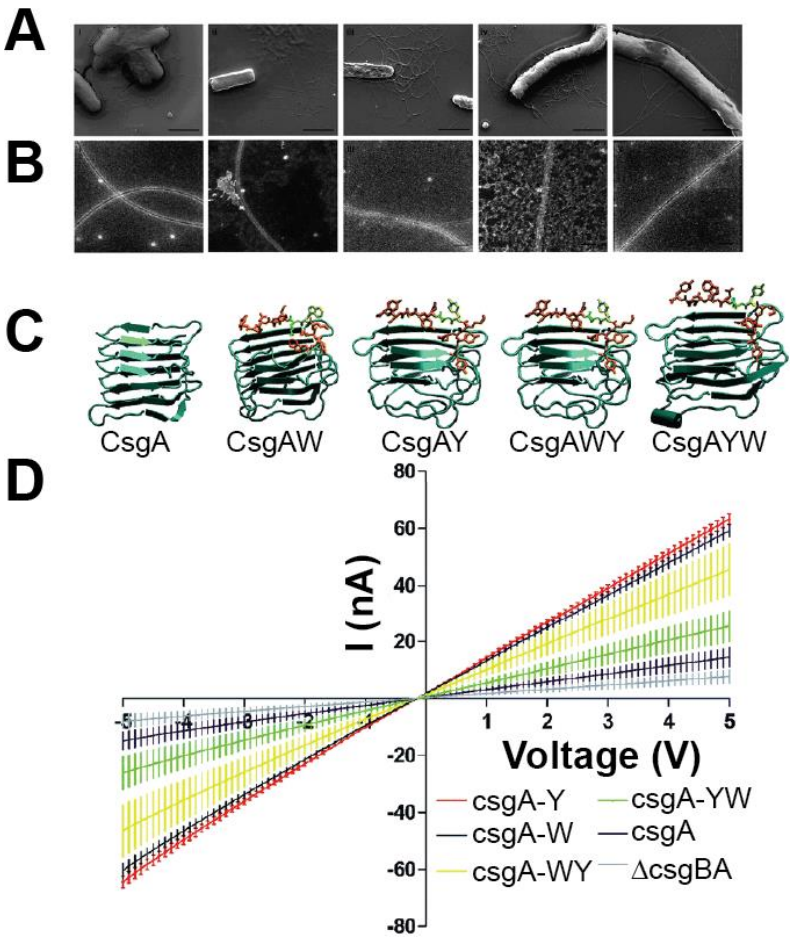

Figure 1.10: (A) Scanning and (B) transmission electron microscopy (TEM) images of the CsgA fibers and the designed conductive CsgA fibers produced by *E. coli* DcsgBA cells: (L to R) CsgA, CsgAW, CsgAY, CsgAWY, and CsgAYW. Diameters of the fibers from TEM were about 12–15 nm and many fibers came together to form thick fibrils. Scale bars are 2 μm for SEM (A) and 100 nm for TEM (B) images. (C) Molecular models of CsgA protein and its conductive motif-fused variants. (D) Output characteristics for CsgA and mutated CsgA proteins representing engineered amyloids fibers. Measurements were taken on three different electrodes for each sample. Curves represent the average of three independent samples. Adapted from ref[58].

1.5: Conclusion

Designing and understanding long-range (micrometer scale) conduction through peptides and proteins is both fundamentally interesting and potentially significant for the development of bioelectronic materials. Herein, we have provided a detailed background of electron transport mechanisms pertinent to conduction along micrometer-scale supramolecular structures. These

transport mechanisms may be distinct from those governing short-range ET and ETp processes through single peptides and proteins on the nanometer scale. Long-range conductivity has been demonstrated in cofactor-based and hybrid-peptide conjugate systems, as well as peptides and proteins with natural and unnatural amino acid side chains. While the redox principles behind long-range cofactor-based conduction can be clearly understood within the framework of an extended ET system, the emergence of long-range conductivity in non-cofactor based supramolecular systems remains an exciting research frontier.

Demonstrations of long-range conductivity in non-π-stacked peptide nanofibers and *G. sulfurreducens* nanofibers are particularly interesting because they are orders of magnitude more conductive than optimally stacked hybrid organic peptide systems. Moreover, they suggest that π-stacking may not be necessary to achieve high, non-thermally-activated conductivities in protein and peptide systems. Given the current structural information on these two systems, their conduction cannot entirely be explained by current long-range conduction models in peptide and proteins. The temperature dependent conductivity measured in the bacterial fibers and the non-π-stacked nanofibers suggests a non-thermally activated transport mechanism, excluding both hopping and semiconducting models. However, metallic-like band conduction in a non-delocalized system, such as the non-π-stacked nanofibers, is highly unlikely. These two demonstrations thus suggest the need for additional structural characterization, such as cryo-EM, to verify the presence or absence of π-stacking and the supramolecular arrangements of these two fibers.

In general, the application of multiple complimentary characterization techniques appears necessary to determining the dominant electronic conduction mechanisms in protein and peptide supramolecular materials. Their molecular dynamics are highly sensitive to different experimental

conditions, and the chemical and structural components contributing to their conductivity, from co-factors to conjugated organic molecules to aromatic side chain, are capable of participating in several different mechanisms of conduction. Consequently, to better understand and improve this class of materials for bioelectronic applications, more comprehensive studies are required. To these ends, mutable building blocks, such as peptides and peptide conjugates, with robust self-assembly behavior, represent promising experimental platforms for systematic investigations of electronic conduction in amino acid based materials. An improved understanding of how biology traffics electronic signals will pave the way for realizing the goal of bioelectronic materials of seamlessly integrating synthetic conductive materials with enzymes, cells, organs, and organisms.

1.6: Overview of the Dissertation

This dissertation outlines an investigation into the electronic properties of various conductive peptide and protein nanofiber systems. The aims of this work are twofold: (1) to demonstrate a novel paradigm of long-range conduction through proteinogenic nanofibers and (2) to demonstrate how amino acid self-assembly can be used to create conductive materials with tunable and dynamic electronic properties, which may be useful for bioelectronic applications.

Chapter 2 explores biological charge transport in *G. sulfurreducens* pili under physiologically-relevant conditions, demonstrating that conduction is non-redox-mediated, non-thermally activated process persistent across micrometer (long-range) distances. In Chapter 3, we use design principles borrowed from pili to create a non- π-stacked peptide nanofiber replicating the unique electronic properties of pili. We demonstrate that, similar to pili, these biomimetic nanofibers exhibit high single fiber conductivities (comparable to conjugated polymers) and non-thermally activated film transport under aqueous conditions. These unique properties do not fit the

common models for long-range transport, and therefore suggest a rethinking of current mechanistic framework.

In Chapter 4 and 5, we use the techniques developed in Chapters 2 and 3 to characterize the electronic properties of other conductive amino-acid based systems. Unlike the nanofibers studied in Chapters 2 and 3, the amino acid components are intrinsically not conductive; they do, however, drive the self-assembly of supramolecular structures with tunable electronic properties. Chapter 4 explores peptide conjugate hybrid systems with temporally regulated electrical conductivity. The assembly dynamics and subsequent supramolecular structures can be tuned through the selection of the amino acid component. In Chapter 5, we characterize the electronic and electrostatic properties of peptide nanofibers with tunable gold nanoparticle seeding. These two systems demonstrate functional properties which may be useful for bioelectronic technologies.

1.7: Acknowledgements

We thank Professor Moh El-Naggar at the University of Southern California for the helpful discussion.

N.L.I. acknowledges support from the U.S. Department of Education Graduate Assistance in Areas of National Need Fellowship, administered through the Chemical Engineering and Materials Science Program at the UC Irvine.

1.8: References

(1) Milroy, C. A.; Manthiram, A. Bioelectronic Energy Storage: A Pseudocapacitive Hydrogel Composed of Endogenous Biomolecules. *ACS Energy Lett.* **2016**, *1* (4), 672–677.

(2) Abdellaoui, S.; Chavez, M. S.; Matanovic, I.; Stephens, A. R.; Atanassov, P.; Minteer, S. D. Hybrid Molecular/Enzymatic Catalytic Cascade for Complete Electro-Oxidation of Glycerol Using a Promiscuous NAD-Dependent Formate Dehydrogenase from Candida Boidinii. *Chem. Commun.* **2017**, *53* (39), 5368–5371.

(3) Song, R.-B.; Wu, Y.; Lin, Z.-Q.; Xie, J.; Tan, C. H.; Loo, J. S. C.; Cao, B.; Zhang, J.-R.; Zhu, J.-J.; Zhang, Q. Living and Conducting: Coating Individual Bacterial Cells with In Situ Formed Polypyrrole. *Angew. Chem. Int. Ed Engl.* **2017**, *56* (35), 10516–10520.

(4) Lee, S.; Peh, W. Y. X.; Wang, J.; Yang, F.; Ho, J. S.; Thakor, N. V.; Yen, S.; Lee, C. Toward Bioelectronic Medicine—Neuromodulation of Small Peripheral Nerves Using Flexible Neural Clip. *Adv. Sci.* **2017**, *4* (11).

(5) Koopman, F. A.; Chavan, S. S.; Miljko, S.; Grazio, S.; Sokolovic, S.; Schuurman, P. R.; Mehta, A. D.; Levine, Y. A.; Faltys, M.; Zitnik, R.; et al. Vagus Nerve Stimulation Inhibits Cytokine Production and Attenuates Disease Severity in Rheumatoid Arthritis. *Proc. Natl. Acad. Sci. U. S. A.* **2016**, *113* (29), 8284–8289.

(6) Mishra, S.; Norton, J. J. S.; Lee, Y.; Lee, D. S.; Agee, N.; Chen, Y.; Chun, Y.; Yeo, W.-H. Soft, Conformal Bioelectronics for a Wireless Human-Wheelchair Interface. *Biosens. Bioelectron.* **2017**, *91*, 796–803.

(7) Tasca, F.; Gorton, L.; Kujawa, M.; Patel, I.; Harreither, W.; Peterbauer, C. K.; Ludwig, R.; Nöll, G. Increasing the Coulombic Efficiency of Glucose Biofuel Cell Anodes by Combination of Redox Enzymes. *Biosens. Bioelectron.* **2010**, *25* (7), 1710–1716.

(8) Tanabe, Y.; Ho, J. S.; Liu, J.; Liao, S.-Y.; Zhen, Z.; Hsu, S.; Shuto, C.; Zhu, Z.-Y.; Ma, A.; Vassos, C.; et al. High-Performance Wireless Powering for Peripheral Nerve Neuromodulation Systems. *PLOS ONE* **2017**, *12* (10), e0186698.

(9) Han, S.; Kim, J.; Won, S. M.; Ma, Y.; Kang, D.; Xie, Z.; Lee, K.-T.; Chung, H. U.; Banks, A.; Min, S.; et al. Battery-Free, Wireless Sensors for Full-Body Pressure and Temperature Mapping. *Sci. Transl. Med.* **2018**, *10* (435), eaan4950.

(10) Choi, J.; Ghaffari, R.; Baker, L. B.; Rogers, J. A. Skin-Interfaced Systems for Sweat Collection and Analytics. *Sci. Adv.* **2018**, *4* (2), eaar3921.

(11) Xu, L.; Gutbrod, S. R.; Bonifas, A. P.; Su, Y.; Sulkin, M. S.; Lu, N.; Chung, H.-J.; Jang, K.-I.; Liu, Z.; Ying, M.; et al. 3D Multifunctional Integumentary Membranes for Spatiotemporal Cardiac Measurements and Stimulation across the Entire Epicardium. *Nat. Commun.* **2014**, *5*, 3329.

(12) Capogrosso, M.; Milekovic, T.; Borton, D.; Wagner, F.; Moraud, E. M.; Mignardot, J.-B.; Buse, N.; Gandar, J.; Barraud, Q.; Xing, D.; et al. A Brain–spine Interface Alleviating Gait Deficits after Spinal Cord Injury in Primates. *Nature* **2016**, *539* (7628), 284–288.

(13) Mastinu, E.; Doguet, P.; Botquin, Y.; Hakansson, B.; Ortiz-Catalan, M. Embedded System for Prosthetic Control Using Implanted Neuromuscular Interfaces Accessed Via an Osseointegrated Implant. *IEEE Trans. Biomed. Circuits Syst.* **2017**, *11* (4), 867–877.

(14) Ciancio, A. L.; Cordella, F.; Barone, R.; Romeo, R. A.; Bellingegni, A. D.; Sacchetti, R.; Davalli, A.; Di Pino, G.; Ranieri, F.; Di Lazzaro, V.; et al. Control of Prosthetic Hands via the Peripheral Nervous System. *Front. Neurosci.* **2016**, *10*.

(15) Chuang, M.-C.; Windmiller, J. R.; Santhosh, P.; Ramírez, G. V.; Katz, E.; Wang, J. High-Fidelity Determination of Security Threats via a Boolean Biocatalytic Cascade. *Chem. Commun.* **2011**, *47* (11), 3087–3089.

(16) Duncan, B.; Le, N. D. B.; Alexander, C.; Gupta, A.; Yesilbag Tonga, G.; Yazdani, M.; Landis, R. F.; Wang, L.-S.; Yan, B.; Burmaoglu, S.; et al. Sensing by Smell: Nanoparticle–Enzyme Sensors for Rapid and Sensitive Detection of Bacteria with Olfactory Output. *ACS Nano* **2017**, *11* (6), 5339–5343.

(17) Lu, Y.; Li, H.; Zhuang, S.; Zhang, D.; Zhang, Q.; Zhou, J.; Dong, S.; Liu, Q.; Wang, P. Olfactory Biosensor Using Odorant-Binding Proteins from Honeybee: Ligands of Floral Odors and Pheromones Detection by Electrochemical Impedance. *Sens. Actuators B Chem.* **2014**, *193*, 420–427.

(18) Xie, X.; Ye, M.; Hsu, P.-C.; Liu, N.; Criddle, C. S.; Cui, Y. Microbial Battery for Efficient Energy Recovery. *Proc. Natl. Acad. Sci.* **2013**, *110* (40), 15925–15930.

(19) Pant, D.; Singh, A.; Bogaert, G. V.; Olsen, S. I.; Nigam, P. S.; Diels, L.; Vanbroekhoven, K. Bioelectrochemical Systems (BES) for Sustainable Energy Production and Product Recovery from Organic Wastes and Industrial Wastewaters. *RSC Adv.* **2012**, *2* (4), 1248–1263.

(20) Kataoka, M.; Miyakawa, T.; Shimizu, S.; Tanokura, M. Enzymes Useful for Chiral Compound Synthesis: Structural Biology, Directed Evolution, and Protein Engineering for Industrial Use. *Appl. Microbiol. Biotechnol.* **2016**, *100* (13), 5747–5757.

(21) Anbu, P.; Gopinath, S. C. B.; Cihan, A. C.; Chaulagain, B. P. Microbial Enzymes and Their Applications in Industries and Medicine. *BioMed Res. Int.* **2013**, *2013*.

(22) Kim, D.-H.; Ghaffari, R.; Lu, N.; Rogers, J. A. Flexible and Stretchable Electronics for Biointegrated Devices. *Annu. Rev. Biomed. Eng.* **2012**, *14*, 113–128.

(23) Wang, S.; Li, M.; Wu, J.; Kim, D.-H.; Lu, N.; Su, Y.; Kang, Z.; Huang, Y.; Rogers, J. A. Mechanics of Epidermal Electronics. *J. Appl. Mech.* **2012**, *79* (3), 31022-031022–031026.

(24) Heary, R. F.; Parvathreddy, N.; Sampath, S.; Agarwal, N. Elastic Modulus in the Selection of Interbody Implants. *J. Spine Surg.* **2017**, *3* (2), 163–167.

(25) Hanefeld, U.; Gardossi, L.; Magner, E. Understanding Enzyme Immobilisation. *Chem. Soc. Rev.* **2009**, *38* (2), 453–468.

(26) Vasylieva, N.; Maucler, C.; Meiller, A.; Viscogliosi, H.; Lieutaud, T.; Barbier, D.; Marinesco, S. Immobilization Method to Preserve Enzyme Specificity in Biosensors: Consequences for Brain Glutamate Detection. *Anal. Chem.* **2013**, *85* (4), 2507–2515.

(27) Mohamad, N. R.; Marzuki, N. H. C.; Buang, N. A.; Huyop, F.; Wahab, R. A. An Overview of Technologies for Immobilization of Enzymes and Surface Analysis Techniques for Immobilized Enzymes. *Biotechnol. Biotechnol. Equip.* **2015**, *29* (2), 205–220.

(28) Agostini, F.; Völler, J.-S.; Koksch, B.; Acevedo-Rocha, C. G.; Kubyshkin, V.; Budisa, N. Biocatalysis with Unnatural Amino Acids: Enzymology Meets Xenobiology. *Angew. Chem. Int. Ed Engl.* **2017**, *56* (33), 9680–9703.

(29) Young, T. S.; Schultz, P. G. Beyond the Canonical 20 Amino Acids: Expanding the Genetic Lexicon. *J. Biol. Chem.* **2010**, *285* (15), 11039–11044.

(30) Wang, L.; Xie, J.; Schultz, P. G. Expanding the Genetic Code. *Annu. Rev. Biophys. Biomol. Struct.* **2006**, *35*, 225–249.

(31) Ravikumar, Y.; Nadarajan, S. P.; Hyeon Yoo, T.; Lee, C.-S.; Yun, H. Incorporating Unnatural Amino Acids to Engineer Biocatalysts for Industrial Bioprocess Applications. *Biotechnol. J.* **2015**, *10* (12), 1862–1876.

(32) Zelzer, M.; Todd, S. J.; Hirst, A. R.; McDonald, T. O.; Ulijn, R. V. Enzyme Responsive Materials: Design Strategies and Future Developments. *Biomater. Sci.* **2012**, *1* (1), 11–39.

(33) Kumar, M.; Ing, N. L.; Narang, V.; Wijerathne, N. K.; Hochbaum, A. I.; Ulijn, R. V. Amino-Acid-Encoded Biocatalytic Self-Assembly Enables the Formation of Transient Conducting Nanostructures. *Nat. Chem.* **2018**, *10*, 696–703.

(34) Brown, J. E.; Moreau, J. E.; Berman, A. M.; McSherry, H. J.; Coburn, J. M.; Schmidt, D. F.; Kaplan, D. L. Shape Memory Silk Protein Sponges for Minimally Invasive Tissue Regeneration. *Adv. Healthc. Mater.* **2017**, *6* (2).

(35) Bayrak, A.; Prüger, P.; Stock, U. A.; Seifert, M. Absence of Immune Responses with Xenogeneic Collagen and Elastin. *Tissue Eng. Part A* **2013**, *19* (13–14), 1592–1600.

(36) DeLustro, F.; Dasch, J.; Keefe, J.; Ellingsworth, L. Immune Responses to Allogeneic and Xenogeneic Implants of Collagen and Collagen Derivatives. *Clin. Orthop.* **1990**, No. 260, 263–279.

(37) Turabee, M. H.; Thambi, T.; Lym, J. S.; Lee, D. S. Bioresorbable Polypeptide-Based Comb-Polymers Efficiently Improves the Stability and Pharmacokinetics of Proteins in Vivo. *Biomater. Sci.* **2017**, *5* (4), 837–848.

(38) Tao, H.; Hwang, S.-W.; Marelli, B.; An, B.; Moreau, J. E.; Yang, M.; Brenckle, M. A.; Kim, S.; Kaplan, D. L.; Rogers, J. A.; et al. Silk-Based Resorbable Electronic Devices for Remotely Controlled Therapy and in Vivo Infection Abatement. *Proc. Natl. Acad. Sci.* **2014**, *111* (49), 17385–17389.

(39) Rajkhowa, R.; Hu, X.; Tsuzuki, T.; Kaplan, D. L.; Wang, X. Structure and Biodegradation Mechanism of Milled Bombyx Mori Silk Particles. *Biomacromolecules* **2012**, *13* (8), 2503–2512.

(40) Giano, M. C.; Pochan, D. J.; Schneider, J. P. Controlled Biodegradation of Self-Assembling β-Hairpin Peptide Hydrogels by Proteolysis with Matrix Metalloproteinase-13. *Biomaterials* **2011**, *32* (27), 6471–6477.

(41) Shi, J.; Schellinger, J. G.; Pun, S. H. Engineering Biodegradable and Multifunctional Peptide-Based Polymers for Gene Delivery. *J. Biol. Eng.* **2013**, *7*, 25.

(42) Fu, J.; Reinhold, J.; Woodbury, N. W. Peptide-Modified Surfaces for Enzyme Immobilization. *PLOS ONE* **2011**, *6* (4), e18692.

(43) Fu, J.; Cai, K.; Johnston, S. A.; Woodbury, N. W. Exploring Peptide Space for Enzyme Modulators. *J. Am. Chem. Soc.* **2010**, *132* (18), 6419–6424.

(44) Wei, G.; Wang, L.; Dong, D.; Teng, Z.; Shi, Z.; Wang, K.; An, G.; Guan, Y.; Han, B.; Yao, M.; et al. Promotion of Cell Growth and Adhesion of a Peptide Hydrogel Scaffold via mTOR/Cadherin Signaling. *J. Cell. Physiol.* **2018**, *233* (2), 822–829.

(45) Wei, G.-J.; Yao, M.; Wang, Y.-S.; Zhou, C.-W.; Wan, D.-Y.; Lei, P.-Z.; Wen, J.; Lei, H.-W.; Dong, D.-M. Promotion of Peripheral Nerve Regeneration of a Peptide Compound Hydrogel Scaffold. *Int. J. Nanomedicine* **2013**, *8*, 3217–3225.

(46) Wang, X.; Qiao, L.; Horii, A. Screening of Functionalized Self-Assembling Peptide Nanofiber Scaffolds with Angiogenic Activity for Endothelial Cell Growth. *Prog. Nat. Sci. Mater. Int.* **2011**, *21* (2), 111–116.

(47) Santis, E. D.; Ryadnov, M. G. Peptide Self-Assembly for Nanomaterials: The Old New Kid on the Block. *Chem. Soc. Rev.* **2015**, *44* (22), 8288–8300.

(48) Bai, Y.; Luo, Q.; Liu, J. Protein Self-Assembly via Supramolecular Strategies. *Chem. Soc. Rev.* **2016**, *45* (10), 2756–2767.

(49) Liu, J.; Xie, C.; Dai, X.; Jin, L.; Zhou, W.; Lieber, C. M. Multifunctional Three-Dimensional Macroporous Nanoelectronic Networks for Smart Materials. *Proc. Natl. Acad. Sci. U. S. A.* **2013**, *110* (17), 6694–6699.

(50) Duan, X.; Gao, R.; Xie, P.; Cohen-Karni, T.; Qing, Q.; Choe, H. S.; Tian, B.; Jiang, X.; Lieber, C. M. Intracellular Recordings of Action Potentials by an Extracellular Nanoscale Field-Effect Transistor. *Nat. Nanotechnol.* **2011**, *7* (3), 174–179.

(51) Parviz, B. A.; Ryan, D.; Whitesides, G. M. Using Self-Assembly for the Fabrication of Nano-Scale Electronic and Photonic Devices. *IEEE Trans. Adv. Packag.* **2003**, *26* (3), 233–241.

(52) Ron, I.; Pecht, I.; Sheves, M.; Cahen, D. Proteins as Solid-State Electronic Conductors. *Acc. Chem. Res.* **2010**, *43* (7), 945–953.

(53) Christopher D. Bostick; Sabyasachi Mukhopadhyay; Israel Pecht; Mordechai Sheves; David Cahen; David Lederman. Protein Bioelectronics: A Review of What We Do and Do Not Know. *Rep. Prog. Phys.* **2018**, *81* (2).

(54) Edwards, P. P.; Gray, H. B.; Lodge, M. T. J.; Williams, R. J. P. Electron Transfer and Electronic Conduction through an Intervening Medium. *Angew. Chem. Int. Ed Engl.* **2008**, *47* (36), 6758–6765.

(55) Xu, H.; Das, A. K.; Horie, M.; Shaik, M. S.; Smith, A. M.; Luo, Y.; Lu, X.; Collins, R.; Liem, S. Y.; Song, A.; et al. An Investigation of the Conductivity of Peptide Nanotube Networks Prepared by Enzyme-Triggered Self-Assembly. *Nanoscale* **2010**, *2* (6), 960–966.

(56) Ardoña, H. A. M.; Besar, K.; Togninalli, M.; Katz, H. E.; Tovar, J. D. Sequence-Dependent Mechanical, Photophysical and Electrical Properties of Pi-Conjugated Peptide Hydrogelators. *J. Mater. Chem. C* **2015**, *3* (25), 6505–6514.

(57) Malvankar, N. S.; Vargas, M.; Nevin, K. P.; Franks, A. E.; Leang, C.; Kim, B.-C.; Inoue, K.; Mester, T.; Covalla, S. F.; Johnson, J. P.; et al. Tunable Metallic-like Conductivity in Microbial Nanowire Networks. *Nat. Nanotechnol.* **2011**, *6* (9), 573–579.

(58) Kalyoncu, E.; Ahan, R. E.; Olmez, T. T.; Seker, U. O. S. Genetically Encoded Conductive Protein Nanofibers Secreted by Engineered Cells. *RSC Adv.* **2017**, *7* (52), 32543–32551.

(59) Ing, N. L.; Spencer, R. K.; Luong, S. H.; Nguyen, H. D.; Hochbaum, A. I. Electronic Conductivity in Biomimetic α-Helical Peptide Nanofibers and Gels. *ACS Nano* **2018**, *12* (3), 2652–2661.

(60) Panda, S. S.; Katz, H. E.; Tovar, J. D. Solid-State Electrical Applications of Protein and Peptide Based Nanomaterials. *Chem. Soc. Rev.* **2018**, *47* (10), 3640–3658.

(61) Winkler, J. R.; Gray, H. B. Long-Range Electron Tunneling. *J. Am. Chem. Soc.* **2014**, *136* (8), 2930–2939.

(62) Gray, H. B.; Winkler, J. R. Long-Range Electron Transfer. *Proc. Natl. Acad. Sci. U. S. A.* **2005**, *102* (10), 3534–3539.

(63) Blumberger, J. Recent Advances in the Theory and Molecular Simulation of Biological Electron Transfer Reactions. *Chem. Rev.* **2015**, *115* (20), 11191–11238.

(64) Shah, A.; Adhikari, B.; Martic, S.; Munir, A.; Shahzad, S.; Ahmad, K.; Kraatz, H.-B. Electron Transfer in Peptides. *Chem. Soc. Rev.* **2015**, *44* (4), 1015–1027.

(65) Amdursky, N. Electron Transfer across Helical Peptides. *ChemPlusChem* **2015**, *80* (7), 1075–1095.

(66) Williamson, H. R.; Dow, B. A.; Davidson, V. L. Mechanisms for Control of Biological Electron Transfer Reactions. *Bioorganic Chem.* **2014**, *57*, 213–221.

(67) Amdursky, N.; Marchak, D.; Sepunaru, L.; Pecht, I.; Sheves, M.; Cahen, D. Electronic Transport via Proteins. *Adv. Mater.* **2014**, *26* (42), 7142–7161.

(68) Venkatramani, R.; Wierzbinski, E.; Waldeck, D. H.; Beratan, D. N. Breaking the Simple Proportionality between Molecular Conductances and Charge Transfer Rates. *Faraday Discuss.* **2014**, *174* (0), 57–78.

(69) Wierzbinski, E.; Venkatramani, R.; Davis, K. L.; Bezer, S.; Kong, J.; Xing, Y.; Borguet, E.; Achim, C.; Beratan, D. N.; Waldeck, D. H. The Single-Molecule Conductance and Electrochemical Electron-Transfer Rate Are Related by a Power Law. *ACS Nano* **2013**, *7* (6), 5391–5401.

(70) Skourtis, S. S. Review: Probing Protein Electron Transfer Mechanisms from the Molecular to the Cellular Length Scales. *Pept. Sci.* **2013**, *100* (1), 82–92.

(71) Marcus, R. A. On the Theory of Oxidation-Reduction Reactions Involving Electron Transfer. I. *J. Chem. Phys.* **1956**, *24* (5), 966–978.

(72) Marcus, R. A. Electrostatic Free Energy and Other Properties of States Having Nonequilibrium Polarization. I. *J. Chem. Phys.* **1956**, *24* (5), 979–989.

(73) Moser, C. C.; Chobot, S. E.; Page, C. C.; Dutton, P. L. Distance Metrics for Heme Protein Electron Tunneling. *Biochim. Biophys. Acta BBA - Bioenerg.* **2008**, *1777* (7), 1032–1037.

(74) Gray, H. B.; Winkler, J. R. Electron Flow through Proteins. *Chem. Phys. Lett.* **2009**, *483* (1–3), 1–9.

(75) Hines, T.; Diez-Perez, I.; Hihath, J.; Liu, H.; Wang, Z.-S.; Zhao, J.; Zhou, G.; Müllen, K.; Tao, N. Transition from Tunneling to Hopping in Single Molecular Junctions by

Measuring Length and Temperature Dependence. *J. Am. Chem. Soc.* **2010**, *132* (33), 11658–11664.

(76) Gray, H. B.; Winkler, J. R. Electron Tunneling through Proteins. *Q. Rev. Biophys.* **2003**, *36* (3), 341–372.

(77) Page, C. C.; Moser, C. C.; Chen, X.; Dutton, P. L. Natural Engineering Principles of Electron Tunnelling in Biological Oxidation–reduction. *Nature* **1999**, *402* (6757), 47–52.

(78) Zhang, Y.; Liu, C.; Balaeff, A.; Skourtis, S. S.; Beratan, D. N. Biological Charge Transfer via Flickering Resonance. *Proc. Natl. Acad. Sci. U. S. A.* **2014**, *111* (28), 10049–10054.

(79) Beratan, D. N.; Liu, C.; Migliore, A.; Polizzi, N. F.; Skourtis, S. S.; Zhang, P.; Zhang, Y. Charge Transfer in Dynamical Biosystems, or The Treachery of (Static) Images. *Acc. Chem. Res.* **2015**, *48* (2), 474–481.

(80) Giese, B.; Graber, M.; Cordes, M. Electron Transfer in Peptides and Proteins. *Curr. Opin. Chem. Biol.* **2008**, *12* (6), 755–759.

(81) Miller, A.; Abrahams, E. Impurity Conduction at Low Concentrations. *Phys. Rev.* **1960**, *120* (3), 745–755.

(82) K. Morigaki. *Physics of Amorphous Semiconductors*; Imperial College Press: London, 1999.

(83) Mott, N. F. Conduction in Non-Crystalline Materials. *Philos. Mag. J. Theor. Exp. Appl. Phys.* **1969**, *19* (160), 835–852.

(84) Davis, E. A.; Mott, N. F. Conduction in Non-Crystalline Systems V. Conductivity, Optical Absorption and Photoconductivity in Amorphous Semiconductors. *Philos. Mag. J. Theor. Exp. Appl. Phys.* **1970**, *22* (179), 0903–0922.

(85) Renger, T.; Marcus, R. A. Variable-Range Hopping Electron Transfer through Disordered Bridge States: Application to DNA. *J. Phys. Chem. A* **2003**, *107* (41), 8404–8419.

(86) Taniguchi, V. T.; Sailasuta-Scott, N.; Anson, F. C.; Gray, H. B. Thermodynamics of Metalloprotein Electron Transfer Reactions. *Pure Appl. Chem.* **1980**, *52* (10), 2275–2281.

(87) Warren, J. J.; Winkler, J. R.; Gray, H. B. Redox Properties of Tyrosine and Related Molecules. *Febs Lett.* **2012**, *586* (5), 596–602.

(88) Cordes Meike; Köttgen Angnieszka; Jasper Christian; Jacques Olivier; Boudebous Hassen; Giese Bernd. Influence of Amino Acid Side Chains on Long-Distance Electron Transfer in Peptides: Electron Hopping via "Stepping Stones." *Angew. Chem. Int. Ed.* **2008**, *47* (18), 3461–3463.

(89) Giese, B.; Wang, M.; Gao, J.; Stoltz, M.; Müller, P.; Graber, M. Electron Relay Race in Peptides. *J. Org. Chem.* **2009**, *74* (10), 3621–3625.

(90) Harriman, A. Further Comments on the Redox Potentials of Tryptophan and Tyrosine. *J. Phys. Chemsistry* **1987**, *91* (24), 6102–6104.

(91) Navaratnam, S.; Parsons, B. J. Reduction Potential of Histidine Free Radicals: A Pulse Radiolysis Study. *J. Chem. Soc. Faraday Trans.* **1998**, *94* (17), 2577–2581.

(92) Morozova, O. B.; Yurkovskaya, A. V. Intramolecular Electron Transfer in the Photooxidized Peptides Tyrosine–Histidine and Histidine–Tyrosine: A Time-Resolved CIDNP Study. *Angew. Chem. Int. Ed.* **2010**, *49* (43), 7996–7999.

(93) Wille, U.; Nathanael, J.; Gamon, L.; Cordes, M.; Rablen, P.; Bally, T.; Fromm, K.; Giese, B. Amide Neighbouring Group Effects in Peptides: Phenylalanine as Relay Amino Acid in Long-Distance Electron Transfer. *Chembiochem Eur. J. Chem. Biol.* **2018**.

(94) Dempsey, J. L.; Winkler, J. R.; Gray, H. B. Proton-Coupled Electron Flow in Protein Redox Machines. *Chem. Rev.* **2010**, *110* (12), 7024–7039.

(95) Zhao, X. G.; Cukier, R. I. Molecular Dynamics and Quantum Chemistry Study of a Proton-Coupled Electron Transfer Reaction. *J. Phys. Chem.* **1995**, *99* (3), 945–954.

(96) Zhang, M.-T.; Hammarström, L. Proton-Coupled Electron Transfer from Tryptophan: A Concerted Mechanism with Water as Proton Acceptor. *J. Am. Chem. Soc.* **2011**, *133* (23), 8806–8809.

(97) Dalton, E. F.; Surridge, N. A.; Jernigan, J. C.; Wilbourn, K. O.; Facci, J. S.; Murray, R. W. Charge Transport in Electroactive Polymers Consisting of Fixed Molecular Redox Sites. *Chem. Phys.* **1990**, *141* (1), 143–157.

(98) Akhoury, A.; Bromberg, L.; Hatton, T. A. Interplay of Electron Hopping and Bounded Diffusion during Charge Transport in Redox Polymer Electrodes. *J. Phys. Chem. B* **2013**, *117* (1), 333–342.

(99) Forster, R. J.; Walsh, D. A.; Mano, N.; Mao, F.; Heller, A. Modulating the Redox Properties of an Osmium-Containing Metallopolymer through the Supporting Electrolyte and Cross-Linking. *Langmuir* **2004**, *20* (3), 862–868.

(100) Snider, R. M.; Strycharz-Glaven, S. M.; Tsoi, S. D.; Erickson, J. S.; Tender, L. M. Long-Range Electron Transport in Geobacter Sulfurreducens Biofilms Is Redox Gradient-Driven. *Proc. Natl. Acad. Sci.* **2012**, *109* (38), 15467–15472.

(101) Strycharz-Glaven, S. M.; Snider, R. M.; Guiseppi-Elie, A.; Tender, L. M. On the Electrical Conductivity of Microbial Nanowires and Biofilms. *Energy Environ. Sci.* **2011**, *4* (11), 4366–4379.

(102) Yates, M. D.; Barr Engel, S.; Eddie, B. J.; Lebedev, N.; Malanoski, A. P.; Tender, L. M. Redox-Gradient Driven Electron Transport in a Mixed Community Anodic Biofilm. *FEMS Microbiol. Ecol.* **2018**, *94* (6).

(103) Subramanian, P.; Pirbadian, S.; El-Naggar, M. Y.; Jensen, G. J. Ultrastructure of Shewanella Oneidensis MR-1 Nanowires Revealed by Electron Cryotomography. *Proc. Natl. Acad. Sci. U. S. A.* **2018**, *115* (14), E3246–E3255.

(104) Blauch, D. N.; Saveant, J. M. Dynamics of Electron Hopping in Assemblies of Redox Centers. Percolation and Diffusion. *J. Am. Chem. Soc.* **1992**, *114* (9), 3323–3332.

(105) Nianduan Lu; Writam Banerjee; Pengxiao Sun; Nan Gao; Ming Liu. Charge Carrier Hopping Transport Based on Marcus Theory and Variable-Range Hopping Theory in Organic Semiconductors. *J. Appl. Phys.* **2015**, *118* (4), 45701.

(106) Endres, R. G.; Cox, D. L.; Singh, R. R. P. Colloquium: The Quest for High-Conductance DNA. *Rev. Mod. Phys.* **2004**, *76* (1), 195–214.

(107) Tao, K.; Makam, P.; Aizen, R.; Gazit, E. Self-Assembling Peptide Semiconductors. *Science* **2017**, *358* (6365).

(108) Evans, M. G.; Gergely, J. A Discussion of the Possibility of Bands of Energy Levels in Proteins Electronic Interaction in Non Bonded Systems. *Biochim. Biophys. Acta* **1949**, *3*, 188–197.

(109) J. Ladik. Energy Band Structure of Proteins. *Nature* **1964**, *202*, 1208–1209.

(110) Wang, Y.-F.; Yu, Z.-Y.; Wu, J.; Liu, C.-B. Electron Delocalization and Charge Transfer in Polypeptide Chains. *J. Phys. Chem. A* **2009**, *113* (39), 10521–10526.

(111) Chelli, R.; Gervasio, F. L.; Procacci, P.; Schettino, V. Stacking and T-Shape Competition in Aromatic−Aromatic Amino Acid Interactions. *J. Am. Chem. Soc.* **2002**, *124* (21), 6133–6143.

(112) McGaughey, G. B.; Gagné, M.; Rappé, A. K. π-Stacking Interactions ALIVE AND WELL IN PROTEINS. *J. Biol. Chem.* **1998**, *273* (25), 15458–15463.

(113) Takahashi, R.; Wang, H.; Lewis, J. P. Electronic Structures and Conductivity in Peptide Nanotubes. *J. Phys. Chem. B* **2007**, *111* (30), 9093–9098.

(114) Sepunaru, L.; Refaely-Abramson, S.; Lovrinčić, R.; Gavrilov, Y.; Agrawal, P.; Levy, Y.; Kronik, L.; Pecht, I.; Sheves, M.; Cahen, D. Electronic Transport via Homopeptides: The Role of Side Chains and Secondary Structure. *J. Am. Chem. Soc.* **2015**, *137* (30), 9617–9626.

(115) Guo, C.; Yu, X.; Refaely-Abramson, S.; Sepunaru, L.; Bendikov, T.; Pecht, I.; Kronik, L.; Vilan, A.; Sheves, M.; Cahen, D. Tuning Electronic Transport via Hepta-Alanine Peptides Junction by Tryptophan Doping. *Proc. Natl. Acad. Sci. U. S. A.* **2016**, *113* (39), 10785–10790.

(116) Joseph B. Issa; Karsten Krogh-Jespersen; Stephan S. Isied. Conformational Dependence of Electronic Coupling Across Peptide Bonds: A Ramachandran Map. *J. Phys. Chem. C* **2010**, *114* (48), 20809–20812.

(117) Minnihan, E. C.; Nocera, D. G.; Stubbe, J. Reversible, Long-Range Radical Transfer in E. Coli Class Ia Ribonucleotide Reductase. *Acc. Chem. Res.* **2013**, *46* (11), 2524–2535.

(118) Larsson, A.; Sjöberg, B. M. Identification of the Stable Free Radical Tyrosine Residue in Ribonucleotide Reductase. *EMBO J.* **1986**, *5* (8), 2037–2040.

(119) Costentin, C. Electrochemical Approach to the Mechanistic Study of Proton-Coupled Electron Transfer. *Chem. Rev.* **2008**, *108* (7), 2145–2179.

(120) Barry, B. A. Reaction Dynamics and Proton Coupled Electron Transfer: Studies of Tyrosine-Based Charge Transfer in Natural and Biomimetic Systems. *Biochim. Biophys. Acta* **2015**, *1847* (1), 46–54.

(121) Xiao; Xu; Tao. Conductance Titration of Single-Peptide Molecules. *J. Am. Chem. Soc.* **2004**, *126* (17), 5370–5371.

(122) Jian Gao; Pavel Müller; Min Wang; Sonja Eckhardt; Miriam Lauz; Katharina M. Fromm; Bernd Giese. Electron Transfer in Peptides: The Influence of Charged Amino Acids - Gao - 2011 - Angewandte Chemie International Edition - Wiley Online Library. *Angew. Chem. Int. Ed.* **2011**, *50* (8), 1926–1930.

(123) Shin, Y. K.; Newton, M. D.; Isied, S. S. Distance Dependence of Electron Transfer Across Peptides with Different Secondary Structures: The Role of Peptide Energetics and Electronic Coupling. *J. Am. Chem. Soc.* **2003**, *125* (13), 3722–3732.

(124) Elena Galoppini; Marye Anne Fox. Effect of the Electric Field Generated by the Helix Dipole on Photoinduced Intramolecular Electron Transfer in Dichromophoric α-Helical Peptides. *J Am Chem Soc* **1996**, *118* (9), 2299–2300.

(125) Fox, M. A.; Galoppini, E. Electric Field Effects on Electron Transfer Rates in Dichromophoric Peptides: The Effect of Helix Unfolding. *J. Am. Chem. Soc.* **1997**, *119* (23), 5277–5285.

(126) Lauz, M.; Eckhardt, S.; Fromm, K. M.; Giese, B. The Influence of Dipole Moments on the Mechanism of Electron Transfer through Helical Peptides. *Phys. Chem. Chem. Phys. PCCP* **2012**, *14* (40), 13785–13788.

(127) Chen, X.; Zhang, L.; Zhang, L.; Sun, W.; Zhang, Z.; Liu, H.; Bu, Y.; Cukier, R. I. α-Helix C-Terminus Acting as a Relay to Mediate Long-Range Hole Migration in Proteins. *J. Phys. Chem. Lett.* **2010**, *1* (10), 1637–1641.

(128) Anthony R. Crofts; Colin A. Wraight. The Electrochemical Domain of Photosynthesis. *Biochim. Biophys. Acta BBA - Bioenerg.* **1983**, *762* (3), 149–185.

(129) Rochaix, J.-D. Regulation of Photosynthetic Electron Transport. *Biochim. Biophys. Acta BBA - Bioenerg.* **2011**, *1807* (3), 375–383.

(130) Zickermann, V.; Kerscher, S.; Zwicker, K.; Tocilescu, M. A.; Radermacher, M.; Brandt, U. Architecture of Complex I and Its Implications for Electron Transfer and Proton Pumping. *Biochim. Biophys. Acta BBA - Bioenerg.* **2009**, *1787* (6), 574–583.

(131) Cecchini, G. Function and Structure of Complex II of the Respiratory Chain. *Annu. Rev. Biochem.* **2003**, *72*, 77–109.

(132) Bond, D. R.; Lovley, D. R. Electricity Production by Geobacter Sulfurreducens Attached to Electrodes. *Appl. Environ. Microbiol.* **2003**, *69* (3), 1548–1555.

(133) Malvankar, N. S.; Tuominen, M. T.; Lovley, D. R. Biofilm Conductivity Is a Decisive Variable for High-Current-Density Geobacter Sulfurreducens Microbial Fuel Cells. *Energy Environ. Sci.* **2012**, *5* (2), 5790–5797.

(134) Leang, C.; Malvankar, N. S.; Franks, A. E.; Nevin, K. P.; Lovley, D. R. Engineering Geobacter Sulfurreducens to Produce a Highly Cohesive Conductive Matrix with Enhanced Capacity for Current Production. *Energy Environ. Sci.* **2013**, *6* (6), 1901–1908.

(135) Yates, M. D.; Strycharz-Glaven, S. M.; Golden, J. P.; Roy, J.; Tsoi, S.; Erickson, J. S.; El-Naggar, M. Y.; Barton, S. C.; Tender, L. M. Measuring Conductivity of Living Geobacter Sulfurreducens Biofilms. *Nat. Nanotechnol.* **2016**, *11* (11), 910–913.

(136) Ing, N. L.; Nusca, T. D.; Hochbaum, A. I. Geobacter Sulfurreducens Pili Support Ohmic Electronic Conduction in Aqueous Solution. *Phys. Chem. Chem. Phys.* **2017**, *19* (32), 21791–21799.

(137) Robuschi, L.; Tomba, J. P.; German D. Schrott; P. Sebastian Bonanni; P. Mariela Desimone; Juan Pablo Busalmen. Spectroscopic Slicing to Reveal Internal Redox Gradients in Electricity-Producing Biofilms. *Angew. Chem. Int. Ed. 52* (3), 925–928.

(138) Mark Burgess; Jeffrey S. Moore; Joaquin Rodriguez-López. Redox Active Polymers as Soluble Nanomaterials for Energy Storage. *Acc. Chem. Res.* **2016**, *49* (11), 2649–2657.

(139) Park, H.-S.; Ko, S.-J.; Park, J.-S.; Kim, J. Y.; Song, H.-K. Redox-Active Charge Carriers of Conducting Polymers as a Tuner of Conductivity and Its Potential Window. *Sci. Rep.* **2013**, *3*.

(140) Altamura, L.; Horvath, C.; Rengaraj, S.; Rongier, A.; Elouarzaki, K.; Gondran, C.; Maçon, A. L. B.; Vendrely, C.; Bouchiat, V.; Fontecave, M.; et al. A Synthetic Redox Biofilm Made from Metalloprotein–prion Domain Chimera Nanowires. *Nat. Chem.* **2017**, *9* (2), 157–163.

(141) Wang, J.; Li, D.; Yang, M.; Zhang, Y. A Novel Ferrocene-Tagged Peptide Nanowire for Enhanced Electrochemical Glucose Biosensing. *Anal. Methods* **2014**, *6* (18), 7161–7165.

(142) Yemini, M.; Reches, M.; Rishpon, J.; Gazit, E. Novel Electrochemical Biosensing Platform Using Self-Assembled Peptide Nanotubes. *Nano Lett.* **2005**, *5* (1), 183–186.

(143) Amdursky, N. Enhanced Solid-State Electron Transport via Tryptophan Containing Peptide Networks. *Phys. Chem. Chem. Phys.* **2013**, *15* (32), 13479–13482.

(144) Lee, J. S.; Yoon, I.; Kim, J.; Ihee, H.; Kim, B.; Park, C. B. Self-Assembly of Semiconducting Photoluminescent Peptide Nanowires in the Vapor Phase. *Angew. Chem. Int. Ed.* **2011**, *50* (5), 1164–1167.

(145) Rowe, A. R.; Rajeev, P.; Jain, A.; Pirbadian, S.; Okamoto, A.; Gralnick, J. A.; El-Naggar, M. Y.; Nealson, K. H. Tracking Electron Uptake from a Cathode into Shewanella Cells: Implications for Energy Acquisition from Solid-Substrate Electron Donors. *mBio* **2018**, *9* (1), e02203-17.

(146) Prakash, G. K. S.; Viva, F. A.; Bretschger, O.; Yang, B.; El-Naggar, M.; Nealson, K. Inoculation Procedures and Characterization of Membrane Electrode Assemblies for Microbial Fuel Cells. *J. Power Sources* **2010**, *195* (1), 111–117.

(147) Clarke, T. A.; Edwards, M. J.; Gates, A. J.; Hall, A.; White, G. F.; Bradley, J.; Reardon, C. L.; Shi, L.; Beliaev, A. S.; Marshall, M. J.; et al. Structure of a Bacterial Cell Surface Decaheme Electron Conduit. *Proc. Natl. Acad. Sci.* **2011**, *108* (23), 9384–9389.

(148) El-Naggar, M. Y.; Wanger, G.; Leung, K. M.; Yuzvinsky, T. D.; Southam, G.; Yang, J.; Lau, W. M.; Nealson, K. H.; Gorby, Y. A. Electrical Transport along Bacterial Nanowires from Shewanella Oneidensis MR-1. *Proc. Natl. Acad. Sci. U. S. A.* **2010**, *107* (42), 18127–18131.

(149) Pirbadian, S.; Barchinger, S. E.; Leung, K. M.; Byun, H. S.; Jangir, Y.; Bouhenni, R. A.; Reed, S. B.; Romine, M. F.; Saffarini, D. A.; Shi, L.; et al. Shewanella Oneidensis MR-1 Nanowires Are Outer Membrane and Periplasmic Extensions of the Extracellular Electron Transport Components. *Proc. Natl. Acad. Sci.* **2014**, *111* (35), 12883–12888.

(150) Leung, K. M.; Wanger, G.; El-Naggar, M. Y.; Gorby, Y.; Southam, G.; Lau, W. M.; Yang, J. Shewanella Oneidensis MR-1 Bacterial Nanowires Exhibit P-Type, Tunable Electronic Behavior. *Nano Lett.* **2013**, *13* (6), 2407–2411.

(151) The ultrastructure of Shewanella oneidensis MR-1 nanowires revealed by electron cryo-tomography | bioRxiv https://www.biorxiv.org/content/early/2017/01/28/103242 (accessed Mar 16, 2018).

(152) Yi, H. T.; Gartstein, Y. N.; Podzorov, V. Charge Carrier Coherence and Hall Effect in Organic Semiconductors. *Sci. Rep.* **2016**, *6*, 23650.

(153) Fleming, S.; Ulijn, R. V. Design of Nanostructures Based on Aromatic Peptide Amphiphiles. *Chem. Soc. Rev.* **2014**, *43* (23), 8150–8177.

(154) Diegelmann, S. R.; Gorham, J. M.; Tovar, J. D. One-Dimensional Optoelectronic Nanostructures Derived from the Aqueous Self-Assembly of π-Conjugated Oligopeptides. *J. Am. Chem. Soc.* **2008**, *130* (42), 13840–13841.

(155) Kumar, R. J.; MacDonald, J. M.; Singh, T. B.; Waddington, L. J.; Holmes, A. B. Hierarchical Self-Assembly of Semiconductor Functionalized Peptide α-Helices and Optoelectronic Properties. *J. Am. Chem. Soc.* **2011**, *133* (22), 8564–8573.

(156) Stone, D. A.; Hsu, L.; Stupp, S. I. Self-Assembling Quinquethiophene–oligopeptide Hydrogelators. *Soft Matter* **2009**, *5* (10), 1990–1993.

(157) Klok, H.-A.; Rösler, A.; Götz, G.; Mena-Osteritz, E.; Bäuerle, P. Synthesis of a Silk-Inspired Peptide –oligothiophene Conjugate. *Org. Biomol. Chem.* **2004**, *2* (24), 3541–3544.

(158) Pandeeswar, M.; Khare, H.; Ramakumar, S.; Govindaraju, T. Crystallographic Insight-Guided Nanoarchitectonics and Conductivity Modulation of an N-Type Organic

Semiconductor through Peptide Conjugation. *Chem. Commun.* **2015**, *51* (39), 8315–8318.

(159) Nalluri, S. K. M.; Berdugo, C.; Javid, N.; Frederix, P. W. J. M.; Ulijn, R. V. Biocatalytic Self-Assembly of Supramolecular Charge-Transfer Nanostructures Based on n-Type Semiconductor-Appended Peptides. *Angew. Chem. Int. Ed.* **2014**, *53* (23), 5882–5887.

(160) S. Vadehra, G.; D. Wall, B.; R. Diegelmann, S.; D. Tovar, J. On-Resin Dimerization Incorporates a Diverse Array of π-Conjugated Functionality within Aqueous Self-Assembling Peptide Backbones. *Chem. Commun.* **2010**, *46* (22), 3947–3949.

(161) Eakins, G. L.; Gallaher, J. K.; Keyzers, R. A.; Falber, A.; Webb, J. E. A.; Laos, A.; Tidhar, Y.; Weissman, H.; Rybtchinski, B.; Thordarson, P.; et al. Thermodynamic Factors Impacting the Peptide-Driven Self-Assembly of Perylene Diimide Nanofibers. *J. Phys. Chem. B* **2014**, *118* (29), 8642–8651.

(162) Eakins, G. L.; Pandey, R.; Wojciechowski, J. P.; Zheng, H. Y.; Webb, J. E. A.; Valéry, C.; Thordarson, P.; Plank, N. O. V.; Gerrard, J. A.; Hodgkiss, J. M. Functional Organic Semiconductors Assembled via Natural Aggregating Peptides. *Adv. Funct. Mater.* **2015**, *25* (35), 5640–5649.

(163) Marty, R.; Szilluweit, R.; Sánchez-Ferrer, A.; Bolisetty, S.; Adamcik, J.; Mezzenga, R.; Spitzner, E.-C.; Feifer, M.; Steinmann, S. N.; Corminboeuf, C.; et al. Hierarchically Structured Microfibers of "Single Stack" Perylene Bisimide and Quaterthiophene Nanowires. *ACS Nano* **2013**, *7* (10), 8498–8508.

(164) Draper, E. R.; Walsh, J. J.; McDonald, T. O.; Zwijnenburg, M. A.; Cameron, P. J.; Cowan, A. J.; Adams, D. J. Air-Stable Photoconductive Films Formed from Perylene Bisimide Gelators. *J. Mater. Chem. C* **2014**, *2* (28), 5570–5575.

(165) Draper, E. R.; Greeves, B. J.; Barrow, M.; Schweins, R.; Zwijnenburg, M. A.; Adams, D. J. pH-Directed Aggregation to Control Photoconductivity in Self-Assembled Perylene Bisimides. *Chem* **2017**, *2* (5), 716–731.

(166) Smith, A. M.; Williams, R. J.; Tang, C.; Coppo, P.; Collins, R. F.; Turner, M. L.; Saiani, A.; Ulijn, R. V. Fmoc-Diphenylalanine Self Assembles to a Hydrogel via a Novel Architecture Based on Π–π Interlocked β-Sheets. *Adv. Mater.* **2008**, *20* (1), 37–41.

(167) Draper, E. R.; Morris, K. L.; Little, M. A.; Raeburn, J.; Colquhoun, C.; Cross, E. R.; McDonald, T. O.; Serpell, L. C.; Adams, D. J. Hydrogels Formed from Fmoc Amino Acids. *CrystEngComm* **2015**, *17* (42), 8047–8057.

(168) Hye Kim, S.; R. Parquette, J. A Model for the Controlled Assembly of Semiconductor Peptides. *Nanoscale* **2012**, *4* (22), 6940–6947.

(169) Wall, B. D.; Zacca, A. E.; Sanders, A. M.; Wilson, W. L.; Ferguson, A. L.; Tovar, J. D. Supramolecular Polymorphism: Tunable Electronic Interactions within π-Conjugated Peptide Nanostructures Dictated by Primary Amino Acid Sequence. *Langmuir* **2014**, *30* (20), 5946–5956.

(170) J.B. Birks. Excimers. *Rep. Prog. Phys.* **1975**, No. 38, 903–974.

(171) Hartgerink, J. D.; Granja, J. R.; Milligan, R. A.; Ghadiri, M. R. Self-Assembling Peptide Nanotubes. *J. Am. Chem. Soc.* **1996**, *118* (1), 43–50.

(172) Channon, K. J.; Devlin, G. L.; Magennis, S. W.; Finlayson, C. E.; Tickler, A. K.; Silva, C.; MacPhee, C. E. Modification of Fluorophore Photophysics through Peptide-Driven Self-Assembly. *J. Am. Chem. Soc.* **2008**, *130* (16), 5487–5491.

(173) Vandermeulen, G. W. M.; Klok, H.-A. Peptide/Protein Hybrid Materials: Enhanced Control of Structure and Improved Performance through Conjugation of Biological and Synthetic Polymers. *Macromol. Biosci.* **2004**, *4* (4), 383–398.

(174) Wall, B. D.; Diegelmann, S. R.; Zhang, S.; Dawidczyk, T. J.; Wilson, W. L.; Katz, H. E.; Mao, H.-Q.; Tovar, J. D. Aligned Macroscopic Domains of Optoelectronic Nanostructures Prepared via Shear-Flow Assembly of Peptide Hydrogels. *Adv. Mater.* **2011**, *23* (43), 5009–5014.

(175) Besar, K.; Ardoña, H. A. M.; Tovar, J. D.; Katz, H. E. Demonstration of Hole Transport and Voltage Equilibration in Self-Assembled π-Conjugated Peptide Nanostructures Using Field-Effect Transistor Architectures. *ACS Nano* **2015**, *9* (12), 12401–12409.

(176) Diegelmann, S. R.; Hartman, N.; Markovic, N.; Tovar, J. D. Synthesis and Alignment of Discrete Polydiacetylene-Peptide Nanostructures. *J. Am. Chem. Soc.* **2012**, *134* (4), 2028–2031.

(177) Sanders, A. M.; Dawidczyk, T. J.; Katz, H. E.; Tovar, J. D. Peptide-Based Supramolecular Semiconductor Nanomaterials via Pd-Catalyzed Solid-Phase "Dimerizations." *ACS Macro Lett.* **2012**, *1* (11), 1326–1329.

(178) Nakano, K.; Iino, H.; Usui, T.; Hanna, J. Bulk Mobility of Polycrystalline Thin Films of Quaterthiophene Derivatives. *Appl. Phys. Lett.* **2011**, *98* (10), 103302.

(179) Nalluri, S. K. M.; Shivarova, N.; Kanibolotsky, A. L.; Zelzer, M.; Gupta, S.; Frederix, P. W. J. M.; Skabara, P. J.; Gleskova, H.; Ulijn, R. V. Conducting Nanofibers and Organogels Derived from the Self-Assembly of Tetrathiafulvalene-Appended Dipeptides. *Langmuir* **2014**, *30* (41), 12429–12437.

(180) AK Das; R Collins; RV Ulijn. Exploiting Enzymatic (Reversed) Hydrolysis in Directed Self-Assembly of Peptide Nanostructures. *Small* **2008**, *4* (2), 279–287.

(181) Xu, H.; Das, A. K.; Horie, M.; Shaik, M. S.; Smith, A. M.; Luo, Y.; Lu, X.; Collins, R.; Liem, S. Y.; Song, A.; et al. An Investigation of the Conductivity of Peptide Nanotube Networks Prepared by Enzyme-Triggered Self-Assembly. *Nanoscale* **2010**, *2* (6), 960–966.

(182) Zhu, J.; Dexheimer, M.; Cheng, H. Reconfigurable Systems for Multifunctional Electronics. *Npj Flex. Electron.* **2017**, *1* (1), 8.

(183) Carloni, P.; Andreoni, W.; Parrinello, M. Self-Assembled Peptide Nanotubes from First Principles. *Phys. Rev. Lett.* **1997**, *79* (4), 761–764.

(184) Jishi, R. A. Peptide Nanotubes: An Inert Environment. *Phys. Rev. B* **1998**, *58* (24), R16009–R16011.

(185) Okamoto, H.; Nakanishi, T.; Nagai, Y.; Kasahara, M.; Takeda, K. Variety of the Molecular Conformation in Peptide Nanorings and Nanotubes. *J. Am. Chem. Soc.* **2003**, *125* (9), 2756–2769.

(186) Ashkenasy, N.; Horne, W. S.; Reza Ghadiri, M. Design of Self-Assembling Peptide Nanotubes with Delocalized Electronic States. *Small* **2006**, *2* (1), 99–102.

(187) Horne, W. S.; Ashkenasy, N.; Ghadiri, M. R. Modulating Charge Transfer through Cyclic D,L-Alpha-Peptide Self-Assembly. *Chem. Weinh. Bergstr. Ger.* **2005**, *11* (4), 1137–1144.

(188) Montenegro, J.; Ghadiri, M. R.; Granja, J. R. Ion Channel Models Based on Self-Assembling Cyclic Peptide Nanotubes. *Acc. Chem. Res.* **2013**, *46* (12), 2955–2965.

(189) Yardeni, J. L.; Amit, M.; Ashkenasy, G.; Ashkenasy, N. Sequence Dependent Proton Conduction in Self-Assembled Peptide Nanostructures. *Nanoscale* **2016**, *8* (4), 2358–2366.

(190) Weber, J.; Senior, A. E. ATP Synthesis Driven by Proton Transport in F1F0-ATP Synthase. *FEBS Lett.* **2003**, *545* (1), 61–70.

(191) Proton Transfer Pathways in Bacteriorhodopsin at 2.3 Angstrom Resolution | Science http://science.sciencemag.org/content/280/5371/1934.long (accessed Mar 19, 2018).

(192) Heberle, J. Proton Transfer Reactions across Bacteriorhodopsin and along the Membrane. *Biochim. Biophys. Acta BBA - Bioenerg.* **2000**, *1458* (1), 135–147.

(193) Sineshchekov, O. A.; Govorunova, E. G.; Wang, J.; Li, H.; Spudich, J. L. Intramolecular Proton Transfer in Channelrhodopsins. *Biophys. J.* **2013**, *104* (4), 807–817.

(194) Miyake, T.; Rolandi, M. Grotthuss Mechanisms: From Proton Transport in Proton Wires to Bioprotonic Devices. *J. Phys. Condens. Matter* **2016**, *28* (2), 23001.

(195) Meng, X.; Wang, H.-N.; Song, S.-Y.; Zhang, H.-J. Proton-Conducting Crystalline Porous Materials. *Chem. Soc. Rev.* **2017**, *46* (2), 464–480.

(196) Deng, Y.; Josberger, E.; Jin, J.; Roudsari, A. F.; Helms, B. A.; Zhong, C.; Anantram, M. P.; Rolandi, M. H+-Type and OH−-Type Biological Protonic Semiconductors and Complementary Devices. *Sci. Rep.* **2013**, *3*, 2481.

(197) Ivnitski, D.; Amit, M.; Rubinov, B.; Cohen-Luria, R.; Ashkenasy, N.; Ashkenasy, G. Introducing Charge Transfer Functionality into Prebiotically Relevant β-Sheet Peptide Fibrils. *Chem. Commun.* **2014**, *50* (51), 6733–6736.

(198) Amit, M.; Cheng, G.; Hamley, I. W.; Ashkenasy, N. Conductance of Amyloid β Based Peptide Filaments: Structure–function Relations. *Soft Matter* **2012**, *8* (33), 8690–8696.

(199) Amit, M.; Appel, S.; Cohen, R.; Cheng, G.; Hamley, I. W.; Ashkenasy, N. Hybrid Proton and Electron Transport in Peptide Fibrils. *Adv. Funct. Mater.* **2014**, *24* (37), 5873–5880.

(200) Malvankar, N. S.; Vargas, M.; Nevin, K.; Tremblay, P.-L.; Evans-Lutterodt, K.; Nykypanchuk, D.; Martz, E.; Tuominen, M. T.; Lovley, D. R. Structural Basis for Metallic-like Conductivity in Microbial Nanowires. *mBio* **2015**, *6* (2), e00084-15.

(201) Lampa-Pastirk, S.; Veazey, J. P.; Walsh, K. A.; Feliciano, G. T.; Steidl, R. J.; Tessmer, S. H.; Reguera, G. Thermally Activated Charge Transport in Microbial Protein Nanowires. *Sci. Rep.* **2016**, *6*, 23517.

(202) Malvankar, N. S.; Tuominen, M. T.; Lovley, D. R. Comment on "On Electrical Conductivity of Microbial Nanowires and Biofilms" by S. M. Strycharz-Glaven, R. M. Snider, A. Guiseppi-Elie and L. M. Tender, Energy Environ. Sci., 2011, 4, 4366. *Energy Environ. Sci.* **2012**, *5* (3), 6247–6249.

(203) Strycharz-Glaven, S. M.; Tender, L. M. Reply to the "Comment on 'On Electrical Conductivity of Microbial Nanowires and Biofilms'" by N. S. Malvankar, M. T. Tuominen and D. R. Lovley, Energy Environ. Sci., 2012, 5, DOI: 10.1039/c2ee02613a. *Energy Environ. Sci.* **2012**, *5* (3), 6250–6255.

(204) Adhikari, R. Y.; Malvankar, N. S.; Tuominen, M. T.; Lovley, D. R. Conductivity of Individual Geobacter Pili. *RSC Adv.* **2016**, *6* (10), 8354–8357.

(205) Reardon, P. N.; Mueller, K. T. Structure of the Type IVa Major Pilin from the Electrically Conductive Bacterial Nanowires of Geobacter Sulfurreducens. *J. Biol. Chem.* **2013**, *288* (41), 29260–29266.

(206) Chang, Y.-W.; Rettberg, L. A.; Treuner-Lange, A.; Iwasa, J.; Søgaard-Andersen, L.; Jensen, G. J. Architecture of the Type IVa Pilus Machine. *Science* **2016**, *351* (6278), aad2001-aad2007.

(207) Ing, N. L.; Nusca, T. D.; Hochbaum, A. I. Geobacter Sulfurreducens Pili Support Ohmic Electronic Conduction in Aqueous Solution. *Phys. Chem. Chem. Phys.* **2017**.

(208) Steidl, R. J.; Lampa-Pastirk, S.; Reguera, G. Mechanistic Stratification in Electroactive Biofilms of Geobacter Sulfurreducens Mediated by Pilus Nanowires. *Nat. Commun.* **2016**, *7*, 12217.

(209) Kaiser, A. B. Systematic Conductivity Behavior in Conducting Polymers: Effects of Heterogeneous Disorder. *Adv. Mater.* **2001**, *13* (12–13), 927–941.

(210) Xiao, K.; Malvankar, N. S.; Shu, C.; Martz, E.; Lovley, D. R.; Sun, X. Low Energy Atomic Models Suggesting a Pilus Structure That Could Account for Electrical Conductivity of Geobacter Sulfurreducens Pili. *Sci. Rep.* **2016**, *6*, 23385.

(211) Vargas, M.; Malvankar, N. S.; Tremblay, P.-L.; Leang, C.; Smith, J. A.; Patel, P.; Synoeyenbos-West, O.; Nevin, K. P.; Lovley, D. R. Aromatic Amino Acids Required for Pili Conductivity and Long-Range Extracellular Electron Transport in Geobacter Sulfurreducens. *mBio* **2013**, *4* (2), e00105–e00113.

(212) Boesen, T.; Nielsen, L. P. Molecular Dissection of Bacterial Nanowires. *mBio* **2013**, *4* (3), e00270-13.

(213) Feliciano, G. T.; Steidl, R. J.; Reguera, G. Structural and Functional Insights into the Conductive Pili of Geobacter Sulfurreducens Revealed in Molecular Dynamics Simulations. *Phys. Chem. Chem. Phys.* **2015**, *17* (34), 22217–22226.

(214) Feliciano, G. T.; da Silva, A. J. R.; Reguera, G.; Artacho, E. Molecular and Electronic Structure of the Peptide Subunit of Geobacter Sulfurreducens Conductive Pili from First Principles. *J. Phys. Chem. A* **2012**, *116* (30), 8023–8030.

(215) Tan, Y.; Adhikari, R. Y.; Malvankar, N. S.; Pi, S.; Ward, J. E.; Woodard, T. L.; Nevin, K. P.; Xia, Q.; Tuominen, M. T.; Lovley, D. R. Synthetic Biological Protein Nanowires with High Conductivity. *Small* **2016**, *12* (33), 4481–4485.

(216) Tan, Y.; Adhikari, R. Y.; Malvankar, N. S.; Ward, J. E.; Woodard, T. L.; Nevin, K. P.; Lovley, D. R. Expressing the Geobacter Metallireducens PilA in Geobacter Sulfurreducens Yields Pili with Exceptional Conductivity. *mBio* **2017**, *8* (1).

(217) Creasey, R. C. G.; Mostert, A. B.; Nguyen, T. A. H.; Virdis, B.; Freguia, S.; Laycock, B. Microbial Nanowires – Electron Transport and the Role of Synthetic Analogues. *Acta Biomater.* **2018**, *69*, 1–30.

(218) Creasey, R. C. G.; Shingaya, Y.; Nakayama, T. Improved Electrical Conductance through Self-Assembly of Bioinspired Peptides into Nanoscale Fibers. *Mater. Chem. Phys.* **2015**, *158*, 52–59.

(219) Spencer, R. K.; Hochbaum, A. I. X-Ray Crystallographic Structure and Solution Behavior of an Antiparallel Coiled-Coil Hexamer Formed by de Novo Peptides. *Biochem.* **2016**, *55* (23), 3214–3223.

(220) Zhu, P.; Yan, X.; Su, Y.; Yang, Y.; Li, J. Solvent-Induced Structural Transition of Self-Assembled Dipeptide: From Organogels to Microcrystals. *Chem. – Eur. J.* **2010**, *16* (10), 3176–3183.

(221) Mason, T. O.; Chirgadze, D. Y.; Levin, A.; Adler-Abramovich, L.; Gazit, E.; Knowles, T. P. J.; Buell, A. K. Expanding the Solvent Chemical Space for Self-Assembly of Dipeptide Nanostructures. *ACS Nano* **2014**, *8* (2), 1243–1253.

(222) Akdim, B.; Pachter, R.; Naik, R. R. Self-Assembled Peptide Nanotubes as Electronic Materials: An Evaluation from First-Principles Calculations. *Appl. Phys. Lett.* **2015**, *106* (18), 183707.

(223) Barnhart, M. M.; Chapman, M. R. Curli Biogenesis and Function. *Annu. Rev. Microbiol.* **2006**, *60*, 131–147.

(224) Hammer, N. D.; Schmidt, J. C.; Chapman, M. R. The Curli Nucleator Protein, CsgB, Contains an Amyloidogenic Domain That Directs CsgA Polymerization. *Proc. Natl. Acad. Sci. U. S. A.* **2007**, *104* (30), 12494–12499.

(225) Bian, Z.; Normark, S. Nucleator Function of CsgB for the Assembly of Adhesive Surface Organelles in Escherichia Coli. *EMBO J.* **1997**, *16* (19), 5827–5836.

(226) Chapman, M. R.; Robinson, L. S.; Pinkner, J. S.; Roth, R.; Heuser, J.; Hammar, M.; Normark, S.; Hultgren, S. J. Role of Escherichia Coli Curli Operons in Directing Amyloid Fiber Formation. *Science* **2002**, *295* (5556), 851–855.

(227) Dueholm, M. S.; Nielsen, S. B.; Hein, K. L.; Nissen, P.; Chapman, M.; Christiansen, G.; Nielsen, P. H.; Otzen, D. E. Fibrillation of the Major Curli Subunit CsgA under a Wide Range of Conditions Implies a Robust Design of Aggregation. *Biochem.* **2011**, *50* (39), 8281–8290.

CHAPTER 2 *Geobacter sulfurreducens* Pili Support Ohmic Electronic Conduction in Aqueous Solution

2.1: Abstract

The bacterium *Geobacter sulfurreducens* is a model biological catalyst in microbial electrochemical devices. *G. sulfurreducens* forms electrically conductive, electrode-associated biofilms, but the biological structures mediating electrical conduction from cells to the electrodes are a matter of debate. Bacteria in these communities produce a network of fiber-like Type IV pili, which have been proposed to act either as inherent, protein-based electronic conductors, or as electronically inert scaffolds for cytochromes mediating long-range charge transport. Previous studies have examined pilus conduction mechanisms under vacuum and in dry conditions, but their conduction mechanism under physiologically relevant conditions has yet to be characterized. In this work, we isolate *G. sulfurreducens* pili, and compare the electronic conduction mechanism of both live biofilms and purified pili networks under dry and aqueous conditions. Solid state *I–V* characteristics indicate that electronic transport in films of purified pili is representative of conduction in a fiber percolation network. Electrochemical gating measurements in a bipotentiostat device configuration confirm previous results suggesting redox currents dominate live biofilm conduction. Purified pili films, however, exhibit non-redox electronic conduction under aqueous, buffered conditions, and their conductivity increases with decreasing temperature. These findings show that isolated pili possess inherent, non-redox-mediated conductivity consistent with a metallic-like model of charge carrier transport. The results demonstrate an experimental platform for studying electronic transport in biomaterials and suggest that pili serve as an exemplary model for designing bioelectronic interfaces.

2.2: Introduction

Electronic charge transport in biological molecules, from DNA to photosynthetic enzymes, typically follows a donor–bridge–acceptor model[1–4]. In this model, electrons either tunnel through the molecule over nanometer distances or use thermally activated hopping to traverse longer distances, using active sites such as immobilized redox cofactors[5,6]. The maximum length scales for redox-mediated, biological electron transport have been expanded since the discovery of electronic conduction over microns to centimeters in communities of anaerobic sediment microbes[7–9]. One such bacterium, *Geobacter sulfurreducens*, has been extensively studied for its production of Type IV pili, a class of filamentous protein appendages, required for long-range electron transport in the environment. While nanowires produced by other sediment microbes, such as *Shewenella oneidensis*, have demonstrated long-range conductivity *via* redox-activated cytochrome hopping[10], pili purified from *G. sulfurreducens* exhibit temperature dependent transport inconsistent with thermally activated hopping[11], suggesting a novel paradigm for long-range biological electronic transport.

Structural homology models suggest that the peptide monomer of pili, PilA, has aromatic residues that cluster to from conduction conduits when assembled into the molecular wire[12–15]. Electronic conduction in pili occurs over several micrometers, a length-scale comparable to those observed for thermally activated redox hopping in biological systems[5] but mechanistically distinct. In contrast to the hopping mechanism, the individual pili[16] and dry pili films[11] exhibit a metallic-like temperature dependence[13]. Claims of metallic-like transport have been contested for several reasons[17]. Firstly, the crystal structure of the intact pilus has not been determined to verify the aromatic clustering hypothesis. Rather, the conductive contribution of aromatics has been suggested by deletion experiments, where the removal of aromatic residues from PilA lead to a decrease in current production of electrode-associated communities[18]. However, homology-based structural models present

conflicting results regarding the possibility and spacing of aromatic residue overlap, and several studies imply that delocalized electron transport through the aromatics is unlikely[12–15,19–21].

Secondly, although pili have been implicated in current production in *G. sulfurreducens* biofilms thicker than 10 μm[22], measurements of electronic transport through biofilm are dominated by Faradaic currents at the redox potentials of biofilm-associated cytochromes, as opposed to the linear response expected metallic-like electronic transport models[23–25]. Lastly, biofilms oxidize the electron donor acetate at a finite rate and grow to a thickness limited by the rate of electron transfer between cytochromes, consistent with the idea that these redox active proteins mediate charge transport[26]. Regardless, the contributions of *G. sulfurreducens* cytochromes, which localize along the pilus, have not been conclusively separated from pili conductivity measurements[27]. Further insights into the conduction mechanism of extracted pili in conditions resembling the environment of the live biofilm would provide several key theoretical contributions in addition to potential design principles for technological applications. If pili exhibit metallic-like conductivity, in which charge carriers behave as classical point charges, they defy the standard donor–bridge–acceptor model and suggest the need for a better understanding of long-range biological electron transport[11,13]. As a biological material with electronically conductive properties, these protein wires may function as useful bioelectronics interface materials.

In this study, we isolate native *G. sulfurreducens* pili by salt precipitation from culture supernatants and cast pili films onto solid-state and electrochemical transport devices for the characterization of their electronic properties. Solid-state measurements indicate that pili mats are conducting percolation networks orders of magnitude more conductive than globular protein, *Pseudomonas aeruginosa* pili films, and amyloid-β (Aβ) fiber film controls. Distinct from previous measurements on *G. sulfurreducens* pili[11,28], our electrochemical measurements are performed

in a bipotentiostat configuration with controlled, reference gating of the electrode potentials[25,29,30]. These measurements show that purified pili films exhibit conductivity independent of electrochemical gating potential, and an inverse relationship between temperature and conductivity in aqueous conditions, further supporting a metallic-like rather than cytochrome-mediated charge transport mechanism.

2.3: Results and Discussion

2.3.1: Analytical Characterization of Purified *G. sulfurreducens* Pili

Native pili from *G. sulfurreducens* cultures were isolated from supernatant using a modified magnesium chloride precipitation protocol. Purified pili were then spin coated onto silicon wafers for imaging or onto interdigitated electrodes for electronic characterization and subsequent imaging. The atomic force microscope (AFM) image in Fig. 2.1A shows the typical morphology of intact pili fibers in the purified product. Height profile measurements from small area scans (Fig. 2.1B) reveal that the fibers are approximately 4–6 nm in diameter, consistent with previous findings[31] and existing homology models[14,15,19,32]. The globular debris may be aggregated pilins, cytochromes, or non-proteinaceous cell material that is not detected by the analytical methods discussed below.

Polyacrylamide gel electrophoretic separation (SDS-PAGE) was used to identify the major protein component of purified *G. sulfurreducens* pili preparations. *G. sulfurreducens* pili are resistant to routine denaturing conditions, but they disassemble into their constituent pilin protein building blocks after extended boiling in aqueous sodium-dodecyl sulfate (SDS) or incubation in sufficiently high concentrations of octyl β-D glucopyranoside (OG)[33]. The major pilin component of *G. sulfurreducens* pili, PilA (gsPilA), migrates through the gel after pilus denaturation. gsPilA runs higher on the gel relative to its expected 6.6 kDa molecular weight (Fig. 2.1C) possibly due to their tight α-helical structure in the running buffer, which can interfere with SDS binding[34] and increase the steric

bulk of the protein while migrating in the gel. To help identify gsPilA in the pili extract from silver stained gels, an engineered pilin standard (G_5PilA) with the mature (secreted) gsPilA sequence and a Gly_5 C-terminal spacer was expressed, purified, and separated from its solubility and affinity tags at a TEV protease cleavage site. gsPilA from purified pili aliquots subjected to different denaturing conditions runs at a similar height to the engineered pilin after cleavage by TEV protease (Fig. 2.1C) gsPilA bands migrate through the gels just below the G_5PilA band, commensurate with the added molecular weight of the Gly_5 spacer in the engineered pilin. If not treated with strong denaturants, pili remain intact at the top of the gel lane, such as in previously reported preparative gels[33].

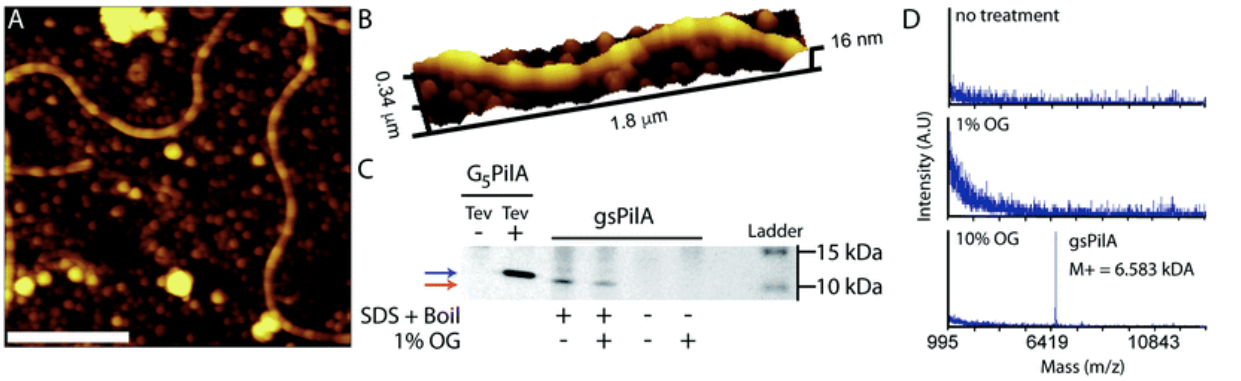

Figure 2.1: Imaging and molecular analysis of purified *G. sulfurreducens* pili. (A) Plane and (B) perpendicular view AFM images of isolated pili. (C) SDS-PAGE gel of purified pili under different denaturation conditions. Red and blue arrows indicate the migration height of gsPilA and the engineered pilin, G_5PilA, respectively. G_5PilA is appended to a solubility and affinity tag until cleavage by TEV protease. (D) MALDI-TOF spectra of purified pili under non-denaturing (no treatment, 1% OG) and denaturing (10% OG, diluted to 1% prior to MALDI analysis) conditions. gsPilA appears at the expected *m/z* = 6.5 kDa for the singly charged species. Scale bar in (A) is µm.

The molecular weight of gsPilA in the intact pili was confirmed by matrix-assisted laser desorption/ionization time-of-flight (MALDI-TOF) mass spectrometry. Mass spectra of the pili extracts were collected from samples without denaturation treatment (Fig. 2.1D, top), exposed to 1% OG (Fig. 2.1D, middle), and exposed to 10% OG diluted to 1% before casting on the MALDI plate (Fig. 2.1D,

bottom). gsPilA appears in the mass spectrum near the expected 6572 m/z[13] of the singly charged species only when the purified pili were denatured with 10% OG[33]. The dilution of the 10% OG denatured pili solutions to a final OG concentration of 1% was necessary to prevent signal interference caused by the denaturant. Consistent with findings in our SDS-PAGE analysis (Fig. 2.1C) 1% OG alone is not enough to denature pili into gsPilA monomers (Fig. 2.1D, middle). The presence of gsPilA in OG denatured pili samples was confirmed by protein sequencing *via* LC-MS/MS after a tryptic digest (Supporting Fig. S2.1)

2.3.2: Solid-State *I-V* Characteristics of Purified *G. sulfurreducens* Pili

Pili films spin coated onto interdigitated electrode devices showed a resistance of 470 Ω at an applied bias of ±0.8 V, with linear current response throughout the applied voltage range. Pili in the device channel had diameters ranged from 4–6 nm, as determined by height profiles of AFM micrographs, and an average length of 4.57 ± 0.26 μm (Supporting Fig. S2.2) Pili fiber film were four orders of magnitude more conductive than an equivalent amount of the globular protein bovine serum albumin (BSA), six orders of magnitude more conductive than cell-free growth media (NBAF) processed in an identical manner to the pili, and seven orders of magnitude more conductive than fibers of amyloid β (Aβ)-forming peptides[35] (Fig. 2.2A) The two protein controls account for the presence of arbitrary protein on the interdigitated electrodes and the aromaticity and secondary structure of gsPilA: film conductivity of BSA, a well-characterized protein with mixed α-helical and β-sheet structure[36], confirmed that a generalized protein deposited on the interdigitated electrodes did not produce appreciable current; comparison with Aβ fiber suggests that the pili possess unique sequence or structural features responsible for electronic conduction.

Aβ fibers have similar diameter and length scales to isolated pili[35] (Supporting Fig. S2.3) and contain aromatic amino acid residues, which have been suggested to confer conductivity to the pili

fibers[12–15,18]. In Aβ fibers, these aromatics are essential for assembly and are located between adjacent sheets at distances <6.5 Å[37–39]. These distances are comparable to those predicted for the aromatic clusters in some *G. sulfurreducens* pilus homology models[12,14,15]. Despite these structural similarities, Aβ fibers and *G. sulfurreducens* pili comprise monomer units assembled in distinctly different secondary structures: Aβ monomers are folded in β-sheets[35,38], whereas the gsPilA monomer assembles into a tight α-helix[12,14,15]. The drastic difference in conductivity between the two fibers may be due to the difference in secondary structure or relative positioning of aromatic residues. Indeed, modeling and measurements of homopeptide monolayers suggest that both aromatics residues and α-helical structure independently contribute to peptide conductance[15,40–45].

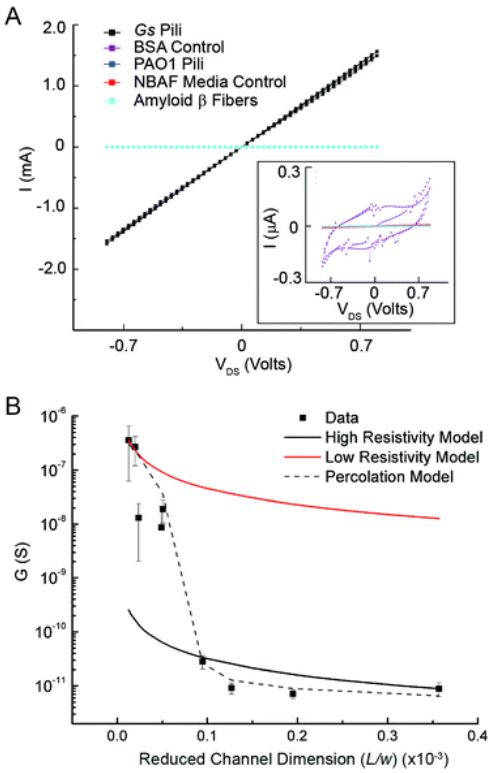

Figure 2.2: Solid-state electronic transport characterization of purified *G. sulfurreducens* pili films. (A) *I–V* characteristics of *G. sulfurreducens* pili films and controls. Inset shows the low current *I–V* characteristics of the control films. *P. aeruginosa* (PAO1) pili, NBAF, and Aβ fibers are overlapping near-baseline data in the main panel and inset. (B) The conductance of pili films in solid-state devices varies with reduced channel dimensions. The solid lines model the behavior of the higher (red) and lower (black) limits for continuous film conduction, extrapolated from the high and low conductance values of the pili film at the reduced channel dimension extremes.

G. sulfurreducens pili are also five orders of magnitude more conductive than Type IV pili purified from *P. aeruginosa* strain PAO1 (Supporting Fig. S2.4) which have previously been demonstrated to be non-conductive[18]. The sum of these measurements suggests that the observed conductivity is specific to the sequence and structure of the purified *G. sulfurreducens* pili fibers.

Pili film conduction was measured as a function of interdigitated electrode spacing (Fig. 2.2B). Identical films were spin coated onto devices with the inter-electrode spacing ranging from 5 to 35 μm. The reduced channel dimension on the independent axis, L/w, is the electrode separation normalized to the width of the channel (Supporting Fig. S2.5). The upper and lower bounds for hypothetical continuous film conduction are shown by the red and black traces in Fig. 2.2B. The upper limit (red) was obtained by extrapolating the conductivity of the most conductive measurement to the normalized conductance across all L/w, assuming a continuous film conduction channel. The lower limit (black) was determined in a similar manner, extrapolating the conductivity of the least conductive measurement to all L/w, assuming a continuous film conduction channel. The experimental data does not follow the conductivity trend of either the red or black curve. Rather, it transitions between the upper and lower limits as the reduced channel dimensions increase. The dashed black line represents a percolation network conduction model fit to the experimental data, as described in the discussion below.

These measurements therefore suggest that the film conductivity of purified pili follows a percolation network model (Fig. 2.2B). In percolating systems, conductance follows a power law dependence centered about a critical threshold value φ_c, which represents a progression of the network topology with increasing component concentration to a point at which the system undergoes a sharp transition in conductivity. This value is used to distinguish percolation transitions at critical volume fractions, density fractions, concentrations, or mass fractions[46–50] and the conductance of a network composed of conductive elements varies as:

$$G \propto (\varphi - \varphi_c)^t \quad \text{(Equation 2.1)}$$

where t is the critical exponent, having a theoretical value of 1.3 and 2 for two- and three-dimensional random, resistive wire networks, respectively.

Pili film conductivity experiments were conducted with identical preparation conditions on interdigitated electrodes of varying dimensions. As a result, the conductance of a given pili film can be expressed in terms of an independent device variable, the reduced channel dimension $\frac{L}{w}$. The conductance of the films can thus be expressed as:

$$G \propto (\frac{L}{w} - \frac{L}{w_c})^n \quad \text{(Equation 2.2)}$$

where $\frac{L}{w_c}$ is the threshold reduced channel dimension and n is the percolation exponent, which is not necessarily identical to t, given that Equation 2.2 pertains to percolation onset due to network geometry on the device as opposed to onset at a particular size or volume of sample.[53] The electrode spacing serves as a proxy for the length scale of continuous pili network conduction for fixed volumes and concentrations of sample. Fitting Equation 2.2 to the data (Fig. 2.2B), the threshold reduced channel dimension is $\frac{L}{w_c} = 9.08 \times 10^{-5}$, corresponding to an electrode spacing between 10–15 μm. The mean statistical length of individual pili obtained through our purification was 4.57 μm (Supporting Fig. S2.2) suggesting that, on average, at least three pili are involved in the formation of each conductive bridge between electrodes. From the above model, the percolation exponent is $n = 3.23$. Although n deviates from theoretical values[48–51], it is consistent with experimental values of n for networks of high aspect

ratio elements, which range from 0.5 to 4.0[51]. Deviation from theoretical values is attributed to a distribution of junction resistances at conductor–conductor interfaces within the network[52–55], which may be present in the random networks of pili which make up the channel in our devices (Fig. S2.6). The above percolation network conduction modeling is agnostic of the mechanism (*i.e.* charge hopping or ohmic transport) of electronic conduction through each pilus fiber. Instead, it describes a dependence of film conduction on the density of junctions and fiber length.

2.3.3: Electrochemical Transport Measurements

To gain a better understanding of charge transport mechanisms in purified pili films, interdigitated electrodes were modified for electrochemical gating in anaerobic, aqueous electrolyte. A bipotentiostat was used to perform these measurements, as this setup can distinguish between redox and non-redox charge transport mechanisms between the electrodes. The source and drain electrodes are each swept with respect to a Ag/AgCl reference at a fixed source–drain offset potential, V_{DS}. Background currents are sunk through a common platinum wire counter electrode (Fig. S2.7) allowing for simultaneous monitoring of oxidation/reduction at each electrode, as well as current between the two electrodes. This experimental setup was previously used to demonstrate redox-mediated conduction in live *G. sulfurreducens* biofilms[23,25,29].

Using this setup, we analyzed the current response from a live *G. sulfurreducens* biofilm (Fig. 2.3A) and three distinct conduction controls: a solution of the soluble redox couple potassium ferro-/ferricyanide (Fig. 2.3B), a redox-active conducting polymer film of polyvinylferrocene (PVF) (Fig. 2.3C), and an ohmic, band-like conducting polymer film of PEDOT:PSS (Fig. 2.3D).

The redox-active potassium ferricyanide and PVF film exhibit characteristic Faradaic current responses to swept gate potential, similar to those observed in the *G. sulfurreducens* biofilm (Supporting Fig. S2.8), where conduction across the device manifests as distinct reduction and oxidation peaks

dependent on the value of the swept gate potential (Fig. 2.3B & C). I_{DS} is dependent on the gate potential, as current is only observed at potentials associated with redox states of the mediator.

The same measurements were conducted for films of the band-like conductor PEDOT:PSS (Fig. 2.3D) over a gate potential range in which the conducting polymer is not oxidized, as evidenced by a lack of color change[56,57]. In this range, the polymer exhibits ohmic or band-like conduction characteristic of a degenerately-doped semiconductor[58–60]. In contrast to the redox mediator controls, the PEDOT:PSS film exhibits constant current in this range, independent of the gate potential but strongly dependent on the V_{DS}, characteristic of a non-redox current response.

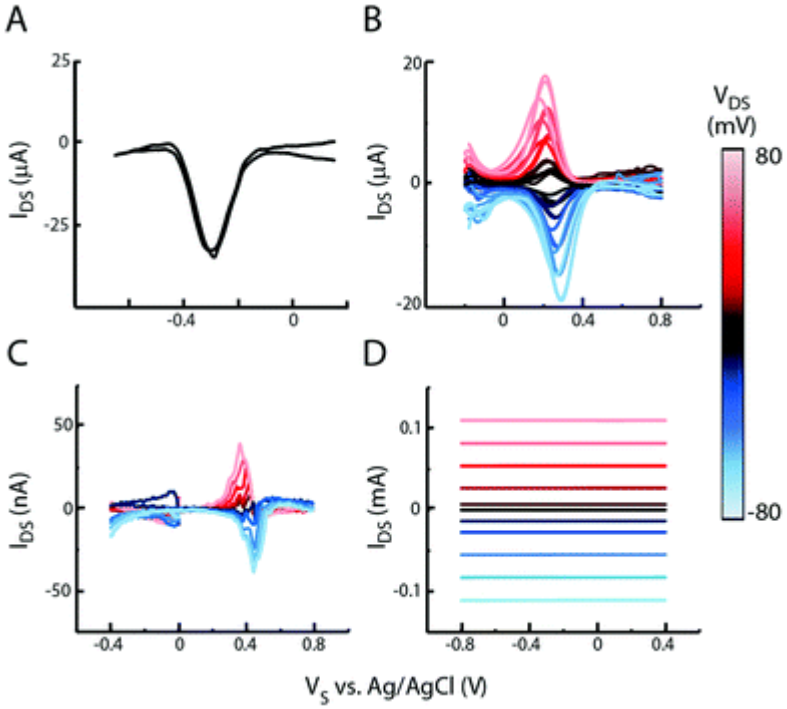

Figure 2.3: Electrochemical transfer characteristics of a live *G. sulfurreducens* biofilm and abiotic controls. The source electrode potential is swept relative to the reference electrode at different V_{DS} values according to the color scale at the right. (A) Total source–drain current of a live *G. sulfurreducens* biofilm channel, at V_{DS} = 10 mV, shows prominent redox peak as a function of gate voltage, V_S. (B) A solution redox mediator, $K_3[Fe(CN)_6]$, and (C) a solid-state, thin film redox conductor, PVF, exhibit similar Faradaic current responses. (D) A solid-state, thin film band conductor, PEDOT:PSS, shows the current response of an ohmic conduction channel in the bipotentiostat devices. Electrode spacing = 5 µm.

Similar to PEDOT:PSS, isolated pili films exhibit a constant current with respect to gate potential, with no apparent redox-mediated transport activity, and current through the channel is

determined by V_{DS}. This current response is similar at neutral pH (Fig. 2.4A) and at pH 4.0 (Supporting Fig. S2.9), at which cytochromes denature due to protonation of the histidine ligand, thus interfering with heme coordination[61,62]. These findings provide further evidence that cytochromes, while dominating the current response in living biofilm, do not contribute to charge transport through films of purified pili, and that purified pili are inherently electronically conductive in buffered aqueous solutions resembling physiologically-relevant conditions. Previous studies have used β-mercaptoethanol to control for a cytochrome contribution to electronic conduction, but the mechanism of inactivation has been contested due to a lack of precedent[27]. Nevertheless, these electrochemical studies show that charge transport through purified *G. sulfurreducens* pili is dominated by a non-redox mechanism, regardless of any residual cytochromes that may be present in the pili sample.

Temperature-dependent conductance measurements provide further confirmation of an inherent, non-redox-mediated transport mechanism in pili. In dry pili films, conductance in pili increases exponentially upon cooling to a point[11], a trend likened to quasi-one-dimensional organic metals[63–66]. We confirmed this temperature dependence on pili films under aqueous, buffered conditions, using our bipotentiostat setup. The bipotentiostat cell was immersed in a temperature-controlled water bath, and I_{DS} was measured at a fixed V_{DS} of 60 mV. Throughout the temperature range measured (2–65 °C), pili films in aqueous conditions exhibit increasing conductance with decreasing temperature (Fig. 2.4B). The Arrhenius plot of temperature-dependent conductance exhibits two apparent linear regimes, both with positive slopes, that cross over near room temperature. Pili conductance increases monotonically with decreasing temperature, a trend consistent with particle-like charge carrier transport in band-like conductors. In such conductors, the Drude model suggests the cross-over between linear regimes indicates distinct scattering rates above and below room temperature. Although the trend of increased conductivity with decreasing temperature is characteristic of metals and metallic-like materials[63–66],

other effects may explain this temperature dependence in organic systems. True band conduction in organic materials is typically observed only in molecular crystals[67]. Additionally, isolated pili exhibit a weak temperature dependence, with conductance changing by 10% over a range of 70 K, which is distinct from the exponential temperature dependence observed in dry films of purified pili[11] and in metallic-like organic conductors[63,64].

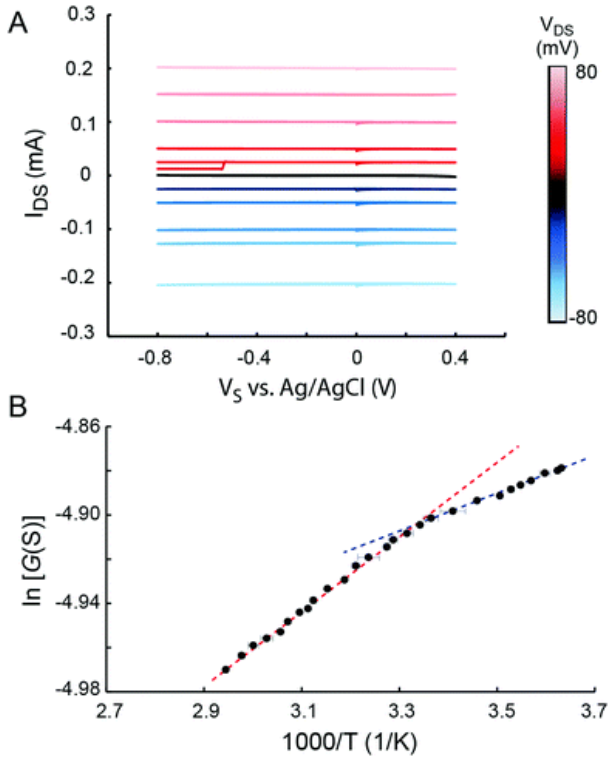

Figure 2.4: Electronic transport in purified *G. sulfurreducens* pili in aqueous buffered conditions. (A) Electrochemical transfer characteristics of the pili film, at different V_{DS} values according to the color scale at the right, in phosphate–citrate buffer at pH 7.0. (B) Temperature-dependent conductance (G) of the pili film at V_{DS} = 60 mV and V_S = 0 *vs.* Ag/AgCl in phosphate–citrate buffer pH 7.0. Dashed red and blue lines indicate linear regimes in the Arrhenius plot above and below room temperature ($1000/T$ = 3.39 K^{-1}), respectively. Electrode spacing = 5 μm.

Whether the proximity and symmetry of residues responsible for electron transport in pili are adequate for the creation of an electronic energy band is an open question that requires, among other things, a *G. sulfurreducens* pilus crystal structure, to resolve. Instead, it is possible that temperature-dependent conformational changes of the pili are responsible for the observed conduction trend[40,68]. Such fluctuations of molecular structure have been observed to facilitate flickering resonance (transient

degeneracy) among electronic states in biomolecules. Because thermal disorder may diminish the probability of energetic state coupling, charge transfer rates are predicted to decrease with increasing temperature[69,70]. Although flickering resonance has not been demonstrated over the micron length scales associated with electron transport along pili, this mechanism may explain the weak temperature dependence of pili film conductance and the ohmic transport observed in *I–V* measurements[70].

Nevertheless, the trend of increasing conductivity with decreasing temperature observed in aqueous buffer confirms the lack of cytochrome involvement in long-range conduction through isolated pili, as redox hopping is a thermally activated process[11,29]. Based on these data, we hypothesize that the inherent conductivity and temperature-dependent behavior observed in purified pili films is due to a combination of aromatic amino acid content and the α-helical nature of the gsPilA monomer, consistent with recent experimental and theoretical work. α-Helical homopeptides support electron transport by increasing electronic coupling between the outer-valence states in peptides[40], possibly due to dipole alignment between peptides[15,71]. Furthermore, this hypothesis is consistent with the seven orders of magnitude difference in conductance of purified pili and the Aβ fiber mats, as well as recent tunneling conductance measurements of individual pili in vacuum, which reveal no observable band gap between conduction states of the pilus at room temperature[31]. These tunneling measurements quantify radial charge transport through *G. sulfurreducens* pili into a conductive substrate in vacuum, as opposed to our experiments which measure charge transport along the axial length of pili and across neighboring pili junctions in the cast films between electrodes in aqueous solution, a configuration that is more relevant to their functional role in living biofilms. Although both adsorption on substrates and vacuum conditions may change the conformation of the pilus[15], these previous observations of activation-less transport at room temperature are corroborated by our measurements of hydrated pili in aqueous buffer. If a hopping transport mechanism exists along the protein backbone of our purified pili films, it is

indistinguishable from band conduction and does not exhibit an observable activation energy within the range of biologically-relevant temperatures explored in the present study. In such a case, our results suggest hydrated pili maintain a conformation in which thermal energy (at a minimum of about 24 meV at 0 °C) is sufficient to overcome any putative activation energy required for hopping between isolated states.

2.4: Conclusion

The data from electrochemically gated *G. sulfurreducens* biofilms corroborate previous findings attributing long-range electron transport to multistep electron hopping between cytochromes. However, identical gating of purified pili films show that pili exhibit an inherent conductivity under conditions similar to those encountered by the source bacterium, and this conductivity is independent of a putative redox hopping mechanism. Together, these results support the hypothesis that pili play a crucial role in mediating conduction through biofilms, and that pili are intrinsically conductive in an environment resembling conditions in live biofilms. The intrinsic, non-redox-mediated conduction of isolated *G. sulfurreducens* pili suggests a rethinking of models for long-range electron transport in amino acid-based systems. Moreover, the electronic conductivity characteristic of pili in hydrated environments may serve as biological inspiration for the study of structure–property relationships in conductive biomaterials and the development of novel bioelectronics interfaces.

2.5: Supporting Information

2.5.1 Biological Sample Preparation

Strains and Cell Culture. All *G. sulfurreducens* cultures (PCA wild type, DSMZ strain 12 127) for pili purification were grown anaerobically at 25 °C[9] from shaken culture tubes in 1 liter cultures of sterilized and degassed NBAF medium[72]: 0.04 g L^{-1} calcium chloride dihydrate, 0.1 g L^{-1}magnesium

sulfate heptahydrate, 1.8 g L^{-1} sodium bicarbonate, 0.5 g L^{-1} sodium carbonate, 0.42 g L^{-1} potassium phosphate monobasic, 0.22 g L^{-1} potassium phosphate dibasic, 0.2 g L^{-1} ammonium chloride, 0.38 g L^{-1} potassium chloride, 0.36 g L^{-1}sodium chloride, vitamins and minerals as listed in ref.[73]. and 20 mM acetate as the electron donor and 40 mM fumerate as the electron acceptor. Resazurin was omitted and 1 mM cysteine was added as an electron scavenger. All chemicals obtained from Fisher Scientific unless otherwise noted.

Purification of *G. sulfurreducens* pili. After reaching stationary phase, *G. sulfurreducens* cells were pelleted from cultures by centrifugation at 5000*g* for 20 min at 4 °C.*G. sulfurreducens* pili were purified from this initial supernatant using a 1 : 10 ratio of 1.1 M aqueous $MgCl_2$ to supernatant. Supernatants were precipitated overnight at 4 °C and centrifuged at 50 000*g* for 1 h at 4 °C to obtain pili. Pili pellets were resuspended with 0.2 μm filtered ultrapure water and additional contaminants were removed with 30–50 kDa dialysis tubing. After three 1 L exchanges of ultrapure water, the dialyzed sample was collected for use and stored at 4 °C. Cytochrome-containing proteins precipitated during storage and pili were collected from the clear supernatant.

Generation of Cleavable Pilin Fusion Standard. Coding sequence for mature G. sulfurreducens PilA was amplified from genomic DNA by PCR using the following primers: CGCGGTACCGAGAACCTGTACTTCCAAGGTTTCACCCTTATCGAG (forward) and CGCGCGGCCGCTTAACTTTCGGGCGGATAGG (reverse). The PCR product was gel purified and cloned into the pMocr plasmid (University of Michigan HTP Expression Lab)[74] using the KpnI and NotI restriction sites. The resultant pMocr-GspilA plasmid has a gene encoding a polyhistidine-tagged N-terminal Mocr solubility domain which is cleavable by an engineered tobacco etch virus (TEV) protease site immediately preceding the C-terminal mature pilin. As this product was found to not cleave efficiently, a second construct encoding 5 glycines immediately

downstream from the TEV cleavage site was created using the QuikChange II protocol (Agilent) with pMocr-GspilA as the template and the following primers: CAAGGCGGTGGCGGTGGCGGTTTCACCCTTATCGAG and ACCGCCACCGCCACCGCCTTGGAAGTACAGGTTCTC. Plasmids were maintained in E. clonii 10G (Lucigen).

The Mocr-gly5-PilA fusion was expressed from Rosetta2 (Novagen) cells grown at 37° C in terrific broth (Amresco) supplemented with 4% glycerol. Upon reaching an OD600 of 0.6, cells were transferred to 20° C, induced with 0.25 mM IPTG, stirred vigorously for 20 hours, and harvested by centrifugation at 8,000g. The resultant pellet was resuspended in 10 ml lysis buffer (50 mM Tris-HCl pH 7.5, 150 mM NaCl, 10 mM imidazole, 2 mM β-mercaptoethanol, 5% glycerol) supplemented with 1 mg lysozyme and submitted to lysis by sonication. Cell lysate was clarified by centrifugation at 15,000g for 45 min; the soluble fraction was combined with 1 ml Ni-NTA slurry pre-equilibrated in lysis buffer and batch bound overnight at 4° C. This mixture was passed through a gravity flow column; retained resin was washed with lysis buffer in 10 ml stepwise increments containing 10, 20 and 40 mM imidazole. Bound protein was eluted with 5 ml lysis buffer containing 300 mM imidazole. Eluate was concentrated using Corning Spin-X 10 kDa MWCO filters and buffer-exchanged into 25 mM Tris-HCl pH 7.5, 50 mM NaCl, 20% glycerol for storage at -80° C. Purified fusion protein was processed using Promega Pro-TEV Plus following the manufacturer's instructions.

***G. sulfurreducens* Biofilm Growth**. G. sulfurreducens biofilm were grown in a standard microbial fuel cell (MFC) configuration purchased from Adams and Chittenden (MFC 100.25.3). The anode and cathode glass compartments are separated by a Nafion membrane (Fuel Cell Store, Nafion 117), held in place by an O-ring and clamp. Wires were inserted through the rubber septum seals

to connect electrodes to external connections. A split electrode with two externally-connected wires functioned as the anode and a carbon cloth electrode functioned as the cathode. Prior to inoculation, the fully assembled MFC was autoclaved. The anode chamber was inoculated with a log-phase culture of Geobacter sulfurreducens strain (PCA wild type, DSMZ strain 12127) and maintained under anaerobic conditions (N2:CO2, 80:20%) with 100 mL of freshwater medium containing fumarate (40 mM) and acetate (10 mM) using previously described methods 6 . Freshwater medium contained 2.5 g/L sodium bicarbonate, 0.1 g/L potassium chloride, 0.25 g/L ammonium chloride, and 0.6 g/L sodium phosphate dibasic, 10 mL vitamin mixture, and 10 mL mineral mixture. 10 mM cysteine was added as an oxygen scavenger[23]. The cathode consisted of 20mM $K_3[Fe(CN)_6]$ in 100 mL of autoclave-sterilized potassium phosphate buffer: 0.31 g/L ammonium chloride, 2.69 g/L sodium phosphate monobasic, 4.33 g/L sodium phosphate dibasic, 0.13 g/L potassium phosphate. The biofilm was grown using established methods[72] by poising both the electrodes as anodes at +0.300 V vs. Ag/AgCl. After three days, biofilms were switched to fumerate-free freshwater medium. Biofilms were maintained until there was an approximately 0 mV potential difference between both sides of the split electrode, corresponding to biofilm spanning the electrode separation. Bipotentiostat electrochemical gating of G. sulfurreducens biofilm was performed in the MFC cell configuration.

2.5.2: Materials Characterization

Mass Spectrometry. For MALDI-TOF analysis, purified pili were denatured with 10% OG overnight and then diluted with ultrapure water to a final OG concentration of 2% prior to combining with the matrix solution of α-Cyano-4-hydroxycinnamic acid dissolved in a 2:1 solution of ultrapure water: acetonitrile and 0.2% trifluoroacetic acid. The final sample for MALDI was a

12:7:5 ratio of matrix to ultrapure water to diluted and denatured protein. Mass spectra were collected in positive ion mode.

For LC-MS/MS identification, OG-denatured gsPilA was subject to digestion by trypsin enzyme (Supporting, Fig. S2.1). Proteomic analysis of the cleaved peptides was performed by the Proteomics Mass Spectrometry Facility at UC Irvine. Results gave complete coverage of the C-terminal domain, whereas the hydrophobicity of the N-terminal domain may have interfered with the sequencing procedure.

Gel Electrophoresis. For SDS-PAGE analysis, unless otherwise noted in the text, all samples were prepared by boiling in 1x SDS loading dye for 20 min. OG-treated samples were incubated in OG overnight prior to SDS preparation. Samples were run on a Tris-HEPES gel with 16% polyacrylamide at a constant voltage of 110 mV for 60 min. Gels were silver stained following overnight fixation.

Atomic Force Microscopy. Pili on devices were imaged using atomic force microscopy (Asylum MF3PD) operating in tapping mode. The measurements were performed with aluminum-coated silicon probes (Asylum Research AC160TS-R3) with a tip radius of 9nm and a resonant frequency of 300kHz. Scans were rastered at either 0.5Hz or 1.0 Hz. Statistical pili lengths were determined by measuring fiber lengths with ImageJ (Supporting Fig. S2.2). Lengths were determined from a total of 14 AFM images.

2.5.3: Electronic Property Characterization

Device Preparation. The electrodes are comprised of 200 parallel 5 μm wide x 2 mm long gold electrode bands patterned onto a Pyrex substrate, with a 5 μm intra-band spacing. For percolation network analysis, 5 μm wide electrodes with intra-band spacings of 5, 7.5, 11.66, 20, and 35 μm; 6.25 μm wide electrodes with an intra-band spacing of 6.25 μm; and 10 μm wide electrodes with

intra-band spacings of 10, 15, 23, and 30 μm were used. Different electrode widths were used to maintain a fixed total device size of 2mm x 2mm, and differences in widths were accounted for by normalizing electrode spacings to reduced channel dimensions. Devices were photolithographically patterned onto silicon oxide or Pyrex wafers using a chrome mask with arrays of the interdigitated electrode pattern. Gold was deposited onto the patterned design with a titanium adhesion layer. The total thickness of the metallic contacts was 50 nm. After liftoff, the wafers were coated with photoresist and diced into individual devices. The photoresist was removed and each device was tested for shorts prior to depositing material. Device fabrication was performed by the foundry services at the University of California, in Irvine and at the University of California, in San Diego. For solution-gated measurements, 22-gauge solid core insulated wire leads were connected to the source and drain with conductive silver epoxy (MG Materials 8331-14g) after film deposition. After drying, exposed electrode and lead connections were sealed with waterproof silicone sealant (DAP All-Purpose Adhesive Sealant).

Solid State *I-V* Measurements. Pili and control films were spun coat onto interdigitated electrode devices in 10 μL intervals to obtain a total mass of 115 μg protein per device. For solid-state measurements, films were measured (Keithley Model 2612B) under ambient conditions at room temperature, with voltage swept between −0.8 and 0.8 V. Data in Fig. 2.2B are averages of $n = 3$ conductance values from independent *I–V* measurements.

Solution-Gated Measurements. For electrical transfer characteristics experiments, all measurements were conducted in 0.1 M phosphate–citrate buffer, with the pH varied by changing the relative amounts of sodium phosphate dibasic and sodium citrate, except the $K_3[Fe(CN)_6]$ control and live biofilms.

$K_3[Fe(CN)_6]$ transfer characteristic data were collected using 20 mM $K_3[Fe(CN)_6]$ in 0.1 M KCl. Biofilm experiments were conducted in growth media under turnover conditions. (see section **2.5.1**, *G. sulfurreducens* Biofilm Growth). Electrolyte solutions were degassed and electrochemical cells were assembled in an anaerobic chamber. Electrochemical cells were 100 mL sealed glass containers with wire connections mediated through rubber septa. Two Gamry potentiostats (series PCI4/300), linked through a bipotentiostat cable, were used to conduct cyclic voltammetry sweeps where the source and drain serve as two working electrodes. Both were referenced to the same Ag/AgCl reference electrode and shared a platinum wire counter electrode. The source electrode was swept for two cycles from 0.4 to 0.8 V with respect to the Ag/AgCl reference electrode, and the drain was swept over the same range at a fixed V_{DS}relative to the source. After subtracting any background catalytic current present at V_{DS} = 0, the difference currents between the source and the drain were plotted as the conducting current I_{con} (Supporting Fig. S2.10) Voltages were scanned at a rate of 10 mV s^{-1}.

Temperature-Dependent Measurements. For temperature-dependent studies, the electrochemical cells were placed in a stirred water bath, and the temperature was regulated using a hot plate with a thermocouple fixed in the water bath. Cooling was achieved by adding ice to the water bath. Bipotentiostat chronoamperometry measurements were performed after maintaining temperature equilibrium for several minutes. Currents from the source and drain were independently monitored while the drain was held at V_{DS} = 60 mV offset from the source. The steady-state currents at the source and drain were averaged over 1 min acquisition. The total current was taken to be half the difference between the source and drain currents, which were symmetric but with opposite polarity (Supporting Fig. S2.11)[29]. Measurements were performed with 0.1 M phosphate–citrate buffer at pH 7.0 as the supporting electrolyte.

Preparation of Control Channels for Conductivity Measurements. Aβ fibers were self-assembled from synthesized peptides[75,76]. Lyophilized peptides were incubated in 150 mM phosphate buffered saline at 37° C for two weeks to form fibers. Fiber formation was verified using atomic force microscopy (Fig. S8). P. aeruginosa PAO1 strains were cultured for pili purification as described in ref [77] and verified by AFM (Supporting Fig. S2.4). PEDOT:PSS (Heraeus Clevios PH1000) films were spun cast and baked overnight at 70° C prior to electrode assembly. PVF (Sigma Aldrich) was dried overnight under vacuum prior to dispersal in dichloromethane and were drop cast onto devices prior to electrode assembly. Due to the volatility of the dichloromethane, drop casting PVF was observed to be the most efficient method to obtain uniform films. G. sulfurreducens biofilm electrode fabrication: Electrode fabrication for biofilm growth was similar to the procedure detailed in ref [11]. To construct the electrodes, glass slides (2.5 cm x 3 cm) were cleaned ultrasonically using successive rinses of acetone, isopropanol, and ultrapure water, following blow drying with nitrogen. A 25-μm-diameter tungsten wire (Sigma Aldrich) was placed on the glass substrate as a deposition mask to achieve an insulating gap in the electrodes. An 8 nm chromium adhesion layer and a 40 nm gold film were thermally evaporated onto the substrates to produce gold split electrodes with a 25 ± 2 μm non-conductive spacing. Uniformity of the gap was confirmed through optical microscopy and electrical insulation between the two sides of the gap was confirmed through resistance measurements. A single 22 gauge core insulated wire lead was connected to each electrode using conductive silver epoxy. After drying, the lead connections were sealed with waterproof silicone sealant.

Matched peptides shown in ***bold red***.

1 MANYPHTPTQ AAKRRKETLM LQKLRNRKGF TLIELLIVVA IIGILAAIAI

51 PQFSAYR**VKA YNSAASSDLR NLKTALESAF ADDQTYPPES**

Peptide residues detected:

(R) VKAYNSAASSDLR (N)
(R) VKAYNSAASSDLR (N) + De-amidated (NQ)
(K) VKAYNSAASSDLR (N)
(K) VKAYNSAASSDLR (N) + De-amidated (NQ)
(K) AYNSAASSDLRNLK (T)
(R) NLKTALESAFADDQTYPPES

Figure S2.1: LC-MS/MS identification of mature gsPilA (sequence highlighted in yellow). The amino acids noted in parenthesis indicate the cleavage sites of the digestion enzyme trypsin, which cleaves after the R and K residues. The error probability in sequence identification ranged from 10^{-6} to 10^{-7}.

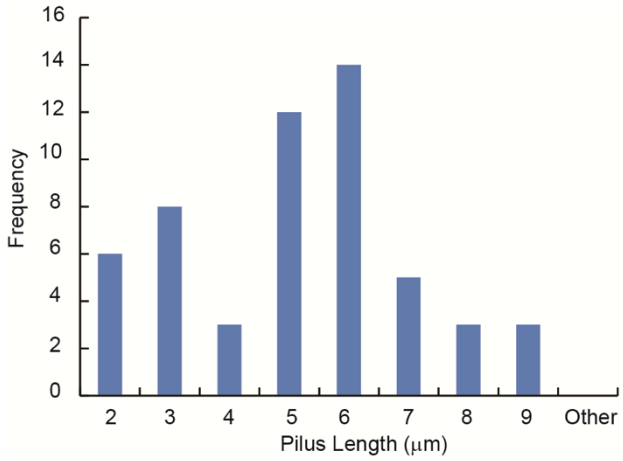

Figure S2.2: Distribution of individual pilus lengths across 14 AFM images. The average pilus length is 4.57 ± 0.26μm.

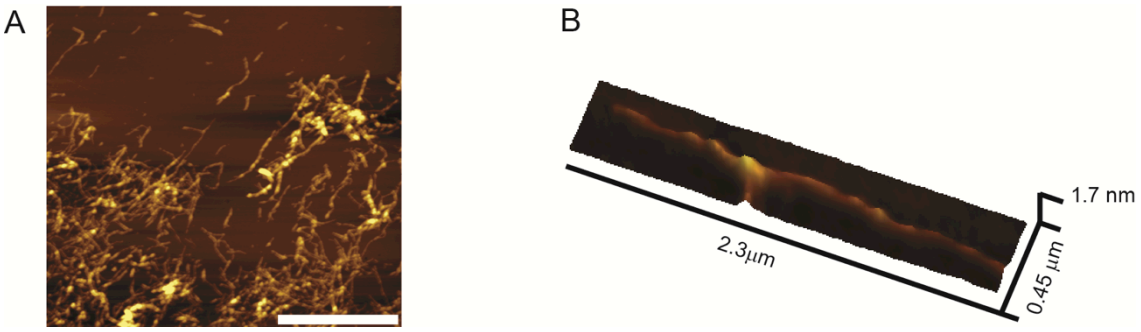

Figure S2.3: (A) Mat of Aβ fibers on interdigitated electrode devices. Scale bar, 5 μm (B) Perspective view of a single Aβ fiber from AFM imaging.

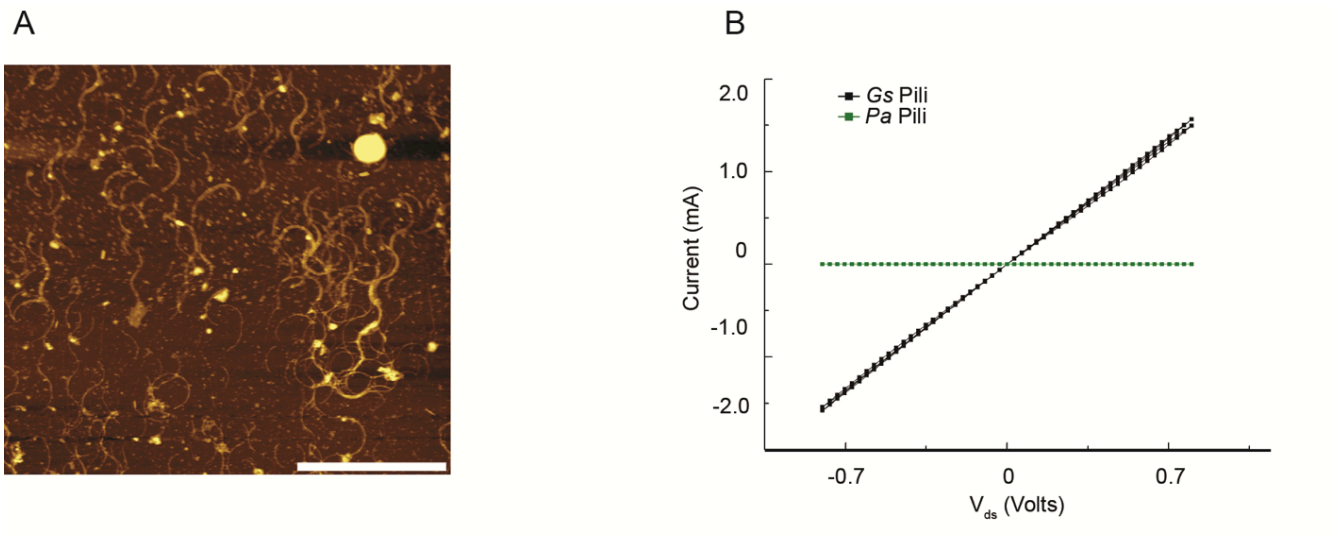

Figure S2.4: (A) Atomic force micrograph of purified PA01 pili fibers (spacing = 5 μm). (B) I-Vs of films of *G. sulfurreducens* and *P. aeruginosa* PA01 pili fibers on interdigated electrode. *G. sulfurreducens* pili films are five orders of magnitude more conductive than PA01 pili fibers.

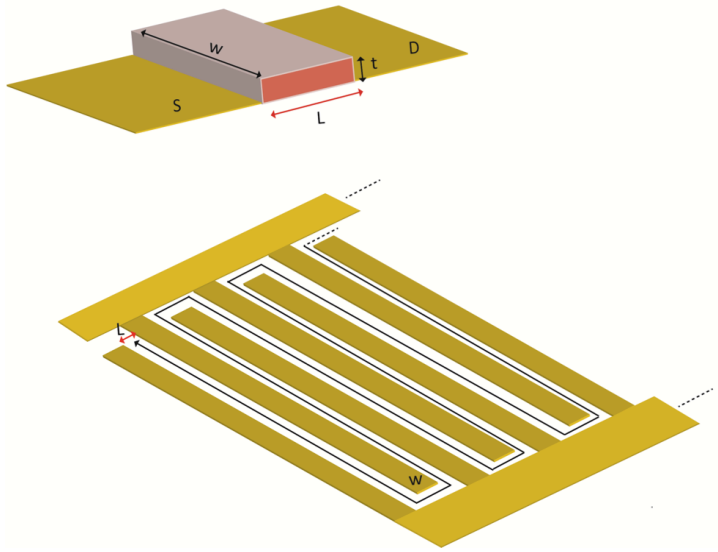

Figure S2.5: Illustration of reduced channel dimension on interdigitated electrode (*L/w*). All devices had a fixed total area, while the spacing between electrodes (*L*) differed, resulting in different channel widths *(w)*. Electrode spacing is thus normalized to the ratio *L/w*.

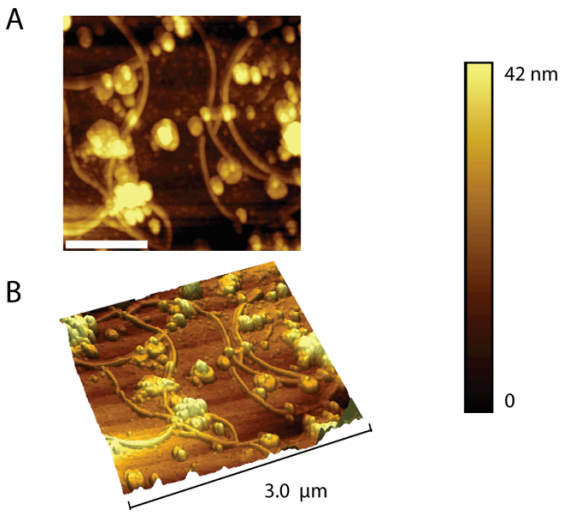

Figure S2.6: (A) Mat of pili fibers bridging gap on interdigitated electrode devices. Scale bar, 1 µm (B) Perspective view of pili fibers bridging gap from AFM imaging.

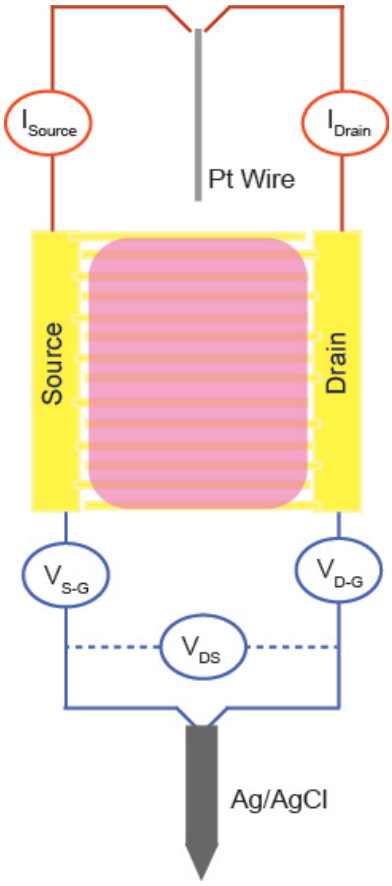

Figure S2.7: Schematic of the electrochemical circuit for biopotentiostat cyclic voltammetry. The pink shaded region is the device area covered by conducting channels of biofilms, pili, or control materials.

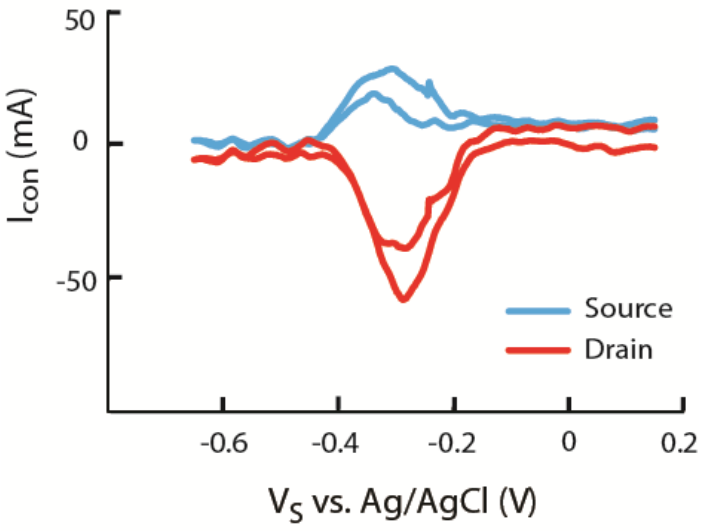

Figure S2.8: Electrochemical gating measurements of a live *G. sulfurreducens* biofilm. Source and drain current responses show symmetric current entering the source and leaving the drain at V_{DS} = 10 mV. Electrode spacing = 25 µm.

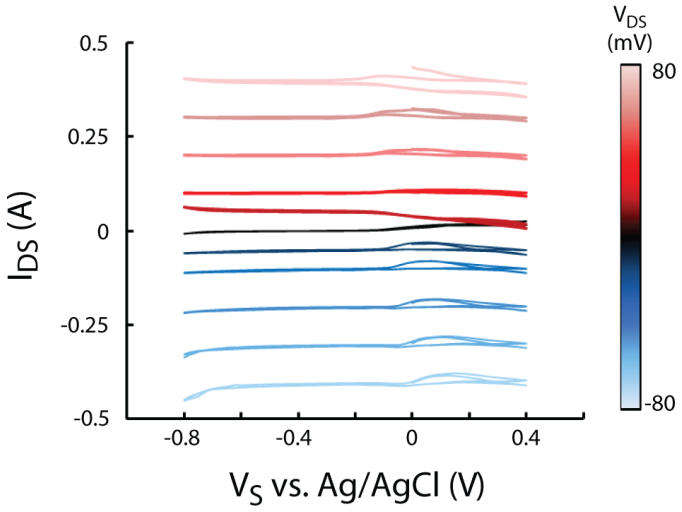

Figure S2.9: Electrochemical transfer characteristics of pili film, at different V_{DS} values according to the color scale at the right, in 0.1 M phosphate citrate buffer at pH 4.0.

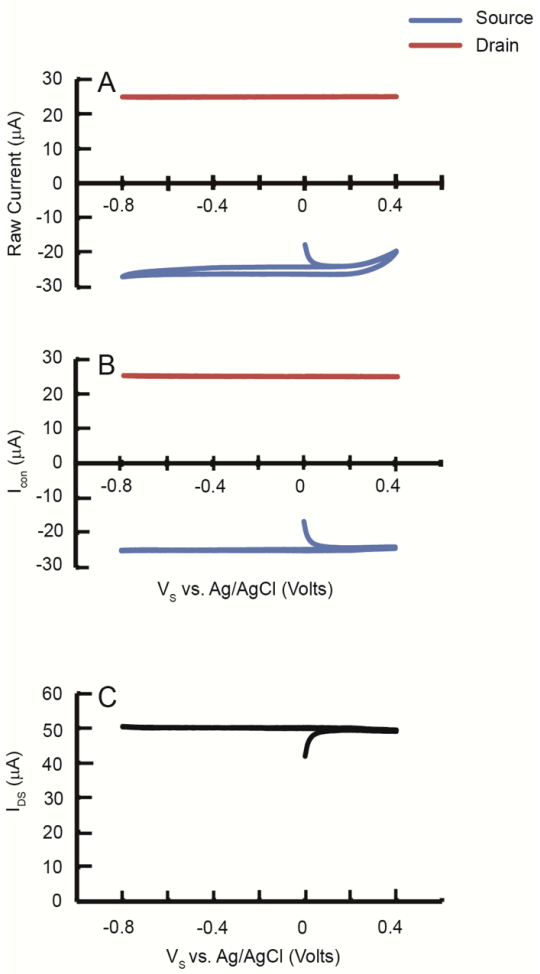

Figure S.10: Gated bipotentiostat cyclic voltammograms of pili films: (A) crude source and drain currents at V_{DS} = 10 mV, (B) conducting source and drain currents with background subtraction (background currents obtained from V_{DS} = 0 mV), and (C) source-drain current I_{DS} (drain current minus source current). Measurements taken in 0.1M phosphate citrate buffer.

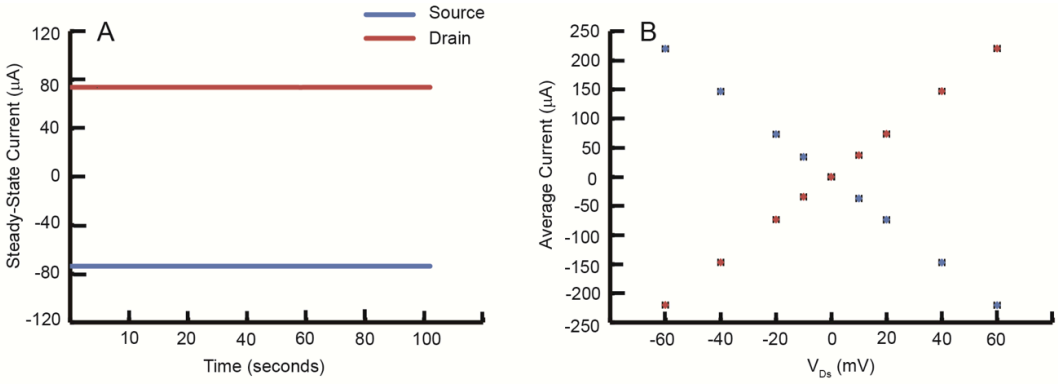

Figure S2.11: (A) Steady-state source and drain currents of pili film obtained at room temperature. (B) Average steady-state source and drain currents of pili film plotted as a function of V_{DS}. Measurements taken in 0.1 M phosphate citrate buffer pH 7.0.

2.6: Acknowledgements

The authors thank Prof. Paul Gershon for gsPilA protein sequencing, Prof. Matthew Law and Prof. Reginald Penner for access to the atomic force microscope maintained in their labs, and Dr Ryan K. Spencer for providing amyloid-β samples. Funding for this research was provided by the Air Force Office of Scientific Research (FA9550-14-1-0350) and by the National Science Foundation (NSF Graduate Research Fellowship for NLI).

Author Contributions. A.I.H. and N.L.I designed the experiments and prepared the manuscript. T.D.N. designed and purified the G_5PilA and provided microbiology expertise and training. N.L.I. ran the experiments.

This chapter is an adaptation of the material as it appears in: Ing, N.L.; Nusca, T.D.; Hochbaum, A.I. *Geobacter sulfurreducens* Pili Support Ohmic Electronic Conduction in Aqueous Solution. *Phys. Chem. Chem. Phys.* **2017**, *19* (32), 21791-21799.

2.7: References

(1) Gray, H. B.; Winkler, J. R. Long-Range Electron Transfer. *Proc. Natl. Acad. Sci. U. S. A.* **2005**, *102* (10), 3534–3539.

(2) Kharkyanen, V. N.; Petrov, E. G.; Ukrainskii, I. I. Donor-Acceptor Model of Electron Transfer through Proteins. *J. Theor. Biol.* **1978**, *73* (1), 29–50.

(3) Jortner, J.; Bixon, M.; Langenbacher, T.; Michel-Beyerle, M. E. Charge Transfer and Transport in DNA. *Proc. Natl. Acad. Sci.* **1998**, *95* (22), 12759–12765.

(4) Gray, H. B.; Winkler, J. R. Electron Tunneling through Proteins. *Q. Rev. Biophys.* **2003**, *36* (3), 341–372.

(5) Skourtis, S. S. Review: Probing Protein Electron Transfer Mechanisms from the Molecular to the Cellular Length Scales. *Pept. Sci.* **2013**, *100* (1), 82–92.

(6) Gray, H. B.; Winkler, J. R. Electron Flow through Metalloproteins. *Biochim. Biophys. Acta* **2010**, *1797* (9), 1563–1572.

(7) Nielsen, L. P.; Risgaard-Petersen, N.; Fossing, H.; Christensen, P. B.; Sayama, M. Electric Currents Couple Spatially Separated Biogeochemical Processes in Marine Sediment. *Nature* **2010**, *463* (7284), 1071–1074.

(8) Pfeffer, C.; Larsen, S.; Song, J.; Dong, M.; Besenbacher, F.; Meyer, R. L.; Kjeldsen, K. U.; Schreiber, L.; Gorby, Y. A.; El-Naggar, M. Y.; et al. Filamentous Bacteria Transport Electrons over Centimetre Distances. *Nature* **2012**, *491* (7423), 218–221.

(9) Reguera, G.; McCarthy, K. D.; Mehta, T.; Nicoll, J. S.; Tuominen, M. T.; Lovley, D. R. Extracellular Electron Transfer via Microbial Nanowires. *Nature* **2005**, *435* (7045), 1098–1101.

(10) Pirbadian, S.; Barchinger, S. E.; Leung, K. M.; Byun, H. S.; Jangir, Y.; Bouhenni, R. A.; Reed, S. B.; Romine, M. F.; Saffarini, D. A.; Shi, L.; et al. Shewanella Oneidensis MR-1 Nanowires Are Outer Membrane and Periplasmic Extensions of the Extracellular Electron Transport Components. *Proc. Natl. Acad. Sci.* **2014**, *111* (35), 12883–12888.

(11) Malvankar, N. S.; Vargas, M.; Nevin, K. P.; Franks, A. E.; Leang, C.; Kim, B.-C.; Inoue, K.; Mester, T.; Covalla, S. F.; Johnson, J. P.; et al. Tunable Metallic-like Conductivity in Microbial Nanowire Networks. *Nat. Nanotechnol.* **2011**, *6* (9), 573–579.

(12) Xiao, K.; Malvankar, N. S.; Shu, C.; Martz, E.; Lovley, D. R.; Sun, X. Low Energy Atomic Models Suggesting a Pilus Structure That Could Account for Electrical Conductivity of Geobacter Sulfurreducens Pili. *Sci. Rep.* **2016**, *6*, 23385.

(13) Malvankar, N. S.; Vargas, M.; Nevin, K.; Tremblay, P.-L.; Evans-Lutterodt, K.; Nykypanchuk, D.; Martz, E.; Tuominen, M. T.; Lovley, D. R. Structural Basis for Metallic-like Conductivity in Microbial Nanowires. *mBio* **2015**, *6* (2), e00084-15.

(14) Reardon, P. N.; Mueller, K. T. Structure of the Type IVa Major Pilin from the Electrically Conductive Bacterial Nanowires of Geobacter Sulfurreducens. *J. Biol. Chem.* **2013**, *288* (41), 29260–29266.

(15) Feliciano, G. T.; da Silva, A. J. R.; Reguera, G.; Artacho, E. Molecular and Electronic Structure of the Peptide Subunit of Geobacter Sulfurreducens Conductive Pili from First Principles. *J. Phys. Chem. A* **2012**, *116* (30), 8023–8030.

(16) Malvankar, N. S.; Yalcin, S. E.; Tuominen, M. T.; Lovley, D. R. Visualization of Charge Propagation along Individual Pili Proteins Using Ambient Electrostatic Force Microscopy. *Nat. Nanotechnol.* **2014**, *9* (12), 1012–1017.

(17) Strycharz-Glaven, S. M.; Snider, R. M.; Guiseppi-Elie, A.; Tender, L. M. On the Electrical Conductivity of Microbial Nanowires and Biofilms. *Energy Environ. Sci.* **2011**, *4* (11), 4366–4379.

(18) Vargas, M.; Malvankar, N. S.; Tremblay, P.-L.; Leang, C.; Smith, J. A.; Patel, P.; Synoeyenbos-West, O.; Nevin, K. P.; Lovley, D. R. Aromatic Amino Acids Required for Pili Conductivity and Long-Range Extracellular Electron Transport in Geobacter Sulfurreducens. *mBio* **2013**, *4* (2), e00105–e00113.

(19) Boesen, T.; Nielsen, L. P. Molecular Dissection of Bacterial Nanowires. *mBio* **2013**, *4* (3), e00270-13.

(20) Yan, H.; Chuang, C.; Zhugayevych, A.; Tretiak, S.; Dahlquist, F. W.; Bazan, G. C. Inter-Aromatic Distances in Geobacter Sulfurreducens Pili Relevant to Biofilm Charge Transport. *Adv. Mater.* **2015**, *27* (11), 1908–1911.

(21) Feliciano, G. T.; Steidl, R. J.; Reguera, G. Structural and Functional Insights into the Conductive Pili of Geobacter Sulfurreducens Revealed in Molecular Dynamics Simulations. *Phys. Chem. Chem. Phys.* **2015**, *17* (34), 22217–22226.

(22) Steidl, R. J.; Lampa-Pastirk, S.; Reguera, G. Mechanistic Stratification in Electroactive Biofilms of Geobacter Sulfurreducens Mediated by Pilus Nanowires. *Nat. Commun.* **2016**, *7*, 12217.

(23) Snider, R. M.; Strycharz-Glaven, S. M.; Tsoi, S. D.; Erickson, J. S.; Tender, L. M. Long-Range Electron Transport in Geobacter Sulfurreducens Biofilms Is Redox Gradient-Driven. *Proc. Natl. Acad. Sci.* **2012**, *109* (38), 15467–15472.

(24) Bond, D. R.; Strycharz-Glaven, S. M.; Tender, L. M.; Torres, C. I. On Electron Transport through Geobacter Biofilms. *ChemSusChem* **2012**, *5* (6), 1099–1105.

(25) Yates, M. D.; Strycharz-Glaven, S. M.; Golden, J. P.; Roy, J.; Tsoi, S.; Erickson, J. S.; El-Naggar, M. Y.; Barton, S. C.; Tender, L. M. Measuring Conductivity of Living Geobacter Sulfurreducens Biofilms. *Nat. Nanotechnol.* **2016**, *11* (11), 910–913.

(26) Liu, Y.; Kim, H.; Franklin, R. R.; Bond, D. R. Linking Spectral and Electrochemical Analysis to Monitor c-Type Cytochrome Redox Status in Living Geobacter Sulfurreducens Biofilms. *ChemPhysChem* **2011**, *12* (12), 2235–2241.

(27) Strycharz-Glaven, S. M.; Tender, L. M. Reply to the "Comment on 'On Electrical Conductivity of Microbial Nanowires and Biofilms'" by N. S. Malvankar, M. T. Tuominen and D. R. Lovley, Energy Environ. Sci., 2012, 5, DOI: 10.1039/c2ee02613a. *Energy Environ. Sci.* **2012**, *5* (3), 6250–6255.

(28) Malvankar, N. S.; Tuominen, M. T.; Lovley, D. R. Lack of Cytochrome Involvement in Long-Range Electron Transport through Conductive Biofilms and Nanowires of Geobacter Sulfurreducens. *Energy Environ. Sci.* **2012**, *5* (9), 8651.

(29) Yates, M. D.; Golden, J. P.; Roy, J.; Strycharz-Glaven, S. M.; Tsoi, S.; Erickson, J. S.; El-Naggar, M. Y.; Barton, S. C.; Tender, L. M. Thermally Activated Long Range Electron Transport in Living Biofilms. *Phys. Chem. Chem. Phys.* **2015**, *17* (48), 32564–32570.

(30) Strycharz, S. M.; Malanoski, A. P.; Snider, R. M.; Yi, H.; Lovley, D. R.; Tender, L. M. Application of Cyclic Voltammetry to Investigate Enhanced Catalytic Current Generation by Biofilm-Modified Anodes of Geobacter Sulfurreducens Strain DL1 vs. Variant Strain KN400. *Energy Environ. Sci.* **2011**, *4* (3), 896–913.

(31) Lampa-Pastirk, S.; Veazey, J. P.; Walsh, K. A.; Feliciano, G. T.; Steidl, R. J.; Tessmer, S. H.; Reguera, G. Thermally Activated Charge Transport in Microbial Protein Nanowires. *Sci. Rep.* **2016**, *6*, 23517.

(32) Bonanni, P. S.; Massazza, D.; Busalmen, J. P. Stepping Stones in the Electron Transport from Cells to Electrodes in Geobacter Sulfurreducens Biofilms. *Phys. Chem. Chem. Phys. PCCP* **2013**, *15* (25), 10300–10306.

(33) Cologgi, D. L.; Lampa-Pastirk, S.; Speers, A. M.; Kelly, S. D.; Reguera, G. Extracellular Reduction of Uranium via Geobacter Conductive Pili as a Protective Cellular Mechanism. *Proc. Natl. Acad. Sci.* **2011**, *108* (37), 15248–15252.

(34) Rath, A.; Glibowicka, M.; Nadeau, V. G.; Chen, G.; Deber, C. M. Detergent Binding Explains Anomalous SDS-PAGE Migration of Membrane Proteins. *Proc. Natl. Acad. Sci.* **2009**, *106* (6), 1760–1765.

(35) Rambaran, R. N.; Serpell, L. C. Amyloid Fibrils. *Prion* **2008**, *2* (3), 112–117.

(36) Jachimska, B.; Pajor, A. Physico-Chemical Characterization of Bovine Serum Albumin in Solution and as Deposited on Surfaces. *Bioelectrochemistry* **2012**, *87*, 138–146.

(37) Cukalevski, R.; Boland, B.; Frohm, B.; Thulin, E.; Walsh, D.; Linse, S. Role of Aromatic Side Chains in Amyloid β-Protein Aggregation. *ACS Chem. Neurosci.* **2012**, *3* (12), 1008–1016.

(38) Gazit, E. A Possible Role for π-Stacking in the Self-Assembly of Amyloid Fibrils. *FASEB J.* **2002**, *16* (1), 77–83.

(39) Reymer, A.; Frederick, K. K.; Rocha, S.; Beke-Somfai, T.; Kitts, C. C.; Lindquist, S.; Nordén, B. Orientation of Aromatic Residues in Amyloid Cores: Structural Insights into Prion Fiber Diversity. *Proc. Natl. Acad. Sci.* **2014**, *111* (48), 17158–17163.

(40) Sepunaru, L.; Refaely-Abramson, S.; Lovrinčić, R.; Gavrilov, Y.; Agrawal, P.; Levy, Y.; Kronik, L.; Pecht, I.; Sheves, M.; Cahen, D. Electronic Transport via Homopeptides: The Role of Side Chains and Secondary Structure. *J. Am. Chem. Soc.* **2015**, *137* (30), 9617–9626.

(41) Pawlowski, J.; Juhaniewicz, J.; Tymecka, D.; Sek, S. Electron Transfer across α-Helical Peptide Monolayers: Importance of Interchain Coupling. *Langmuir* **2012**, *28* (50), 17287–17294.

(42) Atanassov, A.; Hendler, Z.; Berkovich, I.; Ashkenasy, G.; Ashkenasy, N. Force Modulated Conductance of Artificial Coiled-Coil Protein Monolayers. *Pept. Sci.* **2013**, *100* (1), 93–99.

(43) Amit, M.; Appel, S.; Cohen, R.; Cheng, G.; Hamley, I. W.; Ashkenasy, N. Hybrid Proton and Electron Transport in Peptide Fibrils. *Adv. Funct. Mater.* **2014**, *24* (37), 5873–5880.

(44) Amdursky, N. Electron Transfer across Helical Peptides. *ChemPlusChem* **2015**, *80* (7), 1075–1095.

(45) Shin, Y. K.; Newton, M. D.; Isied, S. S. Distance Dependence of Electron Transfer Across Peptides with Different Secondary Structures: The Role of Peptide Energetics and Electronic Coupling. *J. Am. Chem. Soc.* **2003**, *125* (13), 3722–3732.

(46) Kim, B.; Pfeifer, S.; Park, S.-H.; Bandaru, P. R. The Experimental Determination of the Onset of Electrical and Thermal Conductivity Percolation Thresholds in Carbon Nanotube-Polymer Composites. In *Materials Research Society Proceedings*; 2011; Vol. 1312, pp 281–286.

(47) Jagota, M.; Tansu, N. Conductivity of Nanowire Arrays under Random and Ordered Orientation Configurations. *Sci. Rep.* **2015**, *5*, 10219.

(48) Khanarian, G.; Joo, J.; Liu, X.-Q.; Eastman, P.; Werner, D.; O'Connell, K.; Trefonas, P. The Optical and Electrical Properties of Silver Nanowire Mesh Films. *J. Appl. Phys.* **2013**, *114* (2), 24302.

(49) Grady, B. P.; Arthur, D. J.; Ferguson, J. Single-Walled Carbon Nanotube/Ultrahigh-Molecular-Weight Polyethylene Composites with Percolation at Low Nanotube Contents. *Polym. Eng. Sci.* **2009**, *49* (12), 2440–2446.

(50) White, S. I.; Mutiso, R. M.; Vora, P. M.; Jahnke, D.; Hsu, S.; Kikkawa, J. M.; Li, J.; Fischer, J. E.; Winey, K. I. Electrical Percolation Behavior in Silver Nanowire–polystyrene Composites: Simulation and Experiment. *Adv. Funct. Mater.* **2010**, *20* (16), 2709–2716.

(51) De, S.; King, P. J.; Lyons, P. E.; Khan, U.; Coleman, J. N. Size Effects and the Problem with Percolation in Nanostructured Transparent Conductors. *ACS Nano* **2010**, *4* (12), 7064–7072.

(52) Johner, N.; Grimaldi, C.; Balberg, I.; Ryser, P. Transport Exponent in a Three-Dimensional Continuum Tunneling-Percolation Model. *Phys. Rev. B* **2008**, *77* (17), 174204.

(53) Balberg, I. Limits on the Continuum-Percolation Transport Exponents. *Phys. Rev. B* **1998**, *57* (21), 13351–13354.

(54) Balberg, I. Tunneling and Nonuniversal Conductivity in Composite Materials. *Phys. Rev. Lett.* **1987**, *59* (12), 1305–1308.

(55) Vionnet-Menot, S.; Grimaldi, C.; Maeder, T.; Strässler, S.; Ryser, P. Tunneling-Percolation Origin of Nonuniversality: Theory and Experiments. *Phys. Rev. B* **2005**, *71* (6), 64201.

(56) Park, H.-S.; Ko, S.-J.; Park, J.-S.; Kim, J. Y.; Song, H.-K. Redox-Active Charge Carriers of Conducting Polymers as a Tuner of Conductivity and Its Potential Window. *Sci. Rep.* **2013**, *3*.

(57) Pei, Q.; Zuccarello, G.; Ahlskog, M.; Inganäs, O. Electrochromic and Highly Stable poly(3,4-Ethylenedioxythiophene) Switches between Opaque Blue-Black and Transparent Sky Blue. *Polymer* **1994**, *35* (7), 1347–1351.

(58) Crispin, X.; Jakobsson, F. L. E.; Crispin, A.; Grim, P. C. M.; Andersson, P.; Volodin, A.; van Haesendonck, C.; Van der Auweraer, M.; Salaneck, W. R.; Berggren, M. The Origin of the High Conductivity of poly(3,4-ethylenedioxythiophene)−Poly(styrenesulfonate) (PEDOT−PSS) Plastic Electrodes. *Chem. Mater.* **2006**, *18* (18), 4354–4360.

(59) Gaspar, D. J.; Polikarpov, E. *OLED Fundamentals: Materials, Devices, and Processing of Organic Light-Emitting Diodes*; CRC Press, 2015.

(60) Elschner, A.; Kirchmeyer, S.; Lovenich, W.; Merker, U.; Reuter, K. *PEDOT: Principles and Applications of an Intrinsically Conductive Polymer*; CRC Press, 2010.

(61) Wang, L.; Waldeck, D. H. Denaturation of Cytochrome c and Its Peroxidase Activity When Immobilized on SAM Films. *J. Phys. Chem. C* **2008**, *112* (5), 1351–1356.

(62) Drew, H. R.; Dickerson, R. E. The Unfolding of the Cytochromes c in Methanol and Acid. *J. Biol. Chem.* **1978**, *253* (23), 8420–8427.

(63) Dallas, P.; Stamopoulos, D.; Boukos, N.; Tzitzios, V.; Niarchos, D.; Petridis, D. Characterization, Magnetic and Transport Properties of Polyaniline Synthesized through Interfacial Polymerization. *Polymer* **2007**, *48* (11), 3162–3169.

(64) Kaiser, A. B. Systematic Conductivity Behavior in Conducting Polymers: Effects of Heterogeneous Disorder. *Adv. Mater.* **2001**, *13* (12–13), 927–941.

(65) Heeger, A. J.; Sariciftci, N. S.; Namdas, E. B. *Semiconducting and Metallic Polymers*; Oxford University Press, 2010.

(66) Skotheim, T. A.; Reynolds, J. R. *Handbook of Conducting Polymers*; CRC Press, 2007; Vol. 2.

(67) May, V.; Kuhn, O. *Charge and Energy Transfer Dynamics in Molecular Systems*, 3rd ed.; Wiley: Weinheim, Germany, 2011.

(68) Shpaisman, H.; Seitz, O.; Yaffe, O.; Roodenko, K.; Scheres, L.; Zuilhof, H.; J. Chabal, Y.; Sueyoshi, T.; Kera, S.; Ueno, N.; et al. Structure Matters : Correlating Temperature Dependent Electrical Transport through Alkyl Monolayers with Vibrational and Photoelectron Spectroscopies. *Chem. Sci.* **2012**, *3* (3), 851–862.

(69) Zhang, Y.; Liu, C.; Balaeff, A.; Skourtis, S. S.; Beratan, D. N. Biological Charge Transfer via Flickering Resonance. *Proc. Natl. Acad. Sci. U. S. A.* **2014**, *111* (28), 10049–10054.

(70) Beratan, D. N.; Liu, C.; Migliore, A.; Polizzi, N. F.; Skourtis, S. S.; Zhang, P.; Zhang, Y. Charge Transfer in Dynamical Biosystems, or The Treachery of (Static) Images. *Acc. Chem. Res.* **2015**, *48* (2), 474–481.

(71) Rissner, F.; Natan, A.; Egger, D. A.; Hofmann, O. T.; Kronik, L.; Zojer, E. Dimensionality Effects in the Electronic Structure of Organic Semiconductors Consisting of Polar Repeat Units. *Org. Electron.* **2012**, *13* (12–2), 3165–3176.

(72) Coppi, M. V.; Leang, C.; Sandler, S. J.; Lovley, D. R. Development of a Genetic System for Geobacter Sulfurreducens. *Appl. Environ. Microbiol.* **2001**, *67* (7), 3180–3187.

(73) Lovley, D. R.; Greening, R. C.; Ferry, J. G. Rapidly Growing Rumen Methanogenic Organism That Synthesizes Coenzyme M and Has a High Affinity for Formate. *Appl. Environ. Microbiol.* **1984**, *48* (1), 81–87.

(74) DelProposto, J.; Majmudar, C. Y.; Smith, J. L.; Brown, W. C. Mocr: A Novel Fusion Tag for Enhancing Solubility That Is Compatible with Structural Biology Applications. *Protein Expr. Purif.* **2009**, *63* (1), 40–49.

(75) Lendel, C.; Bjerring, M.; Dubnovitsky, A.; Kelly, R. T.; Filippov, A.; Antzutkin, O. N.; Nielsen, N. C.; Härd, T. A Hexameric Peptide Barrel as Building Block of Amyloid-β Protofibrils. *Angew. Chem. Int. Ed.* **2014**, *53* (47), 12756–12760.

(76) Pham, J. D.; Spencer, R. K.; Chen, K. H.; Nowick, J. S. A Fibril-like Assembly of Oligomers of a Peptide Derived from β-Amyloid. *J. Am. Chem. Soc.* **2014**, *136* (36), 12682–12690.

(77) Asikyan, M. L.; Kus, J. V.; Burrows, L. L. Novel Proteins That Modulate Type Iv Pilus Retraction Dynamics in Pseudomonas Aeruginosa. *J. Bacteriol.* **2008**, *190* (21), 7022–7034.

CHAPTER 3 Electronic Conductivity in Biomimetic α-Helical Peptide Nanofibers and Gels

3.1: Abstract

Examples of long-range electronic conductivity are rare in biological systems. The observation of micrometer-scale electronic transport through protein wires produced by bacteria is therefore notable, providing an opportunity to study fundamental aspects of conduction through protein-based materials and natural inspiration for bioelectronics materials. Borrowing sequence and structural motifs from these conductive protein fibers, we designed self-assembling peptides that form electronically conductive nanofibers under aqueous conditions. Conductivity in these nanofibers is distinct for two reasons: first, they support electron transport over distances orders of magnitude greater than expected for proteins, and second, the conductivity is mediated entirely by amino acids lacking extended conjugation, π-stacking, or redox centers typical of existing organic and bio-hybrid semiconductors. Electrochemical transport measurements show that the fibers support ohmic electronic transport and a metallic-like temperature dependence of conductance in aqueous buffer. At higher solution concentrations, the peptide monomers form hydrogels, and comparisons of the structure and electronic properties of the nanofibers and gels highlight the critical roles of α-helical secondary structure and supramolecular ordering in supporting electronic conductivity in these materials. These findings suggest a structural basis for long-range electronic conduction mechanisms in peptide and protein biomaterials.

3.2: Introduction

Bioelectronic materials aim to interface synthetic electronic devices with biological systems, from biomolecules to cells, tissues, and entire organisms.[1] Such a union of solid-state

and biological materials enables a broad range of applications such as wearable[2,3] or implantable devices[4,5], portable and biocompatible power sources[6–8], real-time and miniaturized sensors,[9,10] and bionic neural interfaces[11,12]. Finding ideal materials to bridge the biological-electronic interface remains an outstanding challenge[13]. Such a material should be biocompatible, multifunctional, and maintain proper function of the interacting biological system[14]. Proteins and peptides are ideal material building blocks for satisfying these criteria due to their properties of self-assembly and functional molecular recognition[15–18]. In addition, the chemical diversity and specificity of amino acid sequences can be designed to drive the formation of peptide nanostructures, such as wires and tubes[19,20]. These nanometer length scales are comparable to those of biological building blocks, promoting a more seamless integration at the bio-electronic interface than existing micrometer-scale electronic transducers[17,21].

Processes of electron tunneling and transfer across individual enzymes are common in biology[22,23], and electronic conductivity or tunneling in non-enzyme protein and peptide nanomaterials has been studied over short (~nm) distances[24–26]. Over much longer (~μm) distances, inherent electronic conductivity has been established in bacterial protein fiber appendages, called pili, of some anaerobic species[27,28]. Long-range electron transport in conductive pili represents natural inspiration for molecular bioelectronics design and a tunable synthetic platform for studying the electronic properties of conductive protein nanostructures[27,29]. Pili support charge transport through natural amino acid residues over micrometer-scale distances[30,31], much farther than the angstrom to nanometer length scales associated with tunneling[22,23,32]. They are also are orders of magnitude more conductive than amyloid[33] and π-stacked peptide fibers[34]. Unlike examples of long-range electron transport in natural[35] and synthetic assemblies of cytochromes, the conduction observed in pili is not redox-

mediated[28,36], and the exact mechanism of electron transport in these protein fibers is still a matter of debate.

π-stacked moieties are essential for long-range electron conductivity in synthetic peptide bio-organic hybrid nanostructures, in which peptides direct the self-assembly of small molecule semiconductors[37,38]. π-stacking amino acid side chains may be important in pili as well. The conductivity of *Geobacter sulfurreducens* Type IV pili, the most commonly studied conductive pilus system, is sensitive to mutations at aromatic residues[39–41], and pilus conductivity correlates with aromatic amino acid content of pilin protein building blocks from different *Geobacter* species[42]. Some homology models suggest sufficiently small distances between aromatic residues in the pilus for π-stacking interactions[29,43,44], but without a crystal structure, such a molecular arrangement has not been conclusively determined. On the other hand, some self-assembled peptide monolayers[24,45–47] and short peptide nanotubes[48] exhibit inherent conductivity over distances up to several nanometers without π-stacking. The composition of the side chains, hydrogen bonds, and an α-helical secondary structure have been identified as important factors contributing to the hopping and tunneling conductivity in these peptide systems over short distances.

Taking sequence and structural inspiration from *G. sulfurreducens* pili, we designed a self-assembling *de novo* peptide that forms electrically conductive nanofibers[49,50]. The peptide self-associates in solution to form coiled-coil hexamers, which were designed to add end-to-end and form elongated nanofibers. Both the peptide nanofibers and the *Geobacter* pili consist of α-helical monomer building blocks, and the crystal structure of the coiled-coil hexamer shows that the peptide oligomer clusters aromatic residues axially in their hydrophobic core[49]. Importantly,

the spacing and arrangement of aromatic side chains preclude π-stacked electronic delocalization in proposed structure of the peptide nanofibers. Nonetheless, these nanofibers are conductive in ambient and wet conditions, and they exhibit metallic-like trends in electrochemical and temperature-dependent transport measurements. Comparison of the structure and conductance of fiber and gel morphologies formed by the peptide at different concentrations suggests that the supramolecular ordering of peptides within the nanofibers plays a critical role in supporting electronic transport. The observed properties and mutability of the peptide sequence suggests that this nanofiber system may serve as an experimental platform for exploring structure-property relationships in peptide and protein bioelectronics materials.

3.3: Results and Discussion

3.3.1: Peptide Nanofiber Self-Assembly

Peptide **1** (Fig. 3.1A) self-assembles to incorporate aromatic amino acids into the core of an antiparallel coiled-coil hexamer (ACC-Hex, PDB 5EOJ) structure, which it adopts in solid-state crystals and in solution[49,50]. Peptide **1** is capped with Glu and Lys residues to induce end-to-end electrostatic interactions and the formation of elongated fibers. The X-ray crystallographic structure shows that peptide **1** indeed crystallizes as stacked ACC-Hex building blocks, suggesting supramolecular assembly of fibers driven by these electrostatic interactions (Fig. 3.1B). Atomic force microscopy (AFM) imaging confirms the formation of nanofiber structures from peptide **1** in phosphate buffered saline (PBS) at 100-200 μM concentrations (0.03-0.06 % w/v), which form overnight and extend up to several microns in length (Fig. 3.2A). Height profiles of the observed nanofibers exhibit a minimum diameter of 2 nm (Fig. 3.2B), consistent with the diameter of a single hexamer unit.[49] That this is the smallest diameter of nanofiber

measured in the sample suggests that these nanofibers are composed of ACC-Hex building blocks, and that larger diameter fibers may be bundles of ACC-Hex nanofibers.

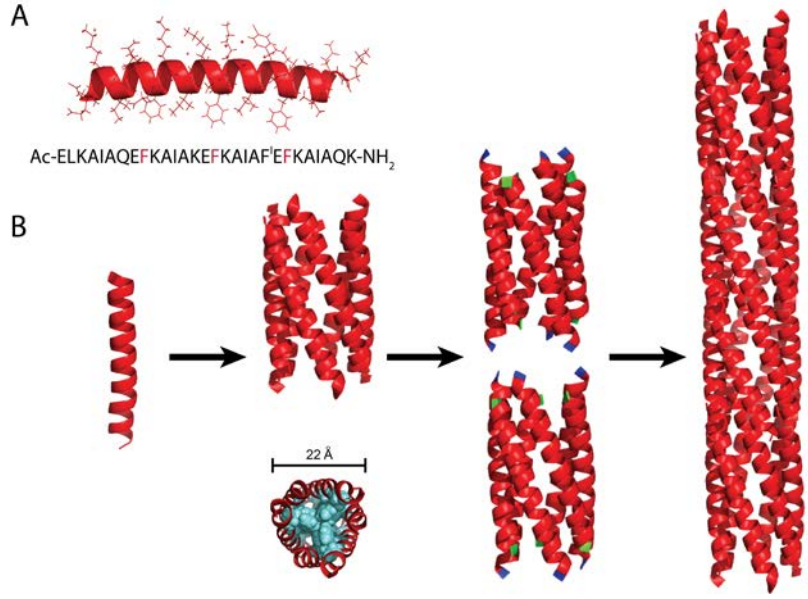

Figure 3.1: (A) Peptide **1** monomer crystal structure and sequence. Red residues highlight the phenylalanines buried in the hydrophobic core; F^{I} denotes the iodo-phenylalanine on the solvent-exposed surface used for phasing in crystal structure determination. (B) Proposed nanofiber self-assembly mechanism from X-ray crystal structures of peptide **1**. *Left to Right*: Peptide **1** monomer forms an antiparallel coiled-coil hexamer (ACC-Hex), shown in radial (top) and axial (bottom) projections; ACC-Hex stacks end-to-end *via* electrostatic interactions between the terminal glutamic acids (green) and amide lysines (dark blue) to form an elongated fiber. The hexamer and extended nanofiber have a predicted diameter of 22 Å filled with a tightly packed hydrophobic core of aromatic residues.

3.3.2: Electrical Conductivity of Peptide Nanofibers

Films deposited from dried ACC-Hex nanofiber suspensions form dense percolation networks that exhibit long-range electronic conductivity. *I-V* characteristics of dried nanofiber films on interdigitated electrode devices exhibit linear behavior (Fig. 3.2C), with an average resistance of 188 ± 36 Ω (n = 6 independent samples). The measured resistance is relatively low for typical organic materials due to the large channel width and short channel length of the interdigitated devices used for electronic property characterization. The ohmic *I-V* behavior may

be attributed to good work function matching between the fibers and gold electrode, since X-ray photoelectron spectroscopy (XPS) measurements suggest ACC-Hex nanocrystals to have a work function ~5.56 eV (~5.31 eV for Au[51]) (Supporting Information, Supporting Fig. S3.1). Typical protein and peptide bandgaps, arising from the periodicity of the backbone, can range from semiconducting ($\leq$ 4 eV) to insulating (> 4 eV)[52–54]. Films of amyloid beta fibers (Aβ), cast onto identical devices from an equivalent volume of solution and concentration of protein, have a resistance of 1.0 x 10^8 Ω. The equivalent volume of PBS cast onto identical devices has a resistance of 1.5 x 10^9 Ω, indicating that any residual contamination from the casting solution contributes negligible conductance to the peptide **1** nanofiber films. Aβ fibers were used as a control material because they assemble with similar aspect ratios to ACC-Hex fibers (Fig. S3.2) and contain aligned aromatic residues[55]. The six orders of magnitude decrease in conductance of the Aβ compared to ACC-Hex nanofiber films suggests a primary role for the α-helical building blocks of ACC-Hex. α-helical secondary structure has been previously demonstrated to lower the energetic barrier for transport across short homopeptides[24]. Our results are consistent with these tunneling conduction experiments and the proposed importance of α-helices to conductivity in *G. sulfurreducens* pili[28,43]. Using an identical electrode geometry, our ACC-Hex nanofiber films exhibit comparable (~mA) current to pili films. 6.9 μg of ACC-Hex nanofibers yielded an average film resistance of 188 Ω, while 115 μg of purified *G. sulfurreducens* pili on the same devices had a resistance of 470 Ω[28].

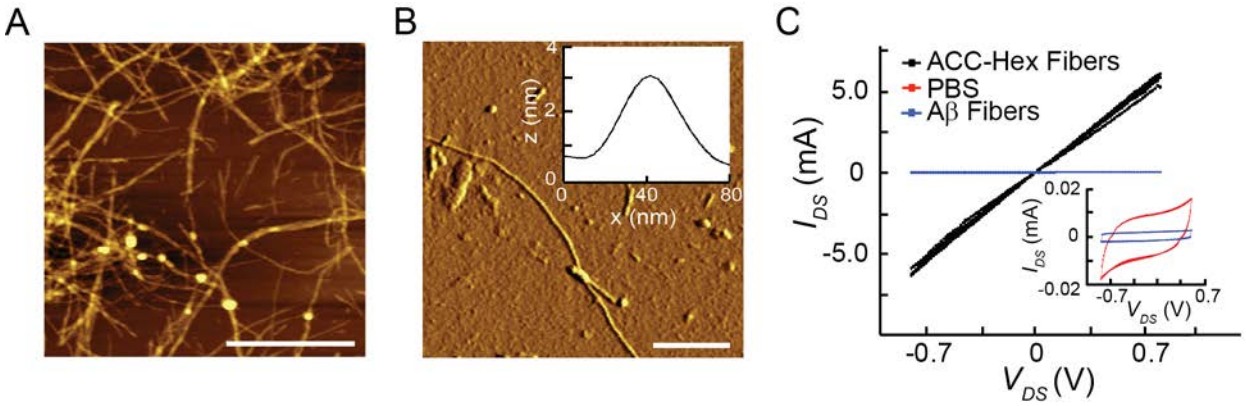

Figure 3.2: (A) Atomic force micrograph of a drop-cast film of ACC-Hex nanofibers. (B) AFM topographical image of a single ACC-Hex nanofiber. Inset shows a z-height line-scan across the fiber, indicating a fiber diameter of 2.3 nm. (C) Current-voltage (*I-V*) characteristics of ACC-Hex fibers, a dried buffer control (PBS), and amyloid-β (Aβ) fibers. Inset: close-up of PBS and Aβ *I-V*s. Scale bars are 5 μm and 500 nm in (A) and (B), respectively.

Single fiber *I-V* characteristics of ACC-Hex nanofibers were used to confirm electronic conduction in the fiber component of the self-assembled peptide and to calculate values of electrical conductivity inherent to the nanofibers. Conductive probe AFM measurements of electron transport in individual ACC-Hex nanofibers show high conductivity values, with an average conductivity of 1.12 ± 0.77 S/cm (n = 4 independent nanofibers) (Fig. S3.3). Wild-type *G. sulfurreducens* pili have conductivities ranging from 0.188 ± 0.034 S/cm (pH 2) to 0.051 ± 0.019 S/cm (pH 7)[31], consistent with the relative resistances obtained from *I-V*s of the ACC-Hex nanofiber and pili films.

Electronic transport in ACC-Hex nanofibers was also characterized in aqueous solution by electrochemical gating measurements in a bipotentiostat setup (Fig. S3.4). Bipotentiostat cyclic voltammetry distinguishes between redox-mediated and ohmic charge transport mechanisms in conductive channel materials[28,56,57]. Current through the ACC-Hex nanofiber channel is independent of gate potential and depends only on the source-drain potential, V_{DS} (Fig. 3.3A), indicative of band-like charge carrier conduction. The conductance of the nanofiber

channels shows a weak dependence on pH and ionic strength (Fig. S3.5), and it increases with decreasing temperature (Fig. 3.3B). The temperature-dependent behavior is also consistent with ohmic, or particle-like, charge conduction and is exclusive of thermally activated conduction mechanisms, such as charge hopping, in ACC-Hex nanofibers.

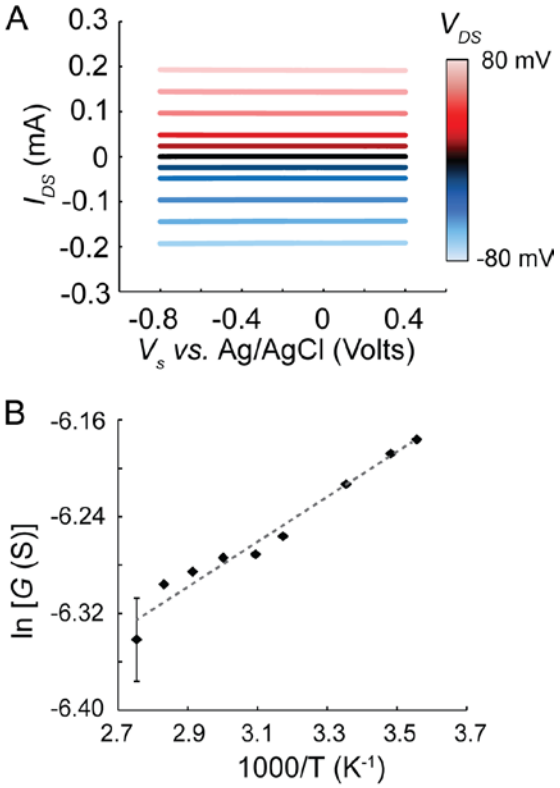

Figure 3.3: Electrochemical gating experiments of ACC-Hex fiber films (A) Source-drain current (I_{DS}) of ACC-Hex nanofiber films gated in solution (pH 7.0) with respect to a reference electrode (V_S). The source-drain voltage (V_{DS}) of each scan is indicated by the color scale on the right. (B) The average source-drain conductance (G) of peptide nanofiber films as a function of temperature at 10 different V_{DS} offsets (±10 mV, ±20 mV, ±40 mV, ±60 mV, and ±80 mV). Error bars represent the standard deviation of measurements at all 10 V_{DS} values and are small as to be obscured by the data points at T < 90°C.

Electrical impedance spectroscopy (EIS) was used to test for proton-mediated and ion-mediated conduction (Fig. 3.4). To test for proton conductivity, the impedance of nanofiber films was compared in H_2O (ultra-pure water) and D_2O (Fig. 3.4A). If protons were facilitating transport, the change to the heavier deuteron isotope in deuterium oxide would be expected to

reduce transport kinetics and thus increase the measured impedance. Contrary to this, the average impedance was slightly lower in D_2O than in H_2O, though this difference was not statistically significant, and therefore is not indicative of a proton-mediated mechanism. Film impedance was also measured in different 0.1M solutions of Hofmeister anions and cations (Fig. 3.4C). The Hofmeister series[58,59] ranks anions and cations based on their ability to stabilize (or destabilize) protein structure, based on an empirical and qualitative ranking of precipitation effects on egg white proteins. It correlates with the kosmotropic (enhances the hydrogen bonding of water) and chaotropic (disrupts the hydrogen bonding of water) classification of ions[60], such that chaotropic cations and kosmotropic anions stabilize protein structure, while kosmotropic cations and chaotropic anions destabilize protein structure . The lack of clear trends between Hofmeister ranking and film impedance suggests that ions do not play a role in mediating conduction, and that the electrolyte does not participate in charge transfer. This observation was also consistent at lower ionic strengths (Supporting Fig. S3.6).

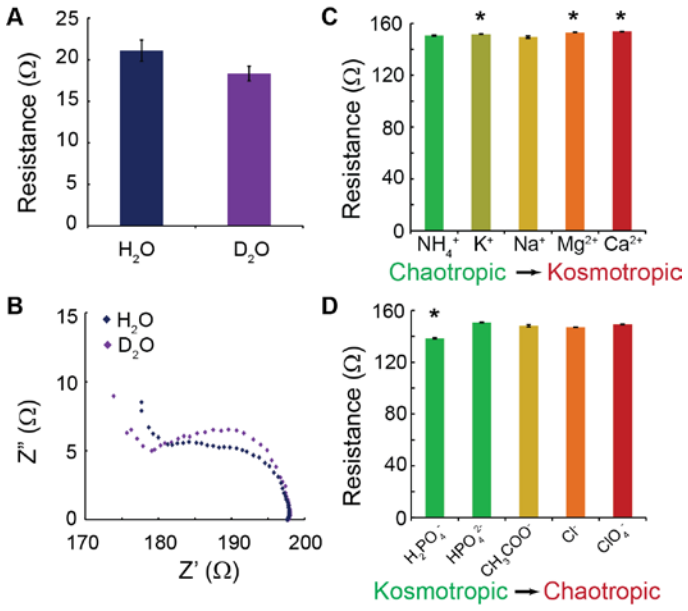

Figure 3.4: (A) Impedance of ACC-Hex nanofiber films in H_2O and D_2O (*n=5* measurements), determined from Randles circuit fitting of Nyquist impedance spectra, with representative spectra (B). Differences between H_2O and D_2O are not statistically significant. Impedance of ACC-Hex nanofiber

films in (C) 0.1 M cation solutions with Cl^- as the counterion and (D) 0.1 M anion solutions with Na^+ as the counterion ($n=8$ measurements). Film resistances in K^+, Mg^{2+}, and Ca^{2+} have *p*-values of 0.08, 0.016, and 0.028, respectively, with respect to Na^+(NaCl). Film resistance in $H_2PO_4^-$ has a *p*-value of 0.0002 with respect to Cl^- (NaCl).

3.3.3: Peptide Hydrogel Formation and Rheological Properties

Peptide **1** forms hydrogels at mM concentrations (above 0.1% w/v) after 20 min incubation at 70 °C. Visible gelation was observed at concentrations ranging from 0.1% to 5% w/v. Rheological studies were performed to measure the mechanical properties of the hydrogels (Fig. 3.5). Strain sweep experiments were performed to assess the storage modulus (*G'*) and the loss modulus (*G"*), which measure the energy stored and dissipated upon application of oscillatory shear in the linear viscoelastic regime. When *G' >>G"*, the material is considered to behave like a viscoelastic solid, and when *G' << G"*, the material behaves like a viscoelastic liquid.[61] The magnitude of *G'* is also an indicator of the relative stiffness of the hydrogel.

Peptide **1** hydrogels demonstrate typical gel-like rheological behavior. *G'* is relatively constant and greater than *G"* at low strain amplitudes, then at higher strains drops off quickly with increasing strain and crosses to a *G' < G"* regime indicative of gel yielding (Fig. 3.5A). Also consistent with gel-like behavior, G'_0 (*G'* at 0.1% strain) increases with increasing concentration of peptide (Fig. 3.5B). The strain amplitude sweeps track the viscoelasticity of the various hydrogels. For the most robust gel (5% w/v), the critical strain γ_c occurs at a *G'* value of 160 Pa: below 3% strain, the structure is intact, as denoted by the strain independence of *G'* with *G' > G"*, suggesting a percolating stress-bearing network (Fig. 3.5A). Increasing the strain above γ_c disrupts the network structure, and the material eventually begins to resemble a viscous liquid at strains above the crossover point *G'= G"*. The value of γ_c increases with peptide concentration

(Fig. 4A inset), indicating that the network structure responsible for load distribution increases in the presence of more material[62].

The storage modulus *G'* of peptide gels follows a power law relationship with concentration, which is determined by factors such as fibril persistence length, fibril flexibility, distance between fibrils, and distance between fibril intersections, and which is directly related to the crosslinking or entanglement in the system[63]. In a crosslinked hydrogel, fibrils are linked by chemical bonds and the exponent *n* has a theoretical value of 2.5 for a dense crosslinking network[63]. *n* is predicted to have a value of 2.2 for entangled hydrogels[63] and 1.4 for strongly entangled hydrogels[64]. A value closer to *n* = 1, such as measured from the peptide **1** hydrogels (*n* = 1.13, Fig. 3.5B), indicates that the gels are semi-dilute viscoelastic solutions that are neither strongly entangled nor extensively crosslinked[65]. These structural characteristics are consistent with the short, rigid α-helical peptide **1** building block of the gels, the hydrophobic interactions driving oligomer and gel backbone assembly, and the lack of specific cross-linking moieties in the peptide **1** and ACC-Hex structures.

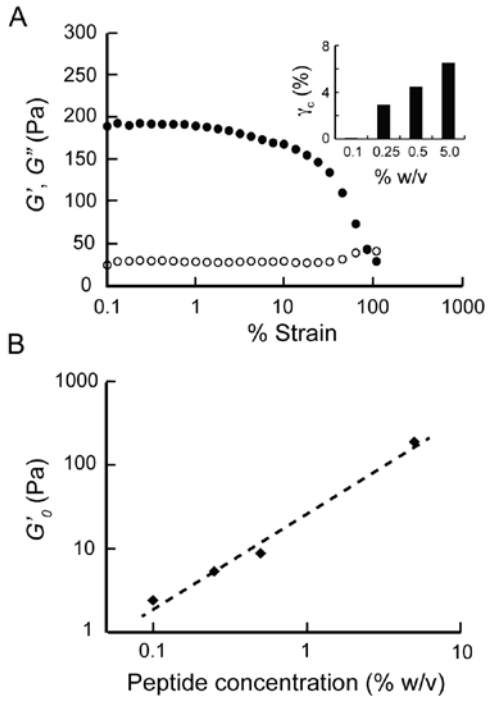

Figure 3.5: Oscillatory rheology measurements of peptide **1** hydrogels. (A) Representative strain sweep values of storage (*G'*, filled circles) and loss (*G"*, open circles) moduli of the 5 % w/v hydrogel conducted at 0.1 Hz. Inset shows the critical strain, γ_c, *versus* concentration of peptide. (B) Storage modulus measured at 0.1% strain (G'_0) and 1 Hz, as a function of peptide concentration (% w/v). The slope of the fit line is 1.13.

3.3.4: Electronic Measurements of Peptide Hydrogels

Films of dried hydrogels exhibit a surprising decrease in conductivity with increasing peptide concentration (Fig. 3.6A). Films cast from nanofibers solutions (0.03 % w/v) exhibit seven orders of magnitude greater conductance than those cast from equal volumes of 5% w/v peptide gels, despite the presence of more peptide material in films cast from higher concentration samples. The conductance of hydrated hydrogels was recorded by taking the inverse of resistance values obtained by EIS (Fig. 3.6B, Fig. S3.7). Conductance through the material was determined by taking the inverse of the difference between impedance values at low frequencies, approaching DC conditions[66,67], and the solution resistance (impedance value at high frequencies). The high frequency solution resistance values were negligible compared to

the impedance values at low frequencies, approaching DC. As with the dried films, conductance through a fixed volume of nanofibers and hydrogel decreases precipitously with increasing peptide concentration. These data indicate that the peptide itself is not inherently conductive and suggest that the conductivity may be strongly dependent on the supramolecular structure present in highly ordered fiber morphology present at low peptide concentrations. SEM images confirm the lack of fiber morphology in peptide gels at concentrations above 0.1 % w/v (Fig. 3.6C), which instead form increasingly large and extended networks of clusters characteristic of hydrogel phase separation during sample desiccation.

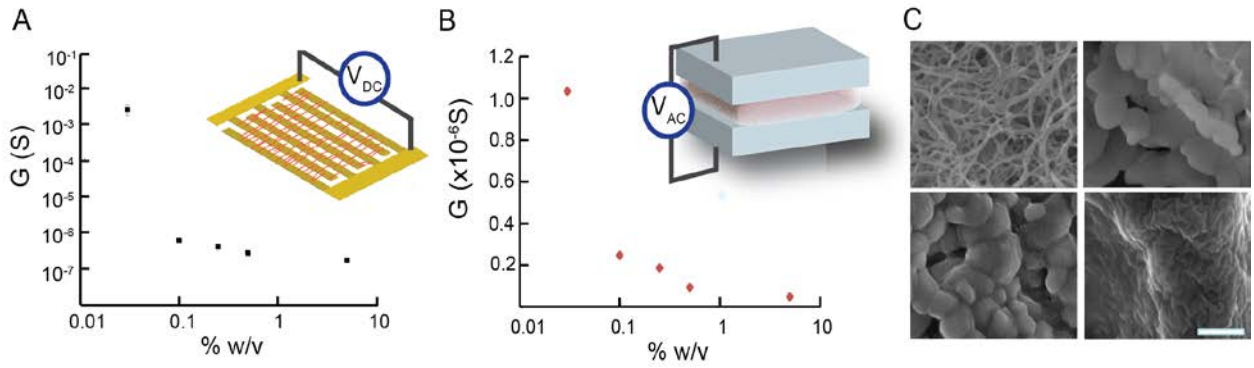

Figure 3.6: Conductance measurements of ACC-Hex nanofibers (0.03% w/v) and gels. (A) Conductance (*G*) of dried fibers and gels deposited from equivalent solution volumes onto interdigitated electrodes. Inset shows device schematic and example of fibers (red) bridging the interdigitated electrodes (gold). (B) Conductance approaching DC as determined by EIS in FTO sandwich electrodes (inset). (C) Scanning electron micrographs of ACC-Hex fibers (0.03% w/v) (*top left*), 0.25% hydrogel (*top right*), 0.5% hydrogel (*bottom left*), and 5% hydrogel (*bottom right*). Scale bar is 500 nm.

3.3.5: Molecular Structure Insights into Peptide Nanofibers and Gels

The solution dynamics and self-assembly of peptide **1** were investigated by molecular dynamics simulations using the coarse-grained MARTINI model for peptides in explicit water and ions. Simulation data show oligomer assembly structures and intermediates consistent with experimental results (Fig. 3.6). Firstly, the fast association of peptide **1** into dimers was observed

in equilibrium with ACC-Hex at ~ 10 μM (Fig. 3.6A-C). The presence of dimers was indicated experimentally by small-angle X-ray scattering profiles of peptide **1** at comparable concentrations, and by structural analysis of the ACC-Hex crystal structure[49]. Secondly, end-to-end association of individual ACC-Hex units was observed at higher concentrations (~ 100 μM, 0.03 %w/v), creating elongated structures suggestive of the initial stages of fiber assembly. The minimum diameter of observed peptide **1** fibers measured by AFM is approximately the ACC-Hex diameter (Fig. 3.2B), consistent with the end-to-end assembly process indicated by these MD data (Fig. 6D). Lastly, at mM concentrations (> 0.1 % w/v), simulation snapshots indicate a transition in supramolecular assembly of ACC-Hex building blocks into larger, branched structures (Fig. 3.6E). While the ACC-Hex building blocks are still stable at these concentrations, the hexamers no longer self-associate exclusively by end-to-end interactions, which would result in one-dimensional fiber growth. Rather, ACC-Hex units attach to ends and sides, creating continuous and branching junctions.

Fiber formation is experimentally observed between 100 and 200 μM (0.03 to 0.06% w/v), and these simulations demonstrate that within this range, the end-to-end axial association of ACC-Hex units represents the potential nucleation step of fiber formation. In contrast, at mM concentrations, the ACC-Hex building blocks associate *via* both lateral and axial interactions to form the branched network structure of the gel backbone. The simulations suggest that peptide **1** still assembles into ACC-Hex units at these high concentrations and bury Phe residues in the hydrophobic core of this gel network, but that the hexamer building blocks lack the axially aligned periodicity present at lower, fiber-forming concentrations of peptide. This structural change is observed in SEM preparations of the fibers and hydrogels (Fig. 3.6C) and is consistent with the rheological data (G_0' vs. concentration, Fig. 3.5B), which suggests that the peptide gel is

weakly cross-linked and lacks chain entanglement. Both of these gel structure characteristics are expected from the short, rigid monomer of peptide **1** and the hydrophobic interactions holding them together in aggregates and the branched gel backbone.

Circular dichroism (CD) spectra of soluble ACC-Hex units, ACC-Hex nanofibers, and gels support the presence of intact oligomer units across all concentrations. CD spectra were acquired from solutions of different peptide concentrations that form isolated oligomers (ACC-Hex, 0.015 % w/v), fibers (0.03% w/v) or gels (0.1 and 5.0 % w/v) (Fig. 3.6F). In dilute solutions, peptide **1** aggregates into ACC-Hex oligomers[49], the CD spectrum of which (Fig. 3.6F) exhibits characteristic α-helical molar ellipticity minima around 208 nm and 220 nm[68–71]. As the peptide forms fibers and gels with increasing concentration, the 208 nm minimum disappears and the 220 nm minimum becomes increasingly red-shifted. These two distortions in the spectra are associated with chiral scattering due to the lateral aggregation of α-helices, further radial expansion of fiber bundles[69–71], and end-to-end assembly of the helices[72]. To verify that the 70 °C incubation used for gel formation does not preclude fiber assembly, we subjected a 0.03% w/v peptide sample, which forms fibers under standard aging conditions, to a 70 °C incubation and still observed aggregated fibers (Fig. S3.8). The CD spectra, therefore, support the MD findings that the α-helical secondary structure and the ACC-Hex tertiary structure are maintained during the aggregation process associated with fiber and gel formation. In all, the structural data from rheological, molecular dynamics, and CD, in conjunction with electronic measurements suggest that the quaternary structure, *i.e.* the axial, end-to-end association of ACC-Hex units, of the nanofibers may be critical to their long-range electron conducting properties.

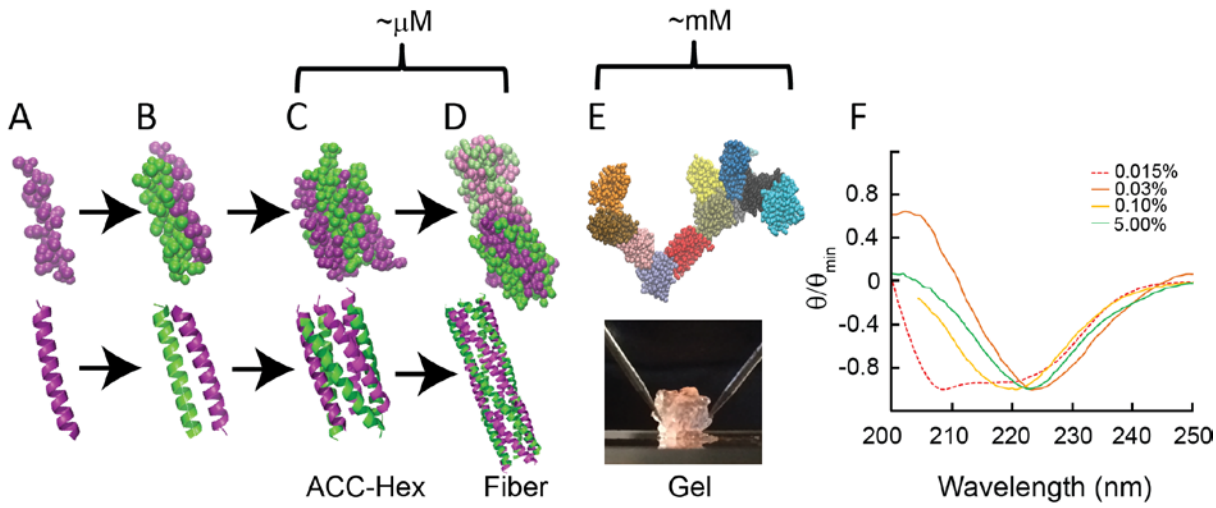

Figure 3.7: Assembly mechanism and structures of peptide **1** from simulations and CD spectra. (A-E) Molecular dynamics simulations (top) of peptide **1** self-assembly and the corresponding assemblies from the X-ray crystal structure (A-D bottom) or gel image (E bottom) of peptide **1**. All purple and all green colored peptides indicate α-helices oriented parallel to each other and antiparallel to the other color. At μM concentrations, peptide **1** forms ACC-Hex units (C), which are driven to stack end-to-end *via* electrostatic interactions (D). At mM concentrations (E), peptide **1** forms gels and a branched backbone structure composed of ACC-Hex units. In this simulation snapshot, peptide **1** monomers within the same hexamer are all colored identically. (F) Normalized CD spectra of soluble, isolated ACC-Hex oligomers (ACC-Hex, 0.015% w/v), fibrilized ACC-Hex (0.03 % w/v), and ACC-Hex gels at 0.1 and 5 % w/v peptide **1**.

While the exact mechanism of charge transport in our ACC-Hex nanofibers remains unknown, our data establish that they are electronically conductive and suggest structure-property relationships that distinguish these nanofiber materials from other conduction paradigms in organic conductors. The conduction mechanism in ACC-Hex nanofibers is likely to be distinct from the delocalized transport observed in explicitly π-stacked bio-hybrid systems, such as the peptide nanostructures and hydrogels formed by peptide-small molecule conjugates[38,73–75] and unnatural aromatic amino acids[76], because the large spacing and off-angle packing of aromatic side chains in ACC-Hex preclude π-stacking interactions[49]. In addition, the electrochemical gating results and the temperature-dependence of conductance of the ACC-Hex

nanofibers show that charge transport along the nanofibers is not facilitated by a series of redox events, as is the case in ferrocene-coupled diphenylalanine nanowires[77], amyloid fiber-conjugated cytochromes[78], or cytochrome hopping in appendages of some electrogenic anaerobes[35]. In the bipotentiostat setup, redox-mediated conduction is facilitated through current exchange at the reduction potentials of the redox-active compound, manifesting as current peaks[28,56,57]. The ACC-Hex nanofiber films, on the other hand, demonstrate ohmic, particle-like transport of charge carriers, which varies linearly with the source-drain potential and is devoid of characteristic redox peaks. This ohmic conduction is insensitive to environmental changes, showing little dependence on pH and ionic strength (Fig. S3.5), demonstrating that neither π-stacking nor redox hopping – or other thermally activated mechanisms – are necessary to facilitate charge transport over micrometer-scale distances in these peptide nanofibers.

Studies of *G. sulfurreducens* pili suggest the importance of aromatic amino acids to conductivity, with some structure homology models implying the presence of π–stacking along the length of the pili[29,43,44], and experimental data showing correlations between aromatic content and conductivity[39–41]. However, to our knowledge there is no direct, spectroscopic evidence of electronic delocalization due to π orbital overlap in pili materials to date, and our results suggest that π-stacking is not present in the peptide nanofibers and therefore may not be necessary for long-range conduction in amino acid-based materials. Similarities in the ohmic charge transport behavior, the lack of redox-mediated conduction, and metallic-like temperature dependence observed in both ACC-Hex nanofiber and pili suggest other common factors that may contribute to long-range conductivity. *G. sulfurreducens* pili and ACC-Hex nanofibers are rich in aromatic residues and both comprise of α-helical monomers arranged into ordered fibers. Supramolecular ordering alone may not be sufficient to support electrical conductivity, as Type IV pili from other

bacteria, which are presumably homologous structures,[79] exhibit substantial variation between species ranging from non-conductive to more conductive than *G. sulfurreducens* pili[28,80,81]. Other ordered protein and peptide materials, such as amyloid-like fibers, show little[82,83] or no conductivity[28]. Nonetheless, the correlation between conductivity and long-range order in the comparison between α-helical peptide nanofibers and gels in the present study demonstrates a critical role for supramolecular structure in supporting charge transport in these materials, even in the absence of electronic delocalization. Evidence of long-range electronic transport in amino acid nanomaterials, lacking both π electron overlap and redox centers, represents a distinct structural paradigm for electronic conduction in organic electronics, and ongoing studies are underway to identify key sequence and structural features supporting charge transport mechanisms in peptide nanofibers.

3.4: Conclusion

The present study demonstrates long-range electronic transport in peptide materials lacking the extended conjugation and π-orbital overlap of conventional organic semiconductors and metals. The supramolecular structure of the peptide nanofibers in this study precludes π orbital overlap between aromatic amino acid side chains, suggesting a mechanism of conduction distinct from the band conduction of periodic, π-stacked organic materials. Electrochemical and temperature-dependent transport data indicate ohmic behavior of charge carriers in this system, which is unexpected in a large unit cell, biological material. Our findings indicate that the supramolecular order and α-helical building blocks of the peptide nanofibers are critical structural features supporting the observed electronic conductivity. These data demonstrate electronic transport in synthetic peptides materials, with sequence and structural motifs borrowed

from naturally conductive bacterial protein fibers, that strongly depends on secondary and quaternary structure. These peptide nanofibers, with their mutable sequence elements, represent a promising experimental platform for further study of structure-property relationships in conductive amino acid materials. Their biocompatible composition and defined surface chemistry hold potential for application as ideal, naturally inspired bioelectronics interface materials. The peptide building blocks of these fibers suggest they can be synthesized by recombinant expression and incorporated as multifunctional material components of the growing synthetic biology toolbox.

3.5: Supporting Information

3.5.1: Peptide Material Preparation

Peptide Nanofiber and Hydrogel Preparation. Peptide **1** was synthesized as described previously.[49] A peptide seeding stock solution was made by dissolving lyophilized peptide in sterile filtered 1X PBS (Fisher) to a final concentration of 200 μM. The sample was vortexed and sonicated for 30 s each, and then incubated for a week at 37 °C prior to use. Lyophilized peptide was dissolved in sterile filtered 1X PBS to a final concentration of 100 μM. Peptide seeding stock solution was added to a final concentration of 0.5% v/v. The sample was vortexed and sonicated for 30 s each and incubated overnight at 37 °C prior to use. Fiber formation of peptide **1** was verified by atomic force microscopy (AFM) imaging as described below. For hydrogel formation, lyophilized peptide was dissolved in sterile filtered 1X PBS at concentrations of 0.1%, 0.25%, 0.5%, and 5% w/v. Samples were vortexed and sonicated for 30 s each and incubated at 70 °C for 20 min to induce gelation.

Amyloid-β (Aβ) Fiber Formation. Aβ 1-40 peptide was purchased from Sigma Aldrich for Aβ fiber formation. Lyophilized peptide was dissolved in 150 mM phosphate buffered saline (PBS) to a concentration of 100μM and incubated at 37° C for two weeks to form fibers. Fiber formation of Aβ peptide was verified using AFM imaging, as shown in Supporting Fig. 3.S1.

ACC-Hex Crystal Growth. ACC-Hex crystals for LIXPS analysis were grown in 0.1 M sodium formate, pH 6.75 – 7.3, with 25%-28% polyethylene glycol MW 3350. pH and PEG concentration were varied across a 24-well plate, with 1 mL of solution per well. For each condition, 1 μL of well solution and 1 μL of a 10 mg/mL solution of peptide **1** in ultra-pure water was dropped onto an 18 mm x 18 mm glass coverslip. The glass coverslip was inverted and sealed against the well with silicone (DAP All-Purpose Adhesive Sealant). Crystals were left undisturbed for several months.

3.5.2: Materials Characterization

Low Intensity XPS (LIXPS) of ACC-Hex Crystals. Crystals were observed under an optical microscope and the largest crystals were selected for LIXPS characterization. Spots containing crystals were re-hydrated with 2.5 μL of ultra-pure water and dropcast onto pristine Au (111)-coated Si chips. Samples were air dried and rinsed with 20 μL of filtered ultra-pure water to remove salts. Excess moisture was wicked away using a kimwipe. The buffer control was prepared using the well solution associated with the crystal sample. LIXPS was performed with a Kratos-SUPRA XPS with a Al K_α source (E_{photon} = 1486.7 eV). The secondary cutoff for each spectrum was determined by taking the intercept of two tangents at the binding energy edge. The work function was determined by subtracting the secondary cutoff value from E_{photon} = 1486.7

eV, and was calibrated using the work function of Au (111) = 5.31 eV[51].

AFM Sample Preparation and Imaging of Peptide Fibers. AFM characterization of sample morphology was conducted on silicon wafer chips. Prior to sample deposition, wafer chips were sonicated for 5 min each in acetone, isopropanol, and ultrapure water, followed by drying under nitrogen. Peptide fiber samples were drop cast onto freshly cleaned wafers and allowed to sit on the substrate for 2 min, upon which excess moisture was removed from the edges of the sample using a Kimwipe. The sample was then briefly rinsed with ultrapure water to remove salts and dried under nitrogen. AFM images were collected with an Asylum MFP3D operating in tapping mode under ambient conditions. Scans were rastered at 0.5 Hz using iridium-coated silicon probes (Asylum Research ASYELEC-01) with a tip radius of 28 nm and a resonant frequency of 70 kHz.

Rheology of Peptide Materials. All rheological experiments were performed with an AR-G2 Rheometer (TA Instruments) in a parallel plate configuration (d = 25 mm) at 25 °C with a gap height of 350 μm. A solvent trap was used to prevent evaporation over the course of the measurements. The storage *G'* and loss moduli *G"* of the hydrogels were acquired as a function of strain amplitude from 0.1 to 100 % at an oscillating frequency of 1 Hz to estimate linear viscoelastic regime for hydrogels.

Circular Dichroism of Peptide Materials. The conformation of peptide **1** in fibers and gels was characterized by circular dichroism (CD) spectroscopy, as described previously.[49] Hydrogels of peptide **1** were prepared at concentrations of 0.1%, 0.25%, and 5% w/v in 1X PBS buffer at pH 7.4. The 0.03% w/v sample of peptide **1** was prepared under typical fiber forming conditions (seeded and incubated overnight at 37 °C). A fresh sample of non-fibrilized peptide **1** (50 μM,

0.015% w/v) was also tested. CD spectra were recorded on a Jasco J-810 spectropolarimeter equipped with a Peltier thermoelectric temperature control device. The 5% w/v sample was deposited on a quartz slide as a thin film and the ellipticity was measured between 190-250 nm at 20 °C. All other samples of peptide **1** were prepared in a quartz cuvette with a 1 mm path length and measured over the same range of wavelengths at 20 °C. The voltage of the photomutiplier tube (PMT) was tracked during the course of the CD measurement, and spectra are truncated at wavelengths at which the PMT voltage exceeded 500 V.

3.5.3: Electronic Property Characterization

Device Preparation. Interdigitated electrodes were used for all DC measurements. Each electrode was comprised of 100 parallel 5 μm x 2 mm long bands with an intra-band spacing of 5 μm. Devices were photolithographically patterned onto Pyrex wafers with 60 nm Au and a 5 nm Ti adhesion layer deposited by electron beam evaporation. Devices were sonicated in washes of acetone, isopropanol, and ultrapure water to prior to use. Devices were individually tested for shorts prior to sample deposition.

Solid-State I-V Measurements of Peptide Films. For sheet resistance comparisons, 6.9 μg of ACC-Hex fibers and Aβ fibers were respectively drop cast onto interdigitated electrodes. Film were dried under laminar flow and rinsed with ultrapure water to remove salts. *I-V* measurements were performed with a Keithley Model 2612B Source Measure Unit. Current was monitored as a function of swept voltage from +0.8V to -0.8V under ambient conditions.

The electrical conductivities of ACC-Hex fibers and hydrogel samples were compared as a

function of weight percentage. 20 μL of ACC-Hex fibers in the fibrilization solution (seeded, 0.03% w/v) and 20 μL of 0.1%, 0.25%, 0.5%, and 5% hydrogels were deposited onto separate interdigitated electrode devices. After air dying under laminar flow, dried films were rinsed with ultrapure water to remove salts. *I-V* measurements were performed as described above.

Single Fiber Conductive AFM Measurements. Prior to fiber deposition, glass slides were sonicated in acetone, isopropanol, and ultrapure water and plasma cleaned. Fibers were drop-cast onto cleaned glass slides and allowed to dry. Samples were rinsed with ultrapure water to remove salts and dried under N_2. Electrode contacts (2 nm of chromium and 80 nm gold) were thermally evaporated onto the glass slide using a shadow mask. The electrodes were shorted to a grounding plate using silver paint and conductive AFM was performed using an Asylum MFP3D in ORCA mode with iridium-coated silicon probes (Asylum Research ASYELEC-01).

Scans were first done in contact and current mode with a 5 V bias to determine the position of the edge of the electrode. The scan was then repeated in tapping mode to obtain better resolution of the fiber. The tip of the conductive probe was then positioned at various distances along the fiber, allowing for a two-point measurement between the patterned electrode and the tip. The current response at each position of the nanofiber was monitored as the voltage was swept between ± 5 V. Individual nanofiber conductivities were calculated from the distance-dependent conductance values and the using the peak height of the nanofibers as measured by AFM as the diameter and assuming a cylindrical conduction cross section. Controls were performed on the gold electrode and on the insulating substrate. Fiber conductivity was determined as an average of 4 different fiber samples.

Electrochemical Conductance Measurements. For solution-gated measurements, 22-gauge

solid core insulated wire leads were connected to the interdigitated source and drain electrodes using conductive silver epoxy (MG Materials). Exposed electrode and lead connections were sealed with waterproof silicone sealant (DAP All-Purpose Adhesive Sealant). ACC-Hex fibers were drop cast onto cleaned electrodes to deposit a total peptide mass of 6.9 μg and were air dried in a laminar flow hood.

Solution gating measurements were conducted in 0.1M phosphate-citrate buffer, and the pH was controlled by changing the ratios of constituent sodium phosphate dibasic (Na_2HPO_4) and sodium citrate ($Na_2C_6H_6O_7$). For ionic strength measurements, 0.2 M Na_2HPO_4 and 0.2M $Na_2C_6H_6O_7$ stocks were prepared and diluted with ultrapure water to achieve the appropriate ionic strength. Electrolyte solutions were degassed with 80% N_2 with 20% CO_2 prior to electrochemical cell assembly in a 100 mL aqueous electrochemical cell (Adam & Chittenden MFC 100.25.3), which was sealed with rubber septa. Titanium wire and microfit connectors were used to connect the electrochemical components to external leads (DigiKey).

Bipotentiostat cyclic voltammograms (CVs) were performed using two Gamry potentiostats (series PC14/300) connected with a bipotentiosat cable. In the bipotentiostat setup (Fig. S3.4), described previously,[28,57,84] the source and drain are monitored as two independent working electrodes, referenced to the same saturated Ag/AgCl reference and sharing the same platinum wire (Sigma Aldrich) as a counter electrode. The source electrode was swept from -0.8 V to +0.4 V with respect to Ag/AgCl, at a scan rate of 10 mV/s. Simultaneously, the drain was swept at a fixed source-drain offset V_{DS} relative to the source, with respect to Ag/AgCl, at a scan rate of 10 mV/s. The background catalytic current was determined by conducting bipotentiostat CVs at V_{DS} = 0, and the background values were subtracted from nonzero offsets to obtain the conducting current I_{con} (Fig. S3.9B). The difference currents between the source and the drain, divided by a

factor of two, were plotted as I_{DS} (Fig. S3.9C).

Temperature-Dependent Electrical Conductance Measurements. To assess the temperature-dependent electrical conductance of ACC-Hex fiber films, electrochemical cells were submerged in a stirred water bath with a metal thermocouple. A hot plate was used to heat the system and ice was added to the water bath to achieve cooling. Once the thermocouple registered a stable bath temperature for several minutes at each temperature set point, bipotentiostat chronoamperometry measurements were performed, wherein the source and drain currents were independently monitored while maintaining a fixed V_{DS} offset. Once steady-state currents were stable for 1 min, the currents were averaged and the steady-state conducting current was taken to be half the difference between the source and drain currents, which mirror each other with opposite polarity (Fig. S3.10). The negligible background current at V_{DS} =0V was subtracted from the steady-state current, which was then divided by V_{DS} to obtain the conductance. Measurements were taken with V_{DS} values of 0 V, 10 mV, 20 mV, 40 mV, 60 mV, 80 mV, -10 mV, -20 mV, -40 mV, -60 mV, and -80 mV and were performed in 0.1 M phosphate citrate buffer at pH 7.0. Each data point in Fig. 3.3B is an average of the 10 bias offset measurements conducted at a single temperature with error bars representing the standard error.

Electrical Impedance Spectroscopy of Samples in Aqueous Salts and D_2O. For EIS measurements testing conductivity with different Hofmeister anions and cations, a film of ACC-Hex nanofibers was prepared for electrochemical measurements, as described above. 0.1 M solutions of NH_4Cl, KCl, NaCl, $CaCl_2$, $MgCl_2$, NaH_2PO_4, Na_2HPO_4, $NaCH_3COO$, and $NaClO_4$ were prepared. EIS was performed over a frequency range of 10 mHz to 100 MHz, with a fixed DC bias of 0 V and an AC perturbation of 10 mV. Films were dipped in two separate vials of fresh ultra-pure water after subsequent measurements, to remove residual salts. The order of ions

was randomly selected and the series was reversed for four rounds, producing a total of 8 different measurements. 1 round of measurements was also performed in 1 mM Hofmeister solutions (Fig. S3.6). Fiber conductivity did not change appreciably over the course of the measurement, suggesting material was not lost over the course of the measurement. EIS was also performed with H_2O (ultra-pure water) and D_2O (Sigma-Aldrich) between series, for a total of 5 different measurements. The measurement order was similarly varied to minimize sampling error. Impedance values were determined by using the Gamry Echem Analyst software to fit data to a Randles circuit using the Simplex Method. Goodness of fit parameters gave *p*-values between 0.967 and 0.999, suggestive of good fits.

Electrical Impedance Spectroscopy Measurements of Fibers versus Hydrogels. For EIS measurements comparing fibers and gels, a sandwich electrode was fabricated from two 2 cm x 2 cm plates of fluorine-doped tin oxide (FTO) coated glass sides (Sigma Aldrich). External leads were attached to the non-conductive backsides of the glass slides using silver epoxy, and silver paste (Ted Pella) was used to connect the leads to the conductive FTO film. Two 540 μm non-conductive spacers were used to insulate the conductive paste and separate the slides, which were then sealed using electrical tape and silicone epoxy. EIS measurements were performed in a Faraday cage and spanning a frequency range of 10 mHz to 100 MHz, with a fixed DC bias of 0 V and an AC perturbation of 10 mV.

Molecular Dynamics Simulations of Peptide Self-Assembly. The coarse grained (CG) MARTINI force field[85,86] was used for biomolecular simulations to model peptides at different concentrations in explicit solvent. The MARTINI model uses a four-to-one mapping in which four atoms and associated hydrogen atoms are represented by one CG bead to represent protein backbone and side chains. Water and ions (which were added to electronically neutralize the

system) are treated explicitly at the same level of coarse-graining. Although MARTINI lacks some atomic detail given its coarse-grained nature, its force field has been undergone extensive parameterization based on comparison with experimental results. Since MARTINI requires that the secondary structure of a peptide needs to be provided *a priori* and is fixed during the simulation, the helical conformation from the X-ray crystal structure of peptide **1** was used[49].

All molecular dynamics (MD) simulations were performed with the GROMACS simulation package in the NPT ensemble. The pressure and temperature were maintained using the Berendsen method at 1 bar and at different constant temperatures, ranging from 330 to 350 K. Initially, the first set of 20 independent simulations were performed on a system containing 50 dipeptides that were placed randomly within a cubic box of 55 nm and solvated in standard MARTINI CG water and ions. Once isolated peptides came together to form the first hexamer, after 20 μs in effective simulation time, the hexamer was extracted for the next set of simulations. 40 copies of the hexamer were randomly placed within a cubic box of either 25 or 55 nm, containing water and ions, for another 20 μs MD simulation at 1 bar. This set of simulations was conducted at different temperatures ranging from 300 to 320 K; these lower temperatures allowed for stability of the hexameric copies. Hexamers in a larger box and thus at a lower concentration came together to form linear fibers, whereas those in a smaller box and at a higher concentration came together to form branched structures at different temperatures.

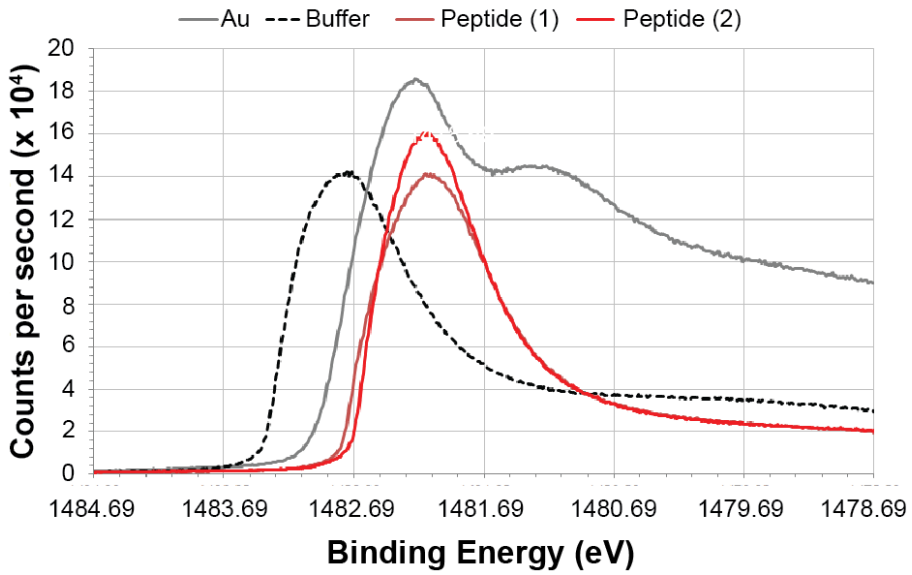

Figure S3.1: LIXPS spectra of Au (111) substrate, PBS on substrate, and two samples of ACC-Hex crystals. The secondary cutoff values are 1482 eV, 1483.4 eV, and 1482.8 eV and 1482.7 eV, respectively, with Al K_α x-rays (E_{photon} = 1486.7 eV).

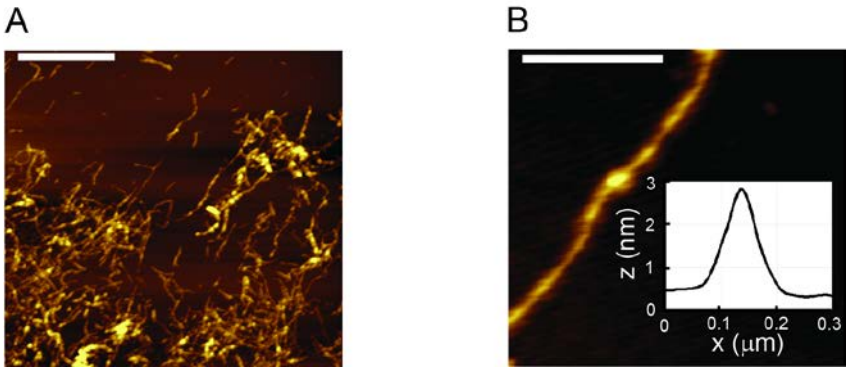

Figure S3.2: Representative AFM micrographs of Aβ fibers. (A) Drop-cast film of Aβ fibers (scale bar 5 μm). (B) Single Aβ fiber. Height profile analysis shows fiber diameters of approximately 2 nm (inset).

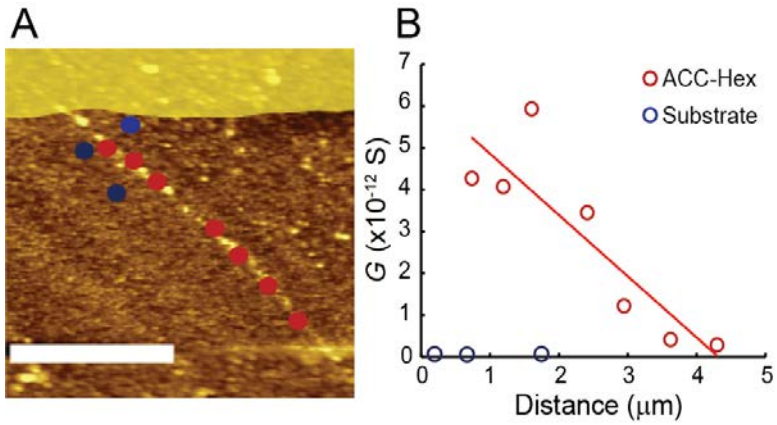

Figure S3.3: Single fiber conductive AFM of an ACC-Hex fiber and substrate. (A) Topographical AFM image of a fiber. Circles indicate measurement positions on the fiber (red) and substrate (blue). Electrode is false-colored, scale bar 2 μm. (B) Conductance as a function of distance plot for single fiber shown in (A).

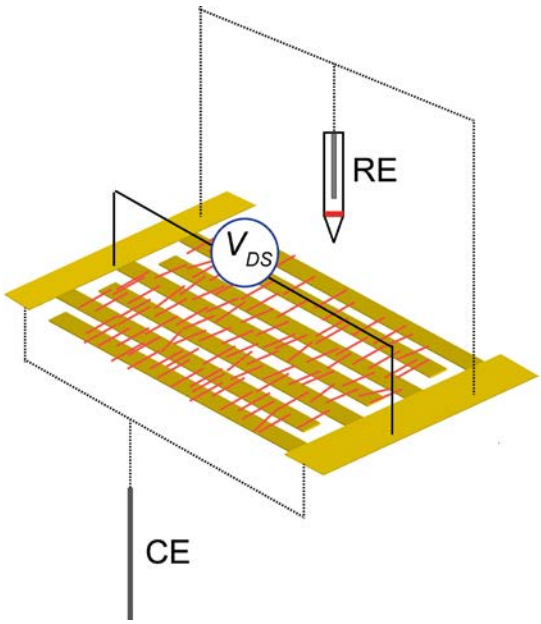

Figure S3.4: Schematic of interdigitated electrode with ACC-Hex fiber samples in bipotentiostat setup. The source and drain electrodes function as two independent working electrodes and are referenced and swept relative to a Ag/AgCl reference electrode (RE). The sweep range for each electrode is such that a fixed V_{DS} offset is maintained between the source and the drain. A platinum wire functions as a common counter electrode (CE).

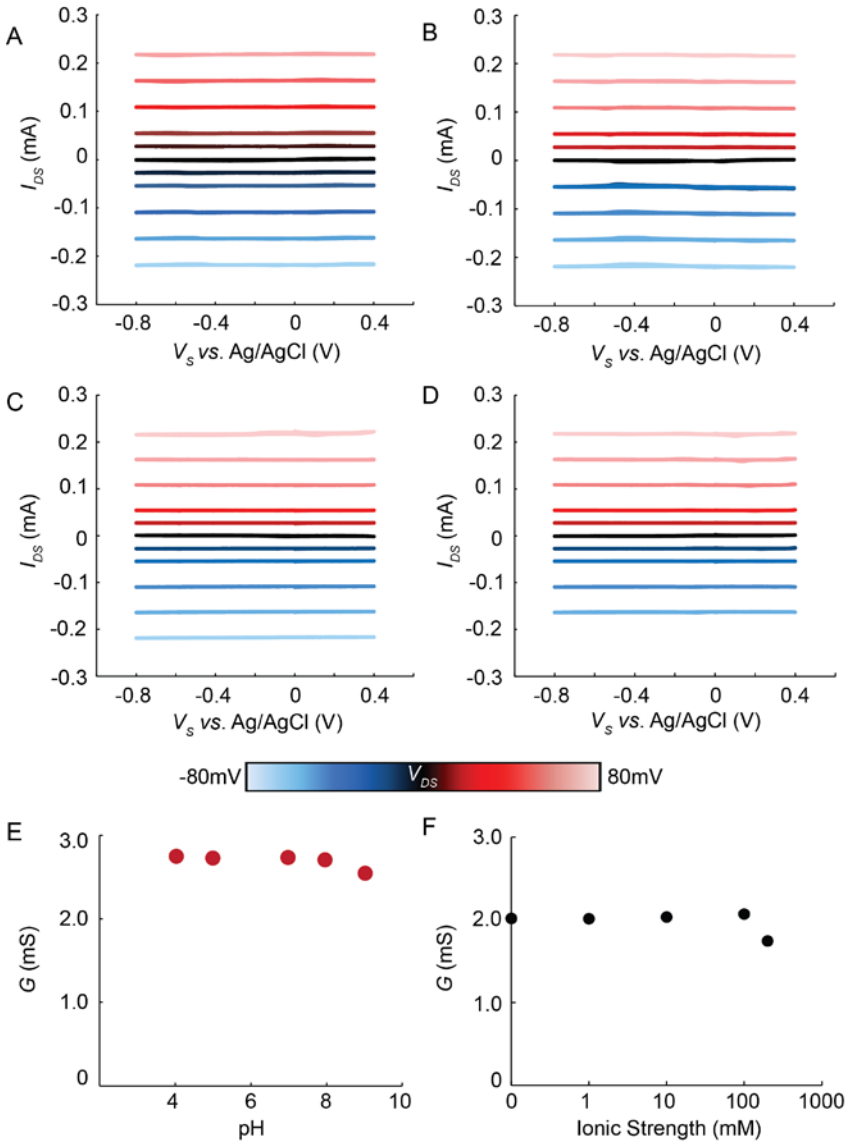

Figure S3.5: Source-drain current of ACC-Hex fiber films obtained from bipotentiostat cyclic voltammograms in 0.1M phosphate citrate buffer at (A) pH 4.0, (B) pH 5.0, (C) pH 8.0, and (D) pH 9.0. (E) Source-drain current as a function of V_{DS} at different pH values. (F) Ionic strength dependence of ACC-Hex fiber films in ultrapure water and phosphate citrate buffer.

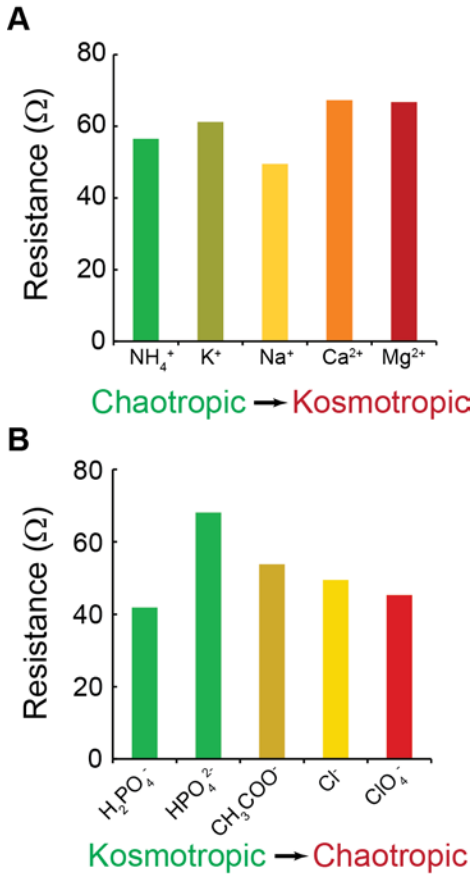

Figure S3.6: Impedance measurement values of ACC-Hex nanofibers in 1 mM Hofmeister ion solution (concentration is 100 x lower than that used in Fig. 3.4).

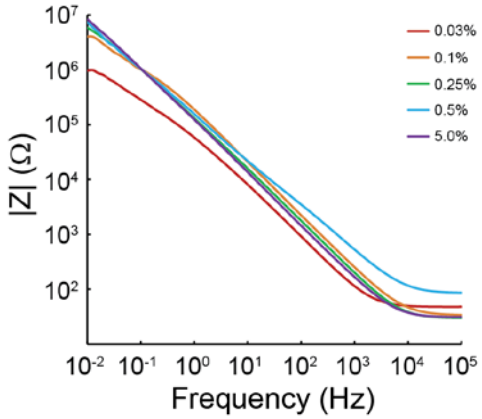

Figure S3.7: Bode plots collected from EIS measurements on ACC-Hex nanofibers and hydrogels at different % w/v concentrations.

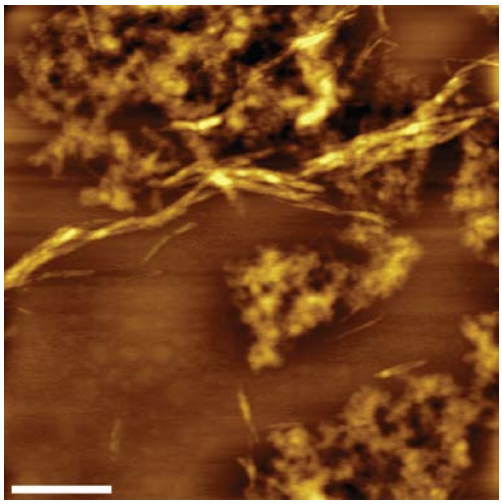

Figure S3.8: Representative AFM micrograph of ACC-Hex fibers (0.03% w/v) prepared in an identical manner to higher % w/v hydrogels. Scale bar is 2 μm.

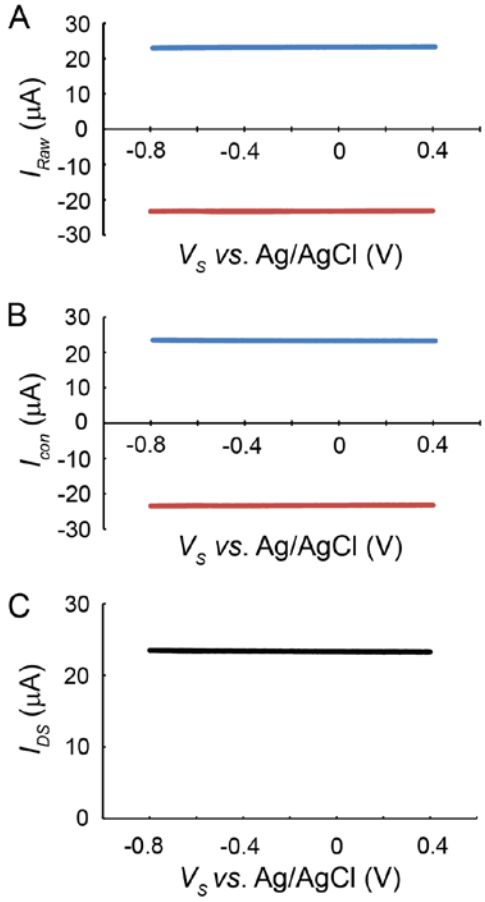

Figure S3.9: Bipotentiostat cyclic voltammograms of ACC-Hex fiber films in electrochemical gating setup. (A) Representative raw source (red) and drain (blue) currents at V_{DS} = 10 mV, (B) source and drain conducting currents after background subtraction of currents at V_{DS} = 0, and (C) I_{DS} determined from background subtracted currents.

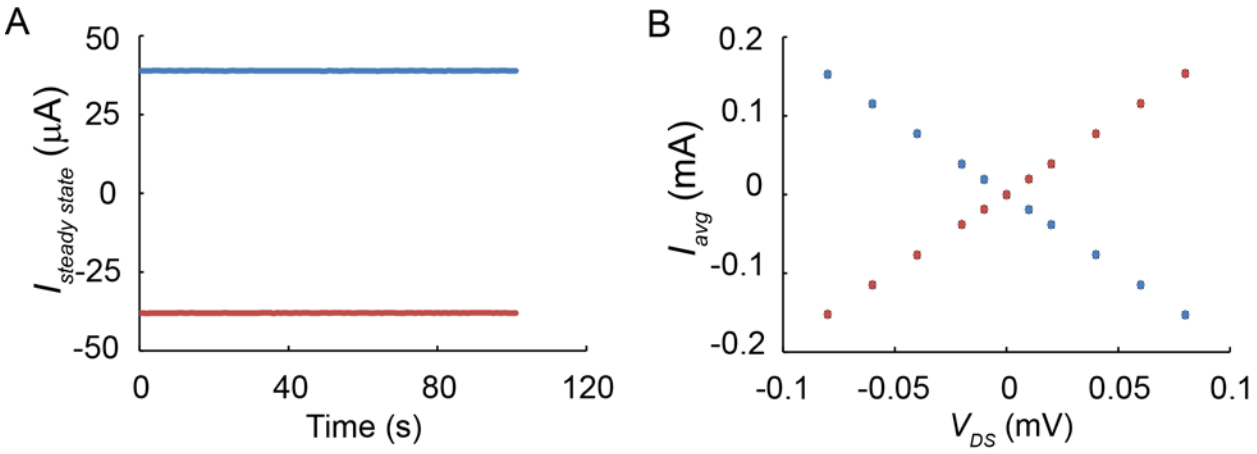

Figure S3.10: (A) Representative steady-state source (red) and drain (blue) currents obtained from temperature-dependent bipotentiostat chronoamperometry scans of ACC-Hex fiber films poised at V_s= 0 V and V_{DS} =20 mV. (B) Average currents obtained from steady-state values at different values of V_{DS}. These representative data were obtained in 0.1M phosphate citrate buffer at pH 7.0 and 42°C.

3.6: Acknowledgements

The authors thank Prof. Ali Mohraz for helpful discussions and the facilities and resources at the Molecular Foundry at the Lawrence Berkeley National Laboratory, where peptides for this study were synthesized and characterized. Work at the Molecular Foundry is supported by the Director, Office of Science, Office of Basic Energy Sciences, of the U.S. Department of Energy under contract DE-AC02-05CH11231. N.L.I. acknowledges support from the National Science Foundation Graduate Research Fellowship Program and from the U.S. Department of Education Graduate Assistance in Areas of National Need Fellowship, administered through the Chemical Engineering and Materials Science Program at the UC Irvine. Research on this project was funded by the Air Force Office of Scientific Research, grant FA9550-14-1-0350 (N.L.I., R.K.S. and A.I.H.), a 3M Non-Tenured Faculty Award (A.I.H.), and the National Science Foundation grant CAREER CBET-1554508 (H.D.N.).

Author Contributions. A.I.H., N.L.I., and H.D.N. designed the experiments and prepared the manuscript. R.K.S. synthesized and characterized the X-ray structure and solution behavior of the peptides, and N.L.I. ran all other experiments. H.D.N. and S.H.L. ran and analyzed results from the MD simulations.

This chapter is an adaptation of the material as it appears in: Ing, N.L.; Spencer, R.K.; Luong, S.H.; Nguyen, H.D.; and Hochbaum, A.I. Electronic Conductivity in Biomimetic α-Helical Peptide Nanofibers and Gels. *ACS Nano* **2017**, *12*(3), 2652-2661.

3.7: References

(1) Nicolini, C. From Neural Chip and Engineered Biomolecules to Bioelectronic Devices: An Overview. *Biosens. Bioelectron.* **1995**, *10* (1), 105–127.

(2) Kaltenbrunner, M.; Sekitani, T.; Reeder, J.; Yokota, T.; Kuribara, K.; Tokuhara, T.; Drack, M.; Schwödiauer, R.; Graz, I.; Bauer-Gogonea, S.; et al. An Ultra-Lightweight Design for Imperceptible Plastic Electronics. *Nature* **2013**, *499* (7459), 458–463.

(3) Lee, H.; Choi, T. K.; Lee, Y. B.; Cho, H. R.; Ghaffari, R.; Wang, L.; Choi, H. J.; Chung, T. D.; Lu, N.; Hyeon, T.; et al. A Graphene-Based Electrochemical Device with Thermoresponsive Microneedles for Diabetes Monitoring and Therapy. *Nat. Nanotechnol.* **2016**, *11* (6), 566–572.

(4) Liu, H.; Zhao, T.; Jiang, W.; Jia, R.; Niu, D.; Qiu, G.; Fan, L.; Li, X.; Liu, W.; Chen, B.; et al. Flexible Battery-Less Bioelectronic Implants: Wireless Powering and Manipulation by near-Infrared Light. *Adv. Funct. Mater.* **2015**, *25* (45), 7071–7079.

(5) Jonsson, A.; Song, Z.; Nilsson, D.; Meyerson, B. A.; Simon, D. T.; Linderoth, B.; Berggren, M. Therapy Using Implanted Organic Bioelectronics. *Sci. Adv.* **2015**, *1* (4), 1–6.

(6) Luz, R. A. S.; Pereira, A. R.; de Souza, J. C. P.; Sales, F. C. P. F.; Crespilho, F. N. Enzyme Biofuel Cells: Thermodynamics, Kinetics and Challenges in Applicability. *ChemElectroChem* **2014**, *1* (11), 1751–1777.

(7) Slaughter, G.; Kulkarni, T. Highly Selective and Sensitive Self-Powered Glucose Sensor Based on Capacitor Circuit. *Sci. Rep.* **2017**, *7* (1), 1471.

(8) Falk, M.; Alcalde, M.; Bartlett, P. N.; De Lacey, A. L.; Gorton, L.; Gutierrez-Sanchez, C.; Haddad, R.; Kilburn, J.; Leech, D.; Ludwig, R.; et al. Self-Powered Wireless Carbohydrate/Oxygen Sensitive Biodevice Based on Radio Signal Transmission. *PloS One* **2014**, *9* (10), e109104.

(9) Lafleur, J. P.; Jönsson, A.; Senkbeil, S.; Kutter, J. P. Recent Advances in Lab-on-a-Chip for Biosensing Applications. *Biosens. Bioelectron.* **2016**, *76*, 213–233.

(10) Medina-Sánchez, M.; Miserere, S.; Merkoçi, A. Nanomaterials and Lab-on-a-Chip Technologies. *Lab Chip* **2012**, *12* (11), 1932–1943.

(11) Liu, J.; Fu, T.-M.; Cheng, Z.; Hong, G.; Zhou, T.; Jin, L.; Duvvuri, M.; Jiang, Z.; Kruskal, P.; Xie, C.; et al. Syringe-Injectable Electronics. *Nat. Nanotechnol.* **2015**, *10* (7), 629–636.

(12) Oxley, T. J.; Opie, N. L.; John, S. E.; Rind, G. S.; Ronayne, S. M.; Wheeler, T. L.; Judy, J. W.; McDonald, A. J.; Dornom, A.; Lovell, T. J. H.; et al. Minimally Invasive Endovascular Stent-Electrode Array for High-Fidelity, Chronic Recordings of Cortical Neural Activity. *Nat. Biotechnol.* **2016**, *34* (3), 320–327.

(13) Someya, T.; Bao, Z.; Malliaras, G. G. The Rise of Plastic Bioelectronics. *Nature* **2016**, *540* (7633), 379–385.

(14) Zhang, A.; Lieber, C. M. Nano-Bioelectronics. *Chem. Rev.* **2016**, *116* (1), 215–257.

(15) Domigan, L. J. Proteins and Peptides as Biological Nanowires: Towards Biosensing Devices. *Methods Mol. Biol. Clifton NJ* **2013**, *996*, 131–152.

(16) Eakins, G. L.; Pandey, R.; Wojciechowski, J. P.; Zheng, H. Y.; Webb, J. E. A.; Valéry, C.; Thordarson, P.; Plank, N. O. V.; Gerrard, J. A.; Hodgkiss, J. M. Functional Organic Semiconductors Assembled via Natural Aggregating Peptides. *Adv. Funct. Mater.* **2015**, *25* (35), 5640–5649.

(17) Kasai, S.; Ohga, Y.; Mochizuki, M.; Nishi, N.; Kadoya, Y.; Nomizu, M. Multifunctional Peptide Fibrils for Biomedical Materials. *Biopolymers* **2004**, *76* (1), 27–33.

(18) Hauser, C. A. E.; Zhang, S. Designer Self-Assembling Peptide Nanofiber Biological Materials. *Chem. Soc. Rev.* **2010**, *39* (8), 2780–2790.

(19) Santis, E. D.; Ryadnov, M. G. Peptide Self-Assembly for Nanomaterials: The Old New Kid on the Block. *Chem. Soc. Rev.* **2015**, *44* (22), 8288–8300.

(20) Bai, Y.; Luo, Q.; Liu, J. Protein Self-Assembly via Supramolecular Strategies. *Chem. Soc. Rev.* **2016**, *45* (10), 2756–2767.

(21) Liu, J.; Xie, C.; Dai, X.; Jin, L.; Zhou, W.; Lieber, C. M. Multifunctional Three-Dimensional Macroporous Nanoelectronic Networks for Smart Materials. *Proc. Natl. Acad. Sci. U. S. A.* **2013**, *110* (17), 6694–6699.

(22) Gray, H. B.; Winkler, J. R. Long-Range Electron Transfer. *Proc. Natl. Acad. Sci. U. S. A.* **2005**, *102* (10), 3534–3539.

(23) Winkler, J. R.; Gray, H. B. Long-Range Electron Tunneling. *J. Am. Chem. Soc.* **2014**, *136* (8), 2930–2939.

(24) Sepunaru, L.; Refaely-Abramson, S.; Lovrinčić, R.; Gavrilov, Y.; Agrawal, P.; Levy, Y.; Kronik, L.; Pecht, I.; Sheves, M.; Cahen, D. Electronic Transport via Homopeptides: The Role of Side Chains and Secondary Structure. *J. Am. Chem. Soc.* **2015**, *137* (30), 9617–9626.

(25) Amdursky, N. Electron Transfer across Helical Peptides. *ChemPlusChem* **2015**, *80* (7), 1075–1095.

(26) Juhaniewicz, J.; Pawlowski, J.; Sek, S. Electron Transport Mediated by Peptides Immobilized on Surfaces. *Isr. J. Chem.* **2015**, *55* (6–7), 645–660.

(27) Malvankar, N. S.; Vargas, M.; Nevin, K. P.; Franks, A. E.; Leang, C.; Kim, B.-C.; Inoue, K.; Mester, T.; Covalla, S. F.; Johnson, J. P.; et al. Tunable Metallic-like Conductivity in Microbial Nanowire Networks. *Nat. Nanotechnol.* **2011**, *6* (9), 573–579.

(28) Ing, N. L.; Nusca, T. D.; Hochbaum, A. I. Geobacter Sulfurreducens Pili Support Ohmic Electronic Conduction in Aqueous Solution. *Phys. Chem. Chem. Phys.* **2017**, *19* (32), 21791–21799.

(29) Malvankar, N. S.; Vargas, M.; Nevin, K.; Tremblay, P.-L.; Evans-Lutterodt, K.; Nykypanchuk, D.; Martz, E.; Tuominen, M. T.; Lovley, D. R. Structural Basis for Metallic-like Conductivity in Microbial Nanowires. *mBio* **2015**, *6* (2), e00084-15.

(30) Reguera, G.; McCarthy, K. D.; Mehta, T.; Nicoll, J. S.; Tuominen, M. T.; Lovley, D. R. Extracellular Electron Transfer via Microbial Nanowires. *Nature* **2005**, *435* (7045), 1098–1101.

(31) Adhikari, R. Y.; Malvankar, N. S.; Tuominen, M. T.; Lovley, D. R. Conductivity of Individual Geobacter Pili. *RSC Adv.* **2016**, *6* (10), 8354–8357.

(32) Amdursky, N.; Marchak, D.; Sepunaru, L.; Pecht, I.; Sheves, M.; Cahen, D. Electronic Transport via Proteins. *Adv. Mater.* **2014**, *26* (42), 7142–7161.

(33) Mercato, L. L. del; Pompa, P. P.; Maruccio, G.; Torre, A. D.; Sabella, S.; Tamburro, A. M.; Cingolani, R.; Rinaldi, R. Charge Transport and Intrinsic Fluorescence in Amyloid-like Fibrils. *Proc. Natl. Acad. Sci.* **2007**, *104* (46), 18019–18024.

(34) Creasey, R. C. G.; Shingaya, Y.; Nakayama, T. Improved Electrical Conductance through Self-Assembly of Bioinspired Peptides into Nanoscale Fibers. *Mater. Chem. Phys.* **2015**, *158*, 52–59.

(35) Pirbadian, S.; Barchinger, S. E.; Leung, K. M.; Byun, H. S.; Jangir, Y.; Bouhenni, R. A.; Reed, S. B.; Romine, M. F.; Saffarini, D. A.; Shi, L.; et al. Shewanella Oneidensis MR-1 Nanowires Are Outer Membrane and Periplasmic Extensions of the Extracellular Electron Transport Components. *Proc. Natl. Acad. Sci.* **2014**, *111* (35), 12883–12888.

(36) Malvankar, N. S.; Tuominen, M. T.; Lovley, D. R. Lack of Cytochrome Involvement in Long-Range Electron Transport through Conductive Biofilms and Nanowires of Geobacter Sulfurreducens. *Energy Environ. Sci.* **2012**, *5* (9), 8651.

(37) Wall, B. D.; Zacca, A. E.; Sanders, A. M.; Wilson, W. L.; Ferguson, A. L.; Tovar, J. D. Supramolecular Polymorphism: Tunable Electronic Interactions within π-Conjugated Peptide Nanostructures Dictated by Primary Amino Acid Sequence. *Langmuir* **2014**, *30* (20), 5946–5956.

(38) Nalluri, S. K. M.; Shivarova, N.; Kanibolotsky, A. L.; Zelzer, M.; Gupta, S.; Frederix, P. W. J. M.; Skabara, P. J.; Gleskova, H.; Ulijn, R. V. Conducting Nanofibers and Organogels Derived from the Self-Assembly of Tetrathiafulvalene-Appended Dipeptides. *Langmuir* **2014**, *30* (41), 12429–12437.

(39) Malvankar, N. S.; Yalcin, S. E.; Tuominen, M. T.; Lovley, D. R. Visualization of Charge Propagation along Individual Pili Proteins Using Ambient Electrostatic Force Microscopy. *Nat. Nanotechnol.* **2014**, *9* (12), 1012–1017.

(40) Tan, Y.; Adhikari, R. Y.; Malvankar, N. S.; Pi, S.; Ward, J. E.; Woodard, T. L.; Nevin, K. P.; Xia, Q.; Tuominen, M. T.; Lovley, D. R. Synthetic Biological Protein Nanowires with High Conductivity. *Small* **2016**, *12* (33), 4481–4485.

(41) Vargas, M.; Malvankar, N. S.; Tremblay, P.-L.; Leang, C.; Smith, J. A.; Patel, P.; Synoeyenbos-West, O.; Nevin, K. P.; Lovley, D. R. Aromatic Amino Acids Required for Pili Conductivity and Long-Range Extracellular Electron Transport in Geobacter Sulfurreducens. *mBio* **2013**, *4* (2), e00105–e00113.

(42) Tan, Y.; Adhikari, R. Y.; Malvankar, N. S.; Ward, J. E.; Woodard, T. L.; Nevin, K. P.; Lovley, D. R. Expressing the Geobacter Metallireducens PilA in Geobacter Sulfurreducens Yields Pili with Exceptional Conductivity. *mBio* **2017**, *8* (1).

(43) Feliciano, G. T.; da Silva, A. J. R.; Reguera, G.; Artacho, E. Molecular and Electronic Structure of the Peptide Subunit of Geobacter Sulfurreducens Conductive Pili from First Principles. *J. Phys. Chem. A* **2012**, *116* (30), 8023–8030.

(44) Xiao, K.; Malvankar, N. S.; Shu, C.; Martz, E.; Lovley, D. R.; Sun, X. Low Energy Atomic Models Suggesting a Pilus Structure That Could Account for Electrical Conductivity of Geobacter Sulfurreducens Pili. *Sci. Rep.* **2016**, *6*, 23385.

(45) Pawlowski, J.; Juhaniewicz, J.; Tymecka, D.; Sek, S. Electron Transfer across α-Helical Peptide Monolayers: Importance of Interchain Coupling. *Langmuir* **2012**, *28* (50), 17287–17294.

(46) Atanassov, A.; Hendler, Z.; Berkovich, I.; Ashkenasy, G.; Ashkenasy, N. Force Modulated Conductance of Artificial Coiled-Coil Protein Monolayers. *Pept. Sci.* **2013**, *100* (1), 93–99.

(47) Morita, T.; Kimura, S. Long-Range Electron Transfer over 4 Nm Governed by an Inelastic Hopping Mechanism in Self-Assembled Monolayers of Helical Peptides. *J. Am. Chem. Soc.* **2003**, *125* (29), 8732–8733.

(48) Mizrahi, M.; Zakrassov, A.; Lerner-Yardeni, J.; Ashkenasy, N. Charge Transport in Vertically Aligned, Self-Assembled Peptide Nanotube Junctions. *Nanoscale* **2012**, *4* (2), 518–524.

(49) Spencer, R. K.; Hochbaum, A. I. X-Ray Crystallographic Structure and Solution Behavior of an Antiparallel Coiled-Coil Hexamer Formed by de Novo Peptides. *Biochem.* **2016**, *55* (23), 3214–3223.

(50) Spencer, R. K.; Hochbaum, A. I. The Phe-Ile Zipper: A Specific Interaction Motif Drives Antiparallel Coiled-Coil Hexamer Formation. *Biochem.* **2017**, *56* (40), 5300–5308.

(51) Farkas, A. P.; Solymosi, F. Activation and Reactions of CO2 on a K-Promoted Au(111) Surface. *J. Phys. Chem. C* **2009**, *113* (46), 19930–19936.

(52) Tao, K.; Makam, P.; Aizen, R.; Gazit, E. Self-Assembling Peptide Semiconductors. *Science* **2017**, *358* (6365).

(53) Evans, M. G.; Gergely, J. A Discussion of the Possibility of Bands of Energy Levels in Proteins Electronic Interaction in Non Bonded Systems. *Biochim. Biophys. Acta* **1949**, *3*, 188–197.

(54) J. Ladik. Energy Band Structure of Proteins. *Nature* **1964**, *202*, 1208–1209.

(55) Vivekanandan, S.; Brender, J. R.; Lee, S. Y.; Ramamoorthy, A. A Partially Folded Structure of Amyloid-Beta(1-40) in an Aqueous Environment. *Biochem. Biophys. Res. Commun.* **2011**, *411* (2), 312–316.

(56) Yates, M. D.; Strycharz-Glaven, S. M.; Golden, J. P.; Roy, J.; Tsoi, S.; Erickson, J. S.; El-Naggar, M. Y.; Barton, S. C.; Tender, L. M. Measuring Conductivity of Living Geobacter Sulfurreducens Biofilms. *Nat. Nanotechnol.* **2016**, *11* (11), 910–913.

(57) Yates, M. D.; Golden, J. P.; Roy, J.; Strycharz-Glaven, S. M.; Tsoi, S.; Erickson, J. S.; El-Naggar, M. Y.; Barton, S. C.; Tender, L. M. Thermally Activated Long Range Electron Transport in Living Biofilms. *Phys. Chem. Chem. Phys.* **2015**, *17* (48), 32564–32570.

(58) Hofmeister, F. Zur Lehre von der Wirkung der Salze. *Arch. Für Exp. Pathol. Pharmakol.* **1888**, *24* (4–5), 247–260.

(59) Hofmeister, F. Zur Lehre von der Wirkung der Salze. *Arch. Für Exp. Pathol. Pharmakol.* **1888**, *25* (1), 1–30.

(60) Tadeo, X.; López-Méndez, B.; Castaño, D.; Trigueros, T.; Millet, O. Protein Stabilization and the Hofmeister Effect: The Role of Hydrophobic Solvation. *Biophys. J.* **2009**, *97* (9), 2595–2603.

(61) Yan, C.; Pochan, D. J. Rheological Properties of Peptide-Based Hydrogels for Biomedical and Other Applications. *Chem. Soc. Rev.* **2010**, *39* (9), 3528–3540.

(62) Lyon, L. A.; Serpe, M. J. *Hydrogel Micro and Nanoparticles*; John Wiley & Sons, 2012.

(63) MacKintosh, F. C. Elasticity of Semiflexible Biopolymer Networks. *Phys. Rev. Lett.* **1995**, *75* (24), 4425–4428.

(64) Hinner, B. Entanglement, Elasticity, and Viscous Relaxation of Actin Solutions. *Phys. Rev. Lett.* **1998**, *81* (12), 2614–2617.

(65) Colby, R. H. Structure and Linear Viscoelasticity of Flexible Polymer Solutions: Comparison of Polyelectrolyte and Neutral Polymer Solutions. *Rheol. Acta* **2010**, *49* (5), 425–442.

(66) Rahman, A. R. A.; Justin, G.; Guiseppi-Elie, A. Bioactive Hydrogel Layers on Microdisk Electrode Arrays: Impedimetric Characterization and Equivalent Circuit Modeling. *Electroanalysis* **2009**, *21* (10), 1135–1144.

(67) Amirudin, A.; Thieny, D. Application of Electrochemical Impedance Spectroscopy to Study the Degradation of Polymer-Coated Metals. *Prog. Org. Coat.* **1995**, *26* (1), 1–28.

(68) Greenfield, N. J. Using Circular Dichroism Spectra to Estimate Protein Secondary Structure. *Nat. Protoc.* **2006**, *1* (6), 2876–2890.

(69) Pandya, M. J.; Spooner, G. M.; Sunde, M.; Thorpe, J. R.; Rodger, A.; Woolfson, D. N. Sticky-End Assembly of a Designed Peptide Fiber Provides Insight into Protein Fibrillogenesis. *Biochem.* **2000**, *39* (30), 8728–8734.

(70) Bromley, E. H. C.; Channon, K. J.; King, P. J. S.; Mahmoud, Z. N.; Banwell, E. F.; Butler, M. F.; Crump, M. P.; Dafforn, T. R.; Hicks, M. R.; Hirst, J. D.; et al. Assembly Pathway of a Designed Alpha-Helical Protein Fiber. *Biophys. J.* **2010**, *98* (8), 1668–1676.

(71) Frost, D. W. H.; Yip, C. M.; Chakrabartty, A. Reversible Assembly of Helical Filaments by de Novo Designed Minimalist Peptides. *Biopolymers* **2005**, *80* (1), 26–33.

(72) Chin, D.-H.; Woody, R. W.; Rohl, C. A.; Baldwin, R. L. Circular Dichroism Spectra of Short, Fixed-Nucleus Alanine Helices. *Proc. Natl. Acad. Sci.* **2002**, *99* (24), 15416–15421.

(73) Xu, H.; Das, A. K.; Horie, M.; Shaik, M. S.; Smith, A. M.; Luo, Y.; Lu, X.; Collins, R.; Liem, S. Y.; Song, A.; et al. An Investigation of the Conductivity of Peptide Nanotube

Networks Prepared by Enzyme-Triggered Self-Assembly. *Nanoscale* **2010**, *2* (6), 960–966.

(74) Ardoña, H. A. M.; Tovar, J. D. Peptide π-Electron Conjugates: Organic Electronics for Biology? *Bioconjug. Chem.* **2015**, *26* (12), 2290–2302.

(75) Ardoña, H. A. M.; Besar, K.; Togninalli, M.; Katz, H. E.; Tovar, J. D. Sequence-Dependent Mechanical, Photophysical and Electrical Properties of Pi-Conjugated Peptide Hydrogelators. *J. Mater. Chem. C* **2015**, *3* (25), 6505–6514.

(76) Ashkenasy, N.; Horne, W. S.; Reza Ghadiri, M. Design of Self-Assembling Peptide Nanotubes with Delocalized Electronic States. *Small* **2006**, *2* (1), 99–102.

(77) Wang, J.; Li, D.; Yang, M.; Zhang, Y. A Novel Ferrocene-Tagged Peptide Nanowire for Enhanced Electrochemical Glucose Biosensing. *Anal. Methods* **2014**, *6* (18), 7161–7165.

(78) Altamura, L.; Horvath, C.; Rengaraj, S.; Rongier, A.; Elouarzaki, K.; Gondran, C.; Maçon, A. L. B.; Vendrely, C.; Bouchiat, V.; Fontecave, M.; et al. A Synthetic Redox Biofilm Made from Metalloprotein–prion Domain Chimera Nanowires. *Nat. Chem.* **2017**, *9* (2), 157–163.

(79) Giltner, C. L.; Nguyen, Y.; Burrows, L. L. Type IV Pilin Proteins: Versatile Molecular Modules. *Microbiol. Mol. Biol. Rev. MMBR* **2012**, *76* (4), 740–772.

(80) Lampa-Pastirk, S.; Veazey, J. P.; Walsh, K. A.; Feliciano, G. T.; Steidl, R. J.; Tessmer, S. H.; Reguera, G. Thermally Activated Charge Transport in Microbial Protein Nanowires. *Sci. Rep.* **2016**, *6*, 23517.

(81) Walker, D. J.; Adhikari, R. Y.; Holmes, D. E.; Ward, J. E.; Woodard, T. L.; Nevin, K. P.; Lovley, D. R. Electrically Conductive Pili from Pilin Genes of Phylogenetically Diverse Microorganisms. *ISME J.* **2017**.

(82) Amit, M.; Cheng, G.; Hamley, I. W.; Ashkenasy, N. Conductance of Amyloid β Based Peptide Filaments: Structure–function Relations. *Soft Matter* **2012**, *8* (33), 8690–8696.

(83) Kalyoncu, E.; Ahan, R. E.; Olmez, T. T.; Seker, U. O. S. Genetically Encoded Conductive Protein Nanofibers Secreted by Engineered Cells. *RSC Adv.* **2017**, *7* (52), 32543–32551.

(84) Snider, R. M.; Strycharz-Glaven, S. M.; Tsoi, S. D.; Erickson, J. S.; Tender, L. M. Long-Range Electron Transport in Geobacter Sulfurreducens Biofilms Is Redox Gradient-Driven. *Proc. Natl. Acad. Sci.* **2012**, *109* (38), 15467–15472.

(85) Marrink, S. J.; Risselada, H. J.; Yefimov, S.; Tieleman, D. P.; de Vries, A. H. The MARTINI Force Field: Coarse Grained Model for Biomolecular Simulations. *J. Phys. Chem. B* **2007**, *111* (27), 7812–7824.

(86) Monticelli, L.; Kandasamy, S. K.; Periole, X.; Larson, R. G.; Tieleman, D. P.; Marrink, S.-J. The MARTINI Coarse-Grained Force Field: Extension to Proteins. *J. Chem. Theory Comput.* **2008**, *4* (5), 819–834.

CHAPTER 4 Biocatalytic Self-Assembly of Transiently Conductive Peptide-Conjugate Hybrid Nanostructures

4.1: Abstract

Aqueous compatible supramolecular materials hold promise for applications in environmental remediation, energy harvesting and biomedicine. One remaining challenge is to actively select a target structure from a multitude of possible options, while maintaining constant, physiological conditions. Here, we demonstrate the use of amino acids to actively decorate a self-assembling core molecule *in situ*, thereby controlling its amphiphilicity and consequent mode of assembly. The core molecule is the organic semiconductor naphthalene diimide, functionalized with *D*- and *L*- tyrosine methyl esters as competing reactive sites. In the presence of α-chymotrypsin and a selected encoding amino acid, kinetic competition between ester hydrolysis and amidation results in covalent or non-covalent amino acid incorporation, and variable supramolecular self-assembly pathways. Taking advantage of the semiconducting nature of the naphthalene diimide core, electronic wires could be formed and subsequently degraded, giving rise to temporally regulated electro-conductivity.

4.2: Introduction

Molecular encoded building blocks enable the assembly of supramolecular materials with precise control over shape and function. This precision enables a tremendous range of potential applications, ranging from biomedicine to energy storage and production materials[1–7]. While many groups have focused on designing and modifying supramolecular structures in their finalized equilibrium state, it is increasingly recognized that regulatory control over the kinetic aspects of assembly enables tremendous opportunities for the design of materials with

dynamic functionality[8–12]. This kinetic control enables materials with transient behavior[13–15], oscillatory behavior[16,17], self-replication[18,19], evolution-like adaption[20], and transient properties coupled to biological functionality[21]. While supramolecular design can give rise to predictable assemblies with varying structures and functions, the ability to actively change or edit the supramolecular assembly instructions (or code) in situ provides a new direction for supramolecular materials design.

Size scales, mechanical properties, and general working principles are critical parameters when attempting to interface living and non-living matter for future therapeutic and diagnostic applications[22]. Living systems are not composed of thermodynamic on/off switches. Instead, they operate by metabolic pathways composed of interconnected catalytic reactions, which in turn control and direct the formation and degradation of functional components. Incorporation of these reactions into supramolecular materials design is an active area of research[11,17,22,23], and may enable a more seamless integration with biological systems.

Peptides are a particularly versatile class of self-assembling materials[3,9,24]. It is increasingly appreciated that even short peptides (two or three amino acids) contain sufficient chemical information to drive the self-assembly of organic nanomaterials with rich sequence-dependent properties[25–29]. Furthermore, combining short peptides with non-biological functional materials, such as organic semiconductors[27,30–34], gives rise to material properties that not accessible to biological or synthetic systems alone. Kinetic aspects of peptide self-assembly can be controlled by in situ formation of self-assembling structures through (bio-) catalytic assembly[35,36]. This approach may similarly enable the in situ formation of peptide building blocks through amide bond formation reactions, either under kinetic[37,38] or thermodynamic[39] control.

We therefore attempted to catalytically incorporate a variety of amino acids around one semiconducting core functional assembly unit to explore a multitude of possible assembly pathways and dynamics (Fig. 4.1A & B). Moreover, by using activated functional precursors[13] and taking advantage of the enantioselectivity of biocatalysis reactions, we designed an assembly system with inbuilt kinetic selection and competition. This enabled a diversity of materials properties than can be actively regulated in terms of shape, composition, chirality, and function over time. We based the system on a self-assembling organic semiconductor naphthalene diimide (NDI) (Fig. 4.1A), with the objective of producing materials that display transient electronic properties in aqueous solutions[40]. Functionality in aqueous environments bears future relevance to the dynamic interfacing of electronics with biological systems.

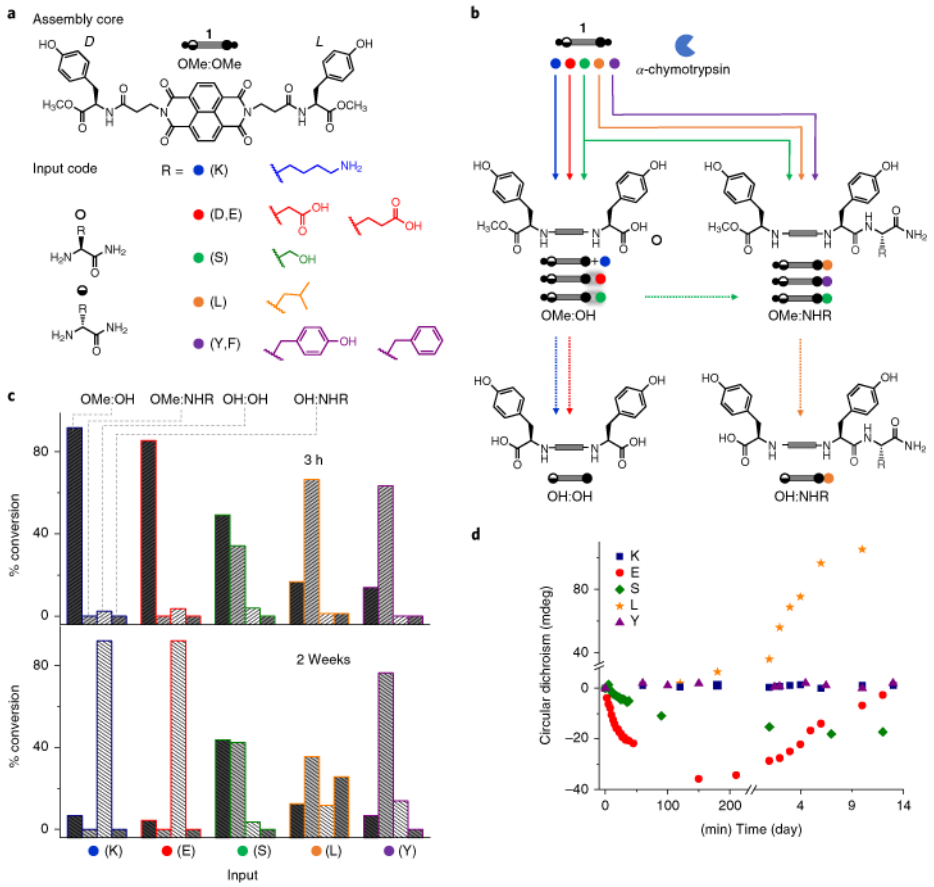

Fig. 4.1: (A) Chemical structure of *meso* molecule **1** (full spheres and half spheres represent *L*- and *D*-enantiomers, respectively) and various input amino acid amides (color-coded spheres). (B) Time-

dependent chemical transformation of **1** upon the action of α-chymotrypsin in the presence of various input amino acids (fast step: 3 h; slow step: 2 weeks) showing kinetic competition and pathway selection leading to hydrolysis or trans-acylation pathways or a combination thereof. (C) Histogram showing the formation of various chemical species by the reactions shown in (B) in the presence of specific input amino acids (top: 3 h; bottom 2 weeks). (D) Corresponding time-dependent changes in circular dichroism signal intensity demonstrating amino acid incorporation results in different helical assembly paths (circular dichroism signals were monitored at higher wavelength circular dichroism maxima of these samples).

4.3: Results and Discussion

Our active biocatalytic amino-acid-encoding approach is based on a bola-type amphiphile core with inbuilt chemical and kinetic competition of two reactive sites around an NDI moiety, through incorporation of *L*- and *D*- enantiomers of the tyrosine methyl ester on two ends. This gives rise to the *meso* structure **1** (OMe:OMe), which has no overall chirality (Fig. 4.1). We used α-chymotrypsin, an enzyme that can catalyze hydrolysis or amide bond formation reactions of the tyrosine methyl ester, which has previously been used in biocatalytic self-assembly of peptide derivatives[37,38]. α-chymotrypsin has a kinetic preference for the *L* amino acid terminus compared with the *D* terminus, thereby introducing an enantio-specific internal time delay in the system. The supramolecular assembly pathway of the system can be regulated by provision of variable encoding amino acid amides.

Depending on the chemical nature of the encoding amino acid side chains (Fig. 4.1A) and the consequent self-assembly propensity of reaction intermediates, a preference for either direct hydrolysis (OMe:OMe→OMe:OH; Fig. 4.1B) or trans-acylation to form a peptide derivative (OMe:OMe→OMe:NHR, where NHR represents peptide bond formation at the *L* terminus, as shown in Fig. 4.1B) may be expected[38]. Moreover, certain amino acids contribute via non-covalent chiral complexation, further enriching the self-assembly behavior.

We will first discuss the kinetic and chemical selection observed at the level of the covalent bond, which will be followed by a discussion of the supramolecular consequences of the formation and breakdown of these species.

Compound **1** was obtained by following a synthetic scheme described in Supporting Fig. S4.1. The first objective was to assess the enantioselective enzymatic preference for the two reactive chiral ends **1** (OMe:OMe) by high-performance liquid chromatography (HPLC), confirming that within 3 h **1** undergoes methyl ester hydrolysis on the *L* terminus (OMe:OMe→OMe:OH) followed by a slow hydrolysis on the *D* terminus over the following 2 weeks (OMe:OH→OH:OH) (Fig. 4.1b and Supporting Fig. S4.2 & S4.3), showing a nearly 100-fold difference in reaction rates on the *L* and *D* termini, thus introducing internal reaction competition. From here on, reactions occurring at the *L* terminus (3 h) and *D* terminus (2 weeks) will be referred to as 'fast' and 'slow', respectively, and *L*/*D* enantiomers are represented in italics to distinguish them from the amino acids L (leucine) and D (aspartic acid).

Next, we investigated how the supramolecular assembly pathway is influenced by incorporation of various amino acid inputs. We observed two predominant pathways, depending on the hydrophobicity of the amino acids supplied (Fig. 4.1b). In the presence of polar amino acids (lysine (K), D or glutamic acid (E)), **1** undergoes fast *L*- methyl ester hydrolysis followed by *D*- methyl ester hydrolysis, resulting in a net chemical reaction (OMe:OMe→OMe:OH→OH:OH) (Fig. 4.1c and Supporting Fig. S4.4 and S4.5). In contrast, when using hydrophobic L, peptide bond formation is favored at the *L* terminus (L–OMe:OMe→L–OMe:NHL) followed by subsequent hydrolysis of the *D*- methyl ester (L–OMe:NHL→L–OH:NHL) (Supporting Fig. S4.6). Aromatic amino acids, such as tyrosine (Y)

and phenylalanine (F) also undergo peptide bond formation; however, they do not show appreciable hydrolysis at the *D* terminus (Supporting Fig. S4.7). Serine (S), with intermediate polarity, follows a combination of both pathways resulting in formation of both S–OMe:OH and S–OMe:NHS (Supporting Fig. S4.8). Thus, we observe that the system displays biocatalytic pathway selection dictated by the chemical nature of the input amino acids, with hydrophobic amino acids favouring enzymatic acylation of the amino acid amide, resulting in peptide bond formation, and hydrophilic amino acids favoring hydrolysis, in line with previously reported selectivity for α-chymotrypsin[13,38,41].

4.3.1: Anion-Acid-Encoded Temporal Control Over Chirality

Having demonstrated the amino-acid-encoded temporal control over chemical pathway selection, we subsequently investigated the supramolecular consequences of these transformations—first, by observing supramolecular chirality. For **1** in the presence of E (**1**–E), we observed transient supramolecular chirality: a fast increase in a negative bisignated circular dichroism signal, indicating left-handed organization of NDI chromophores[42–44], followed by a slow decay to an achiral assembly (Figs. 4.1D (red curve) and 4.2B and Supporting Fig. S4.9). HPLC analysis showed that the formation and degradation of E–OMe:OH closely follows the growth and decay kinetics of the circular dichroism signal (Figs. 4.1D &4.2A (red curve)), indicating its role in governing supramolecular helicity. Notably, in the absence of an input amino acid, or in the presence of the cationic amino acid K, a similar hydrolysis pathway is observed; however, the circular dichroism spectra did not show appreciable changes (Fig. 4.1B & D (blue curve) and Supporting Fig. S4.10), demonstrating that E plays a crucial role in controlling the helicity, mainly through non-

covalent complex formation (Fig. 4.2C). Mass spectrometry analysis indeed showed the presence of species with m/z = 897.2978, corresponding to the proposed 1:1 complex between E and OMe:OH (Supporting Fig. S4.11). Furthermore, the addition of E to pre-synthesized OMe:OH demonstrated an immediate enhancement in the circular dichroism intensity, which was clearly independent of biocatalytic chiral growth kinetics (Supporting Fig. S4.12). These observations confirm that the non-covalent interactions between OMe:OH and E are responsible for the formation of a supramolecular (non-covalent) amphiphile[45], with a hydrophobic *D* terminus and hydrophilic *L* terminus (Fig. 4.2C). Upon further hydrolysis, E–OH:OH eventually forms (Fig. 4.2A), resulting in complete loss of the circular dichroism signal due to disintegration of the amphiphilic assembly. Similar observations were made with the chemically analogous D amide (Supporting Figs. S4.13 and S4.14).

The lifetime and materials properties are dictated by the kinetics of competing catalytic reactions, thus we were able to control the lifetime of **1**–E transient assembly by varying the enzyme concentration. Increasing the enzyme concentration shortened the lifetime of the chiral structures, and the formation of chiral structures could be reactivated by the subsequent addition of compound **1** (Fig. S4.15).

In contrast, the peptide bond that is formed upon exposure to the hydrophobic amino acid L leads to delayed induction of supramolecular chirality, where the observed circular dichroism signal is opposite in sign, suggesting an inversion of supramolecular chirality compared with **1**–E. No circular dichroism signal is observed during fast acylation (L–OMe:OMe→L–OMe:NHL; Figs. 4.1D and 4.3A& B), whereas during slow *D*- hydrolysis (L–OMe:NHL→L–OH:NHL), a positive bisignated circular dichroism signal emerges, indicating the formation of right-handed structures. The kinetics observed via circular dichroism map

onto the formation of L-OH:NHL species (Figs. 4.1D & 4.3A, orange data points and Supporting Figs. S4.16 and S4.17). In this case, the hydrophobic L–OMe:NHL formed during the fast phase is not sufficiently amphiphilic to give rise to a chiral structure. However, subsequent hydrolysis of the methyl ester during the slow step results in OH:NHL containing hydrophilic –COOH on the *D* terminus and hydrophobic –YL dipeptide on the *L* terminus, resulting in an amphiphilic right-handed chiral assembly. Detailed circular dichroism and linear dichroism analysis confirmed that scattering and the linear dichroism signal had only minor contributions, without impacting the overall trends described (Supporting Figs. S4.18, S4.19, & S4.20). Additionally, the introduction of the aromatic amino acids Y or F, which also followed the peptide bond formation pathway (OMe:OMe→OMe:NHY/F) did not result in a circular dichroism signal over the course of the reaction (Fig. 4.1D (purple curve) and Supporting Figs. S4.21 and S4.22), due to the lack of sufficient amphiphilicity in OMe:NHY/F and reduced enzyme access to the buried *D* terminus (not hydrolyzed; see Fig. 4.1C).

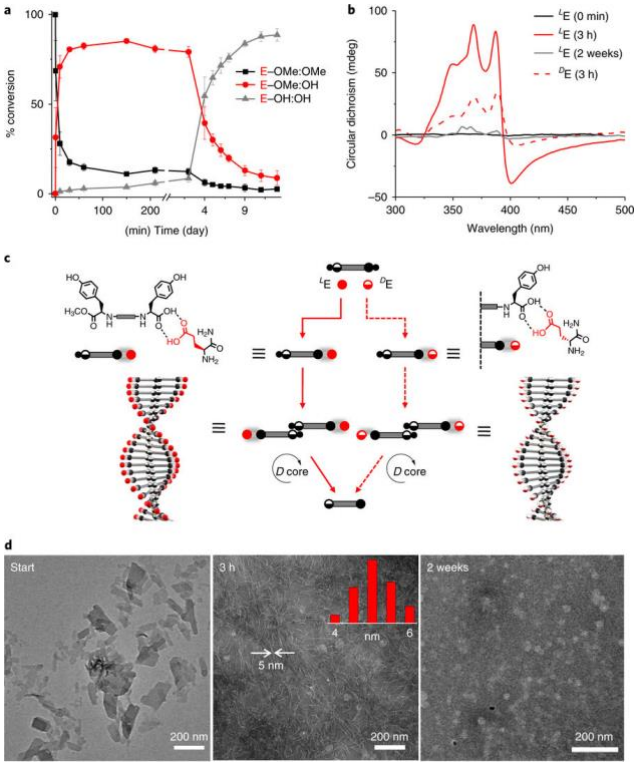

Figure 4.2: (A) HPLC analysis of **1** undergoing an enzymatic reaction in the presence of the E amide (error bars were obtained using the mean and standard deviation of measurements on three independent samples). (B) Corresponding circular dichroism spectra at various stages of assembly (0 h, 3 h and 2 weeks). The solid and dashed red spectra compare the circular dichroism signal in the presence of ^{L}E and ^{D}E. (C) Schematic representation of the amphiphilic bilayer formed with ^{L}E (red solid sphere) and ^{D}E (red half sphere), showing chemical/supramolecular pathway selection towards the formation of a left-handed helix. Also shown are the chemical structure and schematic of the corresponding helical assembly of supramolecular amphiphile formed in the presence of ^{L}E and ^{D}E by a –COOH-based dimeric structure. (D) TEM micrographs showing the sheet-like two-dimensional nanostructure of **1** changing into one-dimensional nanofibers (3 h) and, finally, disintegration to globular aggregates (2 weeks). Inset in (D): widths of 100 fibers.

4.3.2: Rationalizing Amino-Acid-Encoded Supramolecular Chirality

Having established variable, time-dependent self-assembly pathways, we subsequently rationalized the observed supramolecular chirality changes. We propose that the direction of supramolecular helicity is dictated by the position of either a *D*- or *L*- amino acid in the hydrophobic core of the assembly, with **1**–E amphiphiles giving rise to a left helix (Fig. 4.2B), due to the *D* terminus being in the core (*D*-core; Fig. 4.2C), and **1**–L resulting in a right helix

(*L*,*L* core; Fig. 4.3B & C). Thus, the direction of helicity is governed by the chirality of the amino acid present at the core of the nanostructure, which can exert stronger intermolecular interactions compared with the amino acids exposed to the solvent. This was further confirmed by control experiments using *D*- enantiomers of various amino acid inputs. Replacing the *L*- enantiomer (^{L}E) with the *D*- enantiomer (^{D}E) does not change the direction of helicity (Fig. 4.2B and Supporting Figs. S4.13 & S4.14) as the core chirality is unperturbed (Fig. 4.2C). However, changing ^{L}L (*L*-enantiomer of leucine) to ^{D}L (*D*-enantiomer of leucine) resulted in a mirror image circular dichroism signal due to the switch of chirality at the core (Fig. 4.3B & C and Supporting Fig. S4.17). The results confirm the sequence-dependent tuning of the amphiphilic structure, where molecular chirality of the input amino acid dictates helix selection.

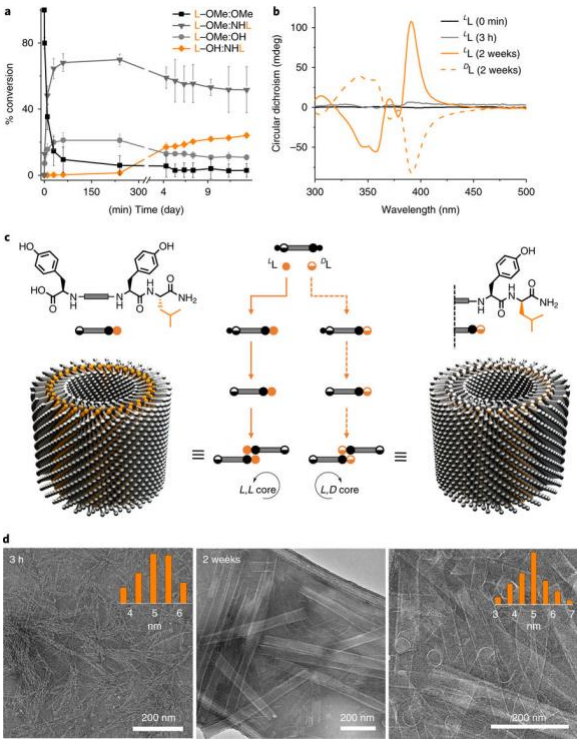

Figure 4.3: (A) HPLC analysis of **1** undergoing an enzymatic reaction with L amide (error bars were obtained using the mean and standard deviation of measurements on three independent samples). (B) Circular dichroism spectra at various stages of assembly (0 h, 3 h and 2 weeks). The solid and dashed

orange spectra compare the circular dichroism signal in the presence of ^{L}L and ^{D}L, respectively. (C) Schematic representation of the amphiphilic bilayer formed with ^{L}L and ^{D}L (full and half orange spheres, respectively) resulting in chemical/supramolecular pathway selection towards the formation of right- and left-handed helical tubes, respectively. The chemical structure and schematic of the corresponding helical assembly of amphiphilic dipeptide (OH:NHR) with ^{L}L and ^{D}L are also presented. **d**, TEM micrographs of **1**–L self-assembly showing nanofibers (3 h) and nanotubes (2 weeks). The magnified image on the right highlights the tubes' open ends. Insets in (D) fiber widths (left) and tube wall thicknesses (right) measured for 100 nanostructures. Wall thicknesses were obtained from images showing the tube openings.

4.3.3: Structural Characterization of Nanostructures

The amino-acid-encoded self-assembly was also reflected in the morphology of resultant nanostructures, as visualized by transmission electron microscopy (TEM), atomic force microscopy and confocal fluorescent microscopy (Figs. 4.2D & 4.3D and Supporting Figs. S.4.23, S4.24, & S4.25). At the start, **1**–E showed two-dimensional sheet-like nanostructures of achiral **1**. Over time, these were transformed into one-dimensional nanofibers (Fig. 4.2D). The average widths of the individual fibers were close to 5 nm, which matched the molecular dimension of the proposed bilayer packing shown in Fig. 4.2C (the molecular length of the E–OMe:OH supramolecular complex is 4.1 nm and thus the proposed interdigitated bilayer structure is expected to be around 5 nm). During the slow step, we observed disintegration of supramolecular ordering resulting in the formation of small, spherical aggregates, consistent with the loss of chirality seen in circular dichroism analysis. For **1**–L, **1** first transformed into well-defined nanofibers (Fig. 4.3D). Upon further catalytic conversion, we observed a supramolecular reconfiguration from nanofibers to tubular nanostructures, which coincided with the induction of chirality observed by circular dichroism. The wall thicknesses of these tubes were approximately 5 nm, which matched the dimension of the proposed bilayer structure shown in Fig. 4.3C (the molecular length of L–

OH:NHL is 3.0 nm and thus the proposed interdigitated bilayer structure is expected to be around 5 nm).

4.3.4: Active Encoding of Helix Chiral Inversion

Having confirmed the amino-acid-dependent chiral selection leading to the opposite helicity of **1**–E (left-handed and fast) and **1**–L (right-handed and slow), we next investigated the possibility of programming the system to access these structures sequentially, by providing both inputs at the start of the reaction, and in direct competition (Fig. 4.4A). Thus, the reaction of **1** with an optimized ratio of E (3 equivalents) and L (0.5 equivalents) resulted, first, in an increasing negative circular dichroism signal due to the formation of an E–OMe:OH left helix (Fig. 4.4B). Simultaneously, HPLC analysis confirmed the formation of OMe:NHL due to a reaction with L, but this did not contribute to the helicity, which has been shown to be silent to circular dichroism. Over time, the chiral signal decreased gradually due to two chemical conversions: (1) E–OMe:OH→E–OH:OH (left helix to racemic); and (2) L–OMe:NHL→L–OH:NHL (racemic to right helix), ultimately resulting in a reversal of circular dichroism from a negative to positive bisignated signal. The programmed supramolecular reconfiguration was also validated by the morphology change from elongated nanofibers (**1**–E) obtained in the fast step to nanotubes (**1**–L) obtained in the slow step (Fig. 4.4C). While other examples of chiral inversion through competing biocatalytic reactions have recently been described[14,15], they did not rely on the sequential incorporation of a chiral chemical structure (amino acid) into the supramolecular system.

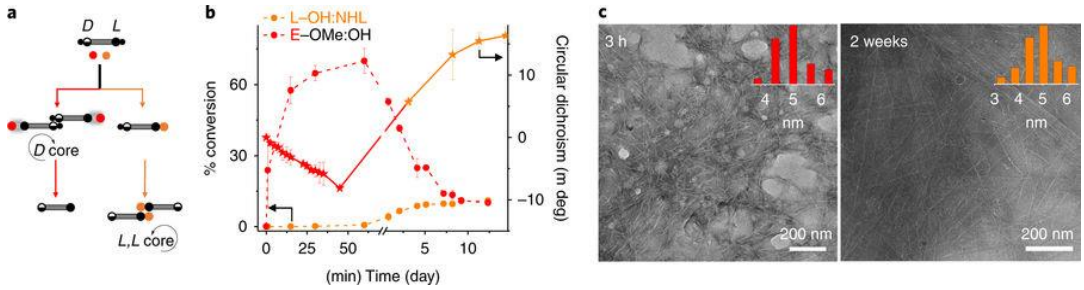

Figure 4.4: (A) Schematic representation of coordinated competition between the inputs E and L and the kinetic/chemical pathway selection resulting in differential assembly during the fast and slow steps of the reaction. (B) Variation in circular dichroism intensity showing autonomous helix evolution of **1** containing 3 eq. E and 0.5 eq. L. This is mapped with the HPLC trace of the two chiral species (E–OMe:OH and L–OH:NHL) responsible for the circular dichroism signal (the data presented for each trace are an average of three independent samples). (C) TEM micrographs after 3 h (fibers) and 2 weeks (tubes) confirming the formation of E–OMe:OH and L–OH:NHL, respectively. Insets in **c**: fiber widths (left) and tube wall thicknesses (right) measured for 100 fibers/tubes.

4.3.5: Encoding Transient Conductance

Due to the electron delocalization within semiconducting NDI and the proposed proximal stacking of NDI within the observed nanostructures, the dynamic assembly and disassembly would result in temporal control over the formation and breakdown of electronic wires, resulting in transient electronic conductance. Thus, electrical impedance spectroscopy was used to measure the time-dependent variation in conductivity. The **1**–E reaction mixture was deposited on top of an interdigitated electrode device, sealed with an inert gasket (Fig. 4.5A). The low-frequency resistance approaching direct current (DC)[46]. (*R*) was monitored as a function of time. We observed that the conductance of **1**–E increased over the course of several hours and decayed over nearly 2 weeks (Fig. 4.5B, red curve). The time-dependent conductance profile was consistent with the observed transient assembly of **1**–E from sheets to one-dimensional fibers to spherical particles and associated circular dichroism spectra (Fig. 4.2), along with HPLC changes for E–OMe-OH species (Fig. 4.5C). We propose that this fiber network bridges the interdigitated electrodes in our device, the formation and dissolution of which is responsible for the transient conductance signal. In contrast,

measurements of **1**–L (Fig. 4.5B (orange curve) and Supporting Fig. S4.26) exhibited a relatively small increase in the conductance of the solution over time, clearly distinct from the transient trend of **1**–E and similarly consistent with the observed nanostructure dynamics of **1**–L (Figs. 4.3 and 4.5C). Moreover, the conductance of the **1**–E sample could be reactivated at least twice by the subsequent addition of compound **1** into an ongoing reaction mixture (Fig. 4.3, 4.5C & D and Supporting Fig. S4.15 & S4.28). We saw a small oscillation in the circular dichroism signal after each reactivation step, and the corresponding conductance value showed a similar cycle. However, the system began to show significant dampening with each cycle due to the accumulation of waste E–OH-OH species (which also resulted in higher conductance values upon refueling, as seen in Fig. 4.5C). Thus, we have demonstrated the formation of transient fibers whose electrical conductance can be temporally modulated.

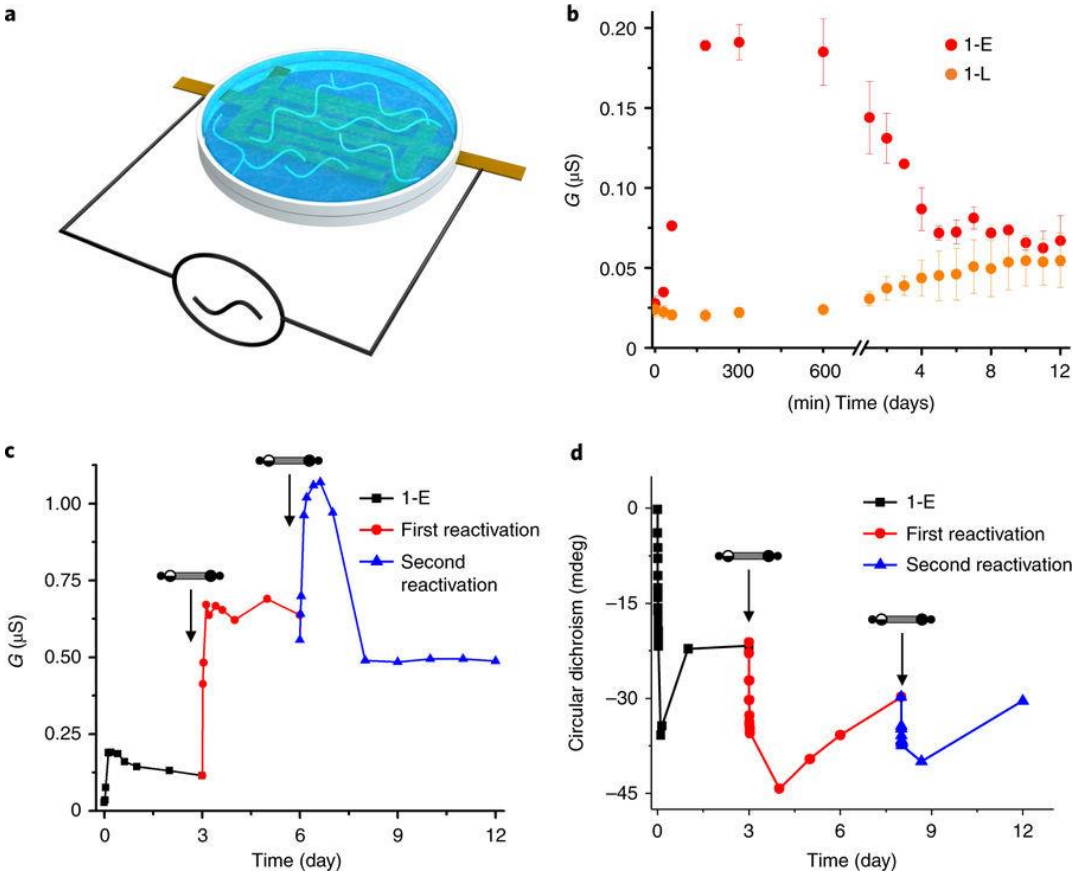

Figure 4.5: (A) Schematic of the electrochemical transport characterization device in which electrical conductivity was measured. (B) Background subtracted time-dependent conductance (*G*) of **1**–E (red curve), showing transient conductance, and **1**–L (orange curve), displaying a continuous increase, in line with their respective structural dynamics (the data presented for each trace are an average of two independent samples). Multiple reactivation of **1**–E transient conducting nanostructures as seen by time-dependent variation in the sample conductance (C) and the circular dichroism signal upon the addition of compound **1** (D) after three and six days of the reaction.

4.4: Conclusion

Rational design of supramolecular structures is becoming increasingly possible with the discovery of more rules governing the relationships between molecular structure and supramolecular properties[16]. Dynamic covalent chemistry has been used to reversibly modify chemical structures *in situ*, with the thermodynamic stability dictating the consequent materials properties changes[47,48]. More recently, reaction kinetics, as opposed to equilibrium composition, have been used to control material properties, exhibiting the potential of non-

equilibrium self-assembling systems[8]. Here, we have taken a next step that combines the *in situ* editing of molecular instructions, achieved by catalytically incorporating amino acid amides into an organic semiconductor, to control the structure and consequent function over time. While we chose to demonstrate this concept using biology's fundamental expression code (amino acids), we stress that the approach followed is not in itself biomimetic, but involves the repurposing of amino acids for use as simple instructional components for the fabrication of supramolecular materials. The approach used here provides further evidence that even single amino acids and simple peptides can encode rich and diverse self-assembly behavior.

While non-equilibrium supramolecular assembly is clearly an area of much interest[11,17,22,23], most work is still focused on structure, rather than function. Here, we demonstrate that supramolecular electronic wires can be formed and broken down on-demand. These structures may have potential applications in interfacing biological systems, such as neuronal cells or tissues, with electronics for future therapeutic and diagnostic applications. The dimensions, dynamics, and mechanical properties of the two systems need to be matched for effective bioelectronic interfacing[49]. Existing approaches to bioelectronics interfacing, such as the incorporation of conductive carbon nanotubes or graphene into nonconductive, biocompatible hydrogels, lack the dynamics of biological systems[50]

Evidently, a remaining challenge is to enhance the control over the active lifetime of the structures, as well as the conductance values observed. These metrics can respectively be improved by better controlling enzyme kinetics *via* a more hydrophilic substrate, and by substituting NDI with appropriately functionalized perylenediimide. Moreover, further

control over the *in situ* reactivation can be achieved using a continuously fueled, 'open' system[15].

In conclusion, we have demonstrated the active editing of self-assembly code in a supramolecular system, which enables regulation of structure and functionality over time. The amino acid input has a profound effect on the subsequent biocatalytic self-assembly process, resulting in either transient or delayed chiral assembly with tunable right- or left-handed nanostructures. In particular, hydrophilic amino acid input (E/D) leads to transient formation of left-handed helical fibers, whereas the hydrophobic amino acid L resulted in delayed chirality in a right-handed tubular structure. Moreover, by creating coordinated competition between two competing amino acid inputs (E and L), we demonstrated an autonomous, sequential induction and inversion of helicity (from racemic to left-handed to right-handed), demonstrating sequential programmability. Such temporal control over nanostructures was shown to demonstrate transient electronic conductivity. We foresee that these dynamic electronic properties may provide a means to effectively interface electronics and biology[50].

4.5 Supporting Information

4.5.1: Sample Material Preparation

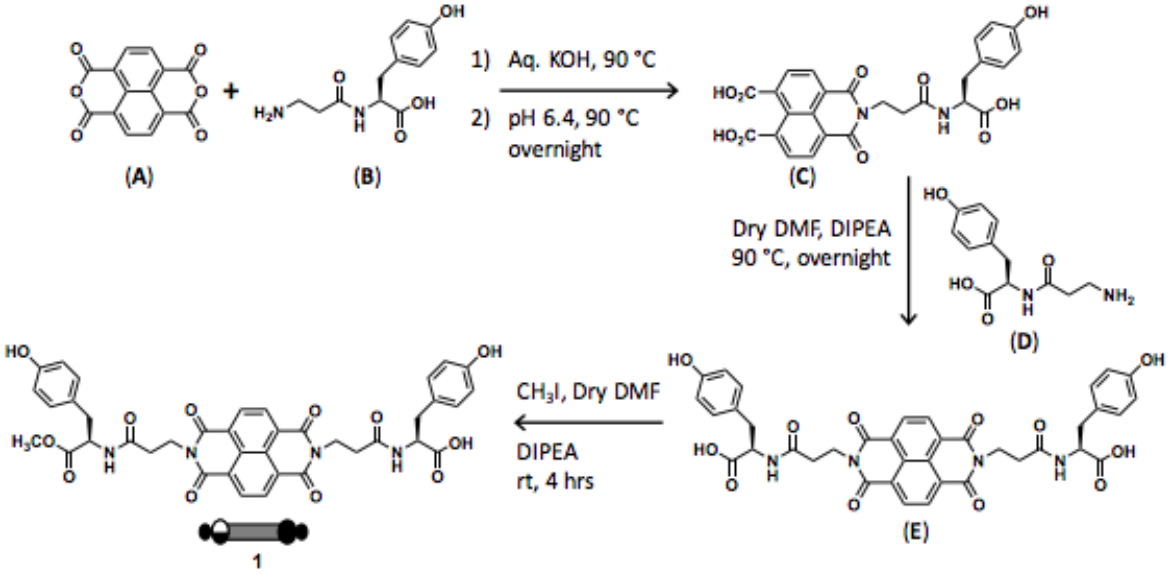

Figure S4.1: Chemical route for the synthesis of 1.

Synthesis of 1 Precursor. Synthesis of B & D (Fig S4.1B & D): This was obtained by following a literature procedure and it was accordingly characterized1 . Synthesis of C: 405 mg of A (1.5 mmol) was dissolved in 110 ml of water and 10 ml of aq. KOH solution (1M) and it was heated to 90 ºC with constant stirring. The solution was stirred for 1 hr O O O O O O O O O N N O N H O O OH N H H3CO O O HO OH O O O N N O N H O O OH N H HO O O HO OH O N HO2C HO2C O N H O O OH OH N NH2 H HO O O HO H2N N H O O OH + OH CH3I, Dry DMF DIPEA room temperature, 4 hrs 1) Aq. KOH, 90 °C 2) pH 6.4, 90 °C overnight Dry DMF, DIPEA 90 °C, overnight (A) (B) (C) (D) (E) 1 and then it was allowed to cool to room temperature. The pH of the solution was adjusted to exactly 6.4 by adding 1M aqueous H3PO4 solution. Then 390 mg (1.54 mmol) of B was added as a solid and pH was readjusted to 6.4 followed by refluxing the whole solution overnight. The solution was cooled to room temperature which resulted in some amount of precipitate which was filtered off. The obtained filtrate was acidified with 5-7 ml of

glacial Acetic acid which resulted in fresh precipitate after 5 min of stirring. The precipitate was filtered, washed with excess water and dried overnight in vacuum oven at around 50 ºC. Thus 294 mg (38% yield) of compound C was obtained. 1 H NMR (300 MHz, DMSO-d6, TMS) : δ 8.50 (d, 2H, J = 7.5 Hz), δ 8.26 (d, 1H, J = 7.8 Hz), δ 8.08 (d, 2H, J= 7.5 Hz), δ 6.98 (d, 2H, J = 8.4 Hz), δ 6.6 (d, 2H, J = 8.4 Hz), δ 4.33 (m, 1H), δ 4.18 (t, 2H, J = 7.5 Hz), δ 2.9-2.7 (m, 4H); 13C NMR (75 MHz, DMSO-d6, TMS) : δ 169.88, δ 169.2, δ 162.99, δ 155.92, δ 139.8, δ 139.6, δ 130.15, δ 130.04, δ 128.61, δ 128.36, δ 127.73, δ 125.6, δ 123.72, δ 115.03, δ 53.93, δ 36.50, δ 36.07, δ 33.15; MS (MALDI): m/z: calcd for C26H20N2O10 : 520.1 [M]+, found : 520.8. Synthesis of E (Fig. S4.1E) : 290 mg (0.56 mmol) of C and 252 mg (1 mmol) of D was dissolved in 10 ml of dry DMF and 1 ml of dry DIPEA. Then solution was stirred at 100 ºC (the reaction mixture was still turbid). After 12 hrs of stirring, the solution was cooled to room temperature and poured into ice-water mixture. The whole solution was acidified with 1 M aq. HCl solution till the precipitation completed. Dark yellow color precipitate was filtered and washed with excess of water followed by washing with cold methanol. It was dried overnight in vacuum oven at around 50 ºC and the color of the precipitate turned into brown. Thus 400 mg of compound E was obtained which still contained some solvent residue but this was used as it is for the next step. 1 H NMR (300 MHz, DMSO- d6, TMS) : δ 12.60 (broad singlet, 2H), δ 9.17 (s, 2H), δ 8.66 (s, 4H), δ 8.29 (d, 2H, J = 7.8 Hz), δ 6.97 (d, 4H, J = 7.8 Hz), δ 6.58 (d, 4H, J = 8.7 Hz), δ 4.33 (m, 2H), δ 4.21 (t, 4H, J = 6.6 Hz), δ 4.11 (q, 2H, J = 5.1 Hz), δ 3.10 (m, 2H), δ 2.88 (m, 2H), δ 2.73 (m, 2H); 13C NMR (75 MHz, DMSO-d6, TMS) : δ 173.08, δ 169.69, δ 162.54, δ 155.81, δ 130.34, δ 129.93, δ 127.62, δ 126.39, δ 126.19, δ 114.9, δ 48.59, δ 37.80, δ 37.60, δ 33.40; MS (ESI-HRMS): m/z: calculated for C38H33N4O12 : 737.2095 [M+H]+, found : 737.2070. Synthesis of 1: 200 mg (0.27 mmol) of E and 800 µl (27 mmol) of Methyl iodide (CH3I) was dissolved in 5 ml of dry DMF and 400 µl

of dry DIPEA. The reaction mixture was stirred at rt for 3 hrs. The resultant solution was poured into ice-water mixture and acidified with 1M HCl till the precipitation completed. The precipitate was filtered, washed with excess water and dried overnight in vacuum oven at around 50 ºC. Thus 171 mg (83 % yield) of compound 1 as brown solid was obtained. 1 H NMR (300 MHz, DMSO-d6, TMS) : δ 9.19 (s, 2H), δ 8.65 (s, 4H), δ 8.45 (d, 2H, J = 7.5 Hz), δ 6.96 (d, 4H, J = 8.7 Hz), δ 6.59 (d, 4H, J = 8.4 Hz), δ 4.38 (m, 2H), δ 4.21 (t, 4H, J = 7.5 Hz), δ 3.55 (s, 6H), δ 2.88-2.70 (m, 4H), δ 2.6 (m, 4H); 13C NMR (75 MHz, DMSO-d6, TMS) : δ 171.83, δ 169.52, δ 162.20, δ 155.62, δ 130.02, δ 129.60, δ 126.82, δ 126.06, δ 120.40, δ 114.68, δ 51.42, δ 30.2, δ 27.2, δ 23.4; MS (ESI-HRMS): m/z: calculated for C40H37N4O12 : 765.2409 [M+H]+, found : 765.2349.

Synthesis of 1. 200 mg (0.27 mmol) of E and 800 µl (27 mmol) of Methyl iodide (CH3I) was dissolved in 5 ml of dry DMF and 400 µl of dry DIPEA. The reaction mixture was stirred at room temperature for 3 hrs. The resultant solution was poured into ice-water mixture and acidified with 1M HCl till the precipitation completed. The precipitate was filtered, washed with excess water and dried overnight in vacuum oven at around 50 ºC. Thus 171 mg (83 % yield) of compound 1 as brown solid was obtained. 1 H NMR (300 MHz, DMSO-d6, TMS) : δ 9.19 (s, 2H), δ 8.65 (s, 4H), δ 8.45 (d, 2H, J = 7.5 Hz), δ 6.96 (d, 4H, J = 8.7 Hz), δ 6.59 (d, 4H, J = 8.4 Hz), δ 4.38 (m, 2H), δ 4.21 (t, 4H, J = 7.5 Hz), δ 3.55 (s, 6H), δ 2.88-2.70 (m, 4H), δ 2.6 (m, 4H); 13C NMR (75 MHz, DMSO-d6, TMS) : δ 171.83, δ 169.52, δ 162.20, δ 155.62, δ 130.02, δ 129.60, δ 126.82, δ 126.06, δ 120.40, δ 114.68, δ 51.42, δ 30.2, δ 27.2, δ 23.4; MS (ESI-HRMS): m/z: calcd for C40H37N4O12 : 765.2409 [M+H]+, found : 765.2349.

Synthesis of 2 Precursor. 200 mg (0.75 mmol) of A and 470 mg (1.86 mmol) of B was dissolved in 10 ml of dry DMF and 1 ml of dry DIPEA. Then solution was stirred at 100 ºC. After 15 hrs of stirring, the solution was cooled to rt and poured into ice-water mixture. The whole solution was acidified with 1M aq. HCl solution till the precipitate completed. The precipitate was filtered and washed with excess of water followed by washing with cold methanol. It was dried overnight in vacuum oven at around 50 ºC. Thus 471 mg (85 % yield) of compound F was obtained. 1 H NMR (300 MHz, DMSO-d6, TMS) : δ 9.16 (s, 2H), δ 8.66 (s, 4H), δ 8.29 (d, 2H, J = 8.1 Hz), δ 6.98 (d, 4H, J = 8.7 Hz), δ 6.59 (d, 4H, J = 8.4 Hz), δ 4.32 (m, 2H), δ 4.21 (t, 4H, J = 7.2 Hz), δ 4.09 (q, 4H, J = 5.1 Hz), δ 2.92-2.68 (m, 4H); 13C NMR (75 MHz, DMSO-d6, TMS) : δ 173.08, δ 169.68, δ 162.49, δ 155.81, δ 130.31, δ 129.93, δ 127.61, δ 126.33, δ 126.12, δ 114.89, δ 53.77, δ 36.69, δ 35.97, δ 32.99; MS (MALDI): m/z: calculated for C38H32N4O12Na : 759.191 [M+Na]+, found : 759.22.

Synthesis of 2. 100 mg (0.14 mmol) of 2 Precursor and 400 µl (14 mmol) of Methyl iodide (CH3I) was dissolved in 3 ml of dry DMF and 200 µl of dry DIPEA. The reaction mixture was stirred at rt for 3 hrs. The resultant solution was poured into ice-water mixture and acidified with 1M HCl till the precipitation completed. The precipitate was filtered, washed with excess water and dried overnight in vacuum oven at around 50 ºC. Thus 81 mg (76 % yield) of compound 2 as brown solid was obtained. 1 H NMR (300 MHz, DMSO-d6, TMS) : δ 9.21 (s, 2H), δ 8.66 (s, 4H), δ 8.45 (d, 2H, J = 7.8 Hz), δ 6.96 (d, 4H, J = 8.4 Hz), δ 6.61 (d, 4H, J = 8.4 Hz), δ 4.37 (m, 2H), δ 4.21 (t, 4H, J = 7.5 Hz), δ 3.55 (s, 6H), δ 2.87-2.70 (m, 4H), δ 2.55 (m, 4H); 13C NMR (75 MHz, DMSO-d6, TMS) : δ 172.14, δ 169.83, δ 162.51, δ 155.93, δ 130.33, δ 129.91, δ 127.13, δ 126.36,

δ 126.14, δ 114.99, δ 53.92, δ 51.74, δ 36.68, δ 35.98, δ 32.97; MS (ESI-HRMS): m/z: calculated for C40H37N4O12 : 765.2409 [M+H]+, found : 765.2391.

Synthesis of 3 Precursor. 42 mg (0.16 mmol) of A and 100 mg (0.40 mmol) of D was dissolved in 3 ml of dry DMF and 0.25 ml of dry DIPEA. Then solution was stirred at 100 ºC. After 15 hrs of stirring, the solution was cooled to rt and poured into ice-water mixture. The whole solution was acidified with 1M aq. HCl solution till the precipitate completed. The precipitate was filtered and washed with excess of water followed by washing with cold methanol. It was dried overnight in vacuum oven at around 50 ºC. Thus 60.5 mg (50 % yield) of compound F was obtained. 1 H NMR (300 MHz, DMSO-d6, TMS) : δ 9.16 (s, 2H), δ 8.66 (s, 4H), δ 8.28 (d, 2H, J = 7.8 Hz), δ 6.98 (d, 4H, J = 8.4 Hz), δ 6.59 (d, 4H, J = 8.4 Hz), δ 4.32 (m, 2H), δ 4.21 (t, 4H, J = 7.2 Hz), δ 2.92-2.68 (m, 4H), δ 2.54 (m, 4H); 13C NMR (75 MHz, DMSO-d6, TMS) : δ 173.10, δ 169.69, δ 163.32, δ 162.53, δ 155.82, δ 130.34, δ 129.95, δ 127.63, δ 126.37, δ 114.90, δ 53.79, δ 37.20, δ 39.10, δ 34.80; MS (ESI-HRMS): m/z: calculated for C38H33N4O12 : 737.2095 [M+H]+, found : 737.2074.

Synthesis of 3: 40 mg (0.05 mmol) of Sample 3 Precursor and 300 µl (14 mmol) of Methyl iodide (CH3I) was dissolved in 2 ml of dry DMF and 100 µl of dry DIPEA. The reaction mixture was stirred at room temperature for 3 hrs. The resultant solution was poured into ice-water mixture and acidified with 1M HCl till the precipitation completed. The precipitate was filtered, washed with excess water and dried overnight in vacuum oven at around 50 ºC. Thus 26 mg (63 % yield) of compound 2 as brown solid was obtained. 1 H NMR (300 MHz, DMSO-d6, TMS) : δ 9.20 (s, 2H), δ 8.64 (s, 4H), δ 8.45 (d, 2H, J = 7.8 Hz), δ 6.96 (d, 4H, J = 8.4 Hz), δ 6.60 (d, 4H,

J = 8.4 Hz), δ 4.37 (m, 2H), δ 4.21 (t, 4H, J = 7.5 Hz), δ 3.55 (s, 6H), δ 2.87-2.71 (m, 4H), δ 2.55 (m, 4H); 13C NMR (75 MHz, DMSO-d6, TMS) : δ 172.13, δ 169.83, δ 162.49, δ 155.92, δ 130.33, δ 129.91, δ 127.13, δ 126.34, δ 126.13, δ 114.99, δ 53.91, δ 51.73, δ 36.67, δ 35.98, δ 32.97; MS (ESI-HRMS): m/z: calculated for C40H37N4O12 : 765.2409 [M+H]+, found : 765.2380.

Sample Preparation. For all measurements, stock solution of **1** was prepared in dimethylsulfoxide (DMSO; 200 mM). The working concentrations of all samples for various measurements were 20 mM of **1**, 80 mM of amino acid amide and 1 mg ml^{-1} of α-chymotrypsin in 10% DMSO-90% of 100 mM phosphate buffer (pH 8). The vial containing amino acid amides and enzyme in phosphate buffer was sonicated while the required amount of DMSO stock solution of **1** was injected into the sample. This reaction mixture was then vortexed and sonicated for about 45 s before measurement. The reactivation experiment in Fig. 4.6C & D was performed by adding 0.5 eq. of **1** after 3 and 6 days such that the total concentration of NDI at the end of the experiment was 40 mM.

4.5.2: Materials Characterization

HPLC. A Dionex P780 HPLC system equipped with a Macherey Nagel C18 column (250 mm length, 4.6 mm internal diameter and 3 µm particle size) was used to quantify the enzyme-catalysed chemical conversions of **1** to various species. For the HPLC sample, 5 µl of various samples at different time points were diluted to 1 ml of acetonitrile:water (50:50) with 1.5% trifluoroacetic acid. The eluting solvent system (all solvent contained 0.1% trifluoroacetic acid; flow rate 1 ml min^{-1}) had a linear gradient of 20% (v/v) acetonitrile in water for 4 min,

which gradually increased to 80% (v/v) acetonitrile in water at 35 min and was kept constant until 40 min. Chromatograms were monitored at 214 nm and the relative areas under the peaks were used to identify the percentage product conversion. All chromatograms were normalized with respect to the total area to allow for direct comparison. HPLC for S was performed using a Phenomenex Luna OmegaC18 UHPLC 50 × 2.1 mm column.

Electron microscopy. Some 5 µl of the sample solution was drop-cast onto the continuous carbon-coated grid. Excess solution was removed by blotting the grid with filter paper, followed by two rounds of washing with water and blotting. Negative stain (5 µl of 1% aqueous methylamine vanadate (NanoVan; Nanoprobes)) was applied and blotted to remove the excess. The samples were imaged with an FEI Titan Halo TEM operating at 300 kV. Images were taken in the low-dose mode (20 e^{-} $Å^{-2}$) on an FEI Ceta 16 M camera (4,096 × 4,096 pixels). A histogram was plotted for the nanostructure dimensions obtained from the TEM images, measured for 100 nanostructures using Image J software. Each bar represents a size range of 0.5 nm.

Circular dichroism. Some 28 µl of each sample were pipetted into a 0.1 mm demountable quartz cuvette and spectra were measured on a JASCO J-1500 spectrometer with 2 s integration, a step size of 1 nm and a single acquisition with a slit width of 1 nm. A significant scattering effect in absorbance was observed because of the opacity of the samples, but the circular dichroism signal majorly remained unaffected. The temperature was maintained at 20 °C for all the measurements.

AFM. Samples were prepared by drop casting 5 µl of sample mixture on freshly cleaved mica surface (G250–2 Mica sheets 1″ × 1 ″ × 0.006″ (Agar Scientific Ltd)) followed by blotting with filter paper. Then the surface was washed with 5 µl of deionized water and blotted again to remove excess buffer salt. The surface was completely dried under vacuum. The images were obtained by scanning the mica surface in air under ambient conditions using a FastScan Microscope (Bruker) operated in ScanAsyst mode. The AFM scans were taken at a resolution of 512 × 512 pixels. The images were analysed using NanoScope Analysis software Version 1.40.

Confocal Fluorescence Imaging. Confocal imaging was performed using Zeiss LSM 880 AIRYSCAN FAST LIVE CELL instrument. Samples were stained with 1% of Thioflavin T dye and 405 nm laser was used as excitation source.

4.5.3: Electronic Property Characterization

Electrical resistance/conductance measurements in aqueous environments were performed using gold interdigitated electrodes patterned on Pyrex. Interdigitated electrodes comprised 160 parallel 5 µm wide x 2 mm long Au lines spaced 7.5 µm apart. Solid core wires were attached to the gold contact pads using silver epoxy and silver paint. An X-profile O-ring was positioned around the active area of the interdigitated electrode and sealed with silicone.

Some 10 µl of each sample was pipetted onto the interdigitated electrode area within the O-ring and the device was sealed with a glass slide clamped against the O-ring and device substrate to prevent water evaporation during the measurement (~12 days). Nail polish was used to seal the interface between the gasket and the glass slide to prevent minor leaks.

Electrical impedance spectroscopy experiments were performed in a faraday cage using a Gamry PCI4-300G potentiostat. An AC voltage oscillation of ±10 mV was applied over a range of 10 mHz to 1 MHz with a DC bias of 0 V. During the scan, the temperature in the Faraday cage was maintained at 25 °C. The impedance of each sample at 10 mV at the low-frequency plateau was recorded as the resistance approaching DC. The conductance G was obtained as $G = 1/R$.

Samples prepared in the absence of enzyme were used as a control, as they contained the conductive components yet lacked the enzyme-driven dynamics. The background charge transfer resistance of the peptide-NDI control (**1**+E or **1**+L without enzyme; Supporting Fig. S4.25) was subtracted from the sample trace to isolate the electronic behavior of the dynamic system.

4.5.4: Error Analysis

Error bars for all relevant figures were obtained using the mean and standard deviation of measurements on three independent samples (two samples for Fig. 4.5).

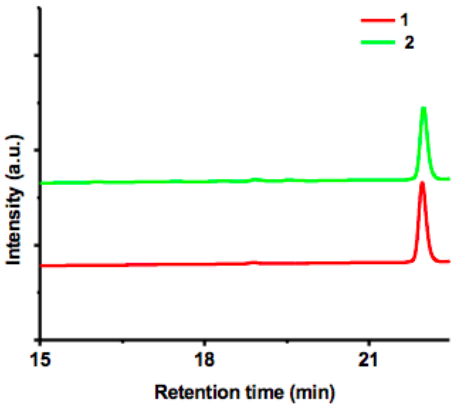

Figure S4.2: HPLC chromatogram of pristine compound 1 and 2 showing their purity.

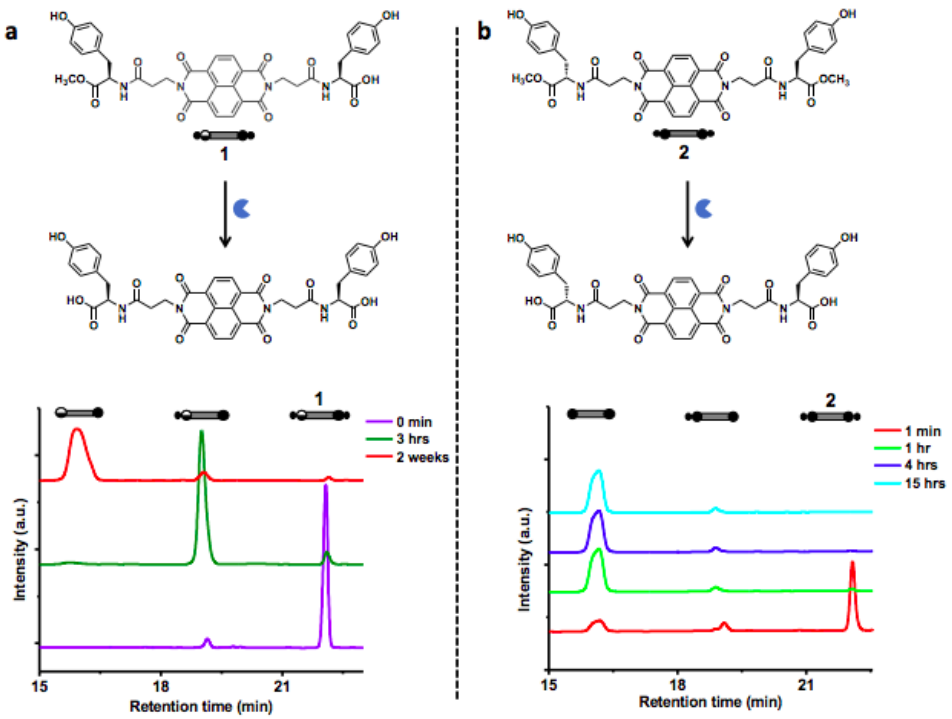

Figure S4.3: Enzymatic reaction pathway of (A) 1 and (B) 2 and corresponding time dependent HPLC chromatogram showing the evolution of various chemical species as shown schematically. We observe that for compound 2 which contains only L enantiomer of tyrosine methyl ester undergo complete hydrolysis on both terminals resulting in direct formation of OH:OH through the fast step (3 hrs). However, 1 which contains L and D enantiomer, follows a 2 step path leading to formation of OMe:OH in the fast step and OH:OH in the slow step. Slight asymmetry in the peak around 16 mins is due to the presence of various ionization state of diacid derivative OH:OH.

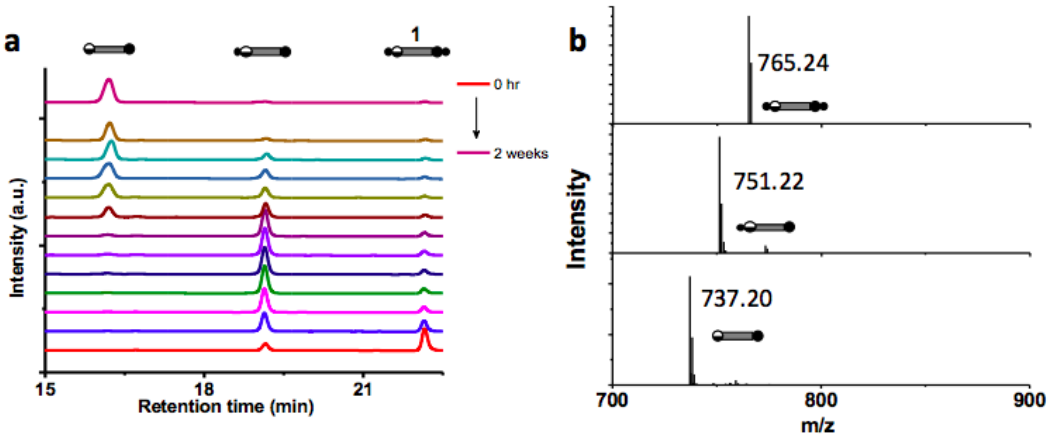

Figure S4.4: (A) Time dependent HPLC profile of 1-E in presence of 1 mg/ml of α- Chymotrypsin showing the formation of various chemical species. (B) Corresponding ESI-MS data from the HPLC fraction at different retention time confirming the formation of various species as shown schematically.

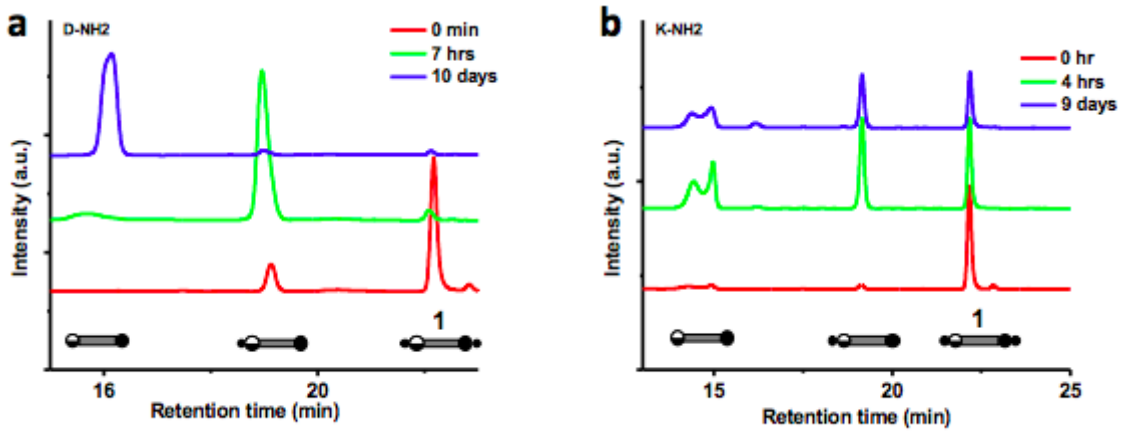

Figure S4.5: Time dependent HPLC profile of (A) 1-D and b) 1-K in presence of 1 mg/ml of α-Chymotrypsin showing the formation of various chemical species as shown schematically. This demonstrate that charged amino acid follow hydrolysis pathway. The splitting of peak around 15 min in (B) is due to different protonation state of the OH:OH and its probable non-covalent association with input KNH_2.

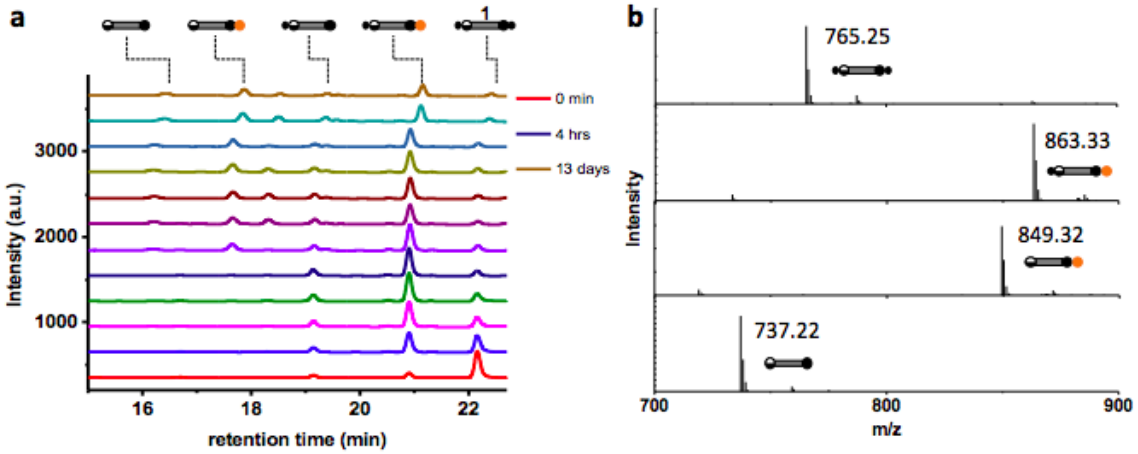

Figure S4.6: (A) Time dependent HPLC profile of 1-L in presence of 1 mg/ml of α- Chymotrypsin showing the formation of various chemical species. (B) Corresponding ESI-MS data from the HPLC fraction at different retention time confirming the formation of various species as shown schematically.

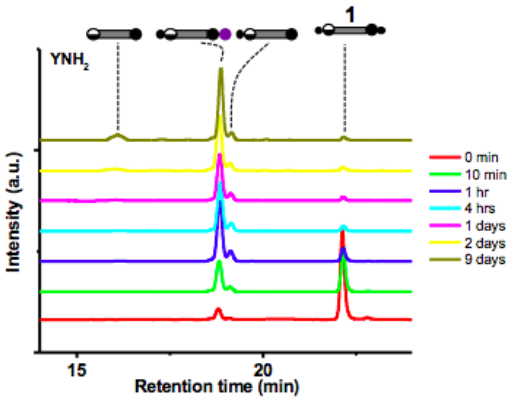

Figure S4.7: Time dependent HPLC profile of 1-Y in presence of 1 mg/ml of α- Chymotrypsin showing the formation of various chemical species as shown schematically.

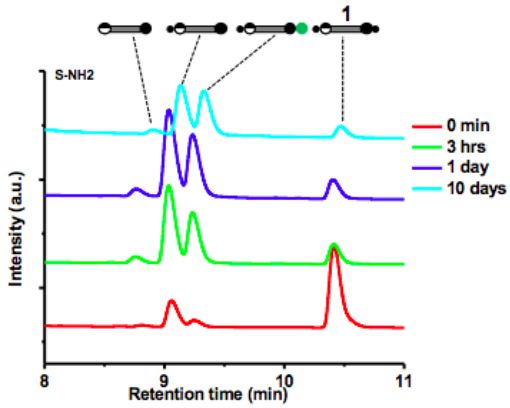

Figure S4.8: Time dependent HPLC profile of 1-S in presence of 1 mg/ml of α- Chymotrypsin showing the formation of various chemical species as shown schematically. As clear from these measurements that SNH2 follows both the hydrolysis and transacylation pathways resulting in formation of S-OMe:NHS and S-OMe-OH which do not undergo any further hydrolysis at the D terminus.

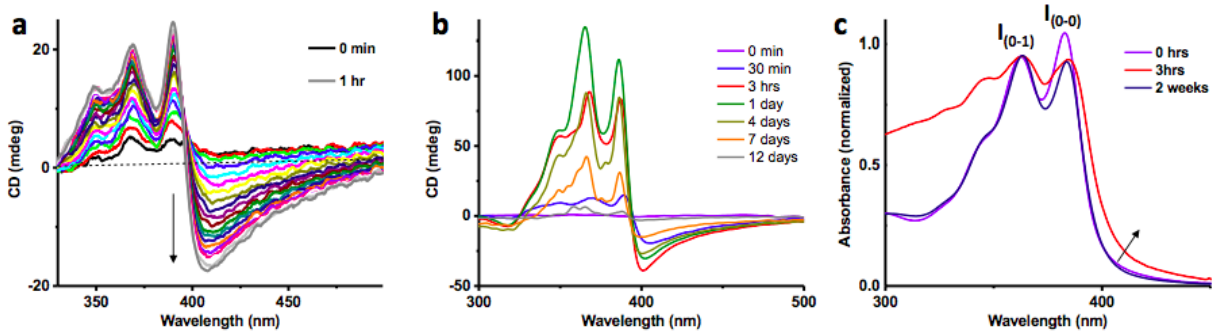

Figure S4.9: Time dependent variation in CD spectra of 1-E in presence of 1 mg/ml of α-Chymotrypsin (A) during the initial one hour, (B) during 2 weeks. We observe a negative bisignated CD signal indicating left-handed organization with excitonic coupling between NDI chromophores. (C) Variation in the absorption spectra (normalized) during different stages of biocatalytic self-assembly process. In the initial 3 hrs we see a red shift of absorption maxima (red curve) along with broadening and small red shifted aggregation peak along with intensity reversal of the ratio of vibronic bands (I0-0/I0-1) indicating strong aggregation of NDI. This is also supported by strong CD signal and formation of nanofibers. These aggregation characteristics diminishes in 2 weeks time in line with disintegration of nanostructure and loss of CD signal.

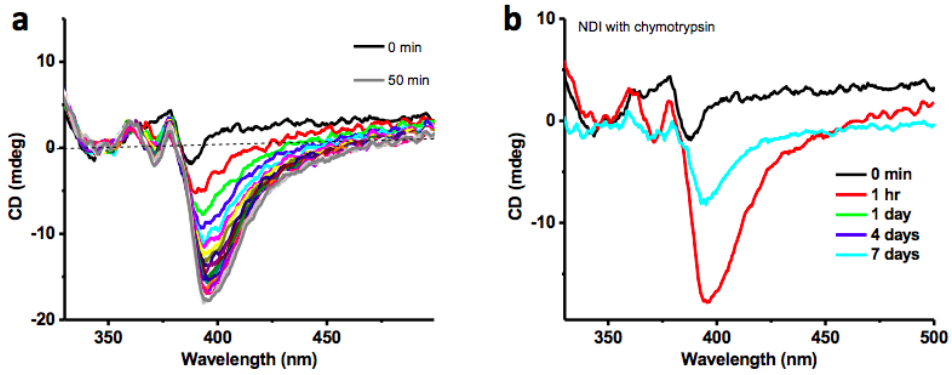

Figure S4.10: Time dependent variation in CD spectra of 1 alone in presence of 1 mg/ml of α-Chymotrypsin over (A) 50 min, (B) 1 week. We see that without any input amino acid, it gives a weak monosignated CD spectra indicating very weak chiral organization with no or weak excitonic coupling between chromophores. Moreover, these spectra are clearly distinguishable from that obtained in presence of input amino acid like 1-E or 1-L shown in Supporting Fig S.4.9 and S4.16.

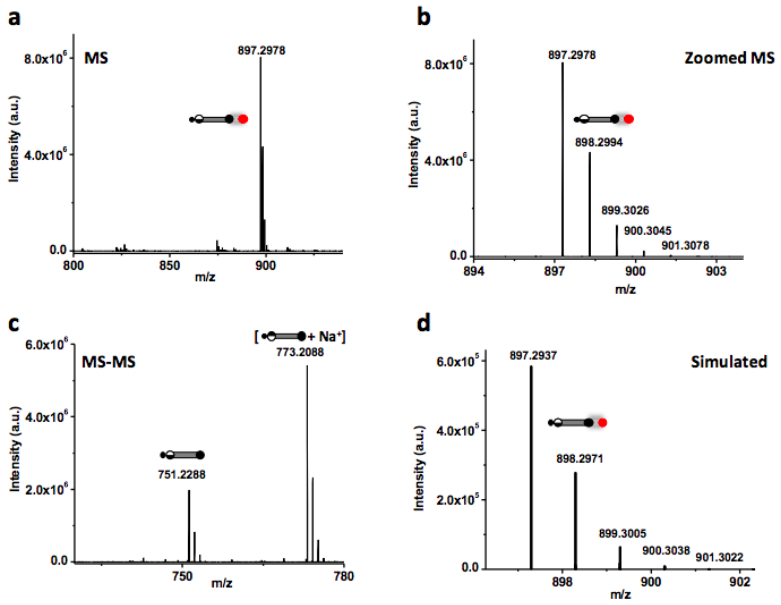

Figure S4.11: a) ESI-MS analysis of 1-E (3 hrs) sample confirming the formation of 1:1 supramolecular complex between OMe-OH and ENH2 as shown schematically. b) is the zoomed in MS portion showing the isotopic pattern, which closely match the d) simulated isotopic patter expected for the complex with chemical formula C44H45N6O15. c) is the MS-MS analysis showing the daughter species obtained from the parent 1:1 complex with m/z= 897.29.

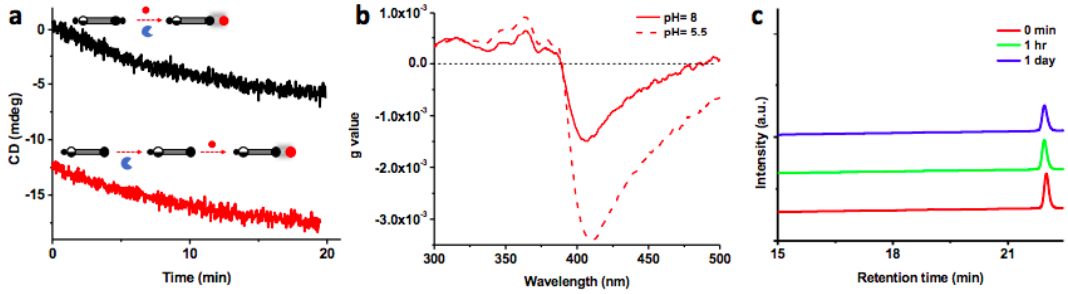

Figure S4.12: (A) Time dependent CD growth kinetics monitored at 405 nm of 1-E (black curve) in comparison with E (glutamic acid amide) added to pre-synthesized OMe:OH solution (red curve). OMe-OH was synthesized by addition of enzyme to 1 and allowing the reaction to happen for 1 hr. To this solution E was added at once and CD signal was monitored as shown in red curve. We notice that the red curve takes a jump in CD intensity at t = 0 min (12.5 mdeg) when compared to black curve starting at 0 mdeg at t = 0 min. This confirms the fact that the CD signal from E-OMe:OH is mainly due to a non-covalent interactions between OMe:OH and E, and not due to any biocatalytic reaction between the two. (B) Variation in CD spectra of E-OMe:OH at pH 8 and at acidic pH showing that signal intensity is higher at lower pH. This along with experiment in (A) confirms the existence of a -COOH based hydrogen bonded dimer formation between the -COOH of E and OMe:OH (as shown in Figure 4.2C, main text). Acidic pH enhances the population of protonated -COOH in E and OMe:OH, thereby shifting equilibrium towards -COOH dimer leading to formation of a supramolecular amphiphile with hydrophobic -OMe at the D-terminus and non-covalently linked E at the hydrophilic L- terminus. This amphiphile self-assembles to form the helical organization as seen by CD signal. (C) HPLC analysis if 1 at pH=5.5 to confirm its stability in acidic medium. We see no time dependent changes in the chemical composition confirming its stability.

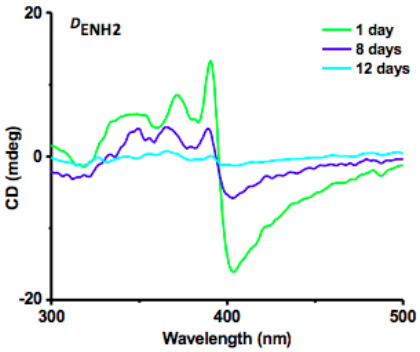

Figure S4.13: Time dependent variation in CD spectra of 1- DE (D enantiomer of glutamic acid amide) in presence of 1 mg/ml of α-Chymotrypsin during 12 days. We observe a negative bisignated CD signal during first one day, indicating left-handed organization with excitonic coupling between NDI chromophores. This also confirms the formation of transient chiral assembly as the CD intensity goes down close to zero in 12 days time.

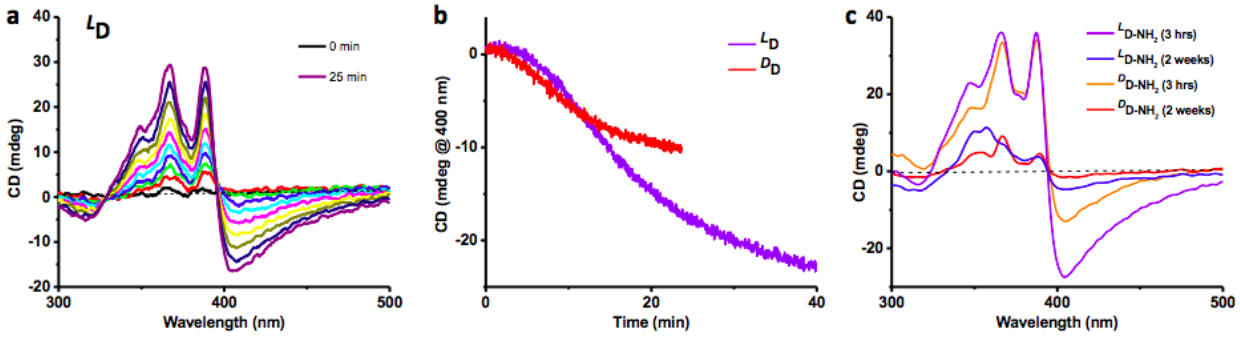

Figure S4.14: Time dependent variation in CD spectra of 1- DD (D enantiomer of aspartic acid amide) in presence of 1 mg/ml of α-Chymotrypsin (A) during the initial 25 min. (B) Plot of CD intensity at 400 nm of 1 in presence of L/D enantiomer of aspartic acid amide (L D, DD). We observe that both enantiomer results in a negative bisignated CD signal indicating lefthanded organization as is expected because of the position of these amino acid at the outside of the bilayer core (as shown in Figure 4.2C, main text). (C) shows that both enantiomer also result in transient chirality as seen by the loss of CD signal in 2 weeks time. These data are also similar to the observations made with E input confirming that both follow the same chemical and supramolecular pathway. The CD signal for DD and L D are similar but not exactly the same as they are diastereomers to each other.

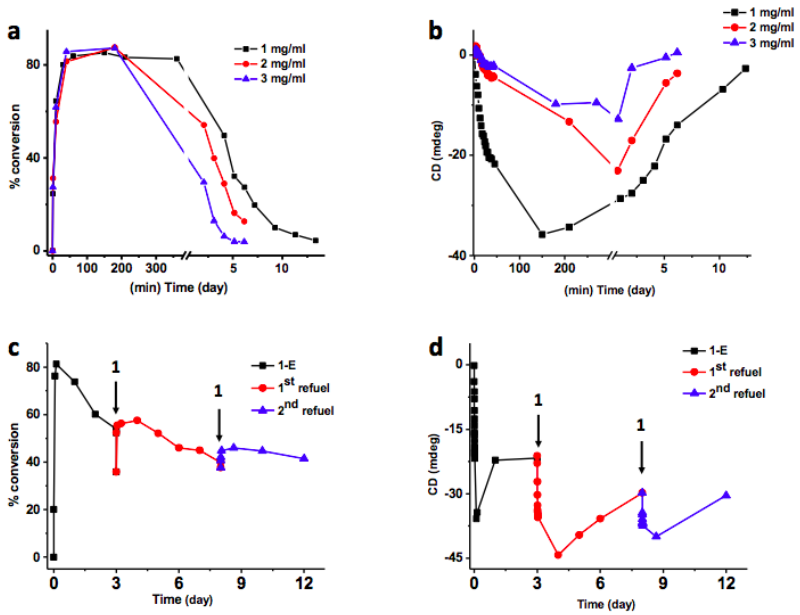

Figure S4.15: (A) Time dependent HPLC analysis of 1-E sample with varying concentration of enzyme (α-Chymotrypsin) showing the variation of E-OME:OH species. (B) is the corresponding changes in the CD signal intensity. As seen by HPLC and CD data, increase in enzyme concentration from 1mg/ml upto 3 mg/ml resulted in a shortened lifetime of the chiral structure (13 days for 1 mg/ml vs 5 days for 3mg/ml). In addition, this also results in lower CD maxima, suggesting that a faster self-assembly process may give rise to a less ordered system, as was shown previously for a related self-assembly system which was driven by chemical catalysis[48] . We notice that the sample with lower enzyme concentration has longer chiral lifetime i.e. time required to reach a CD silent state. This is also reflected in the HPLC analysis, where the chiral species (E-OME:OH) lifetime is longer with lower enzyme concentration. Although, the CD maxima also decreases at higher enzyme concentration, we believe it may be due to the loss of stereoselectivity in enzyme activity at higher enzyme concentration. Multiple refueling of 1-E sample as seen by the time dependent variation in (C) HPLC signal and (D) CD signal intensity upon addition of compound 1 after 3 days and 8 days of the reaction. We see a clear trend where the CD signal as well as the HPLC signal starts to oscillate (increase immediately after addition of 1 followed by decrease again), confirming its ability to cycle the transient assembly. Arrow indicate the time point when compound 1 was added into the sample. We observe that the signal starts to dampen in subsequent cycles due to i) waste accumulation.

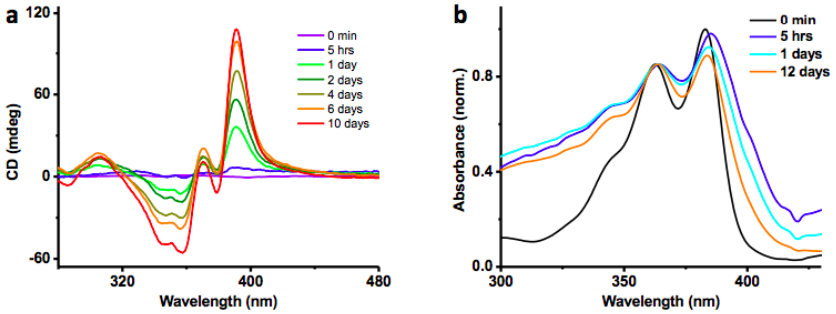

Figure S4.16: Time dependent variation in (A) CD spectra and (B) absorption spectra (normalized) of 1-L in presence of 1 mg/ml of α-Chymotrypsin during 2 weeks of reaction. We observe a positive bisignated CD signal indicating right handed organization with excitonic coupling between NDI chromophores. Normalized absorption spectra during different stages of biocatalytic self-assembly process showed a

bathochromic shift of absorption maxima (orange curve) together with broadening and small red shifted aggregation peak, change in intensity ratio of vibronic bands (I0-0/I0-1) indicating strong aggregation of NDI. This is also supported by strong CD signal and formation of nanotubes.

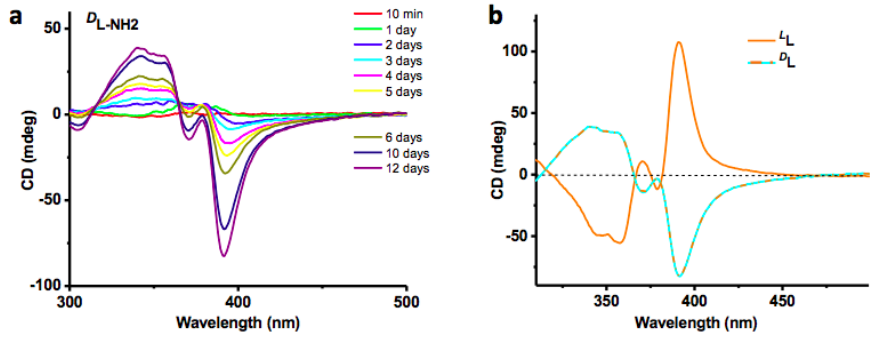

Figure S4.17: (A) Time dependent variation in CD spectra of 1- DL (D enantiomer of leucine amide) in presence of 1 mg/ml of α-Chymotrypsin during 2 weeks of reaction. We observe a negative bisignated CD signal indicating left handed helical organization with excitonic coupling between NDI chromophores. (B) Comparison of CD signal obtained in presence of D and L enantiomer of L showing mirror image CD signal. This is due to the change in chirality of the amino acid present at the core of the bilayer, from L,L core to L,D core in L L and DL respectively (shown in Figure 4.3C, main text).

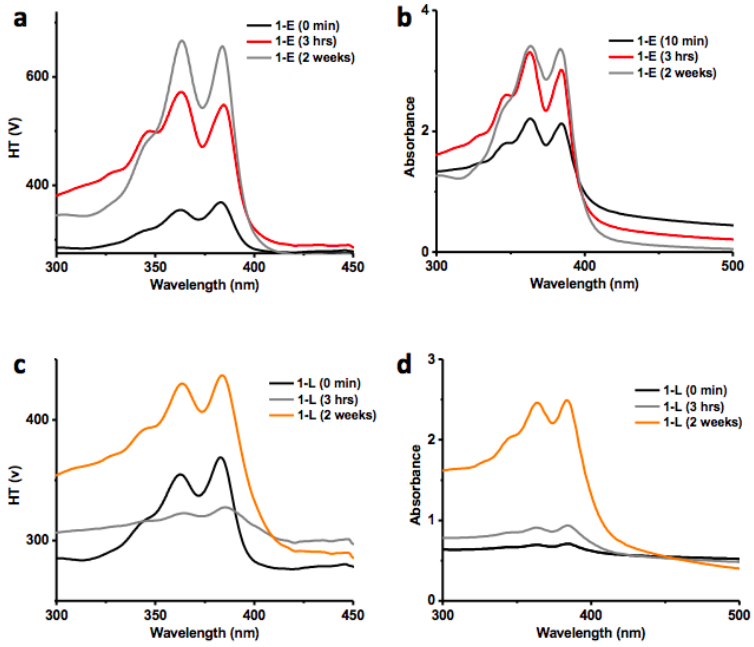

Figure S4.18: Time dependent changes in (A) High Tension (HT, obtained from CD spectroscopy) and (B) UV-vis absorption spectra of 1-E sample, whereas (C) and (D) shows the corresponding HT and UV-vis absorption spectra for 1-L samples respectively. We notice that although HT signal significantly changes with time, it is accompanied by similar changes in the absorption spectra. These changes are mainly due to changes in the self-assembly of NDI chromophores, leading to broadening and decrease in absorption spectra upon interchromophoric interactions. However, we still see a change in the scattering as indicated

by the absorption spectra at higher wavelength (450-500 nm range). These are expected because of the time dependent change in the size and self-assembled structures of 1-E and 1-L samples. To rule out if these scattering also introduce any artifact in the CD signal, we have performed concentration dependent CD measurement as shown below in Supporting Figure S4.19. We notice that upon 10 to 40 times dilution of sample concentration, both 1-E and 1-L samples show a linear trend (with very minimal deviation at higher concentration) following Beer-lambert's law also rules out any prominent effect of scattering on CD signal.

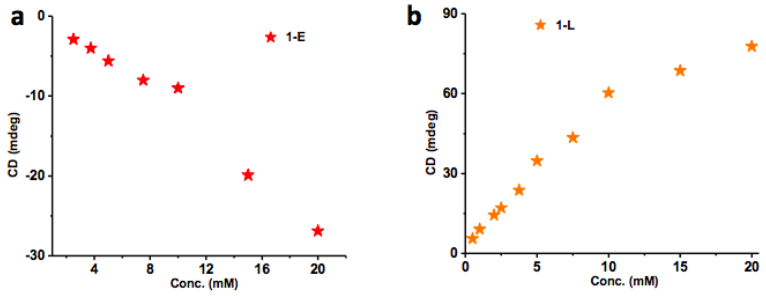

Figure S4.19: Plot of concentration dependent variation in CD intensity for (A) 1-E and (B) 1-L sample showing that 1-E data is almost linear whereas 1-L data slightly deviates from linearity at high concentration (15-20 mM). These data suggest that the CD signal is not significantly affected by the scattering based artifacts.

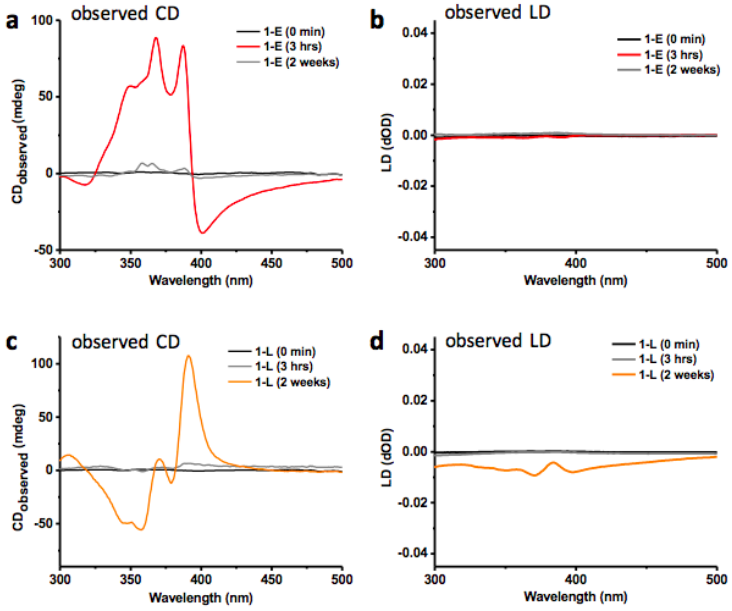

Figure S4.20: Time dependent plot of (A) observed CD spectra (B) LD spectra for 1-E sample. (C) and (D) are corresponding CD and LD spectra for 1-L sample. We clearly notice that the LD intensity is not significant. Moreover, we used the literature reported semi-empirical formula to find out the LD contribution from CD signal as $CD_{corrected} = CD_{observed} - LD_{observed} \times 0.02$[51–53].. Using this formula shows that the LD contribution to CD signal is well below 1% of the observed intensity. Moreover, the reversal of CD signal obtained upon inverting the chirality from L L to DL (Supporting Figure S4.17B) clearly confirms that the CD signal practically remains unaffected by LD.

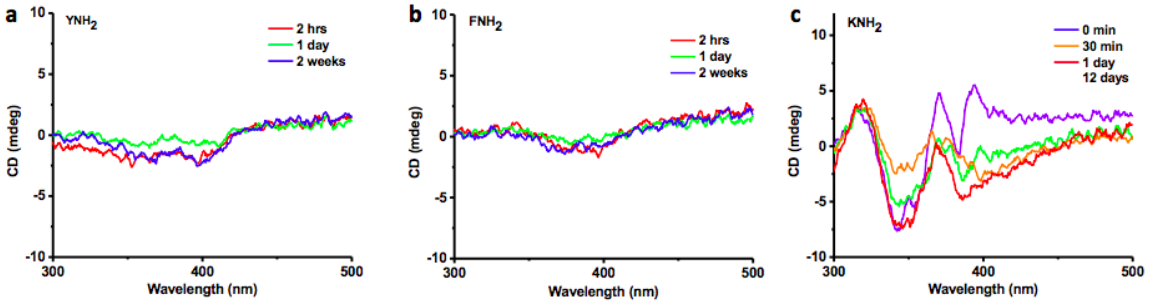

Figure S4.21: Time dependent variation in CD spectra of (A) 1-Y, (B) 1-F and (C) 1-K in presence of 1 mg/ml of α-Chymotrypsin during 2 weeks of reaction. In all 3 cases we observe no characteristic CD signal indicating lack of chiral organization.

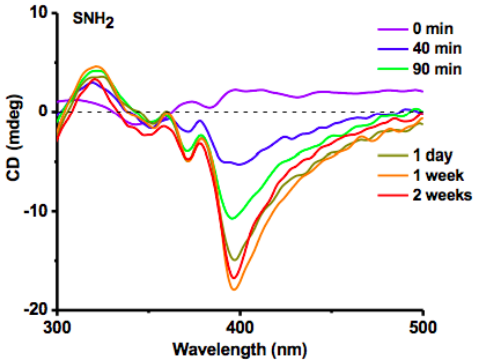

Figure S4.22: Time dependent variation in CD spectra of 1-S in presence of 1 mg/ml of α-Chymotrypsin during 2 weeks of reaction. We observe that the CD signal increases initially indicating formation of left handed helical assembly. However, the signal is stabilized after a few days without any further loss of signal. This observation is in line with the HPLC analysis (Supporting Figure S4.8) where we see that two species i.e. S-OMe:OH and S-OMe:NHS form in the fast step but there is no further hydrolysis in the slow step resulting in retention of CD signal.

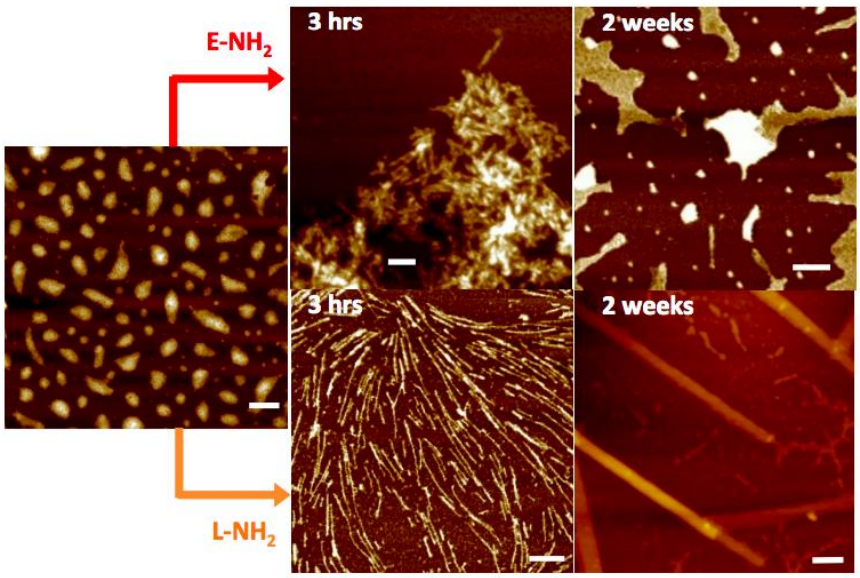

Figure S4.23: Time-dependent AFM micrographs showing catalytic self-assembly of 1-E (top) and 1-L (bottom) in presence of α-Chymotrypsin. 2-D short plates like structure of 1 converts into 1-D nanofibers (3 hrs) and then disintegrates into globular aggregates of 1-E in 2 weeks time. However, for 1-L it forms 1-D fibers in 3 hrs, which finally reconfigures into highly organized nanotubes after the slow step (2 weeks). (Scale bar= 200nm).

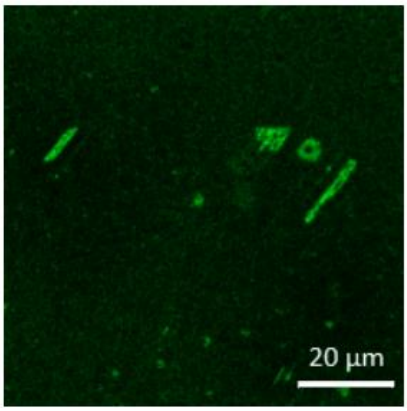

Figure S4.24: Confocal fluorescent image (405 nm excitation, 1% Thioflavin T fluorophore encapsulation). Since confocal has a limit on resolution, only the bigger structures (micrometer size) could be imaged and thus they do not match the dimensions of nanostructure imaged using TEM.

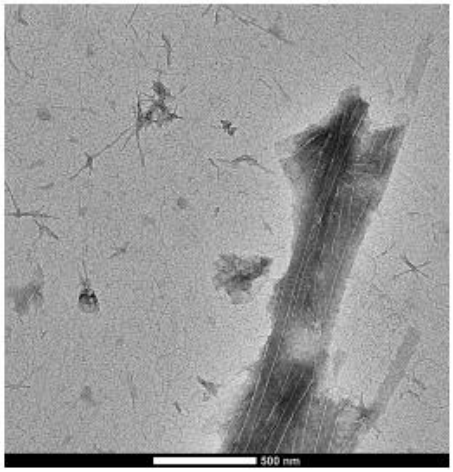

Figure S4.25: TEM micrographs of 1-L (2 weeks) sample. TEM images show the coexistence of tubes with fibers for 1-L sample after 2 weeks. In Figure 1d of main text, we observe that even after 2 weeks of reaction, 40% of L-OMe:NHL intermediate is still present in the system. Since, this intermediate form self-assembled nanofiber as seen in Figure 4.3D (1-L 3 hrs), we observe fibers along with nanotubes formed by the L-OH:NHL specie. This confirms the hypothesis that nanotubes are formed by individual self-assembly of L-OH:NHL and are not due to co-assembly with the intermediate L-OMe:NHL.

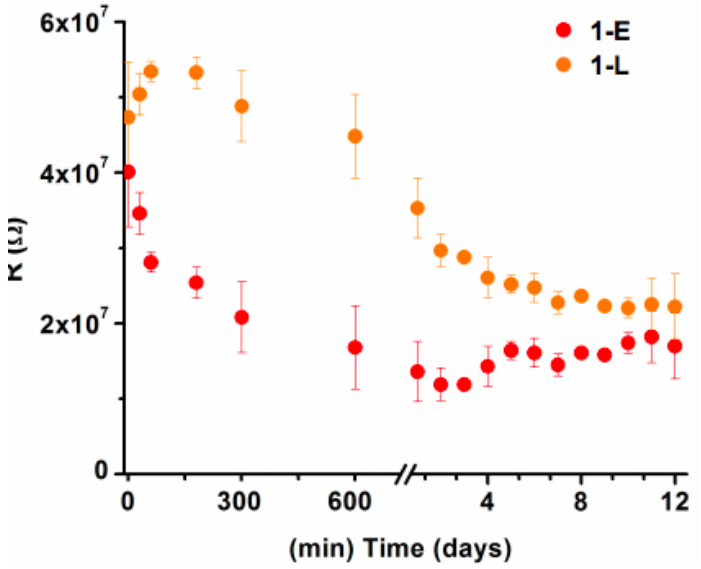

Figure S4.26: Resistance of 1-E (red) 1-L (orange) measured in electrochemical transport devices. Data are averages of n=2 samples.

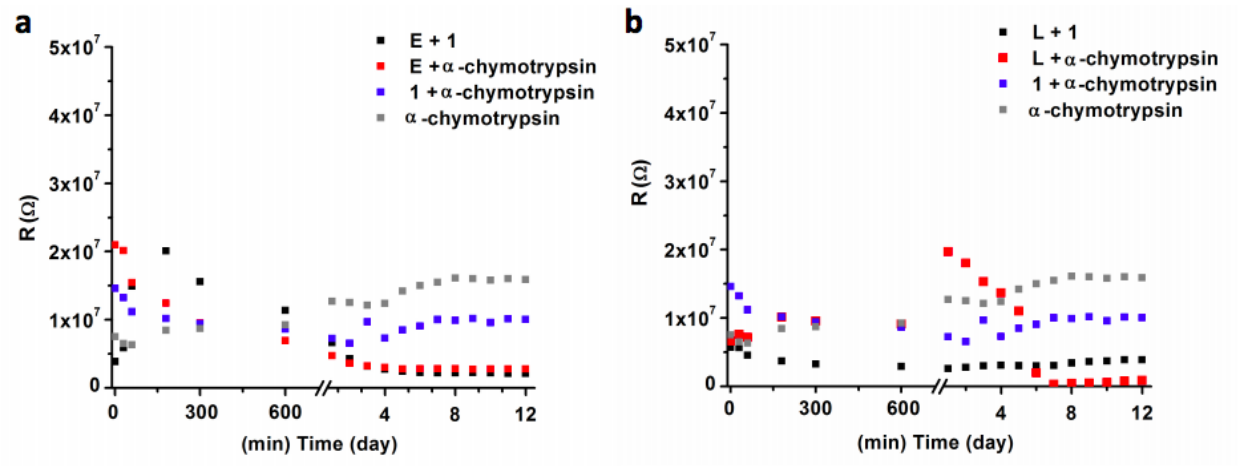

Figure S4.27: Resistance of various control samples measured in electrochemical transport devices. These controls correspond to (A) 1-E and (B) 1-L samples.

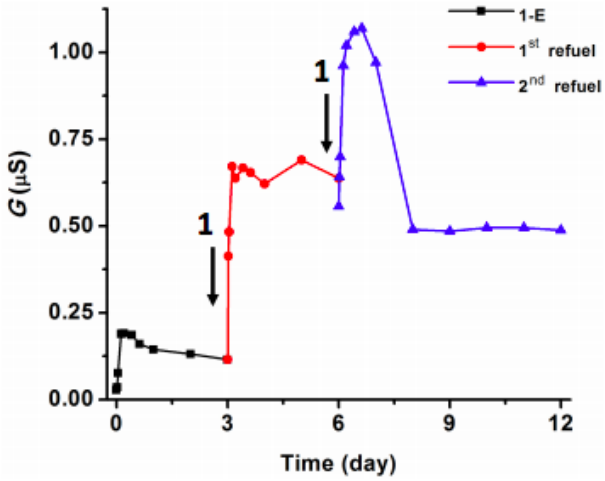

Figure S4.28: Multiple reactivation of 1-E transient conducting nanostructures as seen by the time dependent variation in sample conductance upon addition of compound 1 after 3 days and 6 days of the reaction. With each addition of 1, from the initial sample to the first refueling at 3 days and the second refueling at 6 days, we measure the same transient behavior of sample conductivity. These measurements show that the conductivity of the peptide nanostructures correlates with their transiently assembled structure. Arrows indicate the time point when compound 1 was added into the sample. We observe that the signal starts to slightly deviate from ideal oscillation in subsequent cycles and the conductivity increases with each reactivation step. This could be due to lot of waste NDI (OH:OH species) being present in the medium, which can help in better conductivity. Each Multiple reactivation of 1-E transient conducting nanostructures as seen by the time dependent variation in sample conductance upon addition of compound 1 after 3 days and 6 days of the reaction. With each addition of 1, from the initial sample to the first refueling at 3 days and the second refueling at 6 days, we measure the same transient behavior of sample conductivity. These measurements show that the conductivity of the peptide nanostructures correlates with their transiently assembled structure. Arrows indicate the time point when compound 1 was added into the sample. We observe that the signal starts to slightly deviate from ideal oscillation in subsequent cycles and

the conductivity increases with each reactivation step. This could be due to lot of waste NDI (OH:OH species) being present in the medium, which can help in better conductivity. Each refueling was done with addition of only half equivalents of compound 1 to minimize the amount of accumulated waste.

4.6: Acknowledgements

This chapter is an adaptation of the material as it appears in: Kumar, M; Ing, N.L; Narang, V; Wijerathne, N.K.; Hochbaum, A.I.; Ulijn, R.V. Amino-Acid-Encoded Biocatalytic Self-Assembly Enables the Formation of Transient Conducting Nanostructures. *Nat. Chem*. **2018**, *10*, 696-703.

The authors acknowledge staff at the Biomolecular Spectroscopy Facility for Circular Dichroism, Imaging Suite Facility and Nanofabrication Facility, all of which are part of the Advanced Science Research Center at the Graduate Center, City University of New York. The research leading to these results received funding from the US Air Force (AFOSR, grants FA9550-15-1-0192 and FA9550-014-1-0350), US Army Research Laboratory and US Army Research Office under contract/grant number W911NF-16-1-0113.

Author Contributions. M.K. and R.V.U. conceived the idea, designed and discussed the concept and experiment, and analyzed the data. M.K. performed the experimental work. N.I. and A.H. designed and performed the electronic transport measurement and analyzed the data. N.W. performed and analyzed the infrared spectroscopy (IR) measurement. V.N. performed the atomic force microscopy experiment. M.K., R.V.U., N.I. and A.H. co-wrote the paper.

4.7: References

(1) Aida, T.; Meijer, E. W.; Stupp, S. I. Functional Supramolecular Polymers. *Science* **2012**, *335* (6070), 813–817.

(2) Webber, M. J.; Appel, E. A.; Meijer, E. W.; Langer, R. Supramolecular Biomaterials. *Nat. Mater.* **2016**, *15* (1), 13–26.

(3) Zhang, S. Fabrication of Novel Biomaterials through Molecular Self-Assembly. *Nat. Biotechnol.* **2003**, *21* (10), 1171–1178.

(4) Campbell, V. E.; Hatten, X. de; Delsuc, N.; Kauffmann, B.; Huc, I.; Nitschke, J. R. Cascading Transformations within a Dynamic Self-Assembled System. *Nat. Chem.* **2010**, *2* (8), 684–687.

(5) Lehn, J.-M. From Supramolecular Chemistry towards Constitutional Dynamic Chemistry and Adaptive Chemistry. *Chem. Soc. Rev.* **2007**, *36* (2), 151–160.

(6) Whitesides, G. M.; Grzybowski, B. Self-Assembly at All Scales. *Science* **2002**, *295* (5564), 2418–2421.

(7) Zhang, W.; Jin, W.; Fukushima, T.; Saeki, A.; Seki, S.; Aida, T. Supramolecular Linear Heterojunction Composed of Graphite-like Semiconducting Nanotubular Segments. *Science* **2011**, *334* (6054), 340–343.

(8) Boekhoven, J.; Hendriksen, W. E.; Koper, G. J. M.; Eelkema, R.; van Esch, J. H. Transient Assembly of Active Materials Fueled by a Chemical Reaction. *Science* **2015**, *349* (6252), 1075–1079.

(9) Tantakitti, F.; Boekhoven, J.; Wang, X.; Kazantsev, R.; Yu, T.; Li, J.; Zhuang, E.; Zandi, R.; Ortony, J. H.; Newcomb, C. J.; et al. Energy Landscapes and Function of Supramolecular Systems. *Nat. Mater.* **2016**, *15* (4), 469–476.

(10) Maiti, S.; Fortunati, I.; Ferrante, C.; Scrimin, P.; Prins, L. J. Dissipative Self-Assembly of Vesicular Nanoreactors. *Nat. Chem.* **2016**, *8* (7), 725–731.

(11) Ashkenasy, G.; Hermans, T. M.; Otto, S.; Taylor, A. F. Systems Chemistry. *Chem. Soc. Rev.* **2017**, *46* (9), 2543–2554.

(12) Heuser, T.; Steppert, A.-K.; Molano Lopez, C.; Zhu, B.; Walther, A. Generic Concept to Program the Time Domain of Self-Assemblies with a Self-Regulation Mechanism. *Nano Lett.* **2015**, *15* (4), 2213–2219.

(13) Debnath, S.; Roy, S.; Ulijn, R. V. Peptide Nanofibers with Dynamic Instability through Nonequilibrium Biocatalytic Assembly. *J. Am. Chem. Soc.* **2013**, *135* (45), 16789–16792.

(14) Dhiman, S.; Jain, A.; George, S. J. Transient Helicity: Fuel-Driven Temporal Control over Conformational Switching in a Supramolecular Polymer. *Angew. Chem. Int. Ed Engl.* **2017**, *56* (5), 1329–1333.

(15) Sorrenti, A.; Leira-Iglesias, J.; Sato, A.; Hermans, T. M. Non-Equilibrium Steady States in Supramolecular Polymerization. *Nat. Commun.* **2017**, *8*.

(16) Semenov, S. N.; Wong, A. S. Y.; van der Made, R. M.; Postma, S. G. J.; Groen, J.; van Roekel, H. W. H.; de Greef, T. F. A.; Huck, W. T. S. Rational Design of Functional and Tunable Oscillating Enzymatic Networks. *Nat. Chem.* **2015**, *7* (2), 160–165.

(17) Epstein, I. R.; Xu, B. Reaction–diffusion Processes at the Nano- and Microscales. *Nat. Nanotechnol.* **2016**, *11* (4), 312–319.

(18) Carnall, J. M. A.; Waudby, C. A.; Belenguer, A. M.; Stuart, M. C. A.; Peyralans, J. J.-P.; Otto, S. Mechanosensitive Self-Replication Driven by Self-Organization. *Science* **2010**, *327* (5972), 1502–1506.

(19) Chen, C.; Tan, J.; Hsieh, M.-C.; Pan, T.; Goodwin, J. T.; Mehta, A. K.; Grover, M. A.; Lynn, D. G. Design of Multi-Phase Dynamic Chemical Networks. *Nat. Chem.* **2017**, *9* (8), 799–804.

(20) Sadownik, J. W.; Mattia, E.; Nowak, P.; Otto, S. Diversification of Self-Replicating Molecules. *Nat. Chem.* **2016**, *8* (3), 264–269.

(21) Feng, Z.; Wang, H.; Zhou, R.; Li, J.; Xu, B. Enzyme-Instructed Assembly and Disassembly Processes for Targeting Downregulation in Cancer Cells. *J. Am. Chem. Soc.* **2017**, *139* (11), 3950–3953.

(22) Grzybowski, B. A.; Huck, W. T. S. The Nanotechnology of Life-Inspired Systems. *Nat. Nanotechnol.* **2016**, *11* (7), 585–592.

(23) Mattia, E.; Otto, S. Supramolecular Systems Chemistry. *Nat. Nanotechnol.* **2015**, *10* (2), 111–119.

(24) Ghadiri, M. R.; Granja, J. R.; Milligan, R. A.; McRee, D. E.; Khazanovich, N. Self-Assembling Organic Nanotubes Based on a Cyclic Peptide Architecture. *Nature* **1993**, *366* (6453), 324–327.

(25) Reches, M.; Gazit, E. Casting Metal Nanowires Within Discrete Self-Assembled Peptide Nanotubes. *Science* **2003**, *300* (5619), 625–627.

(26) Du, X.; Zhou, J.; Shi, J.; Xu, B. Supramolecular Hydrogelators and Hydrogels: From Soft Matter to Molecular Biomaterials. *Chem. Rev.* **2015**, *115* (24), 13165–13307.

(27) Fleming, S.; Ulijn, R. V. Design of Nanostructures Based on Aromatic Peptide Amphiphiles. *Chem. Soc. Rev.* **2014**, *43* (23), 8150–8177.

(28) Gazit, E. Self-Assembled Peptide Nanostructures: The Design of Molecular Building Blocks and Their Technological Utilization. *Chem. Soc. Rev.* **2007**, *36* (8), 1263–1269.

(29) Draper, E. R.; Adams, D. J. Low-Molecular-Weight Gels: The State of the Art. *Chem* **2017**, *3* (3), 390–410.

(30) Sanders, A. M.; Magnanelli, T. J.; Bragg, A. E.; Tovar, J. D. Photoinduced Electron Transfer within Supramolecular Donor–Acceptor Peptide Nanostructures under Aqueous Conditions. *J. Am. Chem. Soc.* **2016**, *138* (10), 3362–3370.

(31) Draper, E. R.; Walsh, J. J.; McDonald, T. O.; Zwijnenburg, M. A.; Cameron, P. J.; Cowan, A. J.; Adams, D. J. Air-Stable Photoconductive Films Formed from Perylene Bisimide Gelators. *J. Mater. Chem. C* **2014**, *2* (28), 5570–5575.

(32) Faramarzi, V.; Niess, F.; Moulin, E.; Maaloum, M.; Dayen, J.-F.; Beaufrand, J.-B.; Zanettini, S.; Doudin, B.; Giuseppone, N. Light-Triggered Self-Construction of Supramolecular Organic Nanowires as Metallic Interconnects. *Nat. Chem.* **2012**, *4* (6), 485–490.

(33) Xu, H.; Das, A. K.; Horie, M.; Shaik, M. S.; Smith, A. M.; Luo, Y.; Lu, X.; Collins, R.; Liem, S. Y.; Song, A.; et al. An Investigation of the Conductivity of Peptide Nanotube Networks Prepared by Enzyme-Triggered Self-Assembly. *Nanoscale* **2010**, *2* (6), 960–966.

(34) Nalluri, S. K. M.; Berdugo, C.; Javid, N.; Frederix, P. W. J. M.; Ulijn, R. V. Biocatalytic Self-Assembly of Supramolecular Charge-Transfer Nanostructures Based on n-Type Semiconductor-Appended Peptides. *Angew. Chem. Int. Ed.* **2014**, *53* (23), 5882–5887.

(35) Trausel, F.; Versluis, F.; Maity, C.; Poolman, J. M.; Lovrak, M.; van Esch, J. H.; Eelkema, R. Catalysis of Supramolecular Hydrogelation. *Acc. Chem. Res.* **2016**, *49* (7), 1440–1447.

(36) Yang Z.; Gu H.; Fu D.; Gao P.; Lam J. K.; Xu B. Enzymatic Formation of Supramolecular Hydrogels. *Adv. Mater.* **2006**, *18* (5), 545–545.

(37) Qin, X.; Xie, W.; Tian, S.; Cai, J.; Yuan, H.; Yu, Z.; Butterfoss, G. L.; Khuong, A. C.; Gross, R. A. Enzyme-Triggered Hydrogelation via Self-Assembly of Alternating Peptides. *Chem. Commun.* **2013**, *49* (42), 4839–4841.

(38) Pappas, C. G.; Sasselli, I. R.; Ulijn, R. V. Biocatalytic Pathway Selection in Transient Tripeptide Nanostructures. *Angew. Chem. Int. Ed Engl.* **2015**, *54* (28), 8119–8123.

(39) Pappas, C. G.; Shafi, R.; Sasselli, I. R.; Siccardi, H.; Wang, T.; Narang, V.; Abzalimov, R.; Wijerathne, N.; Ulijn, R. V. Dynamic Peptide Libraries for the Discovery of Supramolecular Nanomaterials. *Nat. Nanotechnol.* **2016**, *11* (11), 960–967.

(40) Ardoña, H. A. M.; Tovar, J. D. Peptide π-Electron Conjugates: Organic Electronics for Biology? *Bioconjug. Chem.* **2015**, *26* (12), 2290–2302.

(41) Gololobov, M. Y.; Voyushina, T. L.; Stepanov, V. M.; Adlercreutz, P. Nucleophile Specificity in α-Chymotrypsin- and Subtilisin-(Bacillus Subtilis Strain 72) Catalyzed Reactions. *Biochim. Biophys. Acta BBA - Protein Struct. Mol. Enzymol.* **1992**, *1160* (2), 188–192.

(42) Harada, N.; Nakanishi, K. Exciton Chirality Method and Its Application to Configurational and Conformational Studies of Natural Products. *Acc. Chem. Res.* **1972**, *5* (8), 257–263.

(43) Kumar, M.; Brocorens, P.; Tonnelé, C.; Beljonne, D.; Surin, M.; George, S. J. A Dynamic Supramolecular Polymer with Stimuli-Responsive Handedness for in Situ Probing of Enzymatic ATP Hydrolysis. *Nat. Commun.* **2014**, *5*, 5793.

(44) Gawroński Jacek; Brzostowska Małgorzata; Kacprzak Karol; Kołbon Halina; Skowronek Paweł. Chirality of Aromatic Bis-imides from Their Circular Dichroism Spectra. *Chirality* **2000**, *12* (4), 263–268.

(45) Wang, C.; Wang, Z.; Zhang, X. Amphiphilic Building Blocks for Self-Assembly: From Amphiphiles to Supra-Amphiphiles. *Acc. Chem. Res.* **2012**, *45* (4), 608–618.

(46) Rahman, A. R. A.; Justin, G.; Guiseppi-Elie, A. Bioactive Hydrogel Layers on Microdisk Electrode Arrays: Impedimetric Characterization and Equivalent Circuit Modeling. *Electroanalysis* **2009**, *21* (10), 1135–1144.

(47) Sun, H.; Kabb, C. P.; Dai, Y.; Hill, M. R.; Ghiviriga, I.; Bapat, A. P.; Sumerlin, B. S. Macromolecular Metamorphosis via Stimulus-Induced Transformations of Polymer Architecture. *Nat. Chem.* **2017**, *9* (8), 817–823.

(48) Boekhoven, J.; Poolman, J. M.; Maity, C.; Li, F.; Mee, L. van der; Minkenberg, C. B.; Mendes, E.; Esch, J. H. van; Eelkema, R. Catalytic Control over Supramolecular Gel Formation. *Nat. Chem.* **2013**, *5* (5), 433–437.

(49) Zhang, A.; Lieber, C. M. Nano-Bioelectronics. *Chem. Rev.* **2016**, *116* (1), 215–257.

(50) Marchesan, S.; Ballerini, L.; Prato, M. Nanomaterials for Stimulating Nerve Growth. *Science* **2017**, *356* (6342), 1010–1011.

(51) Ohira, A.; Okoshi, K.; Fujiki, M.; Kunitake, M.; Naito, M.; Hagihara, T. Versatile Helical Polymer Films: Chiroptical Inversion Switching and Memory with Re-Writable (RW) and Write-Once Read-Many (WORM) Modes. *Adv. Mater.* **2004**, *16* (18), 1645–1650.

(52) Tsuda, A.; Alam, M. A.; Harada, T.; Yamaguchi, T.; Ishii, N.; Aida, T. Spectroscopic Visualization of Vortex Flows Using Dye-Containing Nanofibers. *Angew. Chem. Int. Ed.* **2007**, *46* (43), 8198–8202.

(53) Porcel, C.; Lavalle, P.; Decher, G.; Senger, B.; Voegel, J.-C.; Schaaf, P. Influence of the Polyelectrolyte Molecular Weight on Exponentially Growing Multilayer Films in the Linear Regime. *Langmuir* **2007**, *23* (4), 1898–1904.

CHAPTER 5 Electrical Conductivity and Biocompatibility in Bacteria-Inspired Nanofibers with Au Nanoparticles

5.1: Abstract

Bacterial type IV pili (T4P) are multifunctional protein nanofibers. A reductionist approach allowed for the formation of T4P-like nanofibers from self-assembling 20-mer designed peptide building blocks, derived from the sequence of a metal-binding T4P. Here, we determine the 20-mer structure in atomic resolution and investigate the ability of its nanofibers to interact with metal-containing moieties to form nanocomposites. We show that similarly to their native counterparts, the peptide nanofibers efficiently bind metal oxides and metal ions. Reduction of ionic Au by the nanofibers led to their exceptionally dense decoration by Au nanoparticles (AuNP), which conferred increased physicochemical stability and electrical conductivity from the single-fiber level up. The peptide-AuNP nanocomposite additionally presented substrate-selective adhesion, which enabled the formation of reusable catalytic coating or self-supporting immersible films of desired shapes. The films provided excellent support for cardiac cells and were also used for sensing electrostatic charge. This study presents a novel T4P-inspired biometallic material.

5.2: Introduction

Bacterial type IV pili (T4P) are an abundant class of supramolecular nanofibers composed mainly of pilin protein monomers[1]. In the metal-reducing species *Geobacter sulfurreducens* (GS), T4P facilitate physical contact with and subsequent electron transfer to metal species, such as Fe(III) oxide-containing minerals[2] and U ions[3]. The molecular underpinnings of this interaction are unknown, as is the exact structure of the GS T4P[4], yet it appears that the physical contact is mediated by the evolutionary-variable polar C-terminal region of the GS pilin monomer[5]. This is

in line with the fact that the C-terminal region of homologous pilins is solvent-exposed and interacts with the molecular environment, whereas the N-terminal region is related to their *in vivo* assembly and forms the hydrophobic pilus core[6,7].

Synthetic peptide mimetics of GS T4P are envisioned as a useful class of bioinspired materials[8]. Recently, we reported the formation of T4P-like nanofibers by a self-assembling minimalistic peptide building blocks derived from the pilin sequence of GS[9]. Due to the inherent propensity of native GS T4P to interact with metal oxide particles and metal ions, we hypothesized that a similar interaction would occur between these moieties and the T4P-like nanofibers, leading to their efficient decoration. Although a large variety of self-assembled protein[10–19] or peptide[20–26]. filaments have been decorated by such species previously, substantial decoration at the single nanofilament level typically requires multistep processes or various additives. Here, we show that the T4P-like peptide nanofibers efficiently bind metal and non-metal oxide particles by simple co-incubation. The nanofibers also reduce ionic Au in a single-step, additive-free process that led to their exceptionally dense decoration by gold nanoparticles (AuNP). Unexpectedly, the thus-formed peptide nanofiber-AuNP composite presented electrical conductivity from the single-nanofiber level up and substrate-selective adhesion. Utilizing these properties, we show that coatings and self-supporting films of desired shapes can be easily prepared from this composite and used in chemical catalysis, electrostatic charge sensing, and cardiac tissue scaffolding applications.

5.3: Results and Discussion

5.3.1: Binding of Oxides to Peptide Nanofibers

GS T4P natively interact with Fe(III) oxide. To test for this in the studied peptide nanofibers, potassium phosphate dispersions of Fe(III) oxide nanoparticle were incubated in the

presence or absence of pre-formed nanofibers. While the dispersion of nanoparticles alone retained its macroscopic homogeneity during a period of 3 hours, a sedimenting floccule was observed in the nanofiber-supplemented (0.075 volume fraction) nanoparticle dispersion, and the liquid bulk become transparent, similarly to an equivalent control dispersion of the nanofibers alone (Fig. 5.1A). UV-Vis spectra of the liquid bulks showed significant optical density (OD) reduction in the nanofibers-supplemented condition as compared with the nanoparticles-alone control, resulting in a similar spectrum to that acquired from the nanofibers-alone control (Fig. 5.1B). Complementing transmission electron microscopy (TEM) imaging of the floccule revealed a network of nanofibers decorated with Fe(III) oxide nanoparticles (Fig. 5.1C, pristine nanofibers and oxide are shown for comparison in Supporting Fig. S5.1), suggesting that the peptide nanofibers can bind Fe(III) oxide. Similar results were obtained when Fe(III) oxide nanoparticles were substituted with ZnO or TiO_2 nanoparticles, or with the non-metallic SiO_2 nanoparticles and graphene oxide (GO) flakes (Fig. 5.1, pristine oxides are shown in Supporting Fig. S5.1). Hence, the nanofibers present a general capability of binding oxide materials. This capability can be rationalized as the result of electrostatic attraction, since under the experimental conditions the oxides acquired a negative charge, as expected[27,28], whereas the nanofibers were positively-charged, as was evident by their respective electrophoretic mobilities (Fig. 5.1D). The C-terminal region of native GS pilin, which is presumed to be solvent-exposed, includes four negatively-charged and four positively-charged amino acids. It was shown that denying a negatively-charged glycerophosphate modification of a tyrosine in this region enhanced bacterial attachment to Fe(III) oxide[5], suggesting that a more positive charge of the native fibers favors this interaction. As our bioinspired 20-mer peptide includes two of the positively-charged and none of the negatively-charged amino acids of the GS pilin C-terminal region, it possesses a net positive charge at near-neutral pH, which can facilitate

binding of its nanofiber assemblies to oxides. The peptide nanofibers therefore appear useful for the immobilization of oxide materials, as required in various applications[29–31].

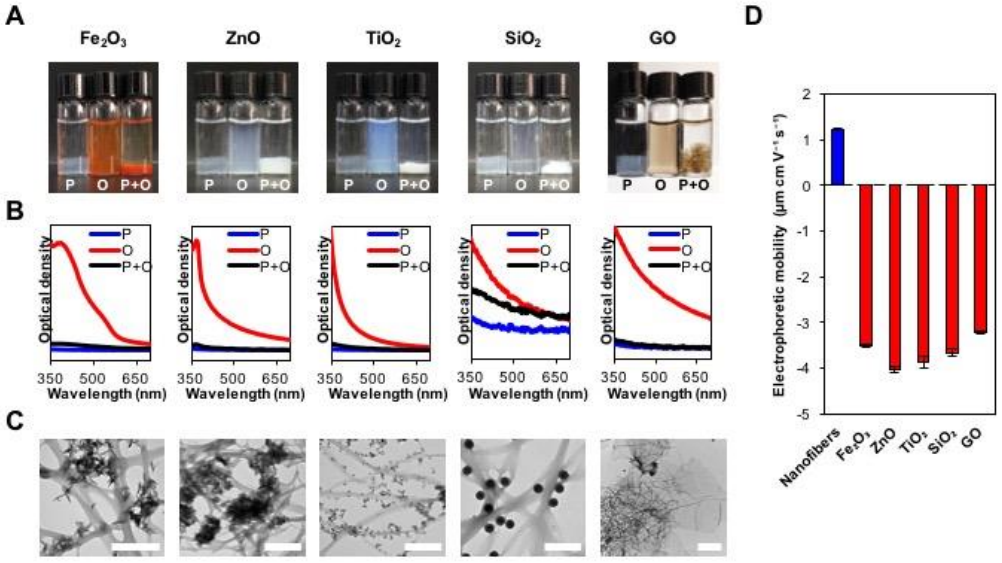

Figure 5.1: (A) Photographs of nanofiber dispersions, different dispersions of oxide particles, and peptide nanofiber-oxide mixtures. P denotes peptide nanofibers, O denotes oxide particles. Photographs were taken following 3 h incubation. A sedimenting floccule is seen at the bottom of the vial in nanofiber dispersions and nanofiber-oxide mixtures, but not in oxide dispersions. (B) UV-Vis spectra of liquid bulk samples corresponding to panel A. (C) TEM images of floccule samples from the nanofibers-oxide mixtures corresponding to panel a. Scale bars are 500 nm except for GO, where scale bar is 2 µm. (D) Electrophoretic mobility of peptide nanofibers and oxide particles. Under the experimental conditions, attraction between opposite electrostatic charge drives the binding of oxide particles to the sedimenting peptide nanofibers. Data represent mean ± standard error of the mean (n = 3 individual samples).

5.3.2: Exceptional AuNP Decoration of Peptide Nanofibers

Inspired by the ability of GS to reduce U ions *via* its T4Ps, we explored the interaction of our 20-mer peptide nanofibers with metal ions. Native GS T4P are associated with a c-type cytochrome[32], which has been implicated as the terminal reductase of a variety of metallic substrates owing to a low midpoint redox potential[33]. In its absence and since the peptide nanofibers assemble in potassium phosphate, we limited our investigation to the interaction with Au ions, which can be reduced by peptides[34], do not precipitate or become reduced in phosphate buffer[9], and yield reduced species that are suitable for a variety of applications[35]. $HAuCl_4$ was

chosen as the ionic Au source due the expected attraction of the $AuCl_4^-$ ion to the positively-charged nanofibers.

Diluting pre-formed peptide nanofibers (1.66 mM stock) to a volume fraction of 0.2 using aqueous $HAuCl_4$ and phosphate potassium (final concentrations of 1 and 9 mM, respectively) led to $AuCl_4^-$ reduction and sparse AuNP decoration of the nanofibers on a time scale of days, as suggested by the gradual appearance of a surface plasmon resonance (SPR) band near 520 nm (Supporting Fig. S5.2). The decoration process was significantly accelerated by overnight incubation of the mixture at 90 °C, a step which was adopted thereafter. High-resolution TEM imaging, selected area electron diffraction (SAED), TEM-based energy-dispersive X-ray spectroscopy (TEM-EDX) confirmed the identity of the decorating particles as spherical AuNP (Supporting Fig. S5.3). An increase in the nanofiber decoration by AuNP was achieved by decreasing the nanofiber volume fraction while maintaining the $HAuCl_4$ concentration fixed at 1 mM. When the volume fraction was lowered from 0.2 to 0.015, the nanofiber floccule appeared to decrease in size and gain a darker color, and coloration of the liquid bulk was observed at the lower volume fractions (Fig. 5.2A). Since nanofibers were not detected in the liquid bulk using electron microscopy, it follows that the liquid bulk coloration at lower volume fractions results from increased presence of soluble peptide species, which reduce $AuCl_4^-$ into suspended AuNP.

We focused on comparing the degree of nanofiber decoration in floccules from volume fractions of 0.2, 0.075 and 0.015. TEM analysis revealed that by lowering the nanofiber volume fraction, coverage of the nanofibers area by AuNP increased remarkably from 22±2% to 52±3% and finally to 93±1% at 0.2, 0.075, and 0.015 nanofiber volume fractions, respectively (Fig. 5.2B & C). The AuNP coverage correlated well with the Au content as determined by thermogravimetric analysis (TGA), which showed a respective increase from 19% to 53% and finally to 88 wt% (Fig.

5.2C and Supporting Fig. S5.4). Hence, these volume fraction conditions are denoted hereafter as sparse, moderate, and dense decoration and refer to Fibers A, B, and C, respectively.

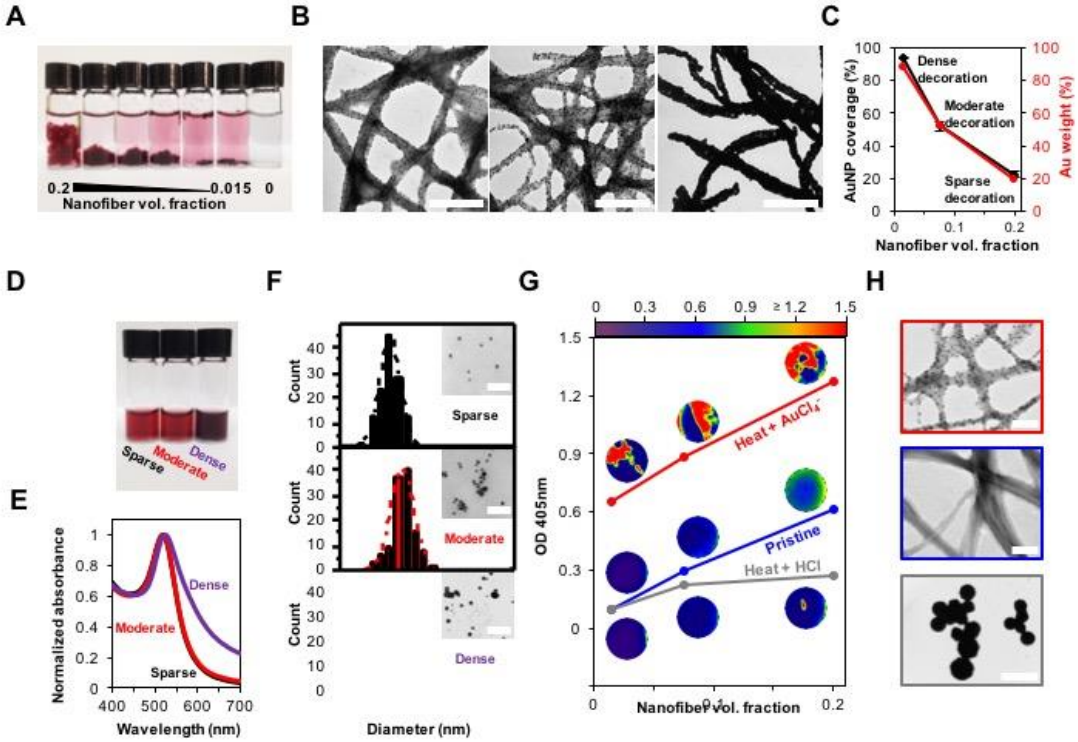

Figure 5.2: (A) Photograph of peptide nanofibers and $HAuCl_4$ mixtures following 16 h incubation at 90 °C. The nanofiber volume fraction, i.e. the added dispersion volume of nanofibers which had pre-formed at a peptide concentration of 1.66 mM, decreases from left to right. Rightmost vial is a similarly prepared control without peptide nanofibers. (B) TEM images of AuNP-decorated nanofibers from 0.2, 0.075, and 0.015 volume fraction conditions (from left to right). Scale bars, 500 nm. (C) TEM image analysis of single decorated nanofibers for estimating their AuNP coverage. Data represent mean ± standard error of the mean (n = 30 nanofibers per condition), for some data points the error bars are smaller than the symbol size. The Au weight fraction as determined by TGA is shown for comparison. In light of the analyses, the examined volume fraction conditions are denoted sparse, moderate, and dense decoration. D-F Comparative characterization of AuNP dispersion formed by dissolution of decorated nanofibers in 1 M ethanolamine, including photograph of the dispersions (D), visible range spectra showing the SPR band (E) and size distributions by TEM (F). In f n = 125 AuNP per condition and insets show example TEM images of the AuNP. Scale bars for insets, 100 nm. g,h, Thermal stabilization of the peptide nanofibers by $HAuCl_4$ as evident by turbidometric well-scanning heat maps (g) and corresponding TEM images of the 0.2 nanofiber volume fraction conditions (H). In g the plotted values are averaged turbidometric maps at 405 nm (4 mm scan diameter) and the heat maps color scale is defined in the top legend. Frame colors in h correspond to line colors in G. Scale bars, 200 nm for red and blue frames, 5 µm for grey frame.

Further characterization was performed following incubation of the decorated nanofibers in 1 M ethanolamine, which led to their disintegration and the release of the decorating AuNP. The

stable AuNP dispersions thus obtained (Fig. 5.2D) were comparatively characterized. AuNP obtained from the sparsely and moderately decorated nanofibers presented similar properties, namely an SPR band at 518 nm, spherical shape and respective average diameters of 11±2.4 and 14±3 nm based on TEM, and a narrow size distribution (Fig. 5.2E & F). In contrast, at the dense decoration condition the obtained AuNP presented a considerably broader and red-shifted SPR band at 524 nm, higher average diameter of 18±8 nm, and a broad size distribution (Fig. 5.2E & F). Taken together, these results show that simple co-incubation of the peptide nanofibers with $AuCl_4^-$ at an elevated temperature yields hybrid biometallic nanofibers with a controllable degree of AuNP decoration. The results also highlight the difference in AuNP decoration at the sparse and moderate decoration conditions in comparison with the dense decoration condition, at which the AuNP are larger and aggregated, thus yielding highly metallized nanofibers.

Interestingly, the interaction with $AuCl_4^-$ during decoration stabilizes the nanofibers. Turbidometric well-scanning showed that nanofiber dispersions subjected to the decoration procedure present increased OD at 405 nm compared to dispersions of pristine nanofibers (Fig. 5.2G). When $HAuCl_4$ is substituted in this procedure with HCl at an equivalent pH, the measured OD is lower than that of pristine nanofibers (Fig. 5.2G). These measurements suggest that pristine nanofibers may be impaired following incubation at 90 °C, unless supplemented by $HAuCl_4$. TEM imaging confirmed this assertion, showing that following incubation at 90 °C, $HAuCl_4$-treated nanofibers retain, do not present morphological impairment and become decorated with AuNP, whereas HCl-treated nanofibers transform into coalescing spheres (Fig. 5.2H). This data clearly shows that interaction with $HAuCl_4$ enhances the thermal stability of the nanofibers and thus prevents phase transition of the peptide.

5.3.3: Physical Properties of AuNP-Decorated Nanofibers

We investigated the electronic, electrostatic, and surface adhesion properties of the AuNP-decorated peptide nanofibers. Single-fiber measurements were carried out using conductive-probe atomic force microscopy (CP-AFM), where current was measured along single nanofibers at varying distances from an evaporated top electrode. Calculated conductance values along nanofibers of the three decoration conditions showed that the densely decorated nanofibers (Fibers C) present high conductance of ~2-5 μS, which remains constant regardless of the distance from the electrode, with an average distance-normalized conductance of 145± 98 μS cm^{-1} (Fig. 5.3A). In contrast, the moderately decorated nanofibers (Fibers B) exhibited lower conductance values overall of ~1-10 nS which were much more sensitive to distance from the electrode, with an average distance-normalized conductance of 12 ± 7 μS cm^{-1} (Fig. 5.3A). Finally, conductance of the sparsely decorated nanofibers (Fibers A) was within the experimental noise limit at all distances, similarly to control measurements of the bare insulating surface adjacent to nanofibers of the previous conditions (Fig. 5.3A). The conductivity of nanofiber films was measured in a temperature-controlled bipotentiostat device. This setup allowed for testing the conductivity of the nanofibers in an aqueous environment under physiologically-relevant range of temperatures. Similar to the single-fiber measurements, only films of the Fibers B and C had measurable conductivity, which was again higher for the former. Films of the Fibers C and B showed thickness-normalized conductances of 445 - 427 and 303-263 S cm^{-1}, respectively, over a temperature range of 275-345 K (Fig. 5.3B). In both cases, higher conductivity was measured at lower temperatures, consistent with a metallic charge conduction between adjacent Au nanoparticles[36]. Although the single fiber conductance values for moderately and densely decorated nanofibers differed by several orders of magnitude, bulk film conductivities differed by

less than a factor of 2. This can be explained by the existence of a charge percolation network in the bulk films[37]. Percolation across neighboring nanofibers *via* their decorating AuNP could support long-range charge transport and account for the proportionately larger conductivity in Fiber B films, similar to those reported for other organic-Au hybrids[38–40]. These measurements indicate that the conductivity of individual fibers and fiber films increases with the density of Au seeding. Importantly, their conductivity also extends into the macro-scale: Au-seeded fibers were fabricated into a 1.5 cm-long film that enabled the activation of a serially connected light-emitting diode (LED, Fig. 5.3C).

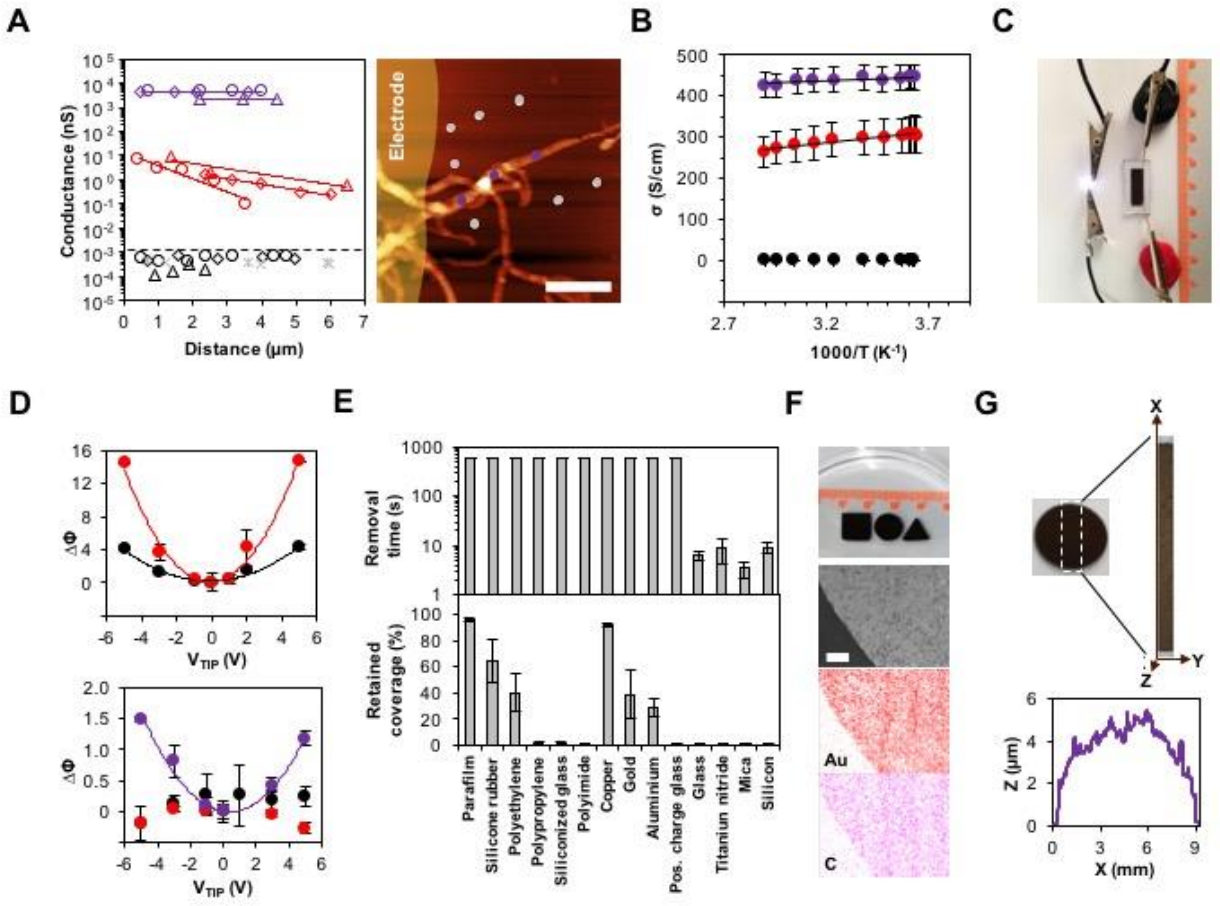

Figure 5.3: (A) Left: CP-AFM measurements along single nanofibers from the sparse (black), moderate (red) and dense (purple) decoration conditions. Each symbol type represents measurements along a given nanofiber that protrudes from beneath a top electrode. Measurements of bare surface adjacent to nanofibers (grey) were performed as control. Red and purple solid lines are exponential and linear fits, respectively. The dashed line represents the instrumental noise level. Right: Corresponding AFM image of densely

decorated nanofibers. Purple and grey circles represent measurements along the nanofiber and on adjacent bare surface, respectively. Evaporated top electrode is presented in false color. Scale bar, 2 µm. (B) Temperature-dependent conductivity of nanofiber films from the sparse (black), moderate (red) and dense (purple) decoration conditions in 0.1 M phosphate-citrate buffer pH 7.0. Solid lines are linear fits. Data represent mean ± standard error of the mean of steady-state current. For sparse nanofibers, vertical error bars are smaller than the symbol size. Horizontal error bars are smaller than the symbol size. (C) Photograph of a 1.5 cm-long film of densely decorated nanofiber permitting the activation of a serially-connected LED. (D) EFM phase shift of single nanofibers from the sparse (black), moderate (red) and dense (purple) decoration conditions deposited on glass (top) or Au (bottom) surface. Densely decorated nanofibers were measurable only on the Au surface. Solid lines are quadratic fits. Data represent mean ± standard error of the mean (n=5 measurements per fiber). (E) Adhesion of densely decorated nanofiber films to various substrate materials, as estimated by film removal time following immersion in water under stirring (top) and remaining covered area following ultrasonication in water (bottom). Data represent mean ± standard error of the mean (n = 5 nanofiber-deposited substrates). (F) Photograph of water-immersed self-supporting films of densely decorated nanofibers with shape side or diameter of 1 cm (top) and corresponding SEM-EDX image and elemental maps following transfer to a substrate and dehydration (bottom). Scale bar, 250 µm. (G) Thickness of densely decorated nanofiber films as measured by confocal microscopy. The curve represents average thickness of 3 individual films following water immersion, transfer to a substrate, and dehydration. Measurements were made along film diameter (9 mm) with 630 µm profile line width.

The above analyses were complemented by electrostatic force microscopy (EFM) measurements to evaluate the nature of the charges in the nanofibers and their general interaction with electrostatic charge. When deposited on an insulating glass surface, all decorated nanofibers responded to non-zero tip voltage due to buildup of static charge in the fiber-associated Au nanoparticles. We observed a parabolic phase response of tip to applied voltage in the range ±5 V, indicating attractive electrostatic force between the tip and the fibers on the substrate. The attraction was weakest for the Fiber A nanofibers and stronger for the Fiber B nanofibers (Fig. 5.4D). Fibers C strongly interacted with the tip to the extent that they detached from the surface during measurement. These nanofibers were only measurable when deposited on a conductive Au surface, where they showed a similar parabolic phase response due to tip-based image charge attraction[41], while the other nanofibers presented only negligible EFM signal due to weak coupling to the underlying conductive Au substrate (Fig. 5.3D, for more details see Supplementary Fig. S5.5). The symmetric tip response at opposite tip bias polarity indicated that Fiber C nanofibers contain mobile charges, which create image charge attraction between the fibers and the biased

tip, and are therefore highly polarizable[42,43]. As will be shown below, this property allowed for the construction of a static charge detector based on macroscopic deflection of the material. Finally, scanning Kelvin probe microscopy (SKPM) showed a persistent decrease in the surface potential of nanofibers with increasing Au-seeding density (Supplementary Fig. S5.6), consistent with a decrease in work function approaching that of elemental Au with increasing Au content of the fibers.

We focused on characterizing Fiber C nanofibers further due to their preferred electrical properties and higher Au content. The surface adhesion of these nanofibers was next examined to better understand how they can be utilized in applications. Dried Fiber C nanofiber films were prepared on a range of substrate materials, which were subsequently immersed in water and subjected to rapid stirring under visual inspection. We observed that for ceramic substrates (glass, titanium nitride, mica, and silicon), within ~10 s of immersion the films had been removed as a single cohesive patch (Fig. 5.3E). In contrast, films on polymeric, metallic, and modified glass substrates adhered and appeared undisturbed during the experimental timeframe, which was limited for 10 min (Fig. 5.3E). Surface adhesion was further tested under more stringent conditions, in which a second set of films on identical substrates was ultrasonicated in water for 5 min. Image analysis of pre- and post-treatment substrates showed the near-complete removal of films from the ceramic, modified glass, and two of the polymeric substrates, and their partial retention on the metallic and remaining polymeric substrates (Fig. 5.3E). From this data, it is evident that densely decorated nanofibers can be utilized as either self-supporting immersible films or water-resistant coating owing to their substrate-selective adhesion. By casting the nanofiber dispersion into molds and allowing it to dry prior to immersion in water, it was possible to obtain cm-scale self-supporting immersed films of specific shapes (Fig. 5.3F). Scanning electron

microscopy-based EDX (SEM-EDX) confirmed that both the Au and peptide constituents are retained after water immersion (Fig. 5.3F and Supporting Fig. S5.7) and confocal scanning laser microscopy (CSLM) revealed that such films are convex and reach ~5 μm in thickness (Fig. 5.3G).

5.3.4: Applications of densely decorated nanofibers

Following characterization, we utilized the densely decorated nanofiber films for three applications to demonstrate their multifunctionality. We first tested the catalytic activity of the films, which was expected due to their AuNP decoration. A common model reaction for testing metal nanostructure catalysis was performed, where 4-nitrophenol is reduced to 4-aminophenol by $NaBH_4$ in the presence of a catalyst[44]. Circular nanofiber film coating was prepared on silicone rubber due to the adhesion of the nanofibers to this material as shown in Figure 5.3A. When immersing the supported film in aqueous 4-nitrophenol with excess $NaBH_4$, a gradual decrease in absorbance at 400 nm and a concomitant increase in absorbance at 296 nm were observed (Fig. 5a), as expected for the reaction[44]. The isosbestic points at 280 and 313 nm indicated that no byproducts had formed[45]. Importantly, the extracted rate constant for this pseudo-first-order reaction (k = 0.0095 min^{-1}) remained nearly identical throughout four additional consecutive reaction cycles utilizing the same nanofiber coating (Fig. 5.4A). Additionally, no catalytic activity was observed by bare silicone rubber (Supporting Fig. S5.8). This data therefore demonstrates that the nanofiber film can function as a reusable catalytic coating.

Next, a static charge detector was prepared based on image charge, as observed by EFM. To this end, a dry self-supporting film was fixed to a conductive element serially connected to an LED, and positioned such that it nearly contacted a second conductive element. A polystyrene dish, a statically-charged object under practical conditions[46], was then set to approach the film

periodically. At a consistent distance of 6-7 mm, the film deflected toward the dish, thereby transiently bridging the gap between the conductive elements and consequently permitting the LED activation (Fig. 5.4B). The film acted as a physical switch in this circuit owing to its attraction to static charge, conductivity, and flexibility. It should be noted that water-recovered films are generally brittle following dehydration, yet they presented sufficient flexibility and durability to enable device operation for at least tens of cycles.

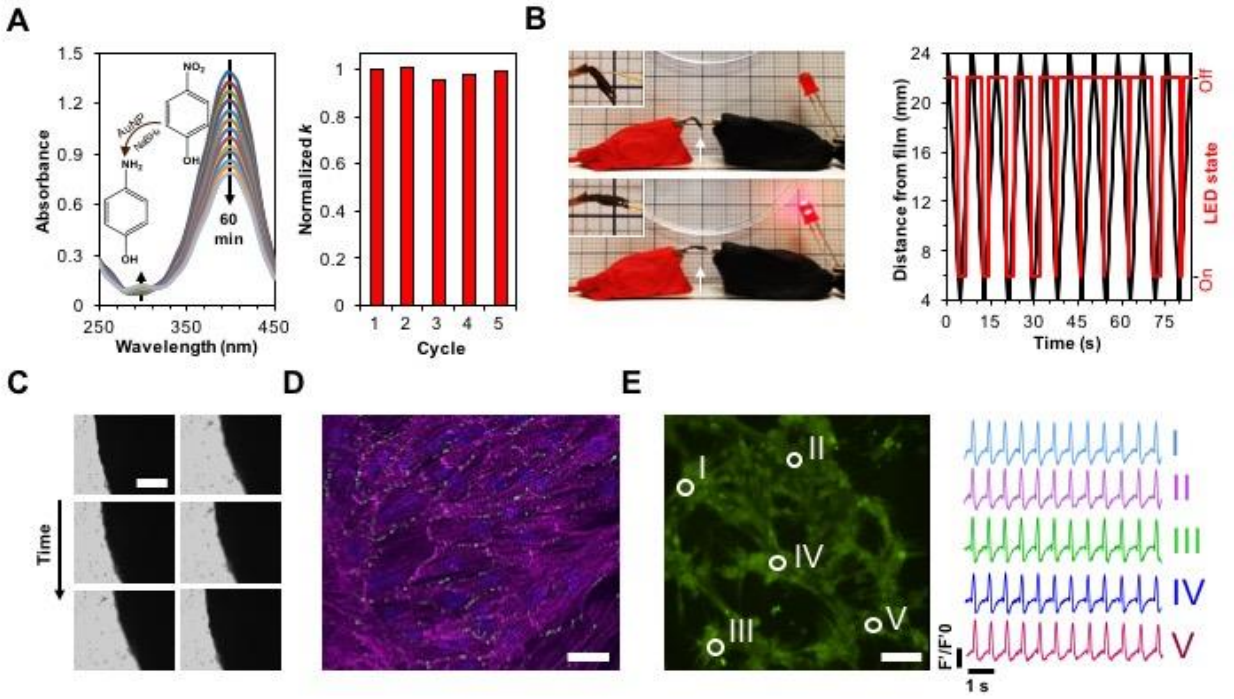

Figure 5.4: (A) Left: Time-dependent UV-Vis spectra of the catalytic reduction of 4-nitrophenol to 4-aminophenol in the presence of nanofiber coating on silicone rubber surface. Inset is the reaction scheme. Right: Normalized rate constant for 5 consecutive reaction cycles using the same coated surface, demonstrating its reusability. (B) Left: Photographs of a static charge detector based on nanofiber film deflection. The circuit is open and the LED is inactive when a statically charged polystyrene dish is far from the film (top). The film deflects to close the circuit, activating the LED, when the dish approaches the film (bottom). White arrows point to the film to guide the eye. Insets are magnified views of the film. Grid square side is 2 mm. Right: Time-dependent distance of the dish from the film (black) and corresponding LED state (red). During dish approach, the LED becomes activated at a distance of 6-7 mm. (C) Optical microscopy image series of a circular nanofiber film cultured with cardiac cells after 5 days of incubation. The order of images is from top-left to bottom-right and the interval between images is 120 ms. The circle appears to contract (left column) and expand (right column). Scale bar, 250 µm. (D) Confocal microscopy fluorescence image of immunostained cardiac α sarcomeric actinin (purple), connexin 43 (green), and nuclei (blue) in cardiac cells cultured on a circular nanofiber film. The image shows elongated and aligned cell bundles with massive striation. Scale bar, 25 µm. (E) Left: Confocal microscopy fluorescence image

showing the regions of interest used for data quantification of calcium transient imaging. Scale bar, 50 μm. Right: Quantification of calcium transients by normalized fluorescence intensity over time, showing synchronized activity at the regions of interest.

Finally, due to their nanofibrous structure, conductivity, and immersibility, we were motivated to test the ability of the Fiber C nanofiber films to support the growth of electrogenic cells. Cardiac cells were especially expected to benefit from the above material properties[47] and were therefore cultured on ethanol-sterilized circular films following their isolation from neonatal rats. After five days of incubation, the films exhibited strong contractions (Fig. 5.4C), which were also visible to the naked eye. Development of the thus-formed cardiac patches was then assessed by immunostaining for α sarcomeric actinin, a protein associated with cell contraction, and connexin 43, which acts in electrical coupling between adjacent cells. As evident by actinin staining (Fig. 5.4D, purple), cardiac cells formed elongated and aligned cell bundles with massive striation, reminiscent of the natural cell morphology in the myocardium[48]. Furthermore, aligned localization of connexin 43 between adjacent cardiomyocytes (Fig. 5.4D, green) was in line with the observable contractions of the patches and suggested efficient electrical signal propagation between cells[49]. Indeed, calcium transient imaging confirmed that synchronized activation of cardiomyocytes occurred throughout the nanofiber films (Fig. 5.4E). The films therefore proved to be excellent biocompatible scaffolds, supporting the synchronized growth of cardiac cells.

5.4: Conclusion

The current work presents for the first time the functionality of the recently-reported T4P-like peptide nanofibers. The bioinspired interaction of these designed self-assembled structures with metal oxides or ions resulted in highly diverse composite materials. The interaction with Au ions is especially remarkable considering the exceptional degree of decoration, the simplicity of

its formation, and the lack of need to employ external additives such as reducing agents. The hybrid AuNP-peptide material presented attractive functional properties that include electrical conductivity from the single-nanofiber level up and substrate-selective adhesion. The latter property allowed for the formation of macroscopic films that were either used as a coating or directly in their extremely thin free forms. The film preparation is notably simple as it is based on a single-step green chemistry process followed by casting. The observed self-support and maintained integrity upon immersion are rarely observed in supramolecular peptide or protein-based materials, even after embedding inorganic materials or at increased film thickness. The absence of these properties typically precludes the use of such materials in various applications, whereas the presented hybrid AuNP-peptide material was successfully utilized in several distinctly different applications. Looking forward, the hybrid material could be used for microelectronic device fabrication or be integrated with electro-responsive tissues for biomedical purposes.

5.5: Supporting Information

5.5.1: Sample Preparation

Preparation of peptide nanofibers. The 20-mer peptide was synthesized by Pepmic Co., Ltd. (Suzhou, China). The peptide was purified to at least 95%, and its identity was confirmed by mass spectrometry. In a typical experiment, lyophilized powder (4.5-5 mg) was dissolved in an Eppendorf tube using Milli-Q water to a concentration of 3.314 mM (8 mg mL^{-1}) by vortexing (2700 RPM, 1 min) and bath ultrasonication (43 kHz, 50 W, 10 s). An equal volume of 20 mM potassium phosphate (pH 7.4) was then added and the mixture was vertically rotated (30 RPM, 3 days, 25 °C). The resulting nanofiber dispersion was used as a concentrated stock (nanofiber volume fraction = 1) within 2 days of preparation.

Binding of oxide particles. Water dispersion of Fe_2O_3 (average particle size 30 nm) was purchased from US Research Nanomaterials (Houston, TX, USA). Water dispersions of ZnO (average particle size 40 nm), TiO_2 (primary particle size ~21 nm) and SiO_2 (particle size 150 nm), were purchased from Sigma-Aldrich (Rehovot, Israel). Water dispersion of graphene oxide (flake size 300-700 nm) was purchased from Graphene Supermarket (Reading, MA, USA). In all cases, the oxide species were not surface-modified. Working stocks were prepared by dilution with Milli-Q water to 0.2 % wt for all dispersion but graphene oxide, which was used as purchased (0.05% wt). In borosilicate glass vials (1.8 mL, Thermo Fisher Scientific, Waltham, MA, USA), working stock samples (140 uL) were supplemented by 10 mM potassium phosphate (pH 7.4, 1155 uL) and by concentrated nanofiber stock (105 uL) to obtain final mixtures (1400 uL) containing 0.02% wt oxide particles (or 0.005% wt graphene oxide flakes), 9 mM potassium phosphate and a nanofiber volume fraction of 0.075. Control mixtures, where the oxide dispersions were replaced with Milli-Q water or the nanofiber dispersion was replaced with potassium phosphate, were prepared similarly. All mixtures were vortexed briefly at ~800 RPM, covered, then incubated undisturbed for 3 h. Samples (100 uL) were then removed from the liquid bulks and pipetted into a 96-well UV-Star UV transparent microplate (Greiner BioOne, Frickenhausen, Germany) and their UV-Vis spectra were acquired using a ClarioStar microplate reader (BMG Labtech, Ortenberg, Germany) and corrected in baseline with the solvent. TEM was subsequently performed by sampling the nanofiber floccule (10 µl) onto 400-mesh copper grids covered by a carbon-stabilized Formvar film (Electron Microscopy Science, Fort Washington, PA, USA), allowing the samples to adsorb for 2 min before excess fluid was blotted off, and finally imaging using a JEM-1400Plus electron microscope (JEOL, Tokyo, Japan) operating at 80 kV.

Electrophoretic mobility was measured on separate oxide or nanofiber dispersions prepared as described above, using a folded capillary cell in a Zetasizer Nano ZS analyzer (Malvern Instruments, Malvern, UK), where 3 runs were performed on 3 individual samples per material and the results were averaged.

AuNP Decoration. Reactions of 1400 uL were prepared in borosilicate glass vials (1.8 mL, Thermo Fisher Scientific), by diluting a concentrated nanofiber stock to the desired nanofiber volume fraction with potassium phosphate (pH 7.4, final concentration 9 mM) and 10 mM gold(III) chloride hydrate (>99.99% trace metal basis, Sigma-Aldrich) prepared in Milli-Q water (final concentration 1 mM). The nanofiber stock was added last. Reactions were vortexed briefly at ~800 RPM and incubated for 16 h in a dry bath with a dark cover set to 90 °C. In cases where larger volume dispersions were required, multiple reactions were set individually and pooled after incubation.

The Au weight fraction was determined by TGA as described by others[19]. Samples were prepared by drying decorated nanofibers on glass overnight and detaching the resulting films by immersion in water. The films were then washed by rocking in Milli-Q water (30 mL, 5 min, 3 cycles) and allowed to dry. Samples of ~2-4 mg were loaded into 250 µL alumina crucibles and measured using a TGA Q5000 thermogravimetric analyzer (TA Instruments, New Castle, DE, USA) in a temperature range of 40 ºC to 900 ºC and a heating rate of 10 ºC min^{-1} under nitrogen atmosphere. The samples were maintained at 900 °C for 30 min and the Au weight fraction was determined by the remaining solid weight fraction.

The AuNP coverage was estimated by TEM. Sample preparation and imaging were performed as described above. Every image captured a single nanofiber and a fixed magnification

was used in all cases. Image analysis was performed using ImageJ 1.51K. For every image, the total nanofiber area in pixels was obtained from the integrated density following automatic threshold adjustment by the Triangle method. The AuNP area in pixels was separately obtained from the integrated density following bandpass filtering and identical threshold adjustment. AuNP coverage was calculated per image as the ratio of AuNP pixels to total nanofiber pixels and the results were averaged per decoration condition. Data represent mean ± standard error of the mean. For comparative characterization of released AuNP, as-prepared decorated nanofibers were centrifuged (700 x g, 1 min) and the supernatant was discarded. The pelleted nanofibers were resuspended in 400 uL of aqueous 1 M ethanolamine (Sigma-Aldrich) and incubated in the dark for 1 month. AuNP size analysis was performed using TEM, where 30 uL dispersion samples were dropped onto 400-mesh copper grids covered by a carbon-only film (SPI, West Chester, PA, USA) and immediately blotted off. Imaging was performed as described above and image analysis was performed using ImageJ 1.51K, where automatic threshold adjustment by the default method was performed prior to employing the built-in particle analyzer. To avoid misidentification, only particles larger than 2 nm^2 and of high circularity (≥ 0.8) were analyzed. UV-Vis spectra were acquired as described above for dispersion samples (25 uL) following their dilution with Milli-Q water to 100 uL.

Turbidometric well-scanning was performed on 100 uL samples in UV-Star UV transparent microplate (Greiner BioOne) using a ClarioStar microplate reader (BMG). OD at 405 nm was measured using the well scan mode (4 mm diameter, 20 x 20 pixels).

5.5.2: Materials Characterization

Surface Adhesion. The substrates, namely Parafilm M (Sigma-Aldrich), silicone rubber (Grace BioLabs, Bend, OR, USA), low density polyethylene, polypropylene, Cu, and Al (Alfa Aesar, Ward Hill, MA, USA), siliconized glass (Hampton Research, Aliso Viejo, CA, USA), polyimide (Kapton HN, DuPont, Wilmington, DE, USA), glass, positively-charged glass (HistoBond, Marienfeld-Superior, Lauda-Königshofen, Germany), titanium nitride-coated stainless steel (2-3 μm coating, Goodfellow, Cambridge, UK) mica (Grade V1, Ted Pella, Redding, CA, USA), and Si (SPI) were cleaned by bath ultrasonication (43 kHz, 50 W, 5 min) in 2-propanol and dried under a stream of N_2. Au substrates (100 nm, deposited onto 5 nm Ti on glass) were prepared by electron beam deposition (VST evaporator, VST, Petah Tikva, Israel) and cleaned similarly. Densely decorated nanofibers (2 uL) were deposited on the cleaned substrates and allowed to dry overnight in petri dishes. For the stirring experiment, the substrates were individually immersed in Milli-Q water (200 mL) and subjected to magnetic stirring at 400 RPM while being held perpendicular to the plane of rotation at a fixed position, as seen in Supplementary Movie 3. The nanofiber film removal time was determined visually using a digital timer. For the ultrasonication experiment, the substrates were individually immersed in Milli-Q water (20 mL) and subjected to bath ultrasonication (43 kHz, 50 W, 5 min). Individual photographs of the substrates pre- and post-treatment were taken and subsequently analyzed using ImageJ 1.51K, where the area covered by nanofibers was obtained from the integrated density at the region of interest following automatic threshold adjustment. Specific thresholding method was chosen per substrate type and the retained coverage was calculated as the ratio of covered area pre-treatment to covered area post-treatment. The experiments were performed in quintuplicate.

Shape-Specific Films. Films were prepared from densely decorated nanofibers by the drop-cast method. Decorated nanofibers were prepared by setting 20 individual reactions as described above. Following incubation, the nanofibers were collectable by pipetting owing to their cohesive nature. Collected nanofibers were pooled in two Eppendorf tubes and centrifuged (700 x g, 10 s) and the supernatant was discarded. The cohesive pellet was washed intact by gentle resuspension in 1 mL of 10 mM potassium phosphate (pH 7.4) and centrifugation (700 x g, 10 s). Two additional washing cycles were performed, the supernatant was discarded, and the nanofibers were dispersed in 200 uL of potassium phosphate per tube and pooled. Nanofibers were drop-cast at 117.9 µl cm^{-2} into molds, which were prepared by fitting glass substrates with silicone rubber isolators (0.5 mm thick, no adhesive, Grace BioLabs). The films were dried overnight in covered glass petri dishes.

SEM-EDX was performed on films following their immersion in 30 mL water for 15 min, transfer to a Si substrate (SPI) and drying under a stream of N_2. Elemental maps were acquired using a NORAN System 7 X-ray microanalysis system (Thermo Fisher Scientific) attached to a JSM-6700F field-emission scanning electron microscope (JEOL) operating at 15 kV. CSLM imaging and thickness measurement were performed on similarly-prepared films but following transfer to glass surfaces, using a LEXT OLS4000 confocal microscope (Olympus, Tokyo, Japan) at 20x magnification. Measurements were made along the diameter of the films (9 mm) with 630 µm profile line width. Automatic noise removal and level adjustment using bare glass regions (3-point method) were then applied and the results were averaged.

Chemical catalysis. Circular films (9 mm diameter) of densely decorated nanofibers were prepared as described above except that silicone rubber was used as the substrate (Grace BioLabs).

In a 1 cm rectangular quartz cuvette (Hellma Analytics, Müllheim, Germany), 200 μL of 1 mM 4-nitrophenol (final concentration 0.08 mM, 200 nmol) were mixed with 425 μL of 26.43 mM $NaBH_4$ (final concentration 4.49 mM, 11.22 μmol) and 1875 μL of Milli-Q water. The substrate was then immersed in the mixture and positioned using two clips at its unimmersed end. UV-Vis spectra in the range of 250-450 nm were then acquired at a 5 min interval for 60 minutes using a T60 spectrophotometer (PG Instruments, Leicestershire, UK) and corrected in baseline with Milli-Q water. The substrate was kept in 5 mL of Milli-Q water between reaction cycles. The reaction rate constant was calculated according to pseudo-first-order reaction kinetics. As the $NaBH_4$ concentration greatly exceeds that of 4-nitrophenol, the reaction can be considered of first order and hence a rate constant can be determined as a function of 4-nitrophenol concentration according to the equation $-dc_t/dt = kc_t$, where c_t is the concentration of 4-nitrophenol at time t, and k is the rate constant. In the integrated equation, $-\ln(c_t/c_0) = kt$, c_0 is the concentration of 4-nitrophenol at $t = 0$ and c_t/c_0 is equivalent to A_t/A_0, where A_t and A_0 are the respective absorbance intensities at 400 nm at time t and 0. The rate constant k can hence be obtained from the slope of $-\ln(A_t/A_0)$ as a function of time.

Static charge detection. For static charge detection, a self-supporting water-immersed circular film of densely decorated nanofibers (9 mm diameter) was transferred to an inert anti-static polypropylene substrate (Kaltek, Padova, Italy). The film was rapidly dried by flowing N_2 in parallel to its surface until it detached from the substrate. An open circuit operating at 3 V d.c. voltage was then prepared to connect the film in series with an LED. The dried film was contacted with adhesive copper tape which was then clamped using a crocodile connector. A tungsten probe needle (American Probe & Technologies, Merced, CA, USA) was clamped using a second

crocodile connector and both connectors were fixed to a glass surface using plasticine. The needle was then positioned above the film and wired to an LED. This device was placed on an optical table and a polystyrene petri dish was set to approach the film using a motorized stage periodically at a rate of ~0.2 mm s^{-1}. Recorded video was analyzed in a frame-by-frame manner using ImageJ 1.51K.

Cardiac patches. Free-floating circular films of densely decorated nanofibers (9 mm diameter) were twice by orbital shaking in Milli-Q water (30 mL, 50 RPM, 5 min) and sterilized by subsequent wash in 70% ethanol (30 mL, 50 RPM, 5 min). Two additional washing cycles in water were performed as above and the films were transferred to glass microscope coverslips.

5.5.3: Electronic Property Characterization

Temperature-Dependent Conductivity Measurements of Films. Interdigitated electrodes were used for all temperature-dependent bulk film measurements. Each electrode consisted of 100 parallel bands (5 μm wide x 2 mm long), with an intra-band spacing of 5 μm. Devices were photolithographically patterned onto Pyrex wafers, with electron beam evaporation of a 5 nm Ti adhesion layer and 60 nm Au at the UC San Diego Nano3 microfabrication facility. Prior to use, devices were subsequently sonicated in acetone, isopropanol, and ultrapure water and tested for shorts.

Samples were used at as-synthesized concentrations, deposited onto the electrodes for a total volume of 7.5 μL of sample per device, and air dried in a laminar flow hood. Exposed electrode and lead connections were sealed using waterproof silicon sealant (DAP All-Purpose Adhesive Sealant).

Solution gated measurements were conducted in septum-sealed scintillation vials containing 0.1M phosphate-citrate buffer, pH 7.0, sparged with 80% N2 with 20% CO2 prior to measurements, with flow maintained in the headspace over the course of the measurements. For temperature-dependent measurement, the vials were submerged in a stirred water bath containing a metal thermocouple. A hot plate was used to apply heat to the system and ice was added to the water bath to achieve cooling. Once the thermocouple registered a stable bath temperature for several minutes at each temperature set point, bipotentiostat chronoamperometry measurements were performed using two Gamry potentiostats (PC14/300 series) connected with a bipotentiostat cable, as described previously[50,51]. Briefly, for these measurements, the source and the drain are independently referenced to a common 3.5M Ag/AgCl reference electrode such that a fixed source-drain (V_{DS}) offset is maintained, and the steady-state current from the source and the drain are simultaneously collected. The steady-state conducting current was taken to be half the difference between the source and drain currents, which was then background-subtracted using the negligible current at V_{DS} =0 V, and then divided by V_{DS} to obtain the conductance. Conductivity values were determined from average height profiles of films, as determined by topographical atomic force microscopy measurements. Vertical error bars (Fig. 4b) are dominated by error associated with height measurements, as deviations in the conductive current responses were negligible.

EFM and SKPM Measurements. Samples for EFM and SKPM were cast onto glass or gold-evaporated glass slides by spin coating (20 sec at 3000 rpm at 1000 rpm/s followed by 5 sec at 5000 rpm at 1200 rpm/s). Both measurements were carried out either in a two-pass EFM mode or two-pass SKPM mode using conductive Ir-coated silicon probes (Asylum Research ASYELEC-

01) in an Asylum MFP3D AFM. A distance of 40 nm from the surface was maintained during the second pass (after preliminary measurements obtained at different tip-substrate distances excluded topographical artifacts). The tip phase shift, $\Delta\phi$, reported is the EFM phase response subtracted from background. SKPM measurements were conducted on glass, and values represent the measured contact potential difference between the tip and the sample. Tip calibration was not performed, so work function values are not presented. All measurements were performed with samples attached to grounding plate, using conductive silver paint.

Single Fiber Conductive AFM. Samples for CP-AFM were deposited onto glass slides by spin coating (conditions above). Electrodes (4 nm Ti adhesion layer and 100 nm Au film) were deposited by thermal evaporation onto the deposited nanofibers through a shadow mask. Samples were attached to a grounding plate using conductive silver paint, and conductive AFM measurements were performed using the Asylum MFP3D in ORCA mode, with Ir-coated silicon probes. Scans were first conducted in tapping mode to identify fibers with one end contacting an electrode. The tip of the conductive probe was then positioned at distances along the length of the fiber, allowing for two-point *I*-*V* measurements between the patterned electrode and the tip. The current response at each position along the nanofiber was monitored as the voltage was swept ± 2 V. Controls were performed on the gold electrode and on the insulating substrate. Fiber conductivity was determined as an average of 3 different fiber samples.

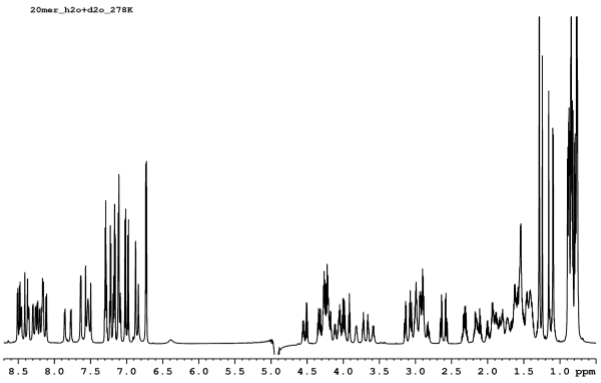

Figure S5.1: ^{1}H 800 MHz 1D spectrum of the 20-mer peptide (2 mM) in water-D_2O (9:1 v/v) at 278 K.

H_2N-**F_1-T_2-L_3-I_4-E_5-L_6-L_7-I_8-P_9-Q_{10}-F_{11}-S_{12}-U_{13}-Y_{14}-R_{15}-V_{16}-K_{17}-U_{18}-Y_{19}-N_{20}**-NH_2

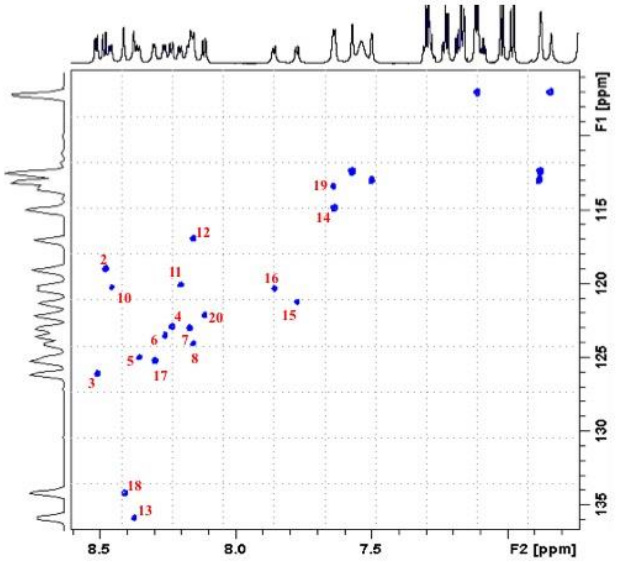

Figure S5.2: ^{1}H-^{15}N HSQC 800 MHz spectrum of the 20-mer peptide at natural isotopic abundance. The peptide sequence is given for reference.

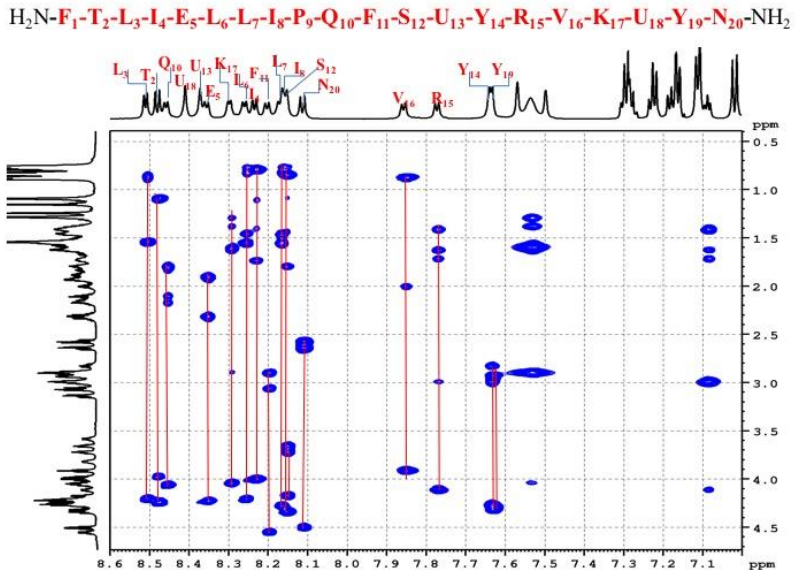

Figure S5.3: Partial TOCSY trace of the 20-mer peptide showing residue-specific assignments. The peptide sequence is given for reference.

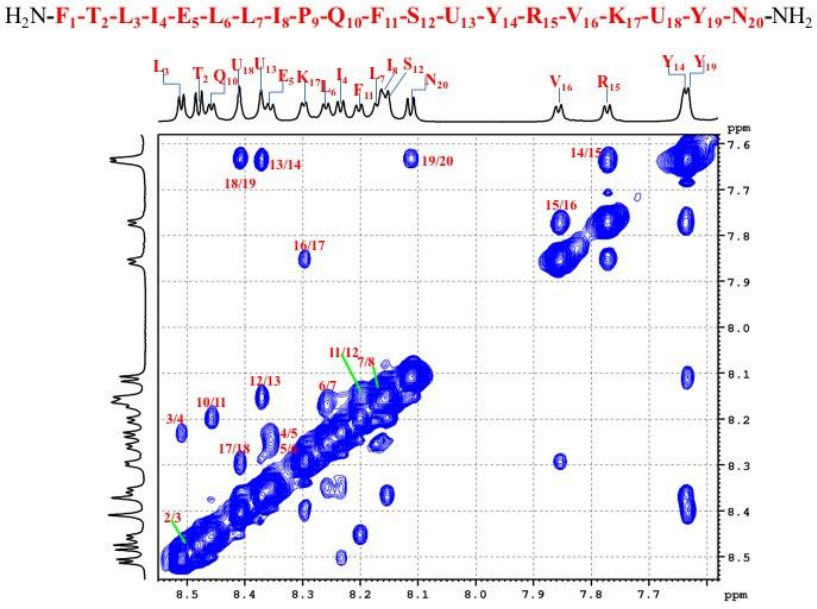

Figure S5.4: Amide region NOESY spectrum of the 20-mer peptide showing sequential d_{NN} connectivities. The peptide sequence is given for reference.

H_2N-**F_1-T_2-L_3-I_4-E_5-L_6-L_7-I_8-P_9-Q_{10}-F_{11}-S_{12}-U_{13}-Y_{14}-R_{15}-V_{16}-K_{17}-U_{18}-Y_{19}-N_{20}**-NH_2

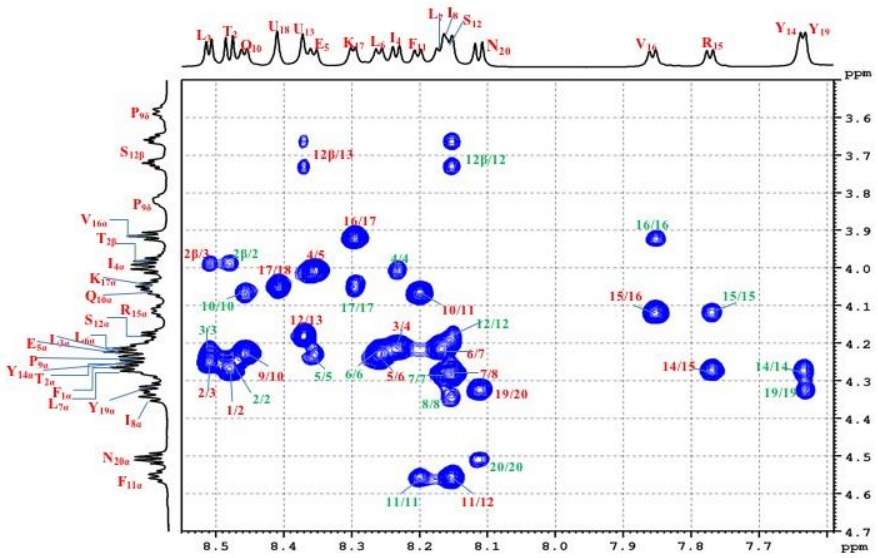

Figure S5.5: Fingerprint region NOESY spectrum of the 20-mer peptide showing sequential $d_{\alpha N}$ connectivities. The peptide sequence is given for reference.

H_2N-**F_1-T_2-L_3-I_4-E_5-L_6-L_7-I_8-P_9-Q_{10}-F_{11}-S_{12}-U_{13}-Y_{14}-R_{15}-V_{16}-K_{17}-U_{18}-Y_{19}-N_{20}**-NH_2

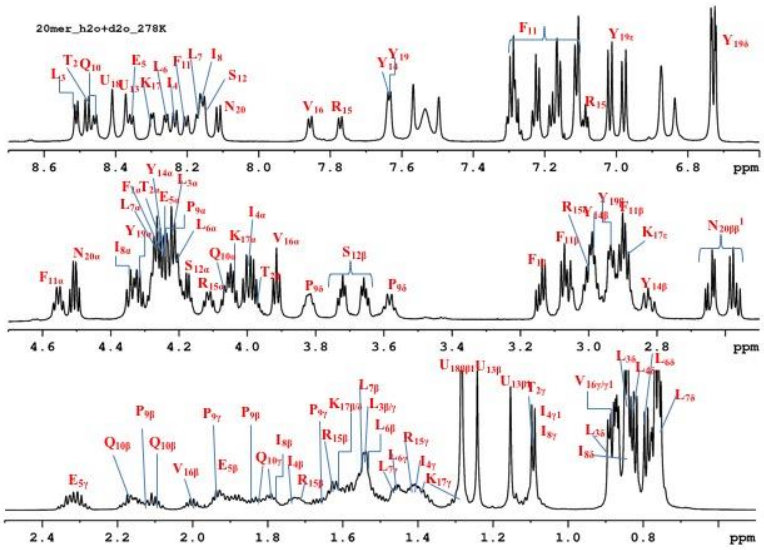

Figure S5.6: ^{1}H 800 MHz 1D spectrum following complete resonance assignment. The peptide sequence is given for reference.

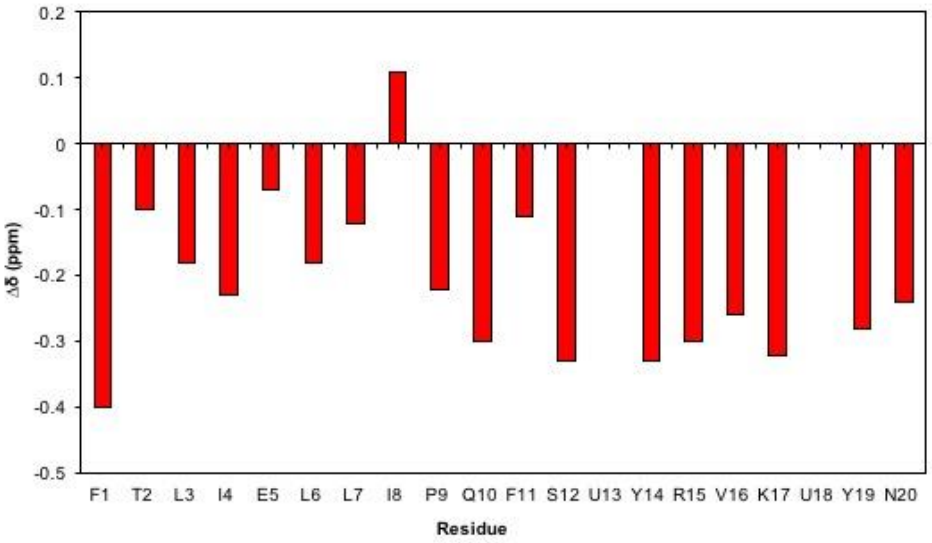

Figure S5.7: CSI plot of the 20-mer peptide, showing chemical shift (Δδ) of C^aH. Higher negativity is associated with increased helicity. U residues are not defined for CSI.

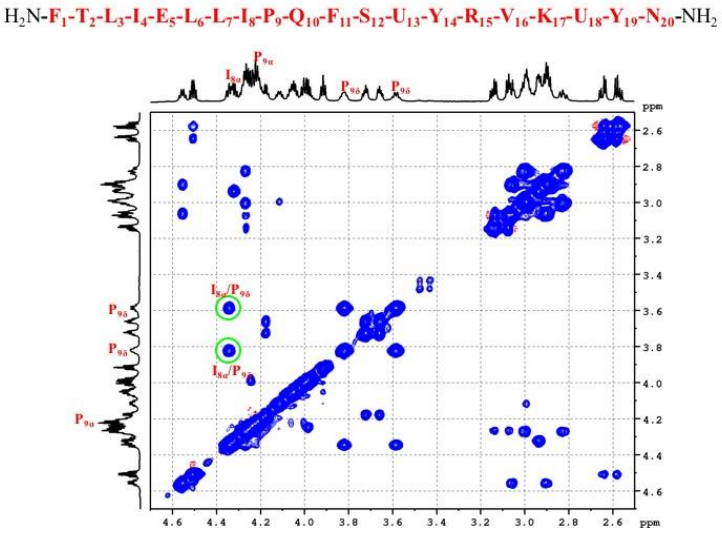

Figure S5.8: I_8 C^a H↔ P_9 C^dH_2 NOEs (circled in green) indicating *trans* peptide bond across Ile_8-Pro_9. The peptide sequence is given for reference.

H_2N-F_1-T_2-L_3-I_4-E_5-L_6-L_7-I_8-P_9-Q_{10}-F_{11}-S_{12}-U_{13}-Y_{14}-R_{15}-V_{16}-K_{17}-U_{18}-Y_{19}-N_{20}-NH_2

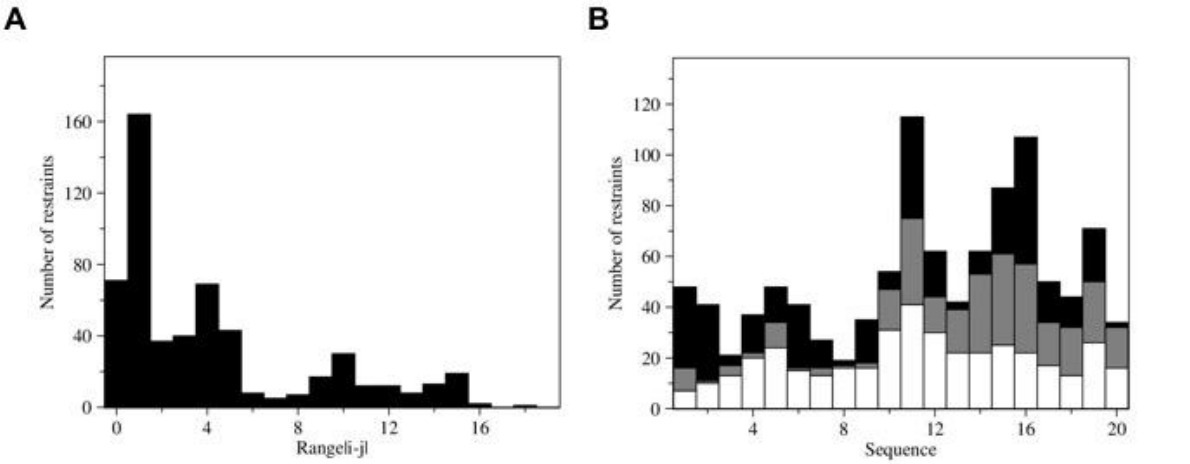

Figure S5.9: Distribution of distance constrains as a function of their range (A) and residue position (B) for CYANA structure calculation. The peptide sequence is given for reference.

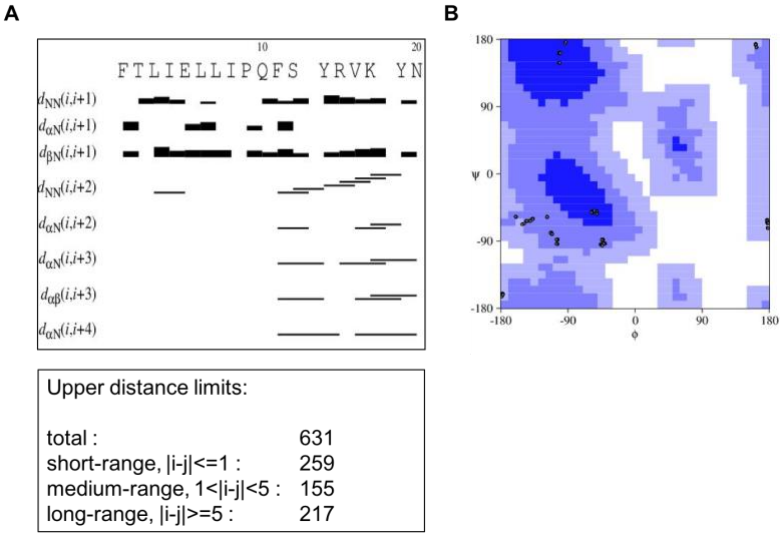

Figure S5.10: NOE distribution (A) and φ,ψ distribution in Ramanchandran plot (B) for CYANA structure calculation.

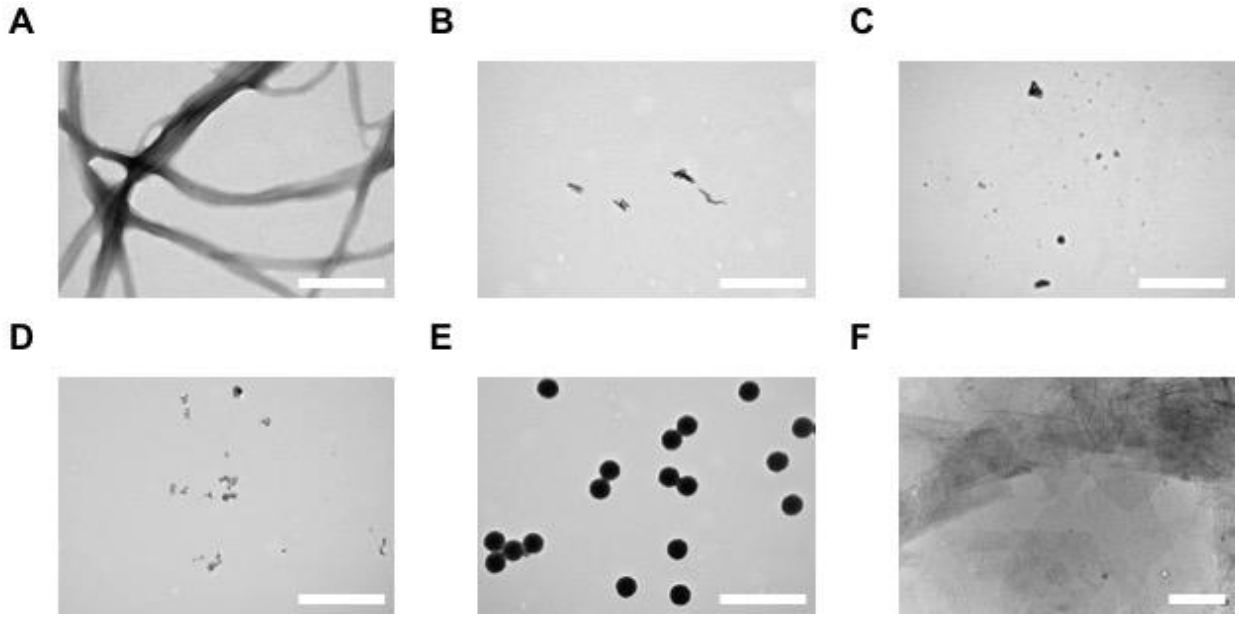

Figure S5.11: TEM images of pristine (A) peptide nanofibers, (B) Fe (III) oxide nanoparticle, (C) ZnO nanoparticles, (D) TiO_2 nanoparticles, (E) SiO_2 nanoparticles, (f) GO flakes. Scale bars (A-E) 500 nm, (F) 2 µm.

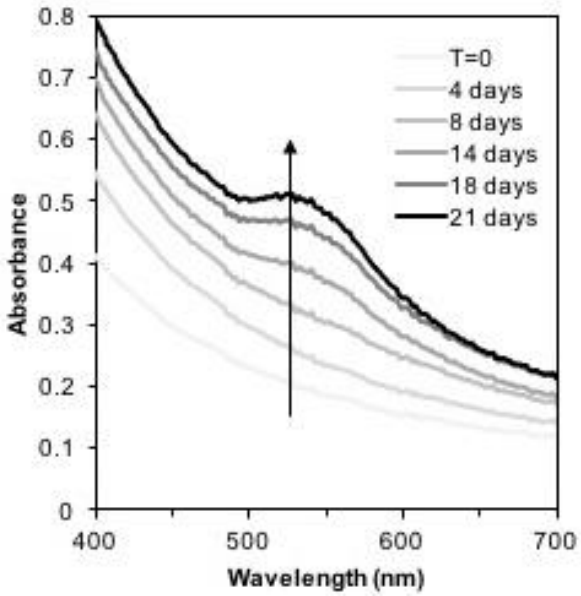

Figure S5.12: Time-dependent UV-Vis spectra of a peptide nanofibers (0.2 volume fraction) and $HAuCl_4$ (1 mM) mixture in 9 mM potassium phosphate (pH 7.4). Arrow denotes the development of a SPR band near 520 nm over time.

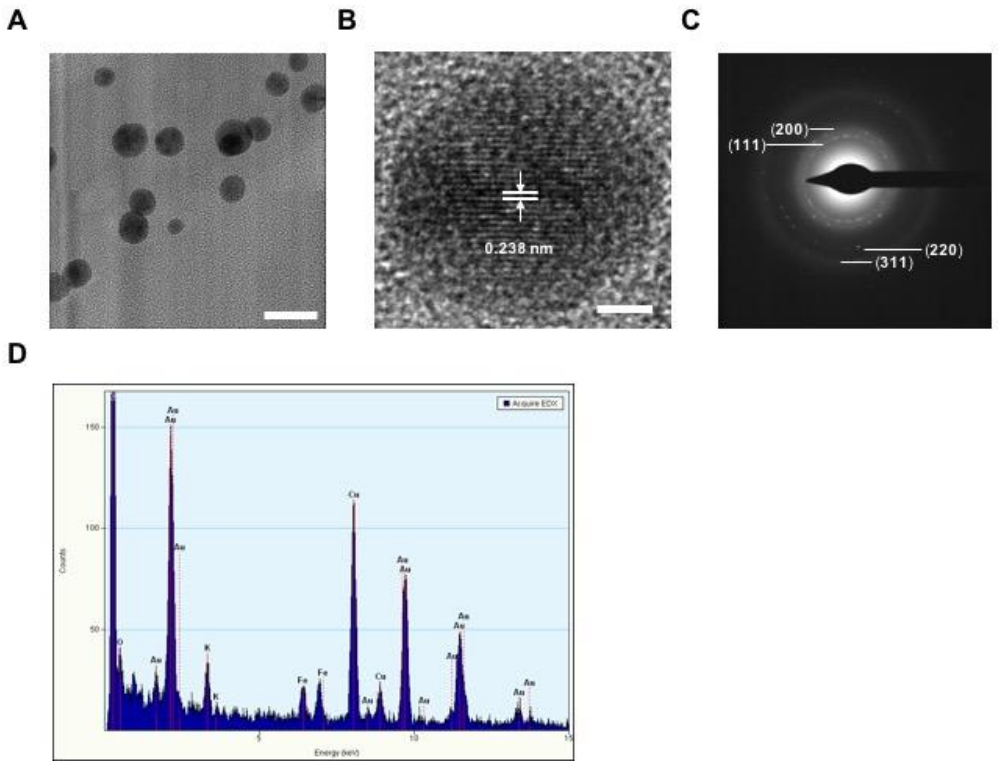

Figure S5.13: Confirmation of AuNP decoration of peptide nanofibers. (A) High-resolution TEM image of a single nanofiber decorated by AuNP. (B) High-resolution TEM image of a single decorating AuNP showing lattice fringes of 0.238 nm, attributed to the (111) plane of face-centered cubic Au. Scale bar, 2 nm. (C) SAED pattern of an AuNP-decorated nanofiber. Reflections are indexed to the (111), (200), (220) and (311) planes of face-centered cubic Au. (D) TEM-EDX analysis of nanofiber-decorating AuNP. The presence of Cu and Fe is due to the deposition of the sample on a Cu-containing TEM grid, and artifactual electron interaction within the microscope (also observed without sample), respectively.

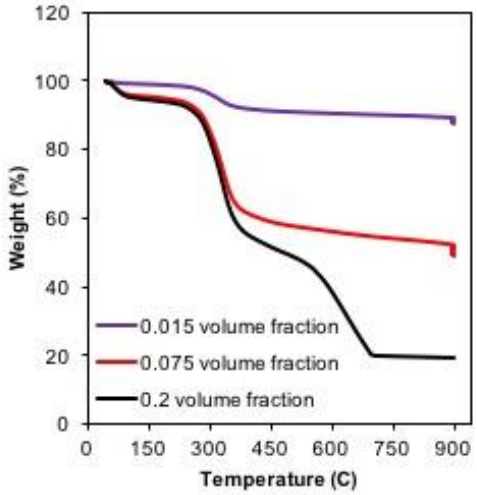

Figure S5.14: TGA curves of decorated nanofiber samples from the studied volume fraction conditions.

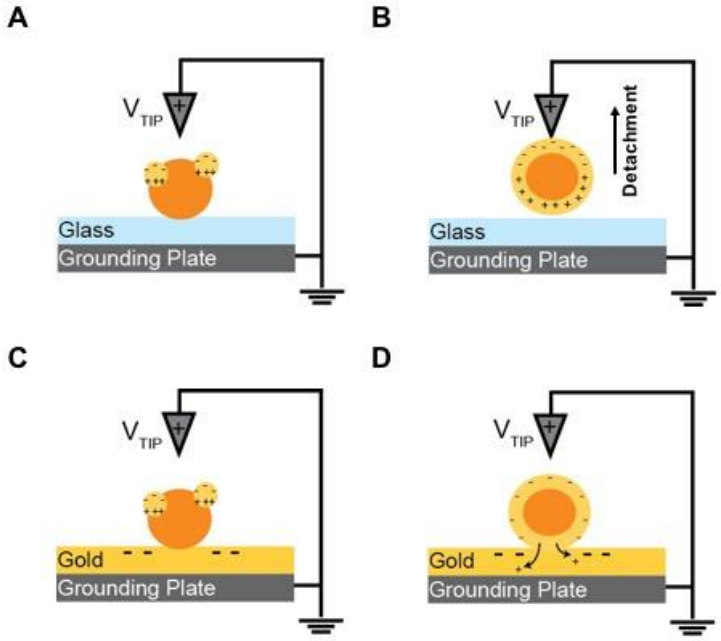

Figure S5.15: Illustration of EFM measurement and data interpretation for nanofibers from the sparse and moderate (A, C) or dense (B, D) decoration conditions on glass (A, B) or Au (C, D) surfaces. The nanofiber (cross section, orange) is decorated by isolated (A, C) or aggregated (B,D) AuNP (yellow). When decorated nanofibers are deposited on an insulating glass surface (A, B), interaction of the decorating AuNP with the EFM tip results in the development of image charge, i.e. induced charge polarization in the AuNP in response to EFM tip potential (V_{TIP}, positive potential is illustrated for example). Due to the insulating nature of glass, mobile charges with identical polarity to V_{TIP} remain within the AuNP boundaries, leading to high density of opposite-polarity charge which induces strong attraction to the tip. The image charge and the corresponding tip attraction are proportional to the degree of AuNP decoration, and so the EFM signal is measurable in (A) but not in (B) as in the latter case the nanofiber detaches from the surface during measurement. In contrast, when decorated nanofibers are deposited on a conductive Au surface (C, D), image charge develops in both the AuNP and Au surface and is stronger in the later case. In (C) the AuNP are isolated and hence the mobile equal-polarity charges remain within the AuNP boundaries. Because the nanofiber is overall insulating, the surface-originating image charge is masked by the nanofiber and this interference results in no EFM signal or slightly negative EFM signal following background correction against the Au surface. The background-corrected EFM signal given in Figure 5.3D deviates from pure parabolic behavior due to AuNP-originating image charge. In (D) the surface-originating image charge is not masked as the AuNP are aggregated and the nanofiber is overall conductive. As charge with identical polarity to V_{TIP} can propagate from the conductive nanofiber to the Au surface, the density of opposite-polarity charge is lower than in (B) and hence the tip attraction is weaker and the EFM signal is measurable.

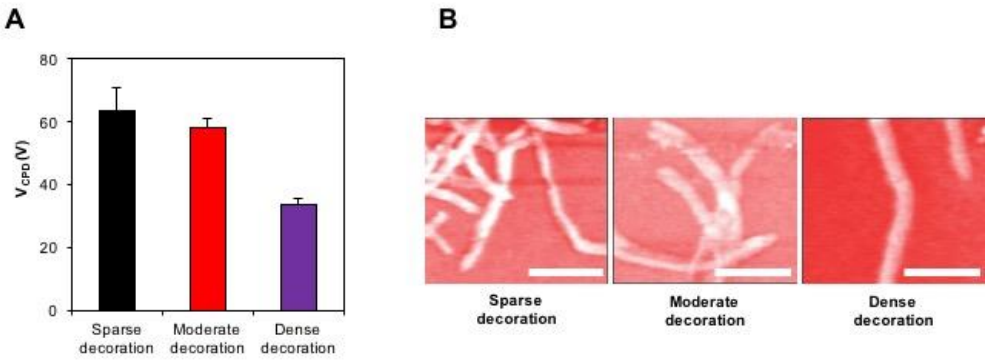

Figure S5.16: (A) Contact potential difference (CPD) between SKPM tip and single decorated nanofibers. Data represent mean ± standard error of the mean (n = 5 single nanofibers). (B) Corresponding CPD images. Scale bars, 2 µm.

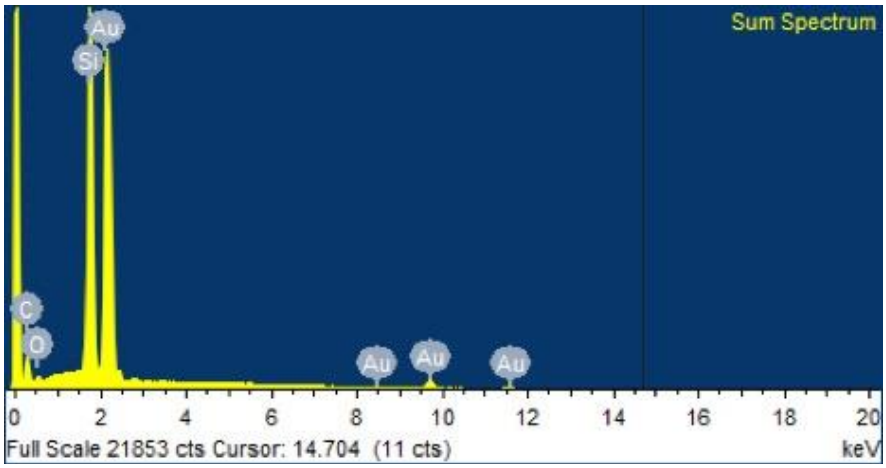

Figure S5.17: SEM-EDX analysis of a film of densely decorated nanofibers following water immersion and dehydration. The presence of Si is due to the substrate.

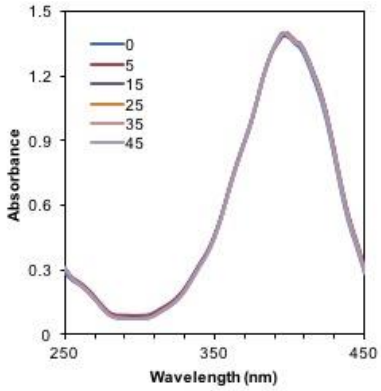

Figure S5.18: Time-dependent UV-Vis control spectra showing the absence of 4-nitrophenol conversion to 4-aminophenol in the presence of bare silicone rubber surface.

5.6: Acknowledgements

The authors acknowledge support from the Argentinian Friends of Tel Aviv University (T.G.), the European Research Council BISON project, the Israeli National Nanotechnology Initiative and Helmsley Charitable Trust (E.G.). We thank George Levi (Tel Aviv University) for high-resolution TEM analysis and Diana Golodnitsky (Tel Aviv University) for TGA. T.G thanks members of the Gazit group for helpful discussions. N.L.I. acknowledges support from the U.S. Department of Education Graduate Assistance in Areas of National Need Fellowship, administered through the Chemical Engineering and Materials Science Program at the UC Irvine. Research on this project was funded by the Air Force Office of Scientific Research, grant FA9550-14-1-0350 (N.L.I. and A.I.H.).

Author Contributions. T.G. and E.G. conceived and designed the experiments. T.G. planned and performed the experiments. N.L.I and A.I.H. measured and analyzed the electrical properties. S.F. and T.D. performed and analyzed the cardiac patch experiments. H.Y., R.D., B.V. and S.R. collected the NMR data and performed structure determination. T.G. and E.G. wrote the paper. All authors discussed the results and commented on the manuscript.

5.7: References

(1) Giltner, C. L.; Nguyen, Y.; Burrows, L. L. Type IV Pilin Proteins: Versatile Molecular Modules. *Microbiol. Mol. Biol. Rev. MMBR* **2012**, *76* (4), 740–772.

(2) Reguera, G.; McCarthy, K. D.; Mehta, T.; Nicoll, J. S.; Tuominen, M. T.; Lovley, D. R. Extracellular Electron Transfer via Microbial Nanowires. *Nature* **2005**, *435* (7045), 1098–1101.

(3) Cologgi, D. L.; Lampa-Pastirk, S.; Speers, A. M.; Kelly, S. D.; Reguera, G. Extracellular Reduction of Uranium via Geobacter Conductive Pili as a Protective Cellular Mechanism. *Proc. Natl. Acad. Sci.* **2011**, *108* (37), 15248–15252.

(4) Lovley, D. R. Electrically Conductive Pili: Biological Function and Potential Applications in Electronics. *Curr. Opin. Electrochem.* **2017**, *4* (1), 190–198.

(5) Richter, L. V.; Franks, A. E.; Weis, R. M.; Sandler, S. J. Significance of a Posttranslational Modification of the PilA Protein of Geobacter Sulfurreducens for Surface Attachment, Biofilm Formation, and Growth on Insoluble Extracellular Electron Acceptors. *J. Bacteriol.* **2017**, *199* (8).

(6) Craig, L.; Volkmann, N.; Arvai, A. S.; Pique, M. E.; Yeager, M.; Egelman, E. H.; Tainer, J. A. Type IV Pilus Structure by Cryo-Electron Microscopy and Crystallography: Implications for Pilus Assembly and Functions. *Mol. Cell* **2006**, *23* (5), 651–662.

(7) Kolappan, S.; Coureuil, M.; Yu, X.; Nassif, X.; Egelman, E. H.; Craig, L. Structure of the Neisseria Meningitidis Type IV Pilus. *Nat. Commun.* **2016**, *7*, 13015.

(8) Creasey, R. C. G.; Mostert, A. B.; Nguyen, T. A. H.; Virdis, B.; Freguia, S.; Laycock, B. Microbial Nanowires – Electron Transport and the Role of Synthetic Analogues. *Acta Biomater.* **2018**, *69*, 1–30.

(9) Guterman, T.; Kornreich, M.; Stern, A.; Adler-Abramovich, L.; Porath, D.; Beck, R.; Shimon, L. J. W.; Gazit, E. Formation of Bacterial Pilus-like Nanofibres by Designed Minimalistic Self-Assembling Peptides. *Nat. Commun.* **2016**, *7*, 13482.

(10) Kirsch, R.; Mertig, M.; Pompe, W.; Wahl, R.; Sadowski, G.; Böhm, K. J.; Unger, E. Three-Dimensional Metallization of Microtubules. *Thin Solid Films* **1997**, *305* (1), 248–253.

(11) Scheibel, T.; Parthasarathy, R.; Sawicki, G.; Lin, X.-M.; Jaeger, H.; Lindquist, S. L. Conducting Nanowires Built by Controlled Self-Assembly of Amyloid Fibers and Selective Metal Deposition. *Proc. Natl. Acad. Sci.* **2003**, *100* (8), 4527–4532.

(12) Patolsky, F.; Weizmann, Y.; Willner, I. Actin-Based Metallic Nanowires as Bio-Nanotransporters. *Nat. Mater.* **2004**, *3* (10), 692–695.

(13) Wei, G.; Reichert, J.; Jandt, K. D. Controlled Self-Assembly and Templated Metallization of Fibrinogen Nanofibrils. *Chem. Commun.* **2008**, *0* (33), 3903–3905.

(14) Plascencia-Villa, G.; Saniger, J. M.; Ascencio, J. A.; Palomares, L. A.; Ramírez, O. T. Use of Recombinant Rotavirus VP6 Nanotubes as a Multifunctional Template for the Synthesis of Nanobiomaterials Functionalized with Metals. *Biotechnol. Bioeng.* **2009**, *104* (5), 871–881.

(15) Orza, A.; Soritau, O.; Olenic, L.; Diudea, M.; Florea, A.; Rus Ciuca, D.; Mihu, C.; Casciano, D.; Biris, A. S. Electrically Conductive Gold-Coated Collagen Nanofibers for Placental-Derived Mesenchymal Stem Cells Enhanced Differentiation and Proliferation. *ACS Nano* **2011**, *5* (6), 4490–4503.

(16) Yang, T.; Zhang, Y.; Li, Z. Formation of Gold Nanoparticle Decorated Lysozyme Microtubes. *Biomacromolecules* **2011**, *12* (6), 2027–2031.

(17) Bolisetty, S.; Adamcik, J.; Heier, J.; Mezzenga, R. Amyloid Directed Synthesis of Titanium Dioxide Nanowires and Their Applications in Hybrid Photovoltaic Devices. *Adv. Funct. Mater.* **2012**, *22* (16), 3424–3428.

(18) Fang, G.; Yang, Y.; Yao, J.; Shao, Z.; Chen, X. Formation of Different Gold Nanostructures by Silk Nanofibrils. *Mater. Sci. Eng. C* **2016**, *64*, 376–382.

(19) Nyström, G.; Fernández-Ronco, M. P.; Bolisetty, S.; Mazzotti, M.; Mezzenga, R. Amyloid Templated Gold Aerogels. *Adv. Mater.* **2016**, *28* (3), 472–478.

(20) Banerjee, I. A.; Yu, L.; Matsui, H. Cu Nanocrystal Growth on Peptide Nanotubes by Biomineralization: Size Control of Cu Nanocrystals by Tuning Peptide Conformation. *Proc. Natl. Acad. Sci.* **2003**, *100* (25), 14678–14682.

(21) Reches, M.; Gazit, E. Casting Metal Nanowires Within Discrete Self-Assembled Peptide Nanotubes. *Science* **2003**, *300* (5619), 625–627.

(22) Gottlieb, D.; Morin, S. A.; Jin, S.; Raines, R. T. Self-Assembled Collagen-like Peptide Fibers as Templates for Metallic Nanowires. *J. Mater. Chem.* **2008**, *18* (32), 3865–3870.

(23) Lamm, M. S.; Sharma, N.; Rajagopal, K.; Beyer, F. L.; Schneider, J. P.; Pochan, D. J. Laterally Spaced Linear Nanoparticle Arrays Templated by Laminated β-Sheet Fibrils. *Adv. Mater.* **2008**, *20* (3), 447–451.

(24) Kasotakis, E.; Mossou, E.; Adler-Abramovich, L.; Mitchell, E. P.; Forsyth, V. T.; Gazit, E.; Mitraki, A. Design of Metal-Binding Sites onto Self-Assembled Peptide Fibrils. *Biopolymers* **2009**, *92* (3), 164–172.

(25) Sone, E. D.; Stupp, S. I. Bioinspired Magnetite Mineralization of Peptide−Amphiphile Nanofibers. *Chem. Mater.* **2011**, *23* (8), 2005–2007.

(26) Ceylan, H.; Ozgit-Akgun, C.; Erkal, T. S.; Donmez, I.; Garifullin, R.; Tekinay, A. B.; Usta, H.; Biyikli, N.; Guler, M. O. Size-Controlled Conformal Nanofabrication of Biotemplated Three-Dimensional TiO_2 and ZnO Nanonetworks. *Sci. Rep.* **2013**, *3*, 2306.

(27) Li, C.; Adamcik, J.; Mezzenga, R. Biodegradable Nanocomposites of Amyloid Fibrils and Graphene with Shape-Memory and Enzyme-Sensing Properties. *Nat. Nanotechnol.* **2012**, *7* (7), 421–427.

(28) Kosmulski, M. The pH Dependent Surface Charging and Points of Zero Charge. VI. Update. *J. Colloid Interface Sci.* **2014**, *426*, 209–212.

(29) Sun, W.; Yang, J.; Zhu, J.; Zhou, Y.; Li, J.; Zhu, X.; Shen, M.; Zhang, G.; Shi, X. Immobilization of Iron Oxide Nanoparticles within Alginate Nanogels for Enhanced MR Imaging Applications. *Biomater. Sci.* **2016**, *4* (10), 1422–1430.

(30) Sharpe, E.; Bradley, R.; Frasco, T.; Jayathilaka, D.; Marsh, A.; Andreescu, S. Metal Oxide Based Multisensor Array and Portable Database for Field Analysis of Antioxidants. *Sens. Actuators B Chem.* **2014**, *193*, 552–562.

(31) Song, W.; Shi, D.; Tao, S.; Li, Z.; Wang, Y.; Yu, Y.; Qiu, J.; Ji, M.; Wang, X. Bio-Inspired Immobilization of Metal Oxides on Monolithic Microreactor for Continuous Knoevenagel Reaction. *J. Colloid Interface Sci.* **2016**, *481*, 100–106.

(32) Leang, C.; Qian, X.; Mester, T.; Lovley, D. R. Alignment of the c-Type Cytochrome OmcS along Pili of Geobacter Sulfurreducens. *Appl. Environ. Microbiol.* **2010**, *76* (12), 4080–4084.

(33) Qian, X.; Mester, T.; Morgado, L.; Arakawa, T.; Sharma, M. L.; Inoue, K.; Joseph, C.; Salgueiro, C. A.; Maroney, M. J.; Lovley, D. R. Biochemical Characterization of Purified OmcS, a c-Type Cytochrome Required for Insoluble Fe(III) Reduction in Geobacter Sulfurreducens. *Biochim. Biophys. Acta BBA - Bioenerg.* **2011**, *1807* (4), 404–412.

(34) Tan, Y. N.; Lee, J. Y.; Wang, D. I. C. Uncovering the Design Rules for Peptide Synthesis of Metal Nanoparticles. *J. Am. Chem. Soc.* **2010**, *132* (16), 5677–5686.

(35) Eustis, S.; El-Sayed, M. A. Why Gold Nanoparticles Are More Precious than Pretty Gold: Noble Metal Surface Plasmon Resonance and Its Enhancement of the Radiative and

Nonradiative Properties of Nanocrystals of Different Shapes. *Chem. Soc. Rev.* **2006**, *35* (3), 209–217.

(36) Pauling, L. The Metallic Orbital and the Nature of Metals. *J. Solid State Chem.* **1984**, *54* (3), 297–307.

(37) Heilmann, A. *Polymer Films with Embedded Metal Nanoparticles*; Springer: New York, 2003.

(38) Li, C.; Bolisetty, S.; Mezzenga, R. Hybrid Nanocomposites of Gold Single-Crystal Platelets and Amyloid Fibrils with Tunable Fluorescence, Conductivity, and Sensing Properties. *Adv. Mater.* **2013**, *25* (27), 3694–3700.

(39) Lyu, J.; Wang, X.; Liu, L.; Kim, Y.; Tanyi, E. K.; Chi, H.; Feng, W.; Xu, L.; Li, T.; Noginov, M. A.; et al. High Strength Conductive Composites with Plasmonic Nanoparticles Aligned on Aramid Nanofibers. *Adv. Funct. Mater.* **2016**, *26* (46), 8435–8445.

(40) Li, J.; Liu, H.; Guo, J.; Hu, Z.; Wang, Z.; Wang, B.; Liu, L.; Huang, Y.; Guo, Z. Flexible, Conductive, Porous, Fibrillar Polymer–gold Nanocomposites with Enhanced Electromagnetic Interference Shielding and Mechanical Properties. *J. Mater. Chem. C* **2017**, *5* (5), 1095–1105.

(41) Stoneham, A. M.; Tasker, P. W. Metal-Non-Metal and Other Interfaces: The Role of Image Interactions. *J. Phys. C Solid State Phys.* **1985**, *18* (19), L543.

(42) Silberbush Ohad; Amit Moran; Roy Subhasish; Ashkenasy Nurit. Significant Enhancement of Proton Transport in Bioinspired Peptide Fibrils by Single Acidic or Basic Amino Acid Mutation. *Adv. Funct. Mater.* **2017**, *27* (8), 1604624.

(43) Kulkarni, D. D.; Kim, S.; Chyasnavichyus, M.; Hu, K.; Fedorov, A. G.; Tsukruk, V. V. Chemical Reduction of Individual Graphene Oxide Sheets as Revealed by Electrostatic Force Microscopy. *J. Am. Chem. Soc.* **2014**, *136* (18), 6546–6549.

(44) Aditya, T.; Pal, A.; Pal, T. Nitroarene Reduction: A Trusted Model Reaction to Test Nanoparticle Catalysts. *Chem. Commun.* **2015**, *51* (46), 9410–9431.

(45) Mei, Y.; Lu, Y.; Polzer, F.; Ballauff, M.; Drechsler, M. Catalytic Activity of Palladium Nanoparticles Encapsulated in Spherical Polyelectrolyte Brushes and Core−Shell Microgels. *Chem. Mater.* **2007**, *19* (5), 1062–1069.

(46) Gechele, G. B.; Convalle, G. Antistatic Polystyrene. *J. Appl. Polym. Sci.* **1964**, *8* (2), 801–811.

(47) Fleischer, S.; Dvir, T. Tissue Engineering on the Nanoscale: Lessons from the Heart. *Curr. Opin. Biotechnol.* **2013**, *24* (4), 664–671.

(48) Dvir, T.; Timko, B. P.; Kohane, D. S.; Langer, R. Nanotechnological Strategies for Engineering Complex Tissues. *Nat. Nanotechnol.* **2011**, *6* (1), 13–22.

(49) Bian, W.; Jackman, C. P.; Bursac, N. Controlling the Structural and Functional Anisotropy of Engineered Cardiac Tissues. *Biofabrication* **2014**, *6* (2), 024109–024109.

(50) Ing, N. L.; Nusca, T. D.; Hochbaum, A. I. Geobacter Sulfurreducens Pili Support Ohmic Electronic Conduction in Aqueous Solution. *Phys. Chem. Chem. Phys.* **2017**, *19* (32), 21791–21799.

(51) Ing, N. L.; Spencer, R. K.; Luong, S. H.; Nguyen, H. D.; Hochbaum, A. I. Electronic Conductivity in Biomimetic α-Helical Peptide Nanofibers and Gels. *ACS Nano* **2018**, *12* (3), 2652-2661.

CHAPTER 6 Summary and Conclusions

The work herein reviews the current mechanistic framework for long-range (micrometer scale) electronic transport in amino acid based materials, demonstrates how current examples of long-range peptide and protein based supramolecular materials do or do not fit within this mechanistic framework, and explores in depth four examples of long-range amino acid based conductors.

Two of the systems we explored, *Geobacter sulfurreducens* pili and non-π-stacked α-helical nanofibers from a *de novo* peptide sequence, do not fit the current models for long-range transport. They demonstrate non-thermally activated transport across distances that are orders of magnitude farther than would be expected for a non-hopping mechanism. Additional conductivity studies with the non-π-stacked α-helical nanofibers confirm that transport is not proton- or ion-mediated and is therefore electronic. Additionally, conductivities in these two systems are comparable to conjugated polymers and higher than many peptide-conjugate hybrids, illustrating a type of conduction which may be unique to pure amino acid systems. Although the mechanism for transport remains to be determined, our findings suggest that an α-helical secondary structure and a well-defined supramolecular structure may be significant for transport. Aromatic amino acids may also be important for conduction, although, contrary to most organic polymers, delocalization does not appear to be required for high conductivities.

We also explored two amino acid based systems which do fit within the current mechanistic framework of long-range conductive materials. In both systems, the amino acid components offer a self-assembly route for the tunable assembly of covalently conductive components, such as a conjugated small molecule (NDI) and Au nanoparticles. In the peptide-hybrid conjugated system, the amino acid component can be selected to tune the enzymatic assembly and disassembly

dynamics and geometry of the resultant conjugated nanostructure(s). The presence of delocalization due to the NDI components suggests bandlike conduction; however, unlike pure NDI nanostructures, this hybrid system is water soluble and offers dynamic functionality. These features suggest that this system may be a promising platform for bioelectronics applications requiring transient or impermanent structures, such as therapeutic or neuronal scaffolds. In the Au nanoparticle system, the natural metal-reducing properties of amino acids facilitated the self-assembly of gold-covered peptide nanofibers. The amount of gold coverage could be varied based on the ratios of peptide to gold ion. The moderate to high surface area coverage of the nanofibers and temperature dependence data suggested that gold coverage was sufficient to form continuous electronic states for metallic-like band conduction. Films of these gold-covered nanofibers exhibited unique electrostatic and selective binding properties, which may also be relevant in bioelectronics applications. Additionally, they demonstrated biocompatibility in facilitating the synchronized growth of cardiac cells.

In conclusion, these findings suggest that amino acid based materials may be a highly functional and viable platform for developing bioelectronic technologies. Although the mechanism of transport through the biological and biomimetic α-helical nanofibers remains unknown, these two systems uniquely demonstrate high conductivities in a pure amino acid system. In our characterization of hybrid amino acid based materials, we have demonstrated that amino acid components can provide unique, tunable properties to the resultant nanostructures. This combination of biological functionality and electronic conductivity may therefore be capable of bridging the materials divide between biology and electronics.